Recovery and analysis of director profiles in liquid crystal cells

Submitted by

Stephen Leslie Cornford

Abstract

This thesis is concerned with the determination of the director profile within a nematic liquid crystal cell from optical experiments. The larger part of the work details the development of computational methods which can be used to find the director profile, and the application of these tools to the fully leaky guided mode experiment. In a second part, a simple conoscopic device is built, and then used to undertake a novel viscodynamic experiment.

In essence, the fully leaky guided mode experiments and its relatives measure the dependence of the transmission and reflection coefficients of a liquid crystal cell upon incident angle. It is simple enough to calculate these coefficients if the director profile is known, but experimentalists actually need to achieve the opposite. That is, having measured the transmission and reflection coefficients, they must determine the director profile. However, this turns out to be an ill-posed problem, and so some additional information about the director profile is required.

There is indeed an appropriate source of additional information - the continuum theory of nematic liquid crystals - and it is exploited here to develop two computational tools. In the first, it is used to adapt a mathematical technique, Tikhonov regularization, to both steady-state and time-dependent situations, so that director profiles can be recovered having made only weak assumptions about their behaviour. A second tool makes stronger assumptions and can be deployed after the first to estimate some of the unknown parameters which appear in the continuum theory.

These tools are use in the first instance to analyze data drawn from two fully leaky guided mode experiments. In the first experiment, a hybrid aligned cell was measured during AC switching, and from its data director profiles and several phenomenological parameters including four viscosities are determined. Following that, the DC switching of the same cell is studied, which turns out to be critically affected by the motion of tiny concentrations of charged impurities. Then, having noted that only limited information about the director profile can be recovered from even the most elaborate optical experiment, a conoscopy experiment is designed to recover it quickly. Following this approach, a previously unknown flow-induced transition between topologically distinct states in a homoetropically aligned cell is observed.

Acknowledgements

It seems quite likely that a list of acknowledgments in any PhD thesis begins with the supervisor. I do think that Roy Sambles deserves that place more than most. Throughout my time as his student, other students complained to me that their owns supervisors were so elusive that some kind of exclusion principle was to be suspected. But if I managed to go a whole week without a discussion with Roy, I was probably on holiday.

Tim Taphouse, who started his PhD two years before me, also deserves special credit. Without his experimental data I might well be presenting tests of the computational techniques developed in this thesis against synthetic data - a serious crime, perhaps. Thanks are also due to Fuzi Yang and Pete Cann, who built a number of the samples I used in chapter 7, including one at about 3 hours notice after a mishap.

Chris Newton at HP Labs really started the ball rolling on this thesis, and was always a source of theoretical and computational assistance. Also at HP Labs, Steve Kitson, John Rudin, Tim Spiller, Suzanne Klein, David Sikharulidze and Adrian Geisow all had something to say at the regular CASE meetings held there.

Fellow School of Physics basement dwellers John Birkett and Tim Atherton kept me entertained for my first year, posing the philosophical question 'Is physical force acceptable punishment for poor password choice?'. Sharon Jewell didn't live in the basement, but remained, along with Lizhen Ruan, a valuable ally. I'd also like to thank Ian Hooper for coming downstairs from time to time, but never distracting me for more than, say, four hours at once. Fellow pirates Baptiste Augie and Martyn Gadsdon always joined me for a rousing chorus of 'R', while Matt Lockyear (the Roger Mellie of the microwave regime) always knew where coffee was to be had. Bill Barnes, George Zorinyants, Euan Hendry, Alistair Hibbins, Gemma Winter, Andy Murray, James Parsons, Tom Isaac, Ciarán Stewart, Stephen Luke, Chris Burrows, Tom Constant, James Edmunds, Melita Taylor and Ed Stone all had to put up with singular value decomposition at various times, so kudos to them.

University of Exeter people beyond the immediate research group who had advice at various times include G P Srivastava, Bob Jones, and Hamid Dehghani. Further afield, Bill Lionheart helped me understand what an inverse problem was right at the start. Nigel Mottram had a useful suggestion practically every time I encountered him, as did Paul Brimicombe. I also had useful discussions with Andrew Smith, Claus Kischka and Christophe Trabi.

The work described in this thesis was funded by an EPSRC CASE award in conjunction with HP Labs, Bristol.

Lowering himself suddenly to his knees he placed his right eye at the keyhole, and controlling the oscillation of his head and the vagaries of his left eye (which was for ever trying to dash up and down the vertical surface of the door), he was able by dint of concentration to observe, within three inches of his keyholed eye, an eye which was *not* his, being not only of a different colour to his own iron marble but being, which is more convincing, on the other side of the door.

— **Mervyn Peake, Titus Groan**

To Cathey,

Contents

List of Figures

Chapter 1

Introduction

At the time of writing, most small- to medium-size displays were liquid crystal devices, from digital watches [1], to PC monitors and small televisions. It is quite possible that organic light emitting diode technology [2] will soon consign liquid crystal displays (LCDs) to the same lay-bys and landfill sites now filled with cathode-ray tube monitors. In the meantime, research and development efforts to improve LCDs go on, to which the work presented in this thesis is intended to contribute.

This chapter introduces some basic liquid crystal physics. Various liquid crystal mesophases are introduced in section 1.1 before concentrating upon the physics of one particular mesophase, the nematic phase, in section 1.2. Liquid crystal cells, experimental models of display devices, are discussed in section 1.3. Section 1.4 sets out the remainder of the thesis.

1.1 Liquid crystal mesophases

A range of materials form one or more liquid crystal mesophases, that is, phases which behave partly like liquids, and partly like crystalline solids. The first such phase was reported at the end of the 19th century, when Reinitzer noticed that upon heating, Cholesterol Benzoate melted first into a cloudy liquid, then turned into a clear liquid at a higher temperature [3, 4]. Subsequent analysis by Lehmann showed that the cloudy liquid was *birefringent*, that is, its refractive index appeared to depend upon the polarization state of light passing through it, a property hitherto only observed in crystalline solids [5].

Cholesterol Benzoate is an example of a *thermotropic* liquid crystal, a material which forms a mesophase in a particular temperature range. All current displays utilize thermotropic materials. Another class of materials form *lyotropic* mesophases, that is, in solution at particular concentrations. While only thermotropic materials will be studied in this thesis, it is interesting to note that lyotropic phases played a part in one of the

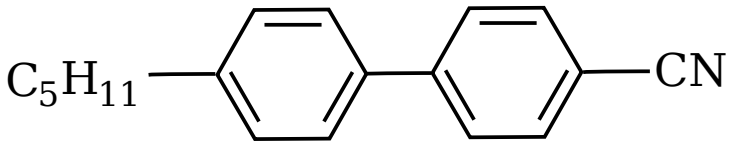

Figure 1.1: Molecular structure of 5CB. 5CB is a calamitic material - it has one long and two short axes.

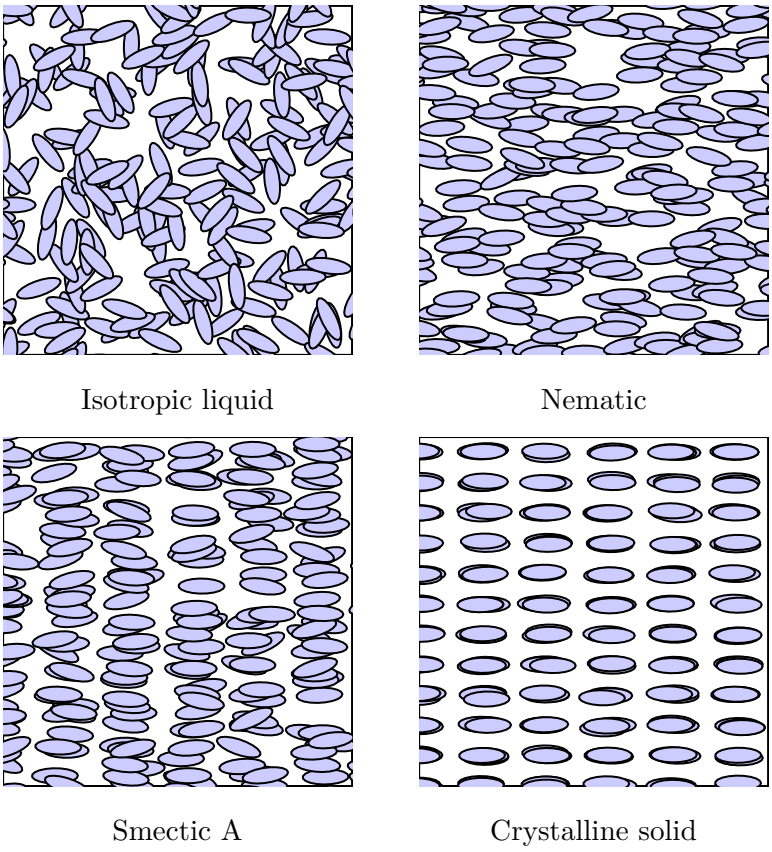

Figure 1.2: Schematics of the liquid, nematic, smectic A and crystalline phases. Each ellipse represents a calamitic molecule.

most important scientific discoveries of the twentieth century. The tobacco mosaic virus was the first pathogen known not to be bacterial - it was the first RNA virus known as such - and this discovery relied in part upon its forming a liquid crystal mesophase [6, 7].

Thermotropic liquid crystals are composed of molecules which have some sort of axis. These molecules may be *calamitic* - shaped like rods , or *discotic* - shaped like discs. Calamitic molecules, such as the 5CB molecule represented in figure 1.1, are the more widely used in display devices [8, 9], and are considered in this thesis. Both types of thermotropic material are capable of possessing *orientational order*, where the molecular axes - the single long axis in the case calamitic molecules and the single short axis in the discotic case - are aligned to some extent.

Calamitic molecules can form a number of mesophases, distinguished from each other, and from the familiar liquid and crystalline solid phases by their structure [10]. These are true phases of matter - the material passes from one to the other sharply, at a given temperature, rather than gradually changing from one to the other. In the liquid phase, molecules are distributed, and aligned, randomly: such a structure must be isotropic (figure 1.2, top left). Upon cooling, a *nematic* phase might be seen, where molecules are still distributed randomly but possess orientational order (figure 1.2, top right). 5CB is found in the nematic phase between 24°C and 35°C. Cholesterol Benzoate forms a *cholesteric* phase, a variation on the nematic phase, where the direction of alignment rotates about an axis perpendicular to itself. Cooling further, various *smectic* phases are known which exhibit limited positional order as well as orientational order. Molecules tend to be stacked in layers, but are otherwise randomly distributed. There are many smectic phases, including the smectic A phase, where molecules are, on average, aligned at right angles to their layers (figure 1.2, bottom left) and the smectic C phase, where molecules are inclined within their layer. Finally, the crystalline phase is reached, when molecules are distributed over lattice sites, and are aligned (figure 1.2, bottom right).

1.2 Nematic liquid crystals

1.2.1 The director

The continuum description of nematic liquid crystals used throughout this thesis, and widely reviewed in the literature [11–13] revolves around *the director*. This is a unit vector $\boldsymbol{n}$, which lies parallel to the molecular axis averaged over a small (but macroscopic) volume. $\boldsymbol{n}$ may vary, both in space ($\boldsymbol{r}$), and in time (t), and one thrust of continuum theory is to determine differential equations which govern such variations. The term *director profile* is often used to refer to spatial variations in $\boldsymbol{n}$.

Since $\boldsymbol{n}$ is a unit vector, it can be described by two *Euler angles*, the tilt angle θ and the twist angle, ϕ. As usual in the Exeter group, the tilt angle is measured from the $z-$axis in this thesis: many others chose to measure it from the $x-$axis. The twist angle is defined to be the angle between the projection of $\boldsymbol{n}$ onto the xy-plane, and the $x-$axis. Expressing $\boldsymbol{n}$ in terms of these angles,

$$\boldsymbol{n} = (\sin\theta\cos\phi, \sin\theta\sin\phi, \cos\theta) \tag{1.1}$$

Although the director is used exclusively in this thesis, there are some specific limitations to it. The first is quite simple - the local molecular distrubtion is not, on average,

polar, so only theories unaffected by replacing $\boldsymbol{n}$ with $-\boldsymbol{n}$ are valid. A number of other limitations are discussed below.

1.2.1.1 The order parameter

Rather than sitting in perfect alignment with the director, the long axis of each molecule is inclined at an angle θ_m which fluctuates thermally. Zwetkoff's order parameter

$$S = \frac{1}{2}\left\langle 3\cos^2\theta_m - 1 \right\rangle \tag{1.2}$$

where the angle brackets imply a thermal average, is used to describe these fluctuations on a macroscopic scale [14]. It varies from 0 in the isotropic phase, through intermediate values in the nematic phase, to 1 in the ideal crystalline phase. Ultimately, S is a measure of anisotropy which depends upon temperature, and quantities such as the dielectric anisotropy ϵ_a discussed in 1.2.4 depend upon it. It is crucial in describing the liquid-nematic phase transition [15], for example, but plays only a limited role in the kind of experiments considered in this thesis - through temperature dependence.

1.2.1.2 Uniaxial versus biaxial media

So far, exclusively *uniaxial* media, that is, media with a single director and a single order parameter have been considered. However, liquid crystals may be *biaxial* - described by two mutually orthogonal directors, $\boldsymbol{n}$ and $\boldsymbol{m}$, and two order parameters, S_1 and S_2. The molecules themselves might be biaxial - book-shaped, rather than rod-shaped, for example, or a mixture of rod- and disc- shaped particles [16]. Even if the molecules are uniaxial, they can form biaxial arrangements [17]

1.2.1.3 Defects

As in a solid crystal, discontinuities of the director, or defects, are commonly seen in liquid crystals. The director in a solid crystal is constant in a given grain, and changes abruptly at the grain surfaces. In contrast, the best known defects of the nematic states, *disclinations*, are line singularities, where $S = 0$ along a contour [18]. Between defects, the director varies smoothly. Friedel [10] named the nematic phase after distinctive dark threads radiating out from nuclei - from the Greek $\nu\eta\mu\alpha$, or thread - which are seen if a thin film of nematic material is examined in a polarising microscope (figure 1.3). The nuclei are the disclinations, viewed along their axis, while the dark threads are curves along which the director is parallel to either the polarizer or analyzer. Since the director is undefined at defects, no theory based exclusively on $\boldsymbol{n}$ will be able to describe them.

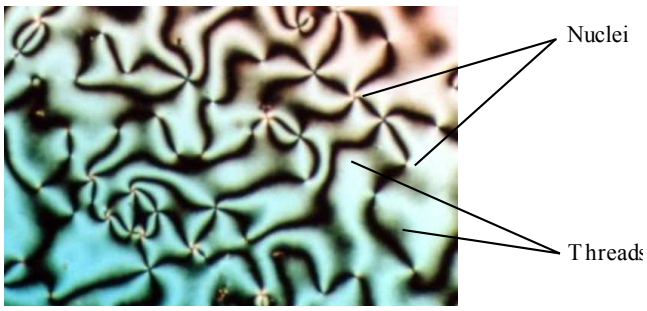

Figure 1.3: Schleiren texture of a nematic film Schleiren - German for 'smeared' - textures are seen when a thin nematic film is viewed under a polarising microscope. The nuclei are line disclinations, viewed along their axis, while the dark threads are curves along which the director parallel to either the polarizer or analyzer. The photograph is licensed from Minutemen under the Creative Commons Attribution ShareAlike 2.5 License (`http://creativecommons.org/licenses/by-sa/2.5/`). It can be found at `http://en.wikipedia.org/wiki/Image:Nematische_Phase_Schlierentextur.jpg`.

1.2.1.4 The Q-tensor

Many of the limitations above can be resolved by describing the liquid crystal in terms of the Q-tensor [19], whose components are

$$Q_{ij} = S_1 n_i n_j + S_2 m_i m_j - \frac{1}{3}(S_1 + S_2)\delta_{ij} \tag{1.3}$$

which reduces to

$$Q_{ij} = S(n_i n_j - \frac{1}{3}\delta_{ij}) \tag{1.4}$$

in the uniaxial case. Q_{ij} is unchanged when $\boldsymbol{n}$ is swapped with $-\boldsymbol{n}$, and because it includes the order parameters, it can describe defects as well.

1.2.2 Surface alignment

When a liquid crystal comes into contact with a solid surface, the director will tend to adopt some preferred direction [20, 21]. If $\boldsymbol{n}$ is normal to the interface, then the alignment is termed *homeotropic*. Homeotropic alignment occurs on a clean, flat glass surface [22], or on glass coated with a thin layer of a surfactant, lecithin for example. The opposite case is *planar* alignment, where $\boldsymbol{n}$ lies in the plane of the interface. This is divided into three types - *planar degenerate*, where the director may adopt any direction within the plane and which leads to the Schleiren texture - *planar homogeneous*, where there is single preferred direction - and *planar heterogeneous*, where there are multiple preferred directions [23]. Only planar homogeneous alignment is considered in this thesis: it can be attained by rubbing either glass, or, more effectively, glass coated with polyimide, forming parallel grooves [24, 25]. It is often referred to simply as planar, or homogeneous alignment.

An assumption made throughout this thesis is that whatever forces impinge upon a bulk liquid crystal, they are weak compared to the forces which promote alignment at surfaces. In other words, differential equations in $\boldsymbol{n}$ are solved to find the director profile within a sample alongside boundary conditions which prescribe $\boldsymbol{n}$ at its boundary. More generally, changing the director near the surface carries an energetic cost, which may be similar to the cost of changes to the bulk. In that case, boundary conditions are derived from an ansatz for the surface energy density, ω_s, such as the formula

$$\omega_s = \frac{1}{2} W_\theta \sin^2(\theta_a - \theta_0) \tag{1.5}$$

due to Rapini and Papoular [26]. Here, θ_a is the preferred tilt angle at the surface, θ_0 the actual angle, and W_θ is an *anchoring strength*. Minimising the sum of the surface and bulk energies leads to a relationship between $\boldsymbol{n}$ and its gradient at the boundary, rather than a simple prescription of $\boldsymbol{n}$.

1.2.3 Elastic energy

Any region of a nematic liquid crystal will have elastic energy due to spatial variation in the director. An appropriate free energy density, ω_F, can be computed by an expression due to Frank [18], and, earlier, Oseen [27]. In cartesian tensor notation[1],

$$\begin{aligned}\omega_F = \frac{1}{2} k_{11} (n_{i,i})^2 + \frac{1}{2} k_{22} (n_i \varepsilon_{ijk} n_{j,k})^2 + \frac{1}{2} k_{33} |n_j n_{i,j} - n_j n_{j,i}|^2 \\ + \frac{1}{2}(k_{22} + k_{24})(n_i n_{j,i} - n_{i,i} n_j)_{,j}.\end{aligned} \tag{1.6}$$

or, in the more familar vector notation,

$$\begin{aligned}\omega_f = \frac{1}{2} k_{11} (\boldsymbol{\nabla}.\boldsymbol{n})^2 + \frac{1}{2} k_{22} (\boldsymbol{n}.\boldsymbol{\nabla} \times \boldsymbol{n})^2 + \frac{1}{2} k_{33} |\boldsymbol{n} \times \boldsymbol{\nabla} \times \boldsymbol{n}|^2 \\ + \frac{1}{2}(k_{22} + k_{24}) \boldsymbol{\nabla}.(\boldsymbol{n}.\boldsymbol{\nabla}\boldsymbol{n} - \boldsymbol{n}\boldsymbol{\nabla}.\boldsymbol{n})\end{aligned} \tag{1.7}$$

This *Frank free energy* is, in essence, a form of Hooke's law, in that restoring torques are proportional to gradients in the director, and so the elastic energy is quadratic in said gradients. Its precise form was found by considering all possible contributions to a quadratic function of the components of $\boldsymbol{\nabla}\boldsymbol{n}$ which are invariant under a change of coordinate system and which do not change if $\boldsymbol{n}$ is replaced with $-\boldsymbol{n}$.

Although the Frank energy is quite complex, it does encapsulate an important, but

[1] Cartesian tensor notation is used in this chapter because it is compact. It expresses a vector $\boldsymbol{v}$ by its components v_i, $i = x, y, y$, tensors of second rank by their components t_{ij}, and so on. $\boldsymbol{\nabla}\boldsymbol{v}$ is a second rank tensor, its components are written $v_{i,j}$. Einstein's summation is employed, where a repeated index indicates a sum over all three components, so that, for example, $\boldsymbol{\nabla}.\boldsymbol{v} = v_{j,j}$.

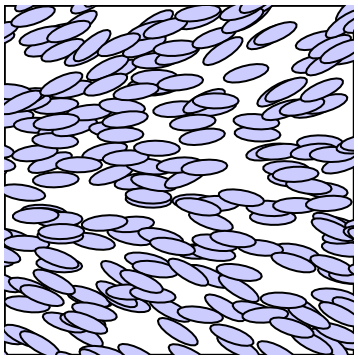

Splay: $\boldsymbol{\nabla}.\boldsymbol{n} \neq 0$, $\boldsymbol{\nabla} \times \boldsymbol{n} = 0$

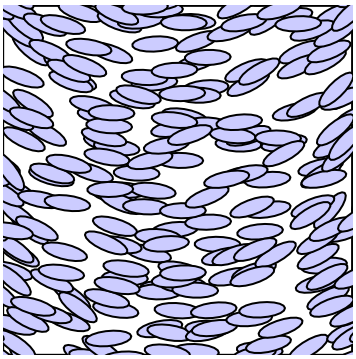

Bend: $\boldsymbol{n}$ is perpendicular to $\boldsymbol{\nabla} \times \boldsymbol{n}$, $\boldsymbol{\nabla}.\boldsymbol{n} = 0$

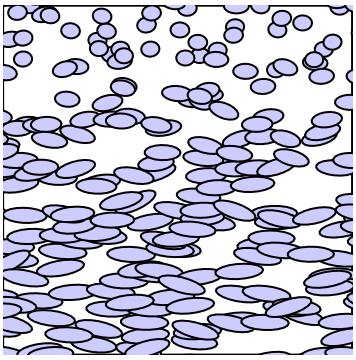

Twist: $\boldsymbol{n}$ is parallel to $\boldsymbol{\nabla} \times \boldsymbol{n}$, $\boldsymbol{\nabla}.\boldsymbol{n} = 0$

Figure 1.4: Schematics of splay, twist, and bend distortions in a nematic liquid crystal.

simple, property of nematic liquid crystals. It depends upon the square of gradients in $\boldsymbol{n}$ so that in thermodynamic equilibrium the director tends to become uniform if free to do so. If a sample is confined between surfaces which promote a different type of alignment, the total energy in the sample is smallest when the director varies smoothly.

The first three terms in (1.6) are known as the splay, twist, and bend energies respectively. Figure 1.4 shows three variations in $\boldsymbol{n}$, which are associated, individually, with these. The fourth term, the saddle-splay energy, ultimately, depends only on the surface conditions of a given sample, and plays no role in this thesis. The coefficients k_{11}, k_{22} and k_{33} are *phenomenological*. They are not computed from first principles, but instead must be measured (much like Young's modulus) for a given material at a given temperature and pressure. They do, of course, depend upon the order parameter, S, in that they are all zero in the isotropic phase, and increase as temperature decreases.

1.2.4 Dielectric anisotropy

Looking at figure 1.2 (top right), it is easy enough to imagine that a horizontal electric field will experience a different permittivity to a vertical electric field. *Dielectric anisotropy* is responsible for two major phenomena: birefringence, and a tendency of the liquid crystal

to be aligned by electric fields. Alignment by magnetic fields is conceptually similar, and was studied first [28].

As in any dielectric, the energy density due to the presence of an electric field $\boldsymbol{E}$ is

$$\omega_E = \frac{1}{2} D_i E_i. \tag{1.8}$$

The anisotropy of the liquid crystal is realised through the electric displacement, whose components are

$$D_i = \epsilon_{ij} E_j = (\epsilon_\perp \delta_{ij} + (\epsilon_\parallel - \epsilon_\perp) n_i n_j) E_j. \tag{1.9}$$

The two coefficients $\epsilon_\parallel$and $\epsilon_\perp$are, like the elastic constants, phenomenological. Because the difference $\epsilon_\parallel$- $\epsilon_\perp$appears so frequently in the continuum theory, it is often written ϵ_a (or $\Delta\epsilon$). It is called the dielectric anisotropy - when it is non-zero, an electric field experiences a relative permittivity which depends upon its direction.

The values of these coefficients vary greatly with the frequency of the applied field - each material has a *dielectric spectrum*. Different physical processes dominate the tensor of polarizability as the frequency changes, typically re-orientation of molecular dipoles at low frequencies (< 100 kHz), and electronic polarization in the optical regime. In the case of 5CB at room temperature, a constant electric field experiences $\epsilon_\perp \approx 7$ and $\epsilon_a \approx 11.5$, while at optical frequencies, $\epsilon_\perp \approx 2.3$, much like glass, and $\epsilon_a \approx 0.5$. Another material discussed in this thesis, Merck ZLI-4788-000, - a mixture, unlike elemental 5CB, has similar optical properties but at low frequencies $\epsilon_a \approx -5$. Dual frequency materials, such as Merck MDA-00-3969, exhibit both positive and negative ϵ_a at low frequencies [29, 30].

When the electric field is parallel to $\boldsymbol{n}$, the electric displacement is simply

$$\boldsymbol{D} = \epsilon_\parallel \boldsymbol{E}. \tag{1.10}$$

This resembles the expression for $\boldsymbol{D}$ in an isotropic material with a relative permittivity $\epsilon_\parallel$. Because this condition is rather specific, the director is said to point along the extraordinary direction, and $\epsilon_\parallel$is known as the extraordinary relative permittivity. On the other hand, if the electric field is perpendicular to $\boldsymbol{n}$, the relative permittivity is $\epsilon_\perp$. This is a less specific condition: $\boldsymbol{E}$ need only be parallel to a particular plane. Thus, $\epsilon_\perp$is the ordinary relative permittivity.

1.2.4.1 Alignment by electric fields

As suggested earlier, dielectric anisotropy drives a change in $\boldsymbol{n}$ under the influence of an electric field. In the absence of constraints, a sample of liquid crystal has a lower

energy density if the director is aligned either parallel to $\boldsymbol{E}$, when $\epsilon_a > 0$ (as in 5CB), or perpendicular to it, when $\epsilon_a < 0$. For typical liquid crystals, ω_E is comparable to ω_F when the potential difference across the sample is about one volt, so by applying a moderate field, the director can be aligned.

1.2.4.2 Birefringence

Birefringence is also linked to dielectric anisotropy. An electromagnetic wave propagating in the $z-$ direction through a uniform sample where the director is parallel to the $x-$axis, is described by the equations

$$\frac{\partial^2 E_x}{\partial z^2} = \frac{\epsilon_\parallel}{c^2}\frac{\partial^2 E_x}{\partial t^2} \tag{1.11}$$

$$\frac{\partial^2 E_y}{\partial z^z} = \frac{\epsilon_\perp}{c^2}\frac{\partial^2 E_y}{\partial t^2} \tag{1.12}$$

It is clear from these expressions that the phase velocity of a wave polarized parallel to the $x-$axis, or more generally the *extraordinary wave*, is different from a wave polarized parallel to the $y-$axis, the *ordinary wave*. Light polarized in an arbitrary direction is split into ordinary and extraordinary components. For the extraordinary wave, the refractive index is $n_\perp = \sqrt{\epsilon_\perp}$ while the ordinary wave experiences a refractive index $n_\parallel = \sqrt{\epsilon_\parallel}$. The difference between the two refractive indices, $\Delta n = n_\parallel - n_\perp$, is the known as the birefringence magnitude, or sometimes simply the birefringence, of the material.

Having passed through a film of thickness h, the phase difference between the fastest and slowest propagating polarization components is ([31] p827):

$$\delta = k_0 \Delta n h, \tag{1.13}$$

where

$$k_0 = \frac{2\pi}{\lambda}, \tag{1.14}$$

and λ is the wavelength. Therefore, linearly polarized light entering a sample of birefringent material will exit the sample elliptically polarized - unless δ is an integer multiple of π, in which case it is linearly polarized, or an odd-integer muliple of $\pi/2$, when it is circularly polarized. If the sample is placed between crossed polarizers, some proportion of light may pass through the entire system, depending upon the orientation of the director. Neglecting any reflections, the fraction of light transmitted is

$$\frac{I}{I_0} = 2\sin^2\psi\cos^2\psi(cos\delta - 1) \tag{1.15}$$

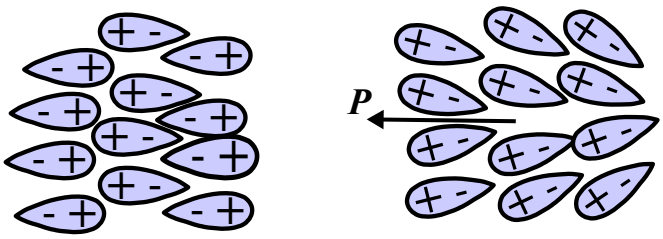

Figure 1.5: Flexoelectric effect in pear-shaped molecules In the absence of splay (left), molecules are arranged so that there is no net polarization. A splay distortion (right) introduces a net polarization $\boldsymbol{P}$ parallel to $\boldsymbol{n}$.

where ψ is the angle between the transmission axis of the first polarizer and the $x-$axis. Altering the director, by applying an electric field for example, changes the transmitted intensity. Display devices rely in large part upon the ease with which δ, that is the *retardance*, through a liquid crystal film can be varied.

1.2.5 The flexoelectric effect

Meyer [32] first postulated the *flexoelectric* effect[2] by considering molecules with a polar character. If pear-shaped molecules with a permanent dipole are splayed by some external agency, a net polarization, parallel to the director, as illustrated in figure 1.5. Alternatively, and equivalently, if an electric field is applied, then the permanent dipoles will align so that the director field is splayed. A similar picture, this time assuming that the molecules are banana-shaped, leads to an association between bend distortions and an electric polarization perpendicular to $\boldsymbol{n}$. Fruit-shaped molecules are not required: a microscopic theory of the flexoelectric effect due to quadrupolar molecules has also been reported [33]. Using the notation of Rudquist [34], the flexoelectric polarization is related to curvature strains by the formula

$$P_i = e_s n_i n_{j,j} + e_b(n_j n_{i,j} - n_j n_{j,i}) \tag{1.16}$$

Once more, the splay flexoelectric coefficient e_s and the bend flexoelectric coefficient e_b are phenomenological.

Without the flexoxelectric effect, the energy density (1.8) is quadratic in the components of $\boldsymbol{E}$, so it is unchanged if the direction of $\boldsymbol{E}$ is reversed. However, if the flexoelectric effect is included, the electric displacement becomes

$$D_i = \epsilon_{ij} E_j + P_i \tag{1.17}$$

[2]Originally, the piezoelectric effect.

The flexoelectric polarization $\boldsymbol{P}$ does not depend directly upon $\boldsymbol{E}$, so (1.17) and hence (1.8) *does* depend upon the sign of $\boldsymbol{E}$. As a result, the flexoelectric field can act in concert with an applied field, or can oppose it.

1.2.6 Ionic impurities

Inevitably, no sample of liquid crystal will be entirely pure. In particular, contaminants which carry some charge, that is, ions, are known to affect the behaviour of liquid crystals when DC electric fields are applied [35]. Because essentially DC fields are used in experiments designed to study the flexoelectric effect, one must take mobile ions into account [36]. These respond to electric fields by drifting, with velocity

$$\boldsymbol{u}_{\text{ion}} = \mu \boldsymbol{E} \tag{1.18}$$

The mobility, μ, is usually of the order of $10^{-10}\text{m}^2\text{V}^{-1}\text{s}^{-1}$ [37], so that ions travel across liquid crystal cells a few microns thick on timescales measured in hundreds of milliseconds - far slower than the timescales on which the director realigns. If ions are present in sufficient numbers, the electric field distribution, and hence the director profile, will be affected over these long timescales. Barbero and Evangelista [38, 39] have written extensively on drift-diffusion models of ion motion inside nematic liquid crystals, which add a component driven by gradients in ion density to $\boldsymbol{u}_{\text{ion}}$, and of the related adsorption of ions at the cell walls [40–42].

1.2.7 The Euler-Lagrange equations

The director profile of a nematic liquid crystal sample in steady state can be found by solving a problem in the calculus of variations. Ignoring any weak anchoring effects, the sample has a total free energy

$$\Omega = \int_{sample} \omega d\boldsymbol{r} \tag{1.19}$$

given the free energy density

$$\omega = \omega_F + \omega_E. \tag{1.20}$$

In thermodynamic equilibrium, the free energy take on its smallest possible value. However, this not an ordinary minimisation problem, because ω depends not upon a variable, but a function $\boldsymbol{n}(\boldsymbol{r})$, or equivalently the functions $\theta(\boldsymbol{r})$ and $\phi(\boldsymbol{r})$. These are solutions of the *Euler-Lagrange equations*, as usual in the calculus of variations,

$$\left(\frac{\partial \omega}{\partial \Theta_{,j}}\right)_{,j} - \frac{\partial \omega}{\partial \Theta} = 0 \tag{1.21}$$

where Θ stands for either θ and ϕ.

These equations can only be solved if the electric field is known throughout the sample. For the slowly varying electric fields used to re-orient the director - as opposed to light, which is assumed to have no effect upon it - the sample can be considered electrostatic. Thus Gauss' law

$$D_{j,j} = Q \tag{1.22}$$

is applicable here. The space charge distribution Q is usually considered negligible, but might be important if ionic impurities are to be accounted for. If the electric displacement is known, this is an easy problem to solve. However, in realistic cases the electric potential at the surface of a sample is known instead. In that case (1.22) must be solved alongside (1.21). Interestingly, it is also an Euler-Lagrange equation, minimising the free energy with respect to the electric potential v.

1.2.8 Flow

If you own a liquid crystal display, you have probably pressed it and seen the screen change colour around your finger. Pressing on the screen introduces a pressure gradient within the liquid crystal layer, which causes it to flow, albeit briefly. The flow is fastest midway through the liquid crystal layer, and slowest at the display's solid surfaces. When a liquid crystal flows like this, its molecules tend to re-orient themselves The result is a change in the director underneath your finger, temporarily altering the display. This is an example of *flow alignment*.

The most widely used theory of flowing liquid crystals is due to Ericksen and Leslie [43–47, 13]. A re-formulation, first reported by Ericksen [47], is outlined below. First, a fluid velocity $\boldsymbol{u}$ is introduced, then a rate of viscous dissipation per unit volume, or dissipation function, $\mathcal{R}$, is constructed in a similar spirit to the Frank energy. It is expressed in terms of the rate-of strain tensor

$$A_{ij} = \frac{1}{2}(u_{i,j} + u_{j,i}). \tag{1.23}$$

and the angular velocity of the director, relative to the fluid

$$N_i = \dot{n}_i - \frac{1}{2}(u_{i,j} - u_{j,i}) \tag{1.24}$$

where

$$\dot{n}_i = \frac{\partial n_i}{\partial t} + u_j n_{i,j} \tag{1.25}$$

These two entities are chosen as the basis of $\mathcal{R}$, because unlike the simple quantities $\boldsymbol{\nabla u}$ and $\dot{\boldsymbol{n}}$, they vanish in rigid body rotation. Since the dissipation function is a rate of work,

it must be (at least) quadratic in them, resulting in

$$\begin{aligned}\mathcal{R} = \alpha_1(n_i A_{ij} n_j)^2 + 2(\alpha_3 + \alpha_2) N_i A_{ij} n_j + \alpha_4 A_{ij} A_{ij} \\ + (\alpha_5 + \alpha_6) n_i A_{ij} A_{jk} n_k + 2(\alpha_3 - \alpha_2) N_i N_i. \end{aligned} \tag{1.26}$$

The anisotropic part of the stress tensor (that is, not including the scalar pressure),

$$\tilde{t}_{ij} = \frac{1}{2} \frac{\partial \mathcal{R}}{\partial u_{i,j}} \tag{1.27}$$

and an internal body torque

$$\tilde{g}_i = -\frac{1}{2} \frac{\partial \mathcal{R}}{\partial \dot{n}_i} - (\alpha_3 - \alpha_2) N_i - (\alpha_3 + \alpha_2) A_{ik} n_k \tag{1.28}$$

are derived in turn. The stress tensor alone would describe viscous dissipation in an uniaxial (or, as the relevant literature has it, transversely isotropic) fluid, but the internal body torque makes the dynamics of liquid crystals rather more interesting. In the simplest case (when there is no flow) it opposes the director's desire to re-orient itself due to, say, a change in the applied field. In more complex cases, it couples rotation of the director to fluid flow, one leading to the other and vice-versa, and is responsible for the flow alignment mentioned earlier.

1.2.8.1 Backflow and kickback

While pressure driven flow is not usually encountered in display devices, flow caused solely by rotation of the director immediately after an electric (or magnetic) field is switched on, or off, is. One upshot of this flow, termed *backflow*, is a reduction in the apparent viscosity of the liquid crystal [48]. In other words, the liquid crystal reaches an equilibrium state more quickly than it would if it did not flow. A related effect is *kickback*, where the director is driven away from equilibrium for a short period after the field is removed [12]. More generally, the internal body torque (1.28) affects the shape of the director profile as it evolves [49, 50], to an extent which is observable in certain experiments [51].

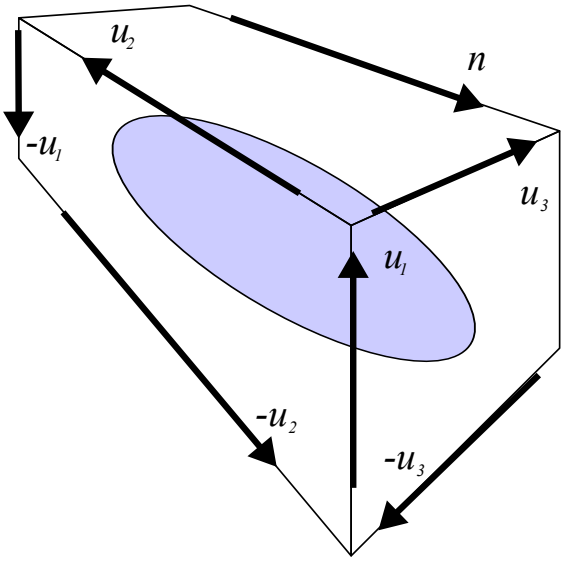

Figure 1.6: The Meisowicz viscosities Each pair of vectors $\boldsymbol{u}_k$ and $-\boldsymbol{u}_k$ represent a flow field which would experience a viscous drag proportional to one of the Meisowicz viscosities, η_k.

1.2.8.2 The Leslie and Meisowicz viscosities

The Leslie viscosities $\alpha_1, \ldots, \alpha_6$ are, like the elastic constants, phenomenological. They cannot take just any value however: the second law of thermodynamics requires that

$$\alpha_3 - \alpha_2 \geq 0, \tag{1.29}$$

$$\alpha_4 \geq 0, \tag{1.30}$$

$$2\alpha_4 + \alpha_5 + \alpha_6 \geq 0 \tag{1.31}$$

$$2\alpha_1 + 3\alpha_4 + 2\alpha_5 + 2\alpha_6 \geq 0 \tag{1.32}$$

$$4\gamma 1(2\alpha_4 + \alpha_5 + \alpha_6) \geq (\alpha_2 + \alpha_3 + \gamma_2) \tag{1.33}$$

Another restriction is the Parodi relation [52],

$$\alpha_2 + \alpha_3 = \alpha_6 - \alpha_5 \tag{1.34}$$

leaving five independent coefficients.

Most of the terms in (1.27) and (1.28) are difficult to visualise, making it hard to understand the Leslie viscosities individually. However, certain combinations are easier to describe. Perhaps the most important is the rotational viscosity, $\gamma_1 = \alpha_3 - \alpha_2$. When the fluid velocity is uniform, the stress tensor vanishes and the internal body torque becomes

$$g_i = \gamma_1 \frac{\partial n_i}{\partial t}. \tag{1.35}$$

In other words, γ_1 determines, on a basic level, the rate at which liquid crystals rotate. A little more complex are the Meisowicz viscosities [53].

$$\eta_1 = \frac{1}{2}(\alpha_3 + \alpha_4 + \alpha_6), \tag{1.36}$$

$$\eta_2 = \frac{1}{2}(\alpha_4 + \alpha_5 - \alpha_2), \tag{1.37}$$

$$\eta_3 = \alpha_4, \tag{1.38}$$

$$\tag{1.39}$$

Note that some authors swap the definitions of η_1 and η_2 [13]. These are all associated with flow fields where $\boldsymbol{u}$ is perpendicular to its gradient, as illustrated in figure 1.6. Viscous drag is proportional to η_1 when $\boldsymbol{u}$ is parallel to the director, to η_2 when $\nabla\boldsymbol{u}$ is parallel to $\boldsymbol{n}$, and to η_3 when both $\boldsymbol{u}$ and $\nabla\boldsymbol{u}$ are perpendicular to $\boldsymbol{n}$. One more coefficient, $\eta_{12} = \alpha_1$, is needed to complete the set of nematic viscosities. It is important, together with η_1 and η_2 when neither $\boldsymbol{u}$ nor $\nabla\boldsymbol{u}$ are perpendicular or normal to $\boldsymbol{n}$.

1.2.9 The Ericksen-Leslie equations

A set of partial differential equations, the Ericksen-Leslie equations, are formed by balancing elastic, dielectric, and viscous forces. Conservation of angular momentum leads to a vector equation

$$\left(\frac{\partial\omega}{\partial n_{i,j}}\right)_{,j} - \frac{\partial\omega}{\partial n_i} + \tilde{g}_i = \lambda n_i \tag{1.40}$$

which, in essence, determines the director profile. The term on the right hand side, with its undetermined Lagrange multiplier λ, serves to ensure that $\boldsymbol{n}$ is a unit vector. Alternatively, (1.40) can be re-stated in terms of the director's Euler angles,

$$\left(\frac{\partial\omega}{\partial\Theta_{,j}}\right)_{,j} - \frac{\partial\omega}{\partial\Theta} - \frac{1}{2}\frac{\partial\mathcal{R}}{\partial\dot{\Theta}} = 0. \tag{1.41}$$

These equations are, of course, the dynamical analogue of the Euler-Lagrange equations (1.21).

A second vector equation, primarily governing flow, is due to the conservation of linear momentum:

$$\rho\dot{u}_i = \tilde{g}_j n_{j,i} + \tilde{t}_{ij,j} - p_{,i} \tag{1.42}$$

This equation contains an unknown, an arbitrary scalar pressure p, so a third equation, the incompressibility condition

$$u_{i,i} = 0 \tag{1.43}$$

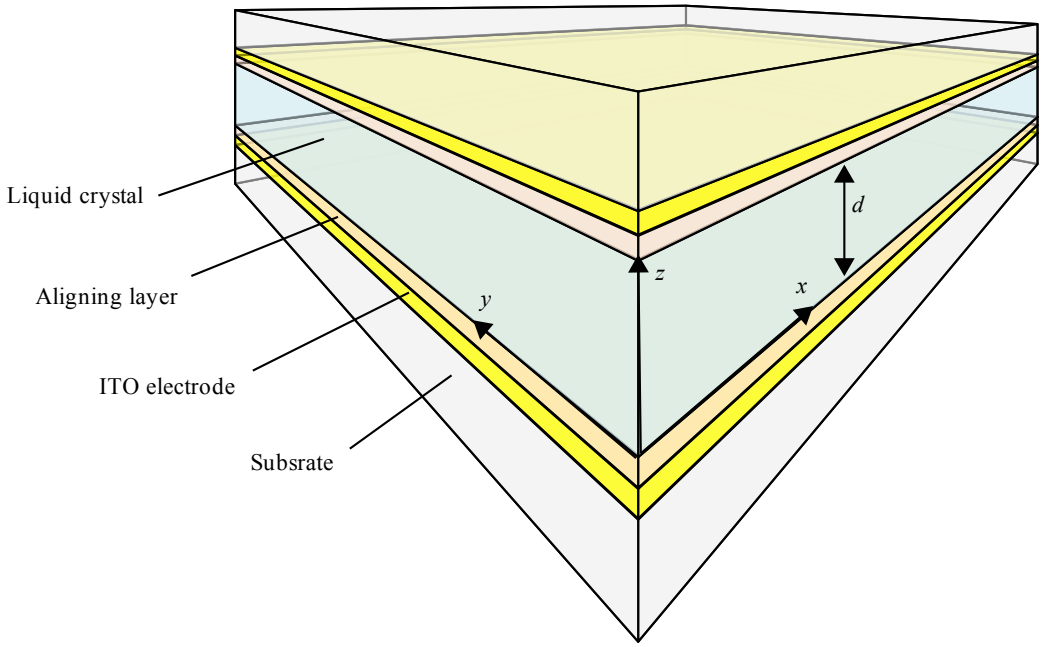

Figure 1.7: Diagram of a simple liquid crystal cell A layer of liquid crystal, thickness d, is sandwiched between substrates coated with an ITO electrode and an aligning treatment.

must be introduced.

Several simplifications to (1.42) apply to the liquid crystal cells considered in this thesis. These are, basically, thin films of liquid crystal confined between solid surfaces, extending indefinitely in the xy-plane. Van Doorn[49] notes that the term on the left hand side can be neglected, because the velocity field relaxes rapidly compared to the director, an approximation also reported by Berreman [50]. Furthermore, cells can be considered one dimensional, varying only along the $z-$axis . Consequently, the first term in the right hand side of the $x-$ and $y-$components of (1.42) vanishes. There is no need to solve the $z-$component of (1.42) at all - if there is to be no flow of liquid crystal through the cell walls, (1.43) implies that u_z must be zero everywhere.

1.3 Liquid crystal cells

Experimentalists do not normally work with entire liquid crystal displays, but with simple models of them, or *cells*. These are akin to a single pixel of a complete display, but with a larger area - around a square centimetre. Cell construction is traditionally arduous: a recent account is given by Taphouse [54], and recapped in appendix A. A thin film of nematic liquid crystal, ranging from a few microns, to a few tens of microns thick, is sandwiched between a pair of transparent glass or plastic substrates, as shown in figure 1.7. Each substrate is a coated with Indium Tin Oxide (ITO), a transparent conductor, which

serves as an electrode. Between the liquid crystal and ITO is an aligning layer, the choice of which determines the cell's internal geometry.

Figure 1.7 also shows the co-ordinate system used throughout this thesis. The $z-$axis is perpendicular to the cell walls with $z = 0$ at the lower wall, and $z = d$ at the upper. The choice of $x-$ and $y-$axis varies: in the vast majority of this thesis the director is confined to a single plane, the $xz-$plane. Because the cell extends far further in the $xy-$plane than along z, it can be treated as one-dimensional, with the director and other quantities varying only in z.

Only one type of electrode is considered in this thesis: a uniform coating of ITO. That leads to an electric field parallel to the $z-$axis. Other arrangements, where intricate electrode design gives rise to electric fields with components in the $xy-$plane [55, 56], are not considered.

1.3.1 Planar homogeneous cells

A planar homogeneous cell is made by treating both substrates to promote planar homogeneous alignment along the same direction. This kind of cell exhibits a *Fréedericksz transition* [28], provided ϵ_a is positive. In the ground state, the director profile is uniform throughout the cell, as it is when any electric field below the *threshold voltage*,

$$v_c = \pi\sqrt{\frac{k_{11}}{\epsilon_0\epsilon_a}} \tag{1.44}$$

is applied. Only when v_c is exceeded does the cell switch into a *distorted state*, with the director at the cell's mid-plane tending to align with the z-axis. Below v_c, the free energy is lowest in the ground state.

A simple *electro-optical effect* can be observed by placing a planar cell between crossed polarizers such that the rubbing direction makes an angle of $\pi/4$ with respect to the transmission axis of either polarizer. Illuminate the cell from beneath so that linearly polarized light propagates through it along the $z-$axis. In the ground state, the radiation will be split into ordinary and extraordinary components which usually emerge out-of-phase, so that some light is transmitted through the second polarizer. At high voltage, the director is parallel to the direction of propagation in much of the cell, so that only an ordinary wave travels through and no light is transmitted. In other words, one can switch the cell from a light state to a dark state by applying a voltage. A display which relied on planar geometry would need to be precisely engineered: a change in cell thickness of just 0.5 μm is enough to take the ground state from light to dark, or rather, change the transmitted colour significantly, according to (1.15).

1.3.2 Twisted nematic cells

The twisted nematic (TN) cell described by Schadt and Helfrich [57] overcomes the limitations of the planar cell for use as a display. Once more, both substrates are treated to promote planar homogeneous alignment, but the cell is built so that the rubbing direction at the upper plate is rotated by $\pi/2$ with respect to the lower. As a result, the director twists smoothly through the cell in the ground state. Provided that the cell thickness is much greater than the wavelength of light- the Mauguin condition - light transmitted through the device emerges with its polarization vector rotated by $\pi/2$, irrespective of its colour or the cell's thickness. The first commercial displays were based on the TN device, as are many modern devices. A variation on the TN cell, the super-twisted nematic (STN) cell, enjoys the advantages of the former and has improved switching speed [58]

1.3.3 Homeotropic cells

Cells with both surfaces treated to promote homeotropic alignment and filled with a negative ϵ_a liquid crystal undergo Fréedericksz transitions, much like planar homogeneous cells. But, because any vector in the $xy-$plane is perpendicular to the electric field, the liquid crystal breaks up into a myriad of domains, leading to a speckled pattern when viewed between crossed polarizers. For this reason, such cells have not been subjected to the kinds of experiment described in chapter 2, which rely on the formation of a single domain. On the other hand, flow through homeotropic cells does lead to distortions which are uniform over large areas [59–61]

1.3.4 HAN cells

In recent years, there has been much interest in the hybrid-aligned nematic cell, or HAN cell. HAN cells are built so that the liquid crystal is aligned homeotropically at one surface, and homogeneously at the other. A number of behaviours set it apart as an experimental device.

1. It experiences no threshold voltage - any applied field at all will alter the director profile[62]

2. Media having positive or negative ϵ_a can be studied, since an electric field would cause either to re-align. This is especially useful when studying negative or dual-frequency materials, because, in contrast to the homeotropic cell, there is a unique alignment direction - the rubbing direction at the planar homogeneous surface - at high voltages[30, 63, 54].

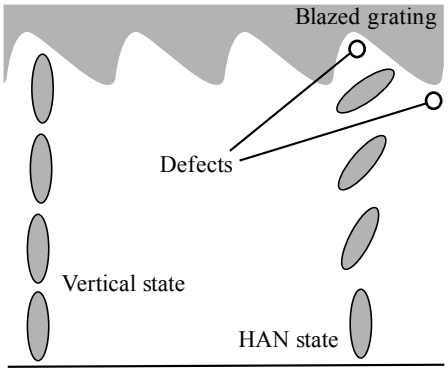

Figure 1.8: Schematic of the stable configurations of ZBND A blazed grating at one surface of ZBND lends it bistability. It occupies either a vertical, defect free state or a HAN state with defects close to the grating surface

3. Since the director profile is asymmetric, the net flexoelectric polarization in the cell will only be zero if $(e_s - e_b)$ is, leading to a number of experiments which attempt to determine that parameter [64–69, 56]. Note that to find $(e_s + e_b)$ it is necessary to build a cell where the electric field and director are not in the same plane, for example a twisted nematic device with electrodes designed to provide an electric field parallel to the cell walls [70].

1.3.5 Bistable devices

Usually, a bistable device is taken to be one which can occupy either of two distinct states when no voltage is applied. Bistable devices are technologically interesting because they may permit higher resolution or, in some circumstances, more energy efficient displays to be made. While there have been promising prototype bistable technologies based upon certain smectic mesophases [71, 72], the work in this thesis is related, if somewhat periphally, to a class of devices based upon the nematic mesophase. In each of these, bistability is achieved by microscopic structures at one of the cell walls, which can promote one of two alignment directions.

1.3.5.1 The Zenithal Bistable Nematic Device

Perhaps the best known bistable device is ZBND (or ZBD), the Zenithally Bistable Nematic Device [73]. The key component is a bistable surface, a blazed grating treated to promote homeotropic alignment. The director can adopt two configurations near to this grating. In the first of these, the director is aligned homeotropically within a plane just above the grating's peaks. In the second, the director is tilted in the same plane. At least two defects per grating period, one at the peak and one in the trough, form in this

second state. Thus, ZBND can occupy either a state which resembles a homeotropic cell, or one which resembles a HAN cell, as illustrated in figure 1.8. When filled with Merck E7, ZBND exhibits sign-dependent switching - they can be driven into the HAN state by applying a positive voltage between the lower and upper surfaces, and the homeotropic state by applying a negative voltage.

1.3.5.2 The post aligned bistable nematic device

As its name suggest, the post aligned bistable nematic (PABN) device employs an array of microscopic posts to effect a bistable surface [74, 75]. The other surface is treated to encourage homeotropic alignment at the upper surface. One state (the P-state) resembles a HAN cell, with planar alignment within a plane parallel to the top of the posts. The other state (the T-state) is rather more like a homeotopic cell: the director is tilted along the top of the posts, and vertically aligned in the wells between them. When filled with Merck ZLI-4788-000, PABN devices can be switched from the P- to the T-state by applying a negative voltage between the homeotropic and bistable surfaces, and back by applying a positive voltage.

1.3.5.3 Switching of bistable devices

How can bistable devices be switched from one state to the other? The simplest model of switching, considering only rotation of the director due to elastic and dielectric forces, predicts that they cannot. Consider a bistable cell, filled with a negative $\epsilon_a < 0$ material and sitting in its HAN state. Applying an electric field can never pull the director away from planar orientation near the lower surface: it will only push it closer to planar.

Models of ZBD implicate the flexoelectric effect in the switching of bistable devices. At the simplest level, the flexoelectric effect introduces dependence on the direction of $\boldsymbol{E}$ (that is, sign dependence) into the Ericksen-Leslie equations. In the literature, a one-dimensional model, which simulated the lower surface by an anchoring energy with two minima, suggested that switching can occur when $(e_s - e_b)$ is greater than 40 pCm^{-1} [76]. This is an experimentally realistic number: values ranging from 15 pCm^{-1} [65] to 35 pCm^{-1} [77] have been reported for the nematic liquid crystal E7. Later, two-dimensional models considered the creation, transport, and annhiliation of defects, using a description based upon the Q-tensor [78].

The flexoelectric effect is not the only sign dependent mechanism in nematic liquid crystals, nor is it the only mechanism which might explain switching in bistable cells. Dozov has described a bistable device [79] whose switching has been attributed to something akin to the backflow and kickback effects [80]. Mazulla [81], and later, Jewell [65] noted

that the flexoelectric effect could only account for part of the sign dependent switching that they observed in their HAN cells. They found that a DC bias voltage across the cell, attributed to polar orientation of calamitic molecules at the homeotropic surface, must also be taken into account. Others have suggested that ionic impurities could be adsorbed onto the cell surfaces to different degrees given the different surface chemistry, also resulting in a DC bias [42, 36].

1.4 Thesis outline

In chapter 2, the optics of uniaxial media is considered in detail, and a review of experimental techniques given. It is simple enough to predict the outcome of these experiments knowing the director, but what about the reverse? Determination of the director profile turns out to be one of a special class of problems, called *inverse problems*, or, more revealingly, *ill-posed problems*. While some ill-posed problems - those that have no solution, or those that have many - are easy to understand, a third kind is more subtle. These have a unique solution in principle, but in practice it is swamped by experimental errors hugely amplified. A heat conduction problem is developed as an example.

The aim of chapter 3 is to examine a simple ill-posed problem, recovery of the ground state director profile in a HAN cell. Quantitative analysis is performed by way of *singular value decomposition*, which, broadly shows which contributions to the director profile will be swamped by noise, and by how much. It will also be used to decide that while standard *Tikhonov regularization* doesn't address the expected difficulties, a modified form, derived from the Ericksen-Leslie equations, might.

The problem formulated in chapter 3 will require numerical solutions to the Ericksen-Leslie equations if it is to be extended beyond the ground state of a HAN cell, as will others formulated in chapter 5 and 6. Furthermore, modelling described in chapters 6 and 7 was beyond the scope of computer programs available to the author. So, a computer program designed to meet the various needs of this thesis is described in chapter 4

The regularization technique described in chapter 3 is extended to account for applied electric fields, and for viscous rotation of the director, in chapter 5. These methods are then tested against fully leaky guided mode experimental data, measured by Taphouse [54] as AC voltages are applied to a HAN cell. A set of tilt profiles is recovered, labelled *weakly-constrained* because they are close to, but not exactly, solutions of a simplified subset of the Ericksen-Leslie equations. These tilt profiles help to formulate a *strongly-constrained* inverse problem. Here, the tilt profiles recovered *are* numerical solutions to a subset of Ericksen-Leslie equations, and various free parameters, together with uncertainties, are

sought. A Monte-Carlo method is used to test the error analysis.

A further set of experimental data, taken during the DC switching of a HAN cell is analyzed in Chapter 6. The weakly-constrained tilt profiles exhibit a sign-dependent effect, and transients not predicted by the Ericksen-Leslie equations. A drift-diffusion model of mobile, charged contaminants is added to the computer program of chapter 4, and produces results consistent with these transients. Both the flexoelectric effect, and charges stuck to the cell walls are considered as mechanisms responsible for the observed sign-dependence, and their effect on the time-dependent behaviour used to decide that the latter dominates.

Chapter 7 deals with pressure driven flow in a homeotropic cell. First, the computer program of chapter 4 is extended to include a pressure gradient terms. Modelling suggests that at low flow rates and/or high voltages, the director should adopt a V state - essentially a perturbation to the homeotropic state. But at high flow rates, the director should switch, via a nucleated transition, to an H state, where the director is homogeneously aligned at the cell mid-plane. In both cases, the director profile is mirror symmetric about the cell's mid-plane, so that distinctive conoscopic figures should be observed. A laser conoscope was built to observe these, and a simple analysis of the them allowed α_2 and ϵ_a to be estimated.

Conclusions, suggestions for further work, and a list of publications and presentations are given in chapter 8.

Chapter 2

The optical study of liquid crystal cells and its relation to inverse problem theory

It is natural to study liquid crystal cells through their interaction with optical radiation. Typical cells are composed of transparent materials which are not photo-sensitive so that light passes through the cell without damaging it. Furthermore, liquid crystal materials intended for display applications are chosen for their strong birefringence at optical frequencies. And finally, the liquid crystal layer is usually a few microns thick, so thin film interference phenomena will be observed. These important phenomena are considered in section 2.1.

A major motivation for the Exeter experimental group is the recovery of depth-dependent information, in particular the director profile, from simple cells. Common optical experiments, such as polarising microscopy, can be used to measure a single quantity (such as the birefringence magnitude) integrated over the depth of a cell. As a result, they cannot be used to determine the depth-dependent director profile. On the other hand, experiments which measure transmission and/or reflection across a range of angles can recover at least part of the required information. A review of these angle scanning experiments, and others, is given in section 2.2.

Calculation of the director from measured optical characteristics is a particular type of problem, known as an *inverse problem*. Inverse problems are stated in terms of a corresponding *forward problem*, which in this case means predicting the optical characteristics of a cell when the the director profile is known. Here, as elsewhere, the inverse problem is formulated as an optimisation problem: find the director profile such that the solution to the forward problem is closest to the experimental data. Clearly then, before the inverse

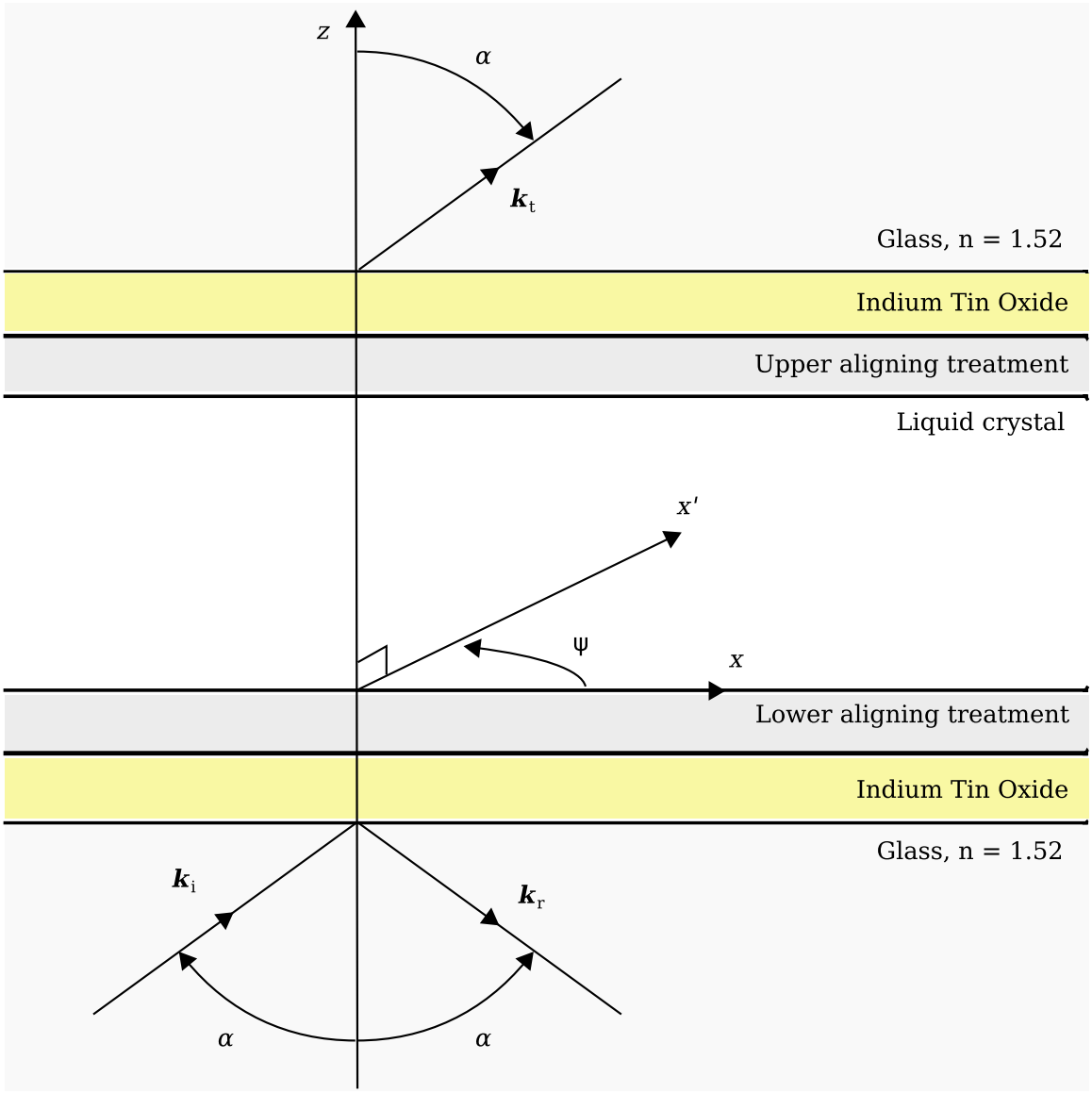

Figure 2.1: A stratified optical system, or multilayer stack. The liquid crystal cell is treated as a sequence of strata, varying only along the $z-$axis, sandwiched between semi-infinite glass substrates. Plane waves directed upward through the lower glass layer along wavevector $\boldsymbol{k}_i$ are propagated through the layers of the stack, eventually being reflected or transmitted along wavevectors $\boldsymbol{k}_r$ and $\boldsymbol{k}_t$. The $x-$axis is defined so that the wavevectors have no $y-$component, and is inclined at angle ψ to the x'-axis, that is, to the $x-$axis of the liquid crystal layer.

problem can be considered, the *forward problem* must be specified: section 2.3 is devoted to this. Similar pairs of forward and inverse problems are found in a wide range of fields, including medical imaging [82], structural mechanics [83, 84], and geophysics [85, 86]. A discussion of the inverse problem , and especially the idea that it is *ill-posed* is given in section 2.4.

2.1 Optics of liquid crystal cells

For the purposes of this thesis, light propagates through simple liquid crystal cells as though they were one-dimensional structures. As was noted in the previous chapter, the director profile varies only along the $z-$axis. Furthermore, the liquid crystal layer, the ITO layer, and the aligning layers are all thin compared to the width of a laser beam, so that the incident radiation can be treated as a plane wave of infinite extent. Conversely, the glass (or other) substrates are relatively thick, so light in that part of the system is usually described by rays. A detailed mathematical treatment of this multi-layer optics problem is left until section 2.3, but some definitions must be outlined here.

Figure 2.1 shows a sequence of strata, or a multi-layer stack, of dielectric media, with semi-infinite glass layers at the top and bottom. A plane wave, with wavevector $\boldsymbol{k}_i$ originates in the lower glass layer and strikes the interface between the glass and ITO. After interacting with the multilayer system, some radiation is transmitted into the upper glass layer, along wavevector $\boldsymbol{k}_t$, and some is reflected into the lower glass layer, along wavevector $\boldsymbol{k}_r$. The co-ordinate system is chosen so that $\boldsymbol{k}_i$ (and hence $\boldsymbol{k}_t$ and $\boldsymbol{k}_r$) have no $y-$component. This means that the $x-$axis may be rotated around the $z-$axis, by an angle ψ, compared to the $x'-$axis - the $x-$axis defined for the liquid crystal layer.

At this point, some terminology describing the polarization states of light must be introduced. When the electric field is perpendicular to the plane of incidence (and hence, given the conventions above, parallel to the $y-$axis), the light is said to be $s-$polarized, or TE-polarized (for transverse electric). If the magnetic field is perpendicular to the plane of incidence, the light is $p-$polarized, or TM-polarized. *Linearly polarized* light is the sum of in-phase $s-$ and $p-$polarized waves, while *elliptically polarized* light is the sum of out-of-phase components. *Circularly polarized light* is the sum of an $s-$ and $p-$ wave which are $\pi/2$ out-of-phase. The term *polarization conversion* is used to refer to a situation where incident $s-$polarised light results in reflected or transmitted $p-$polarised light or vice-versa.

2.1.1 Birefringence

Birefringence was introduced in the previous chapter. A special case, where the optic axis was perpendicular to the propagation direction, was sufficient for that discussion. In the more general case, where the propagation direction is not parallel to the optic axis, the wavevectors of the extraordinary and ordinary wave have different directions as well as magnitudes. Consider the homogeneous system illustrated in figure 2.2, where a beam of light is incident upon an interface between an isotropic material (such as air) and a

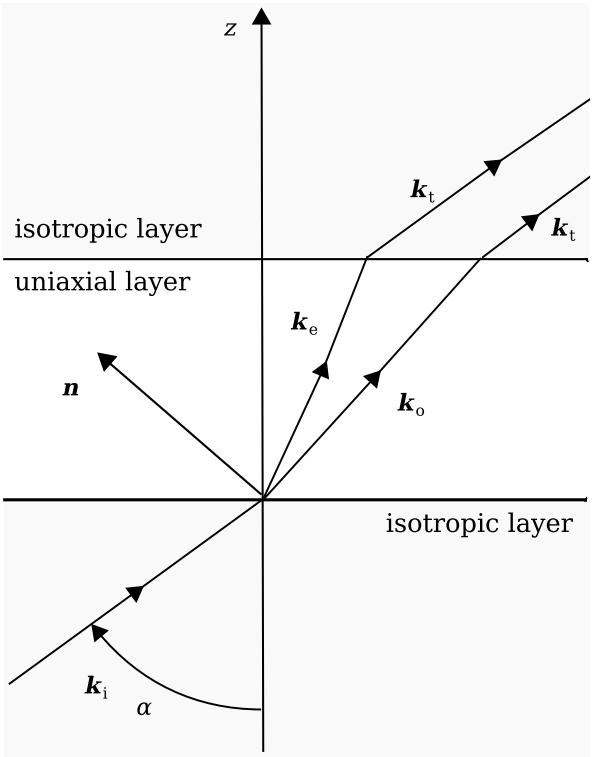

Figure 2.2: Double refraction. Light passing through a uniaxial layer is split into ordinary and extraordinary components, whose wavevectors $\boldsymbol{k}_o$ and $\boldsymbol{k}_e$ differ in both magnitude and direction.

birefringent medium. If the sample is large compared to the beam width, separate beams emerge. This *double refraction* explains the double images formed by calcite crystals, and is exploited by several optical devices, such as the Glan-Thompson polarizer.

Liquid crystal films are so thin that even a narrow laser beam will not be split into two distinct beams. The difference in the path of propagation through the film nonetheless affects the total transmission through an angular dependence of the retardance. In a uniaxial medium, the retardance can be expressed in terms of the tilt angle θ and the layer thickness, h as

$$\delta(\theta, h) = k_0 h \left(\sqrt{\epsilon_{ef} - \epsilon_a sin^2\alpha} - \sqrt{\epsilon_\perp - \epsilon_a sin^2\alpha} \right) \tag{2.1}$$

where

$$\epsilon_{ef} = \frac{\epsilon_\perp \epsilon_\parallel}{\epsilon_\parallel \cos^2\theta + \epsilon_\perp \sin^2\theta}. \tag{2.2}$$

and ϵ_a is the dielectric constant of the isotropic layer.

2.1.1.1 Sensitivity to the director profile

Angle dependent measurements of retardance, or rather, the polarization conversion it causes, can be sensitive to one kind of depth-dependent information over and above mea-

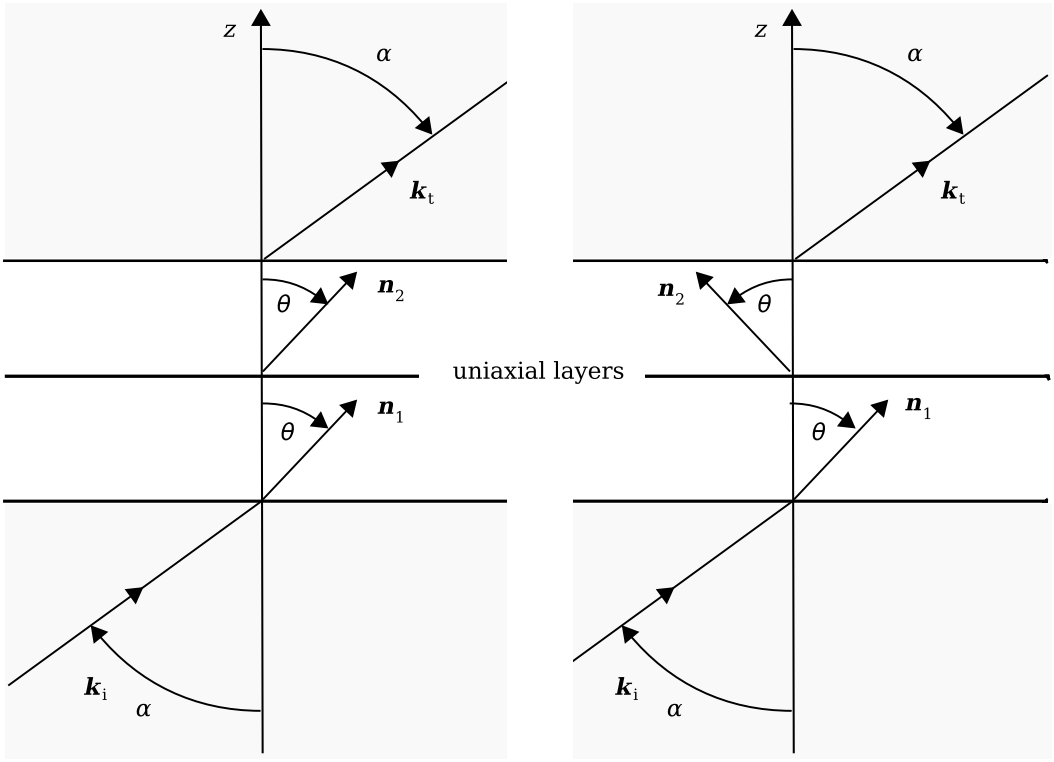

Figure 2.3: Symmetric and anti-symmetric two layer stacks. In each uniaxial layer the director is parallel to the $xz-$plane.

surements at a single angle. A pair of two layer stacks, as shown in figure 2.3, serves to illustrate this. First, consider the left-hand stack, where the director is the same in both layers. When the angle of incidence, α, is such that the wavevector within the liquid crystal layers is parallel to the director, there will be no retardance. In contrast, when the angle of incidence is $-\alpha$, there will be. Overall, the retardance will not be an even function of α. Now consider the right-hand stack, where the director tilts left by θ in the bottom layer and right, by the same amount, in the top, that is, when the director is mirror-symettric about the cell's midplane. Wöhler has shown that the transmitted intensity through any stack where the director is confined to the $xz-$plane remains the same when the stack is rotated by π around (in this case) the $y-$axis [87]. That being the case, the transmission coefficients must be the same whether the angle of incidence is α or $-\alpha$, that is, symettric about $\alpha = 0$. This idea will be important in chapter 7, where just this kind of depth-dependent information will be inferred from conoscopy figures.

Calculations carried out with the extended Jones technique described in section 2.3.1 confirm this kind of sensitivity to depth dependent information. Two stacks, each of two layers and placed between crossed polarizers, were modelled. In the first, the director was inclined at an angle $\theta = \pi/8$ to the z-axis in both layers. In the second, $\theta = \pi/8$ in the top layer, and $\theta = -\pi/8$ in the lower. Polarization converting transmission curves for

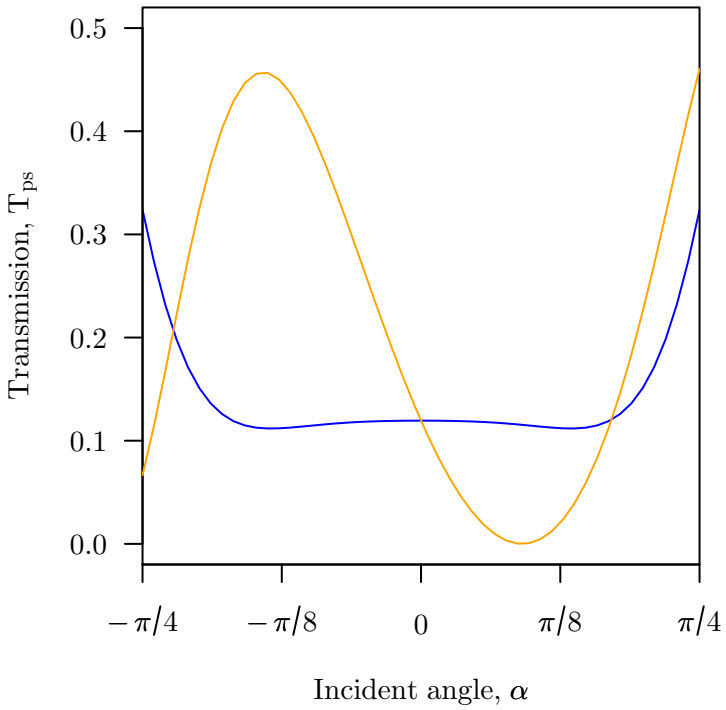

Figure 2.4: Polarization converting transmission through uniaxial stacks. The (blue) symmetric curve corresponds to transmission through the right-hand stack in figure 2.3, while the (orange) asymettric curve corresponds to the left-hand stack.

each case are shown in figure 2.4. As expected, the curve for the antisymmetric stack is symmetric about $\alpha = 0$, while the curve for the symmetric stack has a minimum near near $\alpha = \pi/8$. In both curves, the transmission at $\alpha = 0$ is identical, so the two stacks would appear the same if viewed from above, in a polarizing microscope for example.

2.1.2 Thin-film interference

Thin film interference is significant when the liquid crystal layer is only a few wavelengths of light thick. Some fraction of light incident on each interface between the substrates and the liquid crystal is reflected, so that standing waves, that is Fabry-Perot modes, are excited within the sample. When light is incident at some angle to the sample, these modes are sometimes called *guided modes*, since they propagate parallel to the substrates. Light emerging from the sample, both reflected and transmitted, is comprised of many superposed components. In an isotropic, homogeneous medium, with refractive index n, the phase difference, δ, between these components depends upon the depth of the layer, h, and the angle between the wave and substrate normals, α (see reference [31] p360, for example):

$$\delta = \frac{4\pi}{\lambda} nh \cos\alpha \tag{2.3}$$

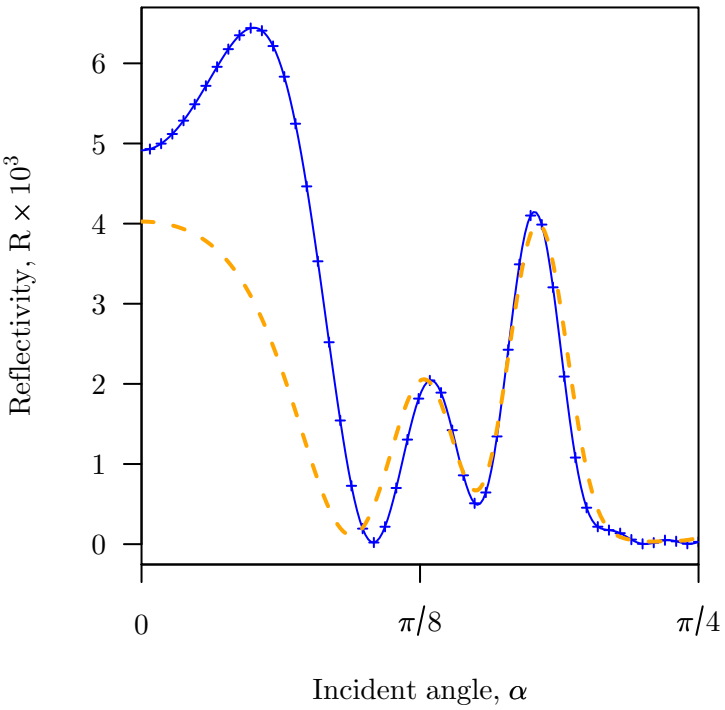

Figure 2.5: Reflection of p-polarized light from an inhomogeneous, 10 layer stack. The ambient medium is glass, while the refractive index varies linearly from n = 1.6 at the upper surface to n = 1.4 at the lower, or vice-versa. The reflection coefficient does not change if the order of the stack is reversed (solid curve versus crosses), but does when layers 3 and 4 are swapped (dashes).

Provided h/λ is not too large, there will be observable modulations, or fringes of equal inclination, in the variation of the reflected and transmitted intensities with α. Both the amplitude and sharpness (or finesse) of the fringes increase with the reflectivity, and hence the refractive index contrast, at the interface with the ambient medium. The situation is more complicated in an inhomogeneous, anisotropic medium such as a liquid crystal, where reflections occur within the layer, and depend upon polarization. A convenient method for computing the reflection and transmission coefficients in such a system will be introduced in 2.3.2.

2.1.2.1 Sensitivity to the director profile

Measurements of thin film interference are also sensitive to depth-dependent information. The modelled reflection intensity coefficient for $p-$polarized light as a function of angle, for three different stacks, each with 10 layers, is shown in figure 2.5. In the first stack, the refractive index varies linearly from $n = 1.6$ at $z = 0$ to $n = 1.4$ at $z = 1$. For the second stack, the refractive indices are reversed, and in this case the reflection coefficient is calculated to be the same as for the first stack. The third stack is identical to the

first but that the third and fourth layers have been interchanged, and in this case the computed reflection coefficient is distinct from the other two. The reflected intensity is, however, very low, and the difference between the two signals only a modest proportion of that. Any experiment which relies on the measurement of these weak Fabry-Perot modes must be performed with great accuracy. On the other hand, if the stack includes highly contrasting isotropic layers, such as silver or ITO electrodes, these modes will be stronger.

2.2 Experimental methods

Polarising microscopy has been used to study liquid crystal materials since their discovery [5], and remains a useful tool today. The sample is placed between crossed polarizers, illuminated with white light, and the transmitted light captured. The colour of each region of the sample will depend upon the alignment of the liquid crystal in that region, according to (1.15). Both the hue and the brightness may change as the sample is rotated. A homeotropic region always appears dark, while a planar homogeneous region appears brightest when the rubbing direction is inclined at $\pi/4$ to the polarizers. Perhaps the most interesting images are those which occur around defects, such as those discussed in 1.2.1.3. In fact, because each mesophase tends to lead to different types of defects, polarising microscopy is one of the most useful tools in studying the phase behaviour of new materials.

Although it is useful for examining variation in the $xy-$plane of a sample, polarising microscopy is insensitive to the details of the director in the $z-$ direction. Fluorescence confocal polarising microscopy (FCPM) [88] overcomes this limitation, but is limited to a resolution along the $z-$axis of a few microns. The liquid crystal is doped with a fluorescent dye, whose molecules, like those of the liquid crystal, are elongated. These dye molecules absorb (and so emit) most strongly light polarized parallel to themselves. Assuming that dye molecules and liquid crystal molecules are aligned, a measurment of flourescent emission can be considred a direct measurement of $\boldsymbol{n}$. To effect depth-sensitivity, the sample is illuminated with a focused beam, so that maximum fluorescence occurs near the focal point, and light collected only after it has passed through a pinhole. By varying the focal point, depth variation in the director can be studied.

The thin film photonics research group at Exeter has long specialised in *guided mode* experiments. These experiments all measure reflectivity, and in some cases, transmittivity, as a function of incident angle, and so are sensitive to localised changes in the director profile. The most recent of these, the fully-leaky guided mode experiment, is one of two techniques studied in detail in this thesis: the other is conoscopy.

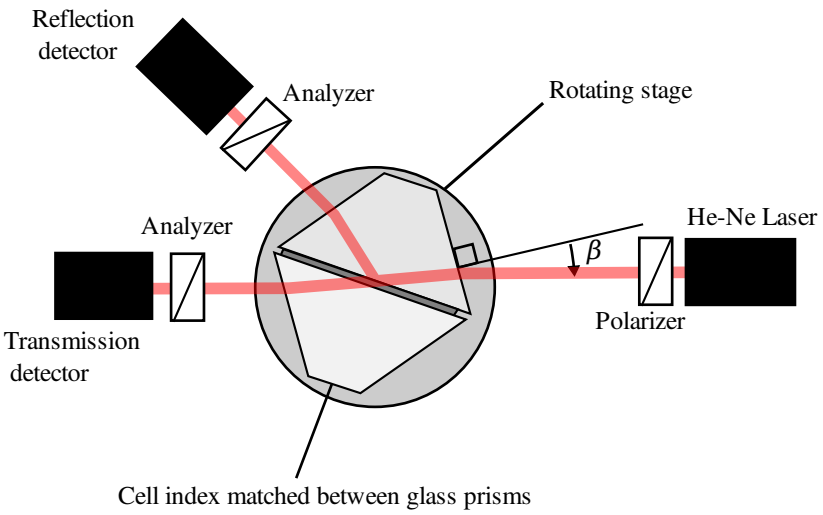

Figure 2.6: The fully-leaky guided mode experiment apparatus. The angle β between the incident beam and the normal to the first prism face is varied, allowing the reflection and transmission coefficients to be measured as a function of β.

2.2.1 The fully-leaky guided mode experiment

The fully-leaky guided mode experiment [89–91, 65], shown in figure 2.6, is intended to characterise realistic cells, with ordinary glass substrates. The cell is coated with index matching fluid and set between glass prisms, then the resulting assembly is mounted on a rotating table so that the prism faces are parallel to the laboratory y-axis. The polarizer and analyzers are set to select either $s-$ or $p-$polarized light and the rotating table set to an initial angle $\beta = \beta_0$. The reflection and transmission intensity coefficients, R and T, are then measured over a range of angles $\beta \in \{\beta_0, \beta_1, \ldots, \beta_n\}$, and for each permutation of polarizer and analyzer states. At each angle eight signals R_{pp}, R_{ps}, R_{sp}, R_{ss}, T_{pp}, T_{ps}, T_{sp} and T_{ss} are recorded, in which the first subscript denotes the state of the polarizer, and the second subscript denotes the state of the analyzer.

Two variants of the fully-leaky guided mode experiment are capable of observing changes in the director with sufficient time-resolution to study switching processes. A lens system, a linear aperture, and a linear CCD array are employed in the convergent beam system [92, 93, 51] to measure simultaneously the optical coefficients for a range of angles. A rotating diffuser is used to suppress artifacts in the image arising from laser coherence. The time-resolution of the experiment is therefore limited by the speed of this diffuser. More recently, the time-resolved fully-leaky guided mode experiment [30, 63] has proved capable of sub-millisecond resolution. Its apparatus is identical to that of the to original experiment, but it is operated differently. For each angle in the chosen range, a time-dependent electric potential is applied across the cell, a set point of which deter-

mines time $t = 0$. The reflection and transmission coefficients are then sampled at many times $t \in \{0, t_1, \ldots, t_m\}$. Overall, $(n+1) \times (m+1)$ measurements of $R_{\mathrm{pp}} \ldots T_{\mathrm{ss}}$ are taken, representing these quantities as a function of both time and angle.

2.2.2 Other guided mode experiments

The half-leaky guided mode experiment [94, 95] is motivated by the rather weak fringes of equal inclination observed in the fully-leaky guided mode experiment[1]. Both the amplitude and width of fringes of equal inclination depend upon the reflection coefficient, and hence the refractive index contrast, at the liquid crystal-substrate interface. As the refractive index contrast increases, the fringes become both narrower and stronger. Since the refractive index of most liquid crystals is similar to that of glass, only broad, low amplitude modes are seen in the fully-leaky guided mode experiment. Replacing the upper cell substrate and prism with high index (n = 1.732) equivalents increases the reflectivity at the first interface, and in turn the amplitude of Fabry-Perot modes excited in the liquid crystal layer. At high angles of incidence, light only 'leaks' out of the bottom surface, hence the term 'half-leaky'. In the end, the result is a sharper set of fringes, and so a better signal-to-error ratio, in the reflectivity measurements.

The first guided mode experiments performed by the Exeter group gave sharper fringes still [97, 98]. The liquid crystal layer is bounded by opaque silver or gold films deposited on the prism faces, so that evanescent fields in the metal layers excite sharply resonant Fabry-Perot modes within the liquid crystal layers. In addition, a surface-plasmon-polariton (SPP), an excitation of the metal films' free electron gas, causes a deep minimum in the $p-$polarized reflectivity. The position of this minimum is altered only by changes in the dielectric tensor close to the surface, because the electric field due to the SPP is strongly evanescent. Consequently, these experiments are considered highly sensitive to changes in the director profile close to the cell surfaces.

2.2.3 Conoscopy

Like the waveguide experiments, conoscopy allows transmission intensities to be collected over a range of angles. In the minimal system depicted in figure 2.7, linearly polarized light is focused by a lens (often the sub-stage condenser on a polarising microscope) such that a convergent beam passes through the sample, then through an analyzer, finally striking a light-sensitive screen. Each position on the screen corresponds to a pair of angles (α, ψ), where α is the angle of incidence for light striking that position, and ψ is the angle between

[1] In fact the original half-leaky guided mode experiment predates the current version of the fully-leaky experiment, and was conceived as an improvement to an earlier fully-leaky variant [96] which sandwiched the liquid crystal layer between high-index prisms coated with ITO.

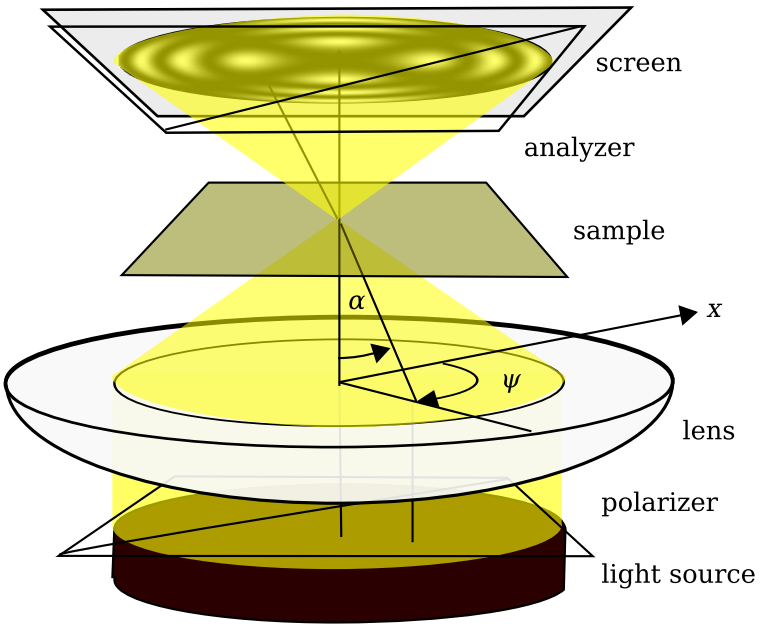

Figure 2.7: Schematic of a simple conoscope. Linearly polarized light is focused so that a convergent beam passes through the sample and then an analyzer, projecting an interference figure onto a screen.

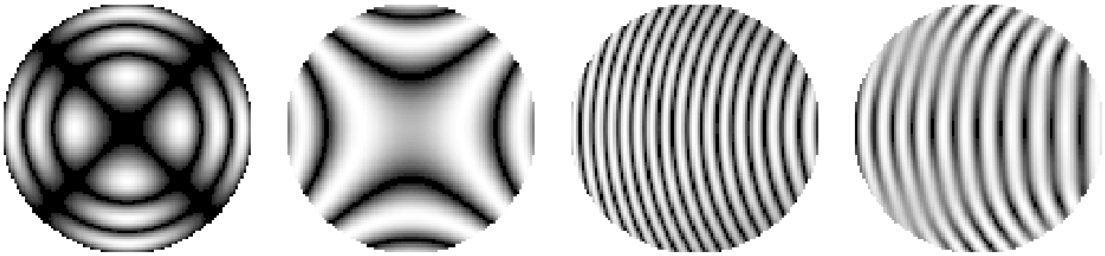

Figure 2.8: Four modelled inteference figures Images from left to right computed for: a homeotropic cell, a planar homogeneous cell, a cell whose director in uniformly tilted at $\pi/4$ and a HAN cell. Thes figures are calculated for monochromatic light, with $\lambda = 633$nm. In each, the liquid crystal layer was 50 μm thick, the polarizer's extinction axis made an angle of $\pi/4$ with the $x-$axis and $\Delta n = 0.2$.

the plane of incidence and the $x-$axis. An interference figure, or conoscopic image, will be formed upon the screen.

The intensity variation across the conoscopic figure is dominated by birefringence effects [99]. Two kinds of dark region can be seen in this kind of figure. Isogyres, such as the dark cross in the leftmost image in figure 2.8, are formed when incident light is polarized such that either no extraordinary or no ordinary wave is excited. The dark circular fringes in the same figure correspond to minima in the retardance and are called isochromes. Due to the wavelength dependence of the retardance, when a white light source is used,

concentric coloured rings are seen instead.

One advantage of conoscopy over the guided mode methods is the visual impact of the figures themselves. Each image in figure 2.8 looks quite different from the other. Even the last two, computed for a layer uniformly tilted at $\pi/4$ and a HAN layer, are different. Thus, some depth dependent information above and beyond that provided by polarizing microscopy can be obtaibned by simply inspecting the director profile. However, the techique does not work so well for cells only a few microns thick (such as real displays) - the resulting image would consist of only a central portion of the images above.

Conoscopy has been used in the study of liquid crystals almost since their discovery [22], and was used in the study of anisotropic materials long before that. It is usually carried out using a polarising microscope, either by removing the eyepiece, or by inserting an intermediate lens, called a Bertrand lens, between the objective and ocular. Flow alignment [100], biaxial materials [16] and lyotropic liquid crystals [101] have all been studied with this kind of conoscopy . Dedicated experiments which use laser light have also been reported [102–104], and have been recently used to analyze the flexoelectric effect [105].

2.3 The forward problem: calculation of the optical characteristics

Two calculations are combined to predict the reflection and transmission intensity coefficients measured in the fully-leaky guided mode experiment. The main calculation accounts for the propagation of light from within the glass media across the liquid crystal, ITO, and aligning layers. In other words, the interaction of a plane wave with a multi-layer dielectric stack is modelled. Berreman's 4×4 matrix method for stratified anisotropic media is introduced in section 2.3.2 for this purpose.

Simple formulae are sufficient for the secondary calculation, which relates both the reflection and transmission coefficients and the angles of incidence that are computed in the main model to those which should be observed at the glass-air interfaces. The glass prisms are large compared to both the wavelength of light and to the width of the laser beam, so interference due to multiple reflections at the glass interfaces may be neglected. Snell's law relates the angle of incidence at the glass-stack interface, α to the angle of incidence at the prism surface, β,

$$\alpha = \gamma - \beta' \tag{2.4}$$

$$n_G \sin\beta' = \sin\beta \tag{2.5}$$

where n_G is the refractive index of the prism relative to air, and γ is the angle between the prism-air interface and the prism-sample interface - usually $\pi/3$. The transmission and reflection coefficients at the detectors are related to those at the prism-sample interface by Fresnel's equations, given in appendix B.

2.3.1 The Jones and extended Jones matrix methods

Before the Berreman 4×4 matrix method is discussed, it is instructive to consider some simpler matrix-based treatments of stratified systems. Both the Jones and extended Jones methods neglect multiple beam interference, so cannot account for all the physics of the fully-leaky guided mode experiment. They are useful when the wavelength of the light source has a narrow but finite bandwidth, causing fringes of equal inclination to be blurred.

The Jones calculus [106] permits the changing polarization state and amplitude of a coherent light beam propagating along the $z-$axis and intersecting normally with a series of anisotropic plates to be computed. The electric field at any point on the beam before entering the first plate is written in terms of the amplitude components E_x, E_y, as the *Jones vector*

$$\boldsymbol{E}_0 = \begin{bmatrix} E_x \\ E_y \end{bmatrix}. \tag{2.6}$$

If the angle between the $x-$axis and the director is ψ, then the electric field between the first and second element is the product of a 2×2 *Jones matrix*, $\boldsymbol{M}_1$ with $\boldsymbol{E}_0$. For a plate of thickness h,

$$\boldsymbol{E}_1 = \boldsymbol{R}(\psi) \begin{bmatrix} \exp(-ik_{zo}h) & 0 \\ 0 & \exp(-ik_{ze}h) \end{bmatrix} \boldsymbol{R}(-\psi)\boldsymbol{E}_0 = \boldsymbol{M}_1\boldsymbol{E}_0, \tag{2.7}$$

where $k_{zo} = k_0\sqrt{\epsilon_\perp}$ and $k_{ze} = k_0\sqrt{\epsilon_\parallel}$ are the $z-$components of the ordinary and extraordinary wavevectors. $\boldsymbol{R}(\psi)$ is a rotation matrix,

$$\boldsymbol{R}(\psi) = \begin{bmatrix} \cos(\psi) & \sin(\psi) \\ -\sin(\psi) & \cos(\psi) \end{bmatrix}. \tag{2.8}$$

Various optical elements, such as $\lambda/4$ plates and polarizers, and birefringent slabs can be represented by a Jones matrix.

Equation (2.7) has a simple physical meaning. The matrix $\boldsymbol{R}(-\psi)$ divides the incoming wave into ordinary and extraordinary *eigenmodes*, with wavenumbers k_o and k_e. The second matrix calculates the phase shift of those eigenmodes as they propagate across the plate. Finally, $\boldsymbol{R}(\psi)$ transforms the resultant vector back into the laboratory coordinate

system. The electric field between the second and third plates is calculated using a similar expression to (2.7), and so on, leading to an expression which treats the whole series:

$$\boldsymbol{E}_n = \boldsymbol{M}_n \boldsymbol{M}_{n-1} \ldots \boldsymbol{M}_1 \boldsymbol{E}_0. \tag{2.9}$$

The original Jones matrix method has since been extended to treat light beams incident at any angle with respect to the layer normal. Yeh considered a single slab, and accounted for a single reflection at the interfaces by the introduction of the Fresnel coefficients into the Jones matrix [107]. Lien [108, 109], and later, Gu [110], derived an extended Jones method, including an inhomogeneous layer by breaking it up into many homogeneous layers. For a given angle of incidence, (2.7) is replaced by

$$\boldsymbol{E}_1 = \boldsymbol{S}(\theta, \psi, \alpha) \begin{bmatrix} \exp(-ik_{oz}h) & 0 \\ 0 & \exp(-ik_{ez}h) \end{bmatrix} \boldsymbol{S}(\theta, \psi, \alpha)^{-1} \boldsymbol{E}_0 \tag{2.10}$$

k_{oz} and k_{ez} are the $z-$components of the ordinary and extraordinary wavevectors, which are expressed in terms of the dielectric tensor and the conserved x-component of the wavevector. The matrices $\boldsymbol{S}$, which replace the rotation matrices, depend on k_{oz} and k_{ez} as well as on ψ. This variant of the extended Jones matrix method was used to compute the conoscopic figures depicted in 2.2.3, and the same application has been reported elsewhere [104, 105].

2.3.2 The Berreman method

The most general mathematical treatment of the one-dimensional problem is the 4×4 matrix method for stratified, anisotropic media proposed by Berreman [111]. The only assumptions made are that waves are time-harmonic throughout the system, and that the system is only inhomogeneous along the $z-$axis. The dielectric tensor of the medium may vary continuously, making the method more general than the earlier 4×4 matrix method reported by Teitler and Henvis [112]. In contrast to the extended Jones method, reflections are not neglected and so thin film interference may be described as well as birefringence.

Starting from Maxwell's curl equations for time-harmonic waves, Berreman eliminates the $z-$components of the electric and magnetic fields, leading to a set of linear ordinary differential equations

$$\frac{d}{dz}\boldsymbol{\psi} = ik_0 \boldsymbol{\Delta} \boldsymbol{\psi}. \tag{2.11}$$

in the wave amplitudes $\boldsymbol{\psi} = (E_x(z), H_y(z), E_y(z), -H_x(z))^T$. The matrix $\boldsymbol{\Delta}$, given in appendix B, depends on the dielectric tensor and the refractive index of the incident

medium. It also depends upon the incident angle of the light wave, and consequently equations (2.11) must be solved anew for each incident wave.

The general solution to (2.11) is

$$\boldsymbol{\psi}(z) = \boldsymbol{P}\boldsymbol{\psi}(z_0), \tag{2.12}$$

when the initial values $\boldsymbol{\psi}(z_0)$ are known. $\boldsymbol{P}$ is called the transfer matrix, or characteristic matrix, of the region $[z_0, z]$.

To describe the entire system, (2.12) must be solved when $z = z_d$ and the incoming wave is specified. Of course $\boldsymbol{\psi}(z_0)$ describes both incoming and reflected waves, while $\boldsymbol{\psi}(z_d)$ describes the transmitted wave, so some rearrangement is required. This re-arrangment is described in some detail in appendix B, but in essence $\boldsymbol{\psi}(z_0)$ is decomposed into incident and reflected parts, and a *scattering matrix* $\boldsymbol{S}$ defined in terms of $\boldsymbol{P}$ which allows allows the reflection and transmission coefficients to be found. Ultimately, the problem is reduced to computation of $\boldsymbol{P}$.

Over a homogeneous region of thickness h, the transfer matrix is given by a series expression:

$$\boldsymbol{P} = \exp(ik_0 h\boldsymbol{\Delta}) = \boldsymbol{I}_4 + ik_0 h\boldsymbol{\Delta} - (k_0 h)^2 \frac{\boldsymbol{\Delta}\boldsymbol{\Delta}}{2!} - \dots . \tag{2.13}$$

It is clear from (2.13) that the transfer matrix of any layer tends to the 4×4 identity matrix $\boldsymbol{I}_4$ as $hk_0 \to 0$. This implies that even a large amplitude perturbation to the dielectric tensor leads to only a small change to $\boldsymbol{\psi}(z)$, if it is limited to a thin region, and therefore the experiment is expected to be diminishingly sensitive to increasingly fine variation in the director profile.

The transfer matrix for a homogeneous layer can also be evaluated through the expression:

$$\boldsymbol{P} = \boldsymbol{\Psi}\boldsymbol{K}\boldsymbol{\Psi}^{-1}. \tag{2.14}$$

$\boldsymbol{\Psi}$ is a matrix whose columns, $\boldsymbol{\psi}_j$, are the eigenvectors of $\boldsymbol{\Delta}$, while $\boldsymbol{K}$ is a diagonal matrix with elements related to k_{zj}, the eigenvalues of $\boldsymbol{\Delta}$.

$$K_{jj} = \exp(ik_{zj}h). \tag{2.15}$$

Equation (2.14) is similar to the Jones matrix expressions (2.7) and (2.10) and has an analogous physical meaning. In this case, four eigenmodes, two travelling forward and two travelling backward are accounted for.

Except for certain special cases, the transfer matrix for an inhomogeneous layer must be found numerically. One approach is to simply solve the ODEs (2.11) using a standard

numerical method [113]. A more common approach is to divide the inhomogeneous region into n sub-layers, each sufficiently small to be assumed homogeneous. Then the transfer matrix of the whole layer is the product of the transfer matrices of each sublayer,

$$\boldsymbol{P} = \boldsymbol{P}_n \boldsymbol{P}_{n-1} \dots \boldsymbol{P}_1. \tag{2.16}$$

Wöhler [114] reports a variant on the sublayer approach, exploiting the Theorem of Cayley and Hamilton to efficiently evaluate $\boldsymbol{P}$. The resulting calculation involves the known eigenvalues of Δ in each layer, and calculation of a fourth order polynomial in Δ. Ko [115] notes that this approach is numerically unstable for beyond-critical incident angles. The instability occurs because exponentially growing and decaying waves are treated together in the matrix multiplications. Rounding error in computation of the growing wave is larger than the entire decaying wave, which is then swamped with inaccuracy. This is resolved by defining a succession of scattering matrices $\boldsymbol{S(0, m)}$ for the sub-region $[z_0, z_m]$. A recursive formula for $\boldsymbol{S(0, m-1)}$ is derived which involves $\boldsymbol{S(0, m-1)}$ and the inverse of $\boldsymbol{P}_m$ (which is calculated from (2.14)). The procedure ensures that growing and decaying waves are manipulated separately, but requires two matrix inversions to be calculated for each layer, leading to a method slightly less efficient, but more robust, than that of Wöhler.

2.4 The inverse problem

While it is a simple matter to predict the reflection and transmission coefficients given the director profile, using the techniques described, one must solve an *inverse problem* [116] to find the director profile given experimental data. A formulation for the steady state fully-leaky guided mode experiment will be described here: variants, such as the time dependent experiments, can be viewed as extensions. First, the measurements are gathered into a data vector

$$\boldsymbol{b} = \left(R_{\mathrm{pp}}(\beta_0), R_{\mathrm{pp}}(\beta_1), ..., R_{\mathrm{pp}}(\beta_n), R_{\mathrm{ps}}(\beta_0), ..., T_{\mathrm{ss}}(\beta_n)\right)^T. \tag{2.17}$$

Then, a model vector $\boldsymbol{m}$ is defined, from which the director profile, and hence the dielectric tensor can be built. The elements of $\boldsymbol{m}$ might be tilt and/or twist angles at points through the cell, or parameters from which the director can be found, such as elastic constants. For a given vector $\boldsymbol{m}$ the results of the Berreman calculation, denoted $\boldsymbol{f}(\boldsymbol{m})$ are sorted in the same order as the data vector (2.17). The inverse problem can now be written as a set of equations

$$\boldsymbol{f}(\boldsymbol{m}) = \boldsymbol{b} \tag{2.18}$$

which are to be solved for $\boldsymbol{m}$.

The idea of an inverse problem defined in terms of a corresponding forward problem is perhaps an arbitrary notion, at least mathematically. After all, if the function $\boldsymbol{f}$ were linear in $\boldsymbol{m}$,

$$\boldsymbol{f}(\boldsymbol{m}) = \boldsymbol{F}\boldsymbol{m}, \tag{2.19}$$

and the vectors $\boldsymbol{m}$ and $\boldsymbol{b}$ had the same number of elements, $\boldsymbol{m}$ would be found simply by evaluating

$$\boldsymbol{m} = \boldsymbol{F}^{-1}\boldsymbol{b}. \tag{2.20}$$

The matrix $\boldsymbol{F}^{-1}$ is not an inverse in any special sense: $\boldsymbol{F}$ could equally be regarded as its inverse. Even if $\boldsymbol{f}$ is not linear in $\boldsymbol{m}$, as in the Berreman calculation, a similar formula can be imagined, although it may be impossible to write down a simple expression for the inverse of $\boldsymbol{f}$. Inverse problems are distinct from forward problems in more meaningful sense: they are usually *ill-posed*.

2.4.1 Ill-posed problems

Hadamard, in his classic text on the theory of partial differential equations [117], considered a problem consisting of a PDE and boundary conditions, or data, *correctly-set* if a solution existed and was unique. He also identified, in the context of Laplace's equation, a situation where an arbitrarily small change in the boundary conditions could lead to a large change in the solution. More recent publications [118, 119] use the term *well-posed* instead of 'correctly-set' to refer to problems which satisfy Hadamard's conditions:

- a solution to the problem exists;
- the solution is unique;
- the solution is stable with respect to perturbations of the data.

A problem is said to be *ill-posed* if any one of Hadamard's conditions is not satisfied[2]. The first kind of ill-posed problem is well known to any experimentalist. In normal practise, more data are collected than parameters sought. The result is an overdetermined set of equations: that is, there are more equations than unknowns, and these equations are inconsistent with each other. This inconsistency is due to experimental error: in its absence the excess equations would be linear combinations of the others. Problems of this type are dealt with by solving some kind of optimisation problem, such as a least squares problem. Optimisation problems will be introduced in some detail in 2.4.2.

[2]Tikhonov, and others, suggest that Hadamard uses the terms 'well-posed' and 'ill-posed', and explicitly listed all three conditions in a later, out-of-print work.

The probabilistic formulation of inverse problem theory [116] is especially concerned with problems which violate the second condition. They occur when the experiment is somehow insensitive to some parameter, or combination of parameters. Either an insufficient quantity of data is available ($\boldsymbol{b}$ is shorter than $\boldsymbol{m}$), or the experiment has a less obvious deficiency to the same effect. To resolve a problem of this type completely, additional experiments must be performed, in which case, one needs to combine the results systematically. Or it may be sufficient to reformulate the inverse problem to recover some smaller set of parameters.

Hadamard's third condition is rather subtle compared to the other two, and is best illustrated through an example. Consider the influence of random error on the solution to the unsteady, one dimensional heat conduction problem. The idea is to model the temperature field $u(x,t)$ along, for example, an iron bar, extending from $x = 0$ to $x = \pi$, and held at constant temperature at each end. A linear second order partial differential equation,

$$\frac{\partial u}{\partial t} + \frac{\partial^2 u}{\partial x^2} = 0, \tag{2.21}$$

is solved together with the boundary conditions $u(0,t) = u(\pi,t) = 0$ and $u(x,0) = \sum_n a_n \sin(nx)$ to give

$$u(x,t) = \sum_n a_n \sin(nx) \exp(-n^2 t). \tag{2.22}$$

The function $u(x,0)$ can be thought of as a set of measurements taken at $t = 0$, in the absence of any error. In this case, it is reasonable to assume that a_n decays as n grows. In other words, the temperature varies smoothly along the bar. Experimental error can be represented by adding a perturbation $\delta u(x,0)$ to $u(x,0)$ such that

$$u(x,0) = \sum_n (a_n + \delta a_n) \sin(nx). \tag{2.23}$$

If the experimental error is random, the Fourier components δa_n will not tend to decay in magnitude with n.

Both well-posed and ill-posed problems can be constructed from (2.22) and (2.23). In the forward heat conduction problem, the task is to calculate u at $t = 1$. Given the perturbed boundary condition (2.23),

$$u(x,1) = \sum_n (a_n + \delta a_n) \sin(nx) \exp(-n^2). \tag{2.24}$$

Notice that high-frequency components of $u(x,1)$ are damped by a factor $\exp(-n^2)$, compared to $u(x,0)$, including the high frequency components of the error. Figure 2.9 shows

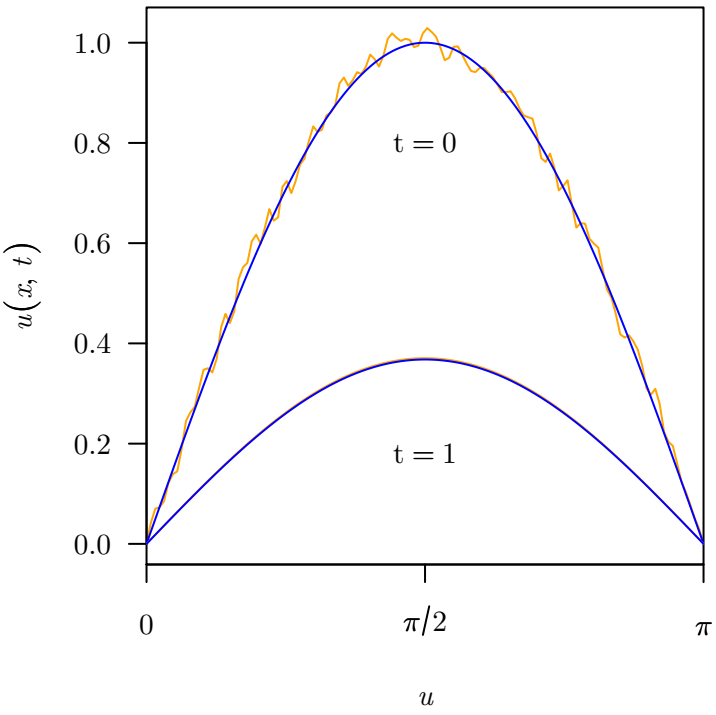

Figure 2.9: Solutions to the forward heat conduction problems. The two upper curves plot a pair of initial temperature fields $u(x,0)$ (blue curve) and $u(x,0)+\delta u(x,0)$)orange curve) which differ by low amplitude noise. Solutions to the forward heat conduction problem at $t=1$, given these initial conditions, are plotted by the two lower curves - which are indistiguishable.

two example solutions to this problem togther with their initial conditions. These initial conditions differ by random noise representing experimental error and they lead to final solutions which are barely distinguishable. This is a well-posed problem, because the solution is not changed much by a small error.

In contrast, high frequency components are amplified in the solution to the ill-posed backward heat problem,

$$u(x,-1)=\sum_n (a_n+\delta a_n)\sin(nx)\exp(n^2). \tag{2.25}$$

The backward heat conduction problem, is of course, an inverse problem with respect to the forward heat problem. Recall that the components a_n decay with n but the perturbations δa_n do not. For infinite dimensional problems (that is, where n is unbounded), no matter how small the amplitude of the error in $u(x,0)$, it is possible to find some n such that error is the largest contribution to $u(x,-1)$. Now the difference between the two example solutions, shown in figure 2.10, is so large that $t=-1/1000$ had to be chosen rather than $t=-1$ to prevent numerical overflow. Such arbitrarily large amplification of the error does not occur in finite dimensional problems, but in practise the error is not vanishingly

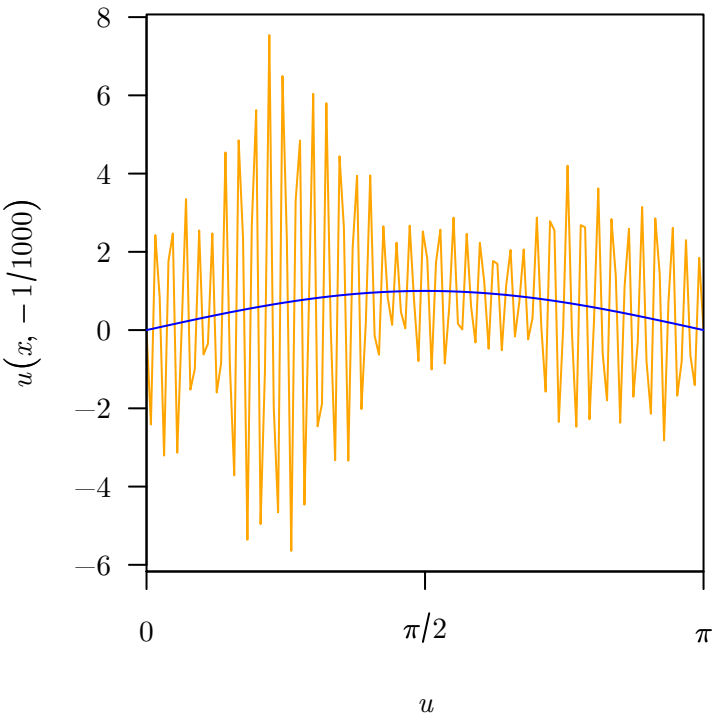

Figure 2.10: Solutions to the backward heat conduction problems. Given the same pair of conditions at $t = 0$ shown in figure 2.9, the solutions at $t = -1/1000$ are vastly different.

small, and so spurious solutions are still expected. In effect, experimental error tends to dominate solutions to the backward heat conduction problem.

Ill-posed problems of the third kind, where a unique solution exists but is dominated by experimental error, can be dealt with by *regularization*. Just as with the second kind of problem, one must introduce some kind of additional information. But given that the problem is already fully- or over-determined, it would seem that further information cannot be included. In practise, a new optimisation problem is formulated, in which some compromise between the additional information and the original problem is sought. Regularization will be discussed in more detail in 2.4.3.

Is the problem formulated in (2.18) ill-posed? Some variants of the experiments described lead to a problem with multiple solutions, and so violate Hadamard's second condition: simple polarisation microscopy for example cannot determine the director profile uniquely. If Hadamard's second condition is not violated, the first surely will be: the quantity of data will exceed the number of free parameters, so in the presence of errors, equations (2.18) will be inconsistent. Most importantly, in the context of this thesis, Lionheart [120] has shown that determination of the dielectric tensor from angle-scanning experiments, such as the fully-leaky guided mode experiment, is an ill-posed problem in the third sense.

2.4.2 Optimisation problems

If set of equations (2.18) are inconsistent through errors in the data, $\boldsymbol{b}$, then the inverse problem becomes an optimisation problem. Assuming that the errors in $\boldsymbol{b}$ are Gaussian, and uncorrelated, then the least-squares function

$$\Phi = (\boldsymbol{f}(\boldsymbol{m}) - \boldsymbol{b})^T(\boldsymbol{f}(\boldsymbol{m}) - \boldsymbol{b}) \tag{2.26}$$

must be minimised with respect to $\boldsymbol{m}$ [86]. In the language of optimization problems, a function to be minimised, like Φ, is often called an *objective function* If the forward problem were linear, then the objective function would be reduced to

$$\Phi = (\boldsymbol{F}\boldsymbol{m} - \boldsymbol{b})^T(\boldsymbol{F}\boldsymbol{m} - \boldsymbol{b}). \tag{2.27}$$

The solution to this linear least squares problem is the vector

$$\boldsymbol{m} = (\boldsymbol{F}^T\boldsymbol{F})^{-1}\boldsymbol{F}^T\boldsymbol{b}. \tag{2.28}$$

Equation 2.27 resembles the solution to the linear system 2.19, but with the matrix $(\boldsymbol{F}^T\boldsymbol{F})^{-1}\boldsymbol{F}^T$, known as the Moore-Penrose generalised inverse of $\boldsymbol{F}$, in place of $\boldsymbol{F}^{-1}$. Of course , the generalised inverse reduces to $\boldsymbol{F}^{-1}$ when $\boldsymbol{F}$ is square.

The generalised inverse still appears in solutions of the nonlinear least squares problem when the Gauss-Newton method is employed. Essentially, the solution to the nonlinear problem is found by solving a sequence of linear least-squares problems.

$$\boldsymbol{m}_{k+1} = \boldsymbol{m}_k + (\boldsymbol{J}^T\boldsymbol{J})^{-1}\boldsymbol{J}^T(\boldsymbol{f}_B(\boldsymbol{m}_k) - \boldsymbol{b}). \tag{2.29}$$

The Jacobian matrix $\boldsymbol{J}$ is the matrix of partial derivatives of $\boldsymbol{f}$ with respect to $\boldsymbol{x}$,

$$J_{ij} = \frac{\partial f_i}{\partial x_j}. \tag{2.30}$$

If the method works as intended, both the objective function and the size of the Gauss-Newton update, $||\boldsymbol{m}_{k+1} - \boldsymbol{m}_k||_2$, should decay rapidly with the *iteration number*, k.

One difficulty with the Gauss-Newton method is the need to evaluate and store the Jacobian matrix. Even when an analytical formula for $\boldsymbol{J}$ exists, it may be costly to compute. And if the number of parameters is and/or data is large, the memory required to store $\boldsymbol{J}$ can be prohibitive. A variety of gradient based methods, such as the BFGS and conjugate gradient methods [121], where it is only necessary to store the gradient vector

$\frac{\partial \Phi}{\partial \boldsymbol{m}}$ can help to deal with the latter problem. The simplex method of Nelder and Mead [122] does not even require the gradient vector to be evaluated.

All the methods described above are unconstrained optimisation methods: it is assumed that the components of $\boldsymbol{m}$ can take on any value. This is not always the case. If the constraints on $\boldsymbol{m}$ are simple, it may be possible to transform its components in some way. For example, a positive definite quantity p can be represented by a quantity q which can take on any real value through the expression

$$p = \exp(q). \tag{2.31}$$

When such a change of parameters is not practical, a constrained optimisation method, such as the L-BFGS-B method, or an adapted version of the Nelder-Mead method can be utilised. A constrained variant of the Gauss-Newton method has been reported [123], but is limited to constraints which can be expressed as linear inequalities in $\boldsymbol{m}$

2.4.3 Regularization

Tikhonov regularization [119], reported independently by Phillips, and further developed by Twomey [124] was originally proposed to stabilise the solutions to ill-posed integral equations. It is equally applicable to least squares problems. A penalty term is added to the least-squares function (2.26), giving a new objective function

$$\Phi = (\boldsymbol{f}(\boldsymbol{m}) - \boldsymbol{b})^T(\boldsymbol{f}(\boldsymbol{m}) - \boldsymbol{b}) + \lambda^2 \boldsymbol{m}^T \boldsymbol{L}^T \boldsymbol{L}\boldsymbol{m} \tag{2.32}$$

which can be minimised through a modified Gauss-Newton scheme:

$$\boldsymbol{m}_{k+1} = \boldsymbol{m}_k + (\boldsymbol{J}^T\boldsymbol{J} + \lambda^2 \boldsymbol{L}^T\boldsymbol{L})^{-1}\boldsymbol{J}^T(\boldsymbol{f}_B(\boldsymbol{m}_k) - \boldsymbol{b}). \tag{2.33}$$

The penalty term, formed from the matrix $\boldsymbol{L}$ and the *regularization parameter* λ, imposes prior knowledge of some kind on the solution. As λ grows, the minimum of Φ comes closer to satisfying the equation

$$\boldsymbol{L}\boldsymbol{m} = 0, \tag{2.34}$$

A common choice for the matrix $\boldsymbol{L}$ is the identity matrix, in which case the additional term acts to keep the solution close to $\boldsymbol{m} = 0$. Clearly, $\boldsymbol{L}$ should reflect some underlying physics: to this end a matrix based upon the continuum theory of nematics will be introduced in chapter 3, and has also been reported by Polydorides[125].

The *regularization parameter*, λ may be known in advance if an *a priori* probability

distribution for $\boldsymbol{m}$ is known. In that case, the objective function (2.32) can be derived from Bayes theorem assuming a Gaussian prior probability density with the covariance matrix $\lambda^2/e^2\boldsymbol{L}^T\boldsymbol{L}$, where e^2 is the variance of the noise in $\boldsymbol{b}$. If such detailed knowledge is unavailable an ansatz for λ which depends upon the error in $\boldsymbol{b}$ can be employed [126], or the effect of varying λ can be examined on a test case.

2.5 Summary

Several experimental techniques have been introduced which characterise liquid crystal cells by their optics. Both birefringence effects and thin film interference are expected in typical cells, and both are affected by changes in the director profile. The simplest technique, polarising microscopy, is sensitive only to on-average changes to the director, but a host of other experiments can recover more. Angle scanning methods, particularly guided mode experiments, are known to be sensitive to localised changes in the director.

The optical characteristics of a simple cell can be predicted numerically, by an implementation of Berreman's 4×4 matrix method. Berreman's method treats stratified, or one dimensional-systems, accounting for both anisotropy and the excitation of Fabry-Perot modes. Laser beams are far wider (of the order of millimetres) than the depth of the liquid crystal layer (no more than 100 microns), and therefore the whole system, sample and radiation combined, can indeed be treated as one-dimensional. An approximate, numerical treatment is required because the liquid crystal layer is inhomogeneous.

Finally, an inverse problem was described. Berreman's method can be used to predict the experimental data, given the director profile, but of course the experimentalist wants to solve the corresponding inverse problem: find the director profile, given the data. Inverse problems are in fact ill-posed problems, in that they have either no solution, many solutions, or may be disproportionately affected by experimental error. Anticipating that the current problem is ill-posed in the first sense, it was reformulated as an optimisation problem. In the next chapter, a powerful numerical technique, *singular value decomposition* will be introduced, which can be used to decide whether, and how severely, a problem is ill-posed in the second and third senses. It will be used to compare experimental scenarios, and will be extended to examine a potential remedy: regularization.

Chapter 3

Singular value decomposition analysis of the inverse problem

3.1 Introduction

This chapter is concerned with 'imaging' the tilt profile in a HAN cell. Ideally, 'imaging' would mean taking experimental measurements and then determining the function $\theta(z)$ without making any assumptions about it. This won't in fact be possible, because the problem which must be solved will turn out to be ill-posed. Instead, a compromise will be detailed, in which the Ericksen-Leslie equations are held to be approximately correct.

It was fairly easy to see why the backward heat conduction problem outlined in the previous chapter is ill-posed. This was because a simple, linear mapping between changes to the data and changes to the solution was given, in (2.25). In that equation it was clear that higher frequency changes to the data (presumably due to random error) were amplified by increasingly large factors in the solution. A similar expression is needed for the Berreman 4×4 matrix method, and that will be found by considering the *singular value decomposition* (SVD) of the Jacobian matrix of $\boldsymbol{f}$.

SVD analysis was first considered in the context of this problem by Lionheart *et al.* [120], who demonstrated several important results. First, determination of all six components of the dielectric tensor as a function of z is a severely ill-posed problem, in the third sense of the previous chapter. Second, they showed that the problem is similarly ill-posed for HAN cells, planar cells, and twisted nematic cells. Thirdly, it was demonstrated that depth dependent information can only be recovered if the liquid crystal is strongly birefringent. Finally, they proved that taking measurements over a wider range of angles improves the situation somewhat.

Here, a restricted problem will be considered, applicable to HAN cells. The liquid

crystal will be assumed to be uniaxial, so that the dielectric tensor within the liquid crystal layer is determined by the director profile and two complex constants, $\epsilon_\perp$ and $\epsilon_\parallel$. For much of this chapter it will be assumed that $\epsilon_\perp$ and $\epsilon_\parallel$ are known. In all the analyses, the director is confined to the $xz-$plane, so that it is specified by the tilt angle, $\theta(z)$.

Despite these simplifications, SVD analysis will show that the imaging problem is still severely ill-posed. The SVD will also be used to show that, in its standard form, Tikhonov regularization cannot be expected to work. A custom regularization method, based on the Ericksen-Leslie equations, will be proposed, and a modified SVD analysis will be developed in order to study it. Some additional questions will be considered. How does uncertainty in the layer depth, in the permittivities, or in the nature of the ITO electrodes affect the inverse problem? What is the effect of taking measurements at higher mean polar angles, or at different azimuthal angles. Can the experiment be improved by choosing a different coloured laser, or combining results from several? How do the various waveguide experiments compare in terms of the SVD?

3.2 Methodology

The simplest imaging problem is formulated as follows. First, break up the liquid crystal layer into n sub-layers, each of thickness h and thin enough to be treated as homogeneous. 'Thin enough' means that breaking up each of those layers into still thinner layers makes effectively no difference to the computed reflection and transmission coefficients. Next, make an initial guess at the solution. In this case, the linear tilt profile

$$\theta(z) = \frac{\theta_0(d-z) + \theta_d z}{d} \tag{3.1}$$

will be used. Then form a column vector $\boldsymbol{m}$ from changes to the tilt angle, $\delta\theta$, at the centre of each layer,

$$\boldsymbol{m} = \left(\delta\theta(z = \frac{h}{2}), \delta\theta(z = \frac{3h}{2}), \ldots, \delta\theta(z = \frac{(2n-1)h}{2})\right)^T. \tag{3.2}$$

Define a vector function $\boldsymbol{f}$ which maps $\boldsymbol{m}$ to the corresponding calculations of R and T and a data vector $\boldsymbol{b}$ containing the experimental data, both as described in 2.4. Finally, minimise the nonlinear least-squares function,

$$\Phi = (\boldsymbol{f}(\boldsymbol{m}) - \boldsymbol{b})^T(\boldsymbol{f}(\boldsymbol{m}) - \boldsymbol{b}), \tag{3.3}$$

with respect to $\boldsymbol{m}$. More complex imaging problems can be formulated by augmenting $\boldsymbol{m}$ with additional parameters which define the depth of the liquid crystal layer and so on.

To consider how minimisation of Φ might be an ill-posed problem, an examination of the Gauss-Newton iterations

$$\boldsymbol{m}_{k+1} = \boldsymbol{m}_k + (\boldsymbol{J}^T\boldsymbol{J})^{-1}\boldsymbol{J}^T(\boldsymbol{f}(\boldsymbol{m}_k) - \boldsymbol{b}). \tag{3.4}$$

and in particular the Jacobian matrix $\boldsymbol{J}$ is in order. For now, the fact that (3.3) might have multiple minima due to its non-linearity will be neglected. Instead, the linear least squares problems which are solved at each iteration will be analysed. At every iteration of (3.4), an update to $\boldsymbol{m}_k$ is calculated by solving the linear equations

$$\boldsymbol{J}^T\boldsymbol{J}\delta\boldsymbol{m}_k = \boldsymbol{J}^T(\boldsymbol{f}(\boldsymbol{m}_k) - \boldsymbol{b}) \tag{3.5}$$

for $\delta\boldsymbol{m}_k$. If $\delta\boldsymbol{m}_k$ is strongly affected by noise, like the solutions to the backward heat problem, then the Gauss-Newton iterations might not converge, or might converge to a spurious solution. For $\delta\boldsymbol{m}_k$ to be dominated by error when $\boldsymbol{b}$ is not - in other words, for (3.5) to be ill-posed in the third sense, implicates the matrix $\boldsymbol{J}$. Our analysis, then, will concentrate on this matrix.

3.2.1 Numerical calculation of the Jacobian matrix

The Jacobian matrix is not generally known for an arbitrary set of parameters, but can be approximated by a matrix whose n columns are $\boldsymbol{g}_i$,

$$\boldsymbol{J} \approx \begin{bmatrix} \boldsymbol{g}_1 & \boldsymbol{g}_2 & \cdots & \boldsymbol{g}_n \end{bmatrix}. \tag{3.6}$$

Each of the column vectors $\boldsymbol{g}_i$ is found by the central difference formula,

$$\boldsymbol{g}_i = \frac{1}{2h}\left(\boldsymbol{f}(\boldsymbol{m_k} + \boldsymbol{h}_i) - \boldsymbol{f}(\boldsymbol{m_k} - \boldsymbol{h}_i)\right) \tag{3.7}$$

where only the ith component of $\boldsymbol{h}_i$ is non-zero:

$$\boldsymbol{h}_i = (0, \ldots, h, \ldots, 0)^T \tag{3.8}$$

and h is some small finite real number.

3.2.2 Weak nonlinearity

Since $\boldsymbol{f}$ is a nonlinear function of $\boldsymbol{m}$, $\boldsymbol{J}$ is not constant. In other words, $\boldsymbol{J}$ should be recalculated at every Gauss-Newton iteration. The results presented in this chapter (but not elsewhere) are derived only from $\boldsymbol{J}$ as it is computed at the first iteration: in other words, it is assumed that $\boldsymbol{J}$ varies slowly. Such an assumption is valid if $\boldsymbol{f}$ is only weakly nonlinear in $\boldsymbol{m}$, at least in the region between the initial guess and the final solution.

3.2.3 Singular value decomposition

The *singular value decomposition* (SVD) of a rectangular matrix, like $\boldsymbol{J}$, is similar to the eigenvalue / eigenvector system of a square matrix. It is formed from three matrices, which satisfy

$$\boldsymbol{J} = \boldsymbol{U}\boldsymbol{S}\boldsymbol{V}^T. \tag{3.9}$$

$\boldsymbol{S}$ is a diagonal matrix,

$$\boldsymbol{S} = \begin{bmatrix} \sigma_1 & 0 & \dots & 0 \\ 0 & \sigma_2 & \dots & 0 \\ \vdots & \vdots & \vdots & \vdots \\ 0 & 0 & \dots & \sigma_n \end{bmatrix}. \tag{3.10}$$

where the *singular values*, σ_j are the square roots of the eigenvalues of $\boldsymbol{J}^T\boldsymbol{J}$, and are ordered such that $\sigma_j \leq \sigma_{j-1}$. The matrices $\boldsymbol{U}$ and $\boldsymbol{V}$ are orthonormal; their columns $\boldsymbol{u}_j$ and $\boldsymbol{v}_j$ are respectively called *left* and *right singular vectors* and are (also respectively) eigenvectors of $\boldsymbol{J}\boldsymbol{J}^T$ and $\boldsymbol{J}^T\boldsymbol{J}$. When $\boldsymbol{J}$ has more rows (m) than columns (n), that is when there are more data than parameters, $\boldsymbol{V}$ is formed from all n eigenvectors of $\boldsymbol{J}^T\boldsymbol{J}$, but only the first n of the m eigenvectors of $\boldsymbol{J}\boldsymbol{J}^T$ go to make up $\boldsymbol{U}$. The remaining eigenvectors of $\boldsymbol{J}\boldsymbol{J}^T$ define a subspace which excludes vectors of the form $\boldsymbol{J}\boldsymbol{m}$. Vectors in this subspace represent portions of the data which cannot be explained by the model - such as experimental error.

When the vector $\boldsymbol{m}$ is a discrete representation of a continuous function, as in this case, updates to it can often be described by the first few $\boldsymbol{v}_j$. Each vector $\boldsymbol{v}_j$ is itself a discrete version of a continuous function, each of which is orthogonal to the others, and of unit magnitude. Put another way, $\boldsymbol{\delta m}$ is built from $\boldsymbol{v}_j$ much like a Fourier series:

$$\delta\boldsymbol{m} = \sum_{j=1}^{j=n} \delta\boldsymbol{m}^T\boldsymbol{v}_j\boldsymbol{v}_j \tag{3.11}$$

Larger values of j typically correspond to increasingly oscillatory $\boldsymbol{v}_j$, so that if $\delta\boldsymbol{m}$ represents a smooth function, the coefficients $\delta\boldsymbol{m}^T\boldsymbol{v}_j$ will decay quickly as j increases. Similarly

the vector

$$\boldsymbol{f}(\boldsymbol{m}) - \boldsymbol{b} = \sum_{j=1}^{j=m} (\boldsymbol{f}(\boldsymbol{m}) - \boldsymbol{b})^T \boldsymbol{u}_j \boldsymbol{u}_j \tag{3.12}$$

is built from contributions parallel to the left singular vectors. In other words, any change to the reflection and transmission coefficients due to changes to $\boldsymbol{m}$ can be built from continuous functions represented by the left singular vectors.

3.2.4 The SVD and ill-posed problems

Rewriting (3.5) in terms of the SVD shows how the solution can be swamped with error, even when the experimental data are extremely accurate. The formula is:

$$\delta \boldsymbol{m}_k = \sum_j \frac{1}{\sigma_j} \boldsymbol{v_j} \boldsymbol{u}_j^T (\boldsymbol{f}(\boldsymbol{m}_k) - \boldsymbol{b}). \tag{3.13}$$

Let the experimental data be composed of the 'true' data $\boldsymbol{b}_0$ and some error $\boldsymbol{\epsilon}$. Then $\delta \boldsymbol{m}_k$ is also the sum of a 'true' solution and an error:

$$\delta \boldsymbol{m}_k = \sum_j \left(\frac{1}{\sigma_j} \boldsymbol{v_j} \boldsymbol{u}_j^T (\boldsymbol{f}(\boldsymbol{m}_k) - \boldsymbol{b}_0) + \frac{1}{\sigma_j} \boldsymbol{v_j} \boldsymbol{u}_j^T \boldsymbol{\epsilon} \right) \tag{3.14}$$

For any j, if $\boldsymbol{u}_j^T \boldsymbol{\epsilon}$ is not small compared to $\boldsymbol{u}_j^T (\boldsymbol{f}(\boldsymbol{m}_k) - \boldsymbol{b}_0)$, then the contribution to the solution proportional to $\boldsymbol{v}_j$ will be strongly affected by error. While it is common for $\boldsymbol{u}_j^T (\boldsymbol{f}(\boldsymbol{m}_k) - \boldsymbol{b}_0)$ to decrease as j increases, $\boldsymbol{u}_j^T \boldsymbol{\epsilon}$ typically does not. Since the factors $1/\sigma_j$ increase with j, the result is increasingly large, oscillatory, spurious contributions to the solution.

Plotting the relative values of σ_j, that is, σ_j/σ_1, is useful in the analysis of ill-posed problems of the second and third kinds. Figure 3.1 contains some artificial examples of this kind of plot. The solid line depicts a set of singular values which decay gradually (exponentially in this case) to a very small value. For every j where σ_j/σ_1 is not large compared to the signal-to-noise ratio,ϵ, one can expect a significant spurious contribution to the solution. Only if the smallest σ_j/σ_1 were much larger than ϵ would sensible solutions be found. Note that this sort of analysis is only meaningful when the 'true' solution is built from contributions which decay as j grows. If the converse is true, the problem cannot be called ill-posed at all.

The SVD also reveals when a problem is ill-posed in the second sense (that is, when $\boldsymbol{J}$ is singular). In this case, some of the singular values will be zero, or very close to zero if some numerical error is accounted for. A plot of the relative values of σ_j against j would gradually decay at first, then suddenly drop to zero (figure 3.1, dotted curve). The formula

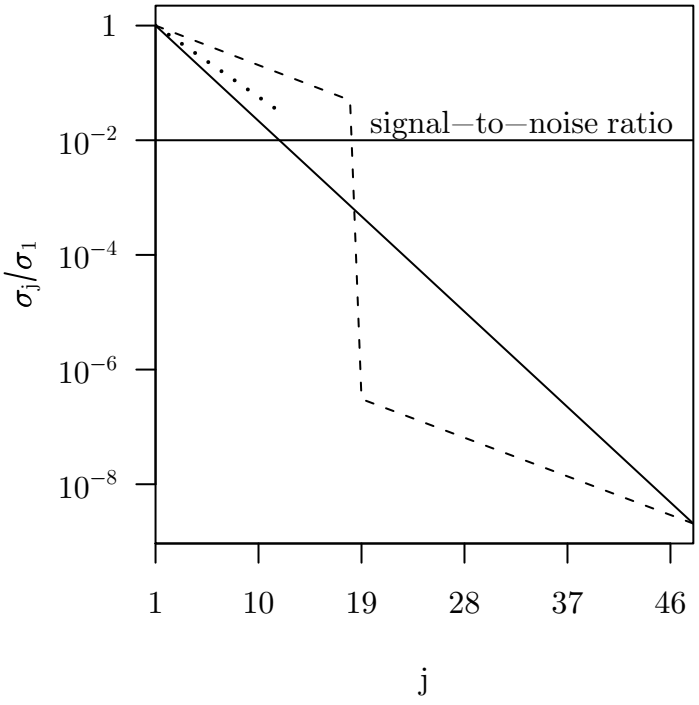

Figure 3.1: Diagram indicating relative decay of the singular values σ_j with j for three classes of ill-posed problems. In an ill-posed problem of the third kind (solid line), σ_j decays gradually, down to a value much smaller then the signal-to-noise ratio . For ill-posed problems of the second kind, σ_j decays gradually for $j < M$, then drops to zero (dotted line, with $M = 12$). The dashed polygon represents a problem which is ill-posed in the third sense, but resembles a problem of the second kind in that σ_j decays suddenly after $j = 18$ to much a smaller value.

(3.13) cannot be used (it involves division by zero), but a modified form can. Assuming that $\sigma_j = 0$ for $j > M$, the *minimum norm* solution is

$$\delta \boldsymbol{m}_k = \sum_{j=1}^{j=M} \frac{1}{\sigma_j} \boldsymbol{v}_j \boldsymbol{u}_j^T (\boldsymbol{f}(\boldsymbol{m}_k) - \boldsymbol{b}). \tag{3.15}$$

This solution reflects the fact that the forward model, and thus the experiment, is completely insensitive to any change to $\boldsymbol{m}$ proportional to $\boldsymbol{v}_j$ where $j > M$.

3.2.5 Regularization and the SVD

If σ_j were to decrease suddenly to some small but non-zero value for some $j = M$, as in the dashed curve shown in figure 3.1, then (3.15) could be used to obtain a *regularized* solution. This is known as the truncated SVD, or TSVD solution [127]. Like all regularized solutions, it is useful only if the 'true' solution can be built from the first few singular vectors, in this case 'few' meaning M. Furthermore, the singular values must not decay very quickly for $j < M$, or else the original difficulties will be encountered.

For ill-posed problems like the backward heat conduction problem, Tikhonov regular-

ization may be a better choice than TSVD regularization. In these problems, the singular values decay to small values without any sudden drops. Assume for now that the matrix $\boldsymbol{L}$ in (2.32) is the identity matrix. Rewriting the modified Gauss-Newton step, (2.33), in terms of the SVD of $\boldsymbol{J}$,

$$\delta \boldsymbol{m}_k = \sum_{j=1}^{j=m} \frac{f_j}{\sigma_j} \boldsymbol{v}_j \boldsymbol{u}_j^T (\boldsymbol{f}(\boldsymbol{m}_k) - \boldsymbol{b}). \tag{3.16}$$

where the *filter factors*, f_j, are

$$f_j = \frac{\sigma_j^2}{\sigma_j^2 + \lambda^2}. \tag{3.17}$$

The filter factors acts to gradually damp contributions parallel to $\boldsymbol{v}_j$ as j increases, because they decay continuously. Once more, the implicit assumption is that the 'true' solution is dominated by contributions parallel to the early singular vectors.

The assumption that the 'true' $\delta \boldsymbol{m}_k$ must include mainly contributions associated with smaller j are summed up by the *Discrete Picard Condition* [128, 118, 126]. This states that, for a regularized solution to be close to the true solution, the factors $\boldsymbol{u}_j^T(\boldsymbol{f}(\boldsymbol{m}_k) - \boldsymbol{b}_0)$ must decay more rapidly than σ_j. In other words, the ratio $\boldsymbol{u}_j^T(\boldsymbol{f}(\boldsymbol{m}_k) - \boldsymbol{b}_0)/\sigma_j$ must shrink as j grows. So, by looking at this ratio for some synthetic data, one can answer the crucial question: is a Tikhonov regularized solution likely to be useful? One of the first results in this chapter will suggest that standard Tikhonov regularization cannot be expected to give useful solutions.

Making use of standard Tikhonov regularization is tantamount to assuming that $\boldsymbol{m}$ is close to zero. In other words, the objective function (2.32) is reduced from

$$\Phi = (\boldsymbol{f}(\boldsymbol{m}) - \boldsymbol{b})^T (\boldsymbol{f}(\boldsymbol{m}) - \boldsymbol{b}) + \lambda^2 \boldsymbol{m}^T \boldsymbol{L}^T \boldsymbol{L} \boldsymbol{m} \tag{3.18}$$

to

$$\Phi = (\boldsymbol{f}(\boldsymbol{m}) - \boldsymbol{b})^T (\boldsymbol{f}(\boldsymbol{m}) - \boldsymbol{b}) + \lambda^2 \boldsymbol{m}^T \boldsymbol{m} \tag{3.19}$$

On the face of it, this seems like a reasonable assumption - one expects the tilt profile in a HAN cell to be close to linear. That said, given that elastic forces cause the director to vary slowly, the 'true' solution is more likely to be a smooth, large amplitude deviation from the linear profile than a low amplitude, high frequency perturbation.

A non-standard variant on Tikhonov regularization, consistent with the notion that director profiles should vary smoothly, may be derived by considering the Ericksen-Leslie equations. Assume that the splay and bend elastic constants k_{11} and k_{33} are equal. In this case, the governing equation for the tilt profile, in steady-state, and with no field applied,

is simply

$$\frac{\partial^2 \theta}{\partial z^2} = 0. \tag{3.20}$$

The linear tilt profile (3.1) is a solution of (3.20), which can therefore be rewritten as

$$\frac{\partial^2}{\partial z^2} \delta\theta = 0. \tag{3.21}$$

The idea is to prefer solutions which are close to satisfying this equation, or rather, a discrete approximation to it

$$\boldsymbol{L}\boldsymbol{m} = 0. \tag{3.22}$$

where

$$\boldsymbol{L} = \begin{bmatrix} 1 & 0 & 0 & 0 & \dots & 0 \\ -1 & 2 & -1 & 0 & \dots & 0 \\ 0 & -1 & 2 & -1 & \dots & 0 \\ \vdots & & & & \dots & \vdots \\ 0 & 0 & 0 & 0 & \dots & 1 \end{bmatrix}. \tag{3.23}$$

Each row of $\boldsymbol{L}$ apart from the first and last is derived by using the central difference approximation. The top and bottom rows are found by assuming that $\delta\theta$ at the ends of the cell are close to zero. From this equation, a penalty term is formed,

$$p = \lambda^2 \boldsymbol{m}^T \boldsymbol{L}^T \boldsymbol{L}\boldsymbol{m} \tag{3.24}$$

which quantifies the misfit between $\boldsymbol{m}$ and (3.22) and has the exact same form as the penalty term in the objective function (3.18).

How does the introduction of $\boldsymbol{L}$ affect the SVD analysis discussed so far? Because $\boldsymbol{L}$ is a square matrix, the rather complex generalised SVD analysis [129] need not be used. Instead, it is possible to rewrite the Gauss-Newton step in terms of the SVD of $\boldsymbol{J}\boldsymbol{L}^{-1}$ (which will be referred to as the modified SVD),

$$\delta\boldsymbol{m}_k = \sum_{j=1}^{j=m} \frac{f_j}{\sigma_j} \boldsymbol{L}^{-1}\boldsymbol{v_j}\boldsymbol{u}_j^T(\boldsymbol{f}(\boldsymbol{m}_k) - \boldsymbol{b}), \tag{3.25}$$

and develop a simpler analysis. First, notice that the solution is built of contributions parallel to vectors $\boldsymbol{L}^{-1}\boldsymbol{v_j}$ which are not of unit magnitude. Therefore, rather than examining the singular values σ_j, the modified singular values $\sigma_j/|\boldsymbol{L}^{-1}\boldsymbol{v_j}|$ are important. Likewise, a revised Discrete Picard Condition must be considered, where the factors

$$c_j = \frac{1}{\sigma_j} |\boldsymbol{L}^{-1}\boldsymbol{v_j}| |\boldsymbol{u}_j^T(\boldsymbol{f}(\boldsymbol{m}_k) - \boldsymbol{b_0})| \tag{3.26}$$

must decay with j for the regularized solution to be close to the 'true' solution.

The definition of $\boldsymbol{L}$ given in (3.23) is not suitable if $\boldsymbol{m}$ is augmented with additional parameters (such as the depth of the liquid crystal layer). In this case, standard and non-standard Tikhonov regularization can be mixed. Let the augmented vector be

$$\boldsymbol{m}' = (p_1, p_2, ..., \boldsymbol{m}) \tag{3.27}$$

Assume also that, prior to the experiment, Gaussian probability distributions for the parameters p_1 are known, with variance $1/a\lambda$. Then the matrix

$$\boldsymbol{L}' = \left[\begin{array}{cccc|c} a & 0 & \dots & 0 & \\ 0 & a & \dots & 0 & \\ \vdots & \vdots & & \vdots & 0 \\ 0 & 0 & \dots & a & \\ \hline \multicolumn{4}{c|}{0} & \boldsymbol{L} \end{array}\right]. \tag{3.28}$$

will be used in place of $\boldsymbol{L}$.

3.3 Results and Discussion

3.3.1 SVD analysis of the fully-leaky guided mode experiment for the determination of the tilt profile in a HAN cell

In this first SVD analysis, a numerical Jacobian matrix was calculated for a model HAN cell. Its 3 μm thick layer of liquid crystal, with dielectric constants $\epsilon_\perp = 2.2 + 0.001i$, and $\epsilon_\parallel = 2.7 + 0.001i$ is subdivided into 48 uniform layers. Both cell walls are glass (with refractive index $n_G = 1.52$) coated with 25nm of ITO (with $\epsilon = 3.8 + 0.08i$ [130]). The azimuthal angle ψ is set to $\pi/4$ - that is, the cell is mounted so that the rubbing direction is inclined at $\pi/4$ to the laboratory $x-$axis.

Simulated transmission and reflection intensity coefficients, computed as a function of internal angle α are shown in figure 3.2. and figure 3.3. The chosen angle range of $\alpha \in [60°, 72°]$ is typical of fully leaky guided mode experiments [89, 30, 54]. Broad modulations, a few degrees wide, due to thin film interference are visible in both the transmission and reflection data. In addition, polarization conserving transmission (T_{pp} and T_{ss}) decays slowly with α, while the converting signals (T_{ps} and T_{sp}) grow.

In agreement with Lionheart [120], the singular values of $\boldsymbol{J}$ (figure 3.4) decay exponentially, suggesting a severely ill-posed problem. Certainly the condition number is large ($\sim 10^8$), but finite, so while it is in principle possible to recover the whole tilt profile,

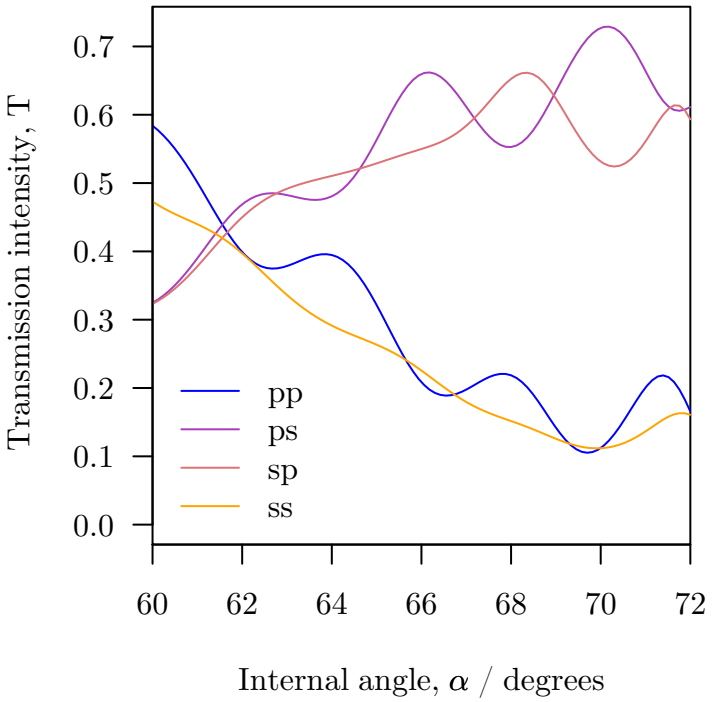

Figure 3.2: Simulated full-leaky guided mode experiment transmission intensity data. The slow trends in each curve are associated with polarization conversion, while the faster modulations are caused by thin film interference.

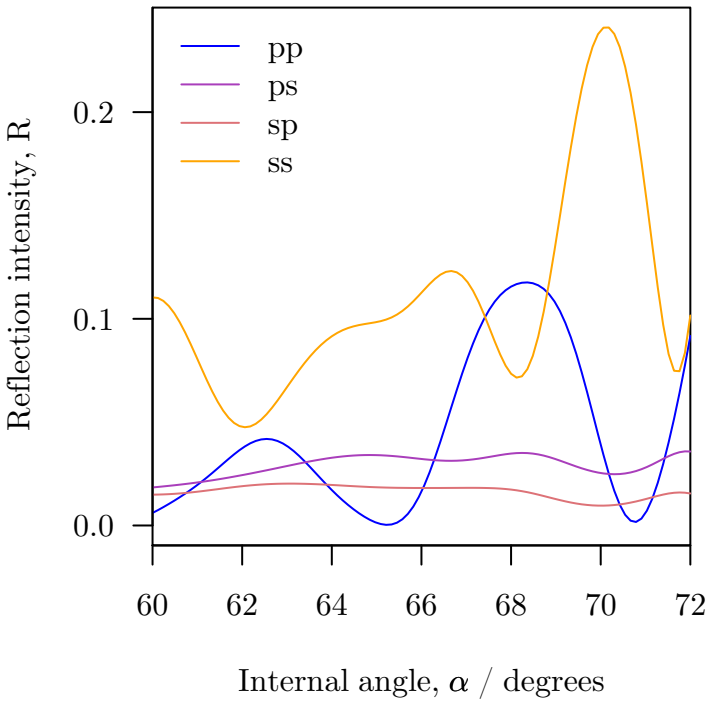

Figure 3.3: Simulated full-leaky guided mode experiment reflection intensity data.

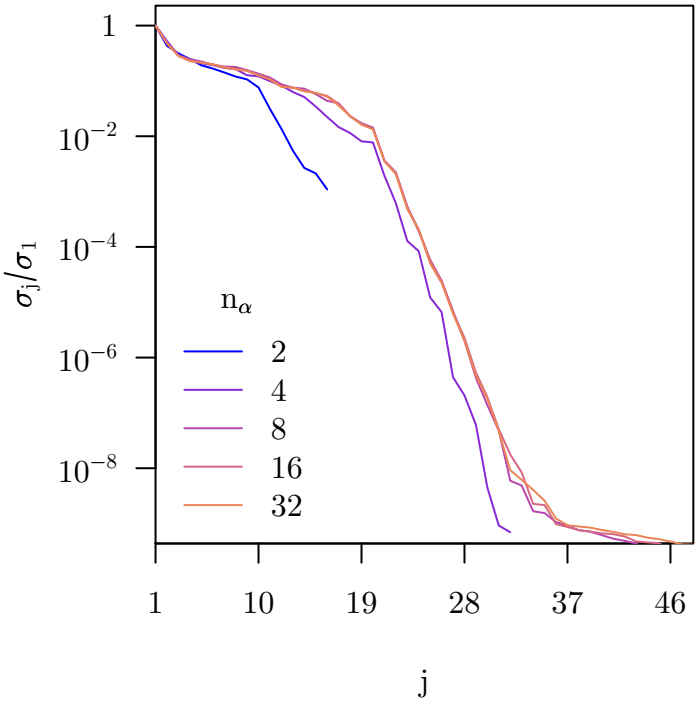

Figure 3.4: Relative size of the singular values σ_j of $\boldsymbol{J}$ Several curves are plotted, one each for several values of n_α, the number of sample angles. Once the number of measurements $n = 8n_\alpha$ is greater than the number of layers (48), the curves barely change. Three regions are visible: initial slow decay followed by rapid decay over six orders of magnitude around $j = 20$, then weak decay beyond $j = 35$.

in practice experimental error will dominate the solution. However, the singular values cannot be said to decay at a uniform rate. Rather, there are three regions in the curve: the singular values decay weakly from $j = 1$ to $j \approx 20$, then very rapidly drop six orders of magnitude, then decay weakly once more.

The singular values drop so steeply after $j = 20$ that a reasonable approach might simply be to truncate (3.13) at that point. Unfortunately, the slow decay in the first part of the curve is sufficiently quick to prevent a simple truncation technique from working. Imagine that random experimental noise with $\sigma \sim 0.01$ is included in the data, and that the real tilt profile can be built from just the first one or two singular vectors. Since the smallest singular value in this weakly decaying region is about 0.01, a spurious contribution with a magnitude of one radian is to be expected.

It is not necessary to use a large sample size when solving this inverse problem. Figure 3.4 also shows how the decay of singular values changes as the number of sample angles n_α is varied. Only when n_α is so small that $\boldsymbol{J}$ is singular can much variation in the curves be seen. Provided the number of measurements $n = 8n_\alpha$ is greater than the number of layers, the decay of singular values barely changes by increasing n_α. Setting $n_\alpha \approx 8$ would

appear to be sufficient. Using a small sample size is desirable in that larger sample sizes lead to longer calculation times.

When the right singular vectors are examined, the chances of extracting a reasonable tilt profile seem even more remote. Recall that when a regularized solution is obtained, it is dominated by contributions from the first few right singular vectors. This idea presupposes that a useful solution *can* be built from just the first $\boldsymbol{v}_j$. Here it cannot: all the right singular vectors contain high frequency components, as illustrated in figure 3.5. Beyond $j = 3$, each $\boldsymbol{v}_j$ is made largely of sub-wavelength oscillations in $\theta(z)$. So, to build a smooth solution, many singular vectors will be required. One expects that the various high-frequency contributions will come close to cancelling each other out in the real tilt profile. But, because the amplitude of the later contributions will be amplified most, experimental error will tend to cause a spurious, oscillatory solution to be calculated.

An examination of the left singular vectors offers no relief. Recall that each $\boldsymbol{u}_j$ represents the direction of change to the calculated reflection and transmission coefficients when the tilt profile is altered in the direction of $\boldsymbol{v}_j$. While later $\boldsymbol{u}_j$ resemble noise, and so might be neglected, the first eight, shown in figure 3.6, represent smooth (and therefore credible) perturbations to the data. An error in, say, $\boldsymbol{u}_8^T\boldsymbol{b}$ will lead to the rather noisy $\boldsymbol{v}_8$ being over-represented in the solution. Finally, calculations of the coefficients of $\boldsymbol{v}_j$,

$$c_j = \boldsymbol{u}_j^T(\boldsymbol{f}(\boldsymbol{0}) - \boldsymbol{b})/\sigma_j \tag{3.29}$$

in (3.13) confirm that this problem violates the Discrete Picard Condition. Two synthetic data vectors, $\boldsymbol{b}_s$ and $\boldsymbol{b}_r$ were prepared. The first of these, $\boldsymbol{b}_s$ was computed by setting the tilt profile to

$$\theta(z) = \frac{\pi z}{2d} + \frac{1}{10}\sin(\frac{\pi z}{d}), \tag{3.30}$$

that is, a linear profile plus a small sinusoidal perturbation with period $2d$. The second was calculated from a linear tilt profile, and then pseudo-random, Gaussian noise with $\sigma = 0.004$ added (so that $\boldsymbol{f}(0) - \boldsymbol{b}_r$ is simply noise). As one would expect, the magnitude of c_j increases with j when $\boldsymbol{b} = \boldsymbol{b}_r$, but it also increases when $\boldsymbol{b} = \boldsymbol{b}_s$. The main difficulty is in the first part of the curve, where $|c_j|$ grows slowly for the synthetic data, and more quickly for the noise. For real data, the noise would cause $|c_j|$ to be increasingly in error, and with no obvious point to truncate (3.16) before $j \approx 20$, this would seriously affect the solution. Tikhonov regularization, at least in its standard form, cannot be expected to work.

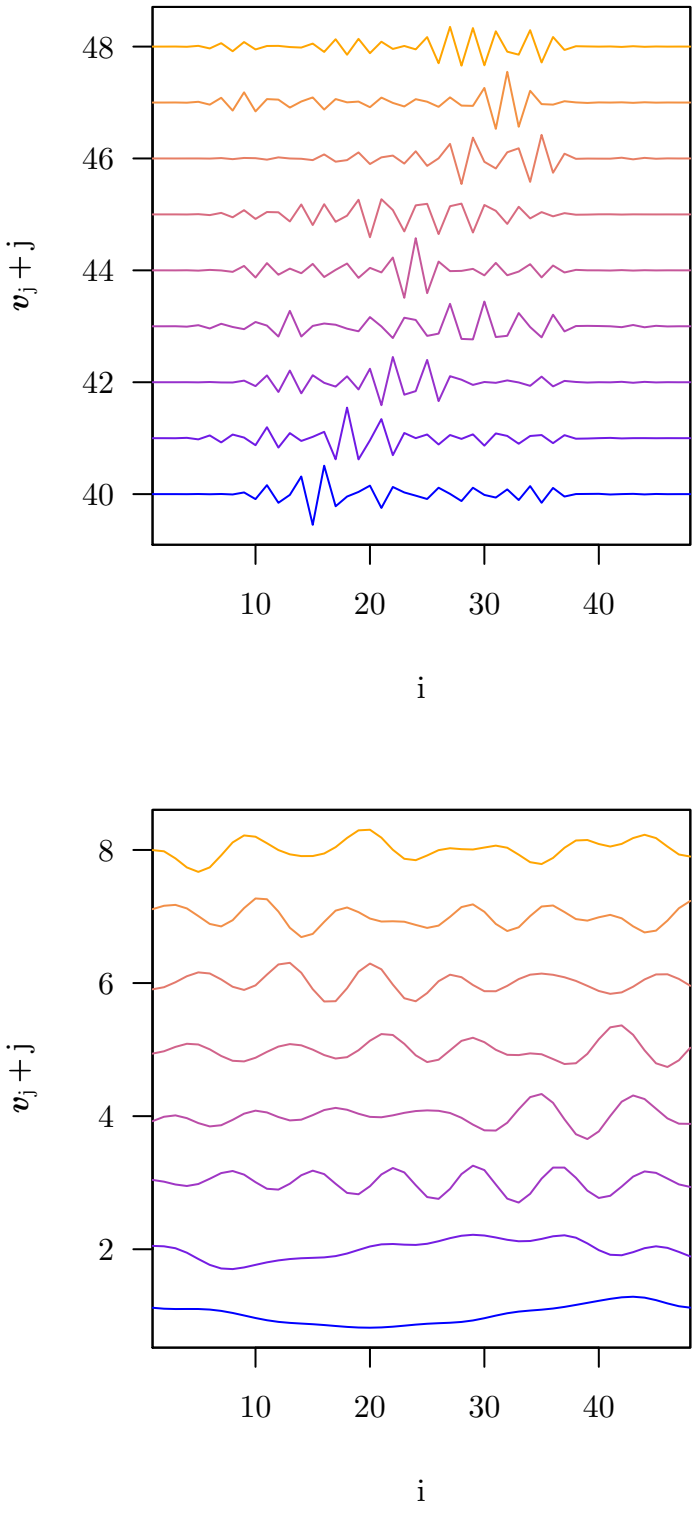

Figure 3.5: Elements v_{ji} of the right singular vectors of $\boldsymbol{J}$, plotted as a function of the sub-layer index i. When plotted this way, the right singular vectors look like the continuous functions of z that they represent. For clarity, every vector $\boldsymbol{v}_j$ is offset vertically by j. Even the first few $\boldsymbol{v}_j$ (bottom) contain high frequency contributions. The last eight vectors (top) change sign in every layer.

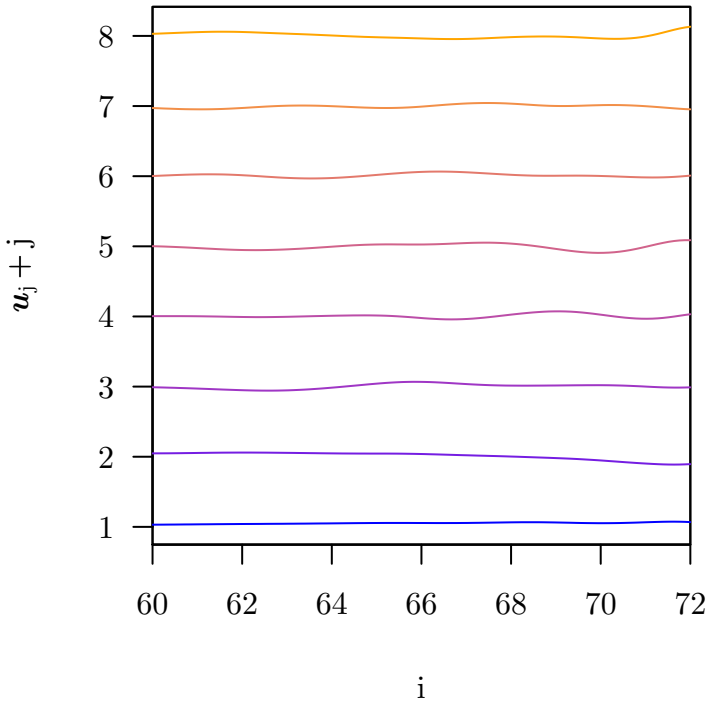

Figure 3.6: Segments of the left singular vectors of J corresponding to T_{pp}. The first few singular vectors represent smooth changes to the data

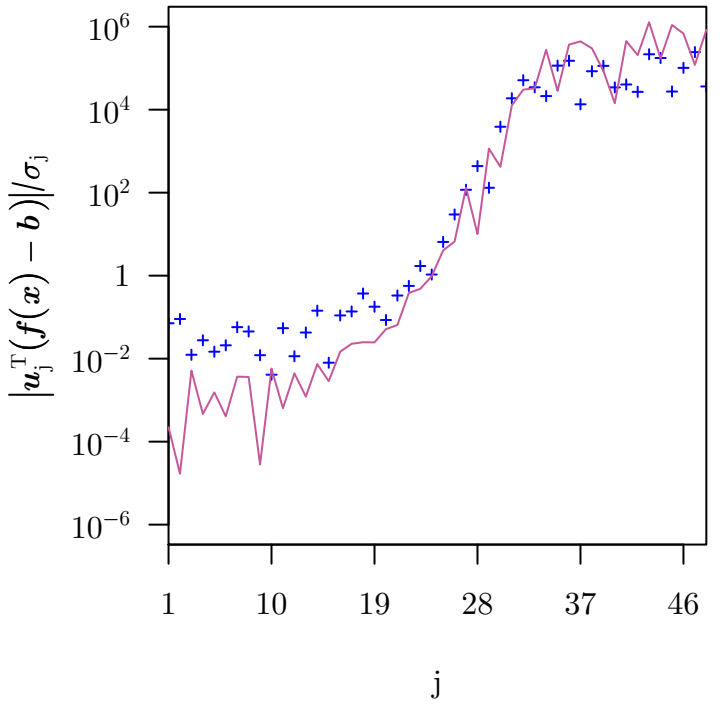

Figure 3.7: The coefficients $|c_j| = u_j^T(f(0) - b)/\sigma_j$ for two simulated data vectors b. For both noiseless synthetic data (crosses) and pseudo-random noise (solid curves), c_j increases with j, weakly at first, then strongly.

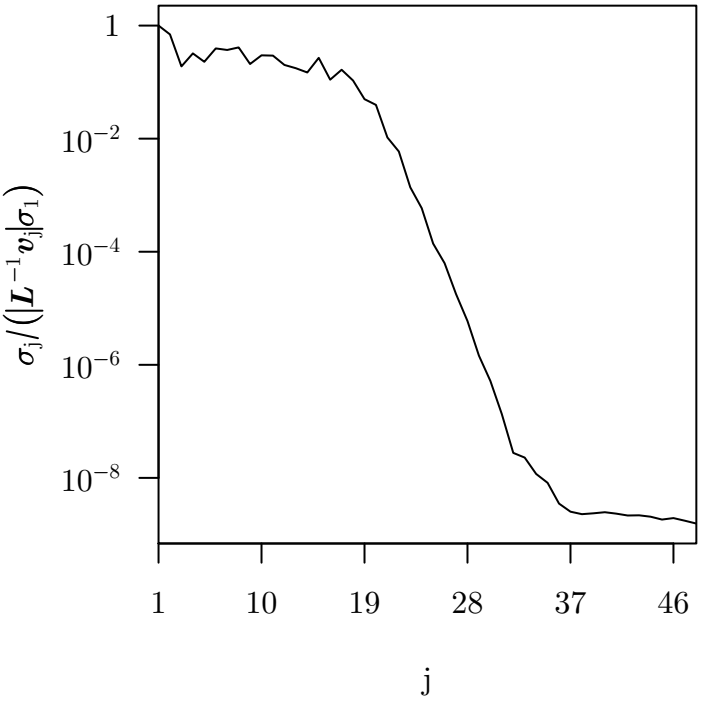

Figure 3.8: Relative size of the factors $\sigma'_j = \sigma_j / \left|\boldsymbol{L}^{-1}\boldsymbol{v}_j\right|$, where the σ_j are the singular values of $\boldsymbol{J}\boldsymbol{L}^{-1}$. These factors decay with j in a similar manner to the singular values of $\boldsymbol{J}$.

3.3.2 Using the SVD to analyse the proposed regularization matrix

Using the numerical Jacobian from 3.3.1, together with the matrix $\boldsymbol{L}$ derived from continuum theory, the singular value decomposition of $\boldsymbol{J}\boldsymbol{L}^{-1}$ was computed in order to analyse the modified formula (3.25). The factors $\sigma_j / \left|\boldsymbol{L}^{-1}\boldsymbol{v}_j\right|$, which occupy the same role as the singular values in the unmodified formula, decay in much the same way as before (figure 3.8). Similarly, the left singular vectors become increasingly oscillatory as j increases.

The real difference between the original and modified problems is expressed through the right singular vectors. The last eight singular vectors, seen in figure 3.9 are oscillatory, as before, but the first few are now smooth. Sub-wavelength oscillations are now not apparent in the first three singular vectors. It is quite conceivable that a realistic director profile could be be constructed from only a few of these $\boldsymbol{v}_j$.

However, the tilt profile will not be built directly from $\boldsymbol{v}_j$ but from vectors parallel to $\boldsymbol{L}^{-1}\boldsymbol{v}_j$. These vectors are smoother still (figure 3.10) , with $\boldsymbol{L}^{-1}$ acting rather like a convolution operator. Furthermore, their amplitudes decay rapidly, so diminishing the usual behaviour where error is amplified as j increases.

The modified problem does not strictly satisfy the discrete Picard condition, but

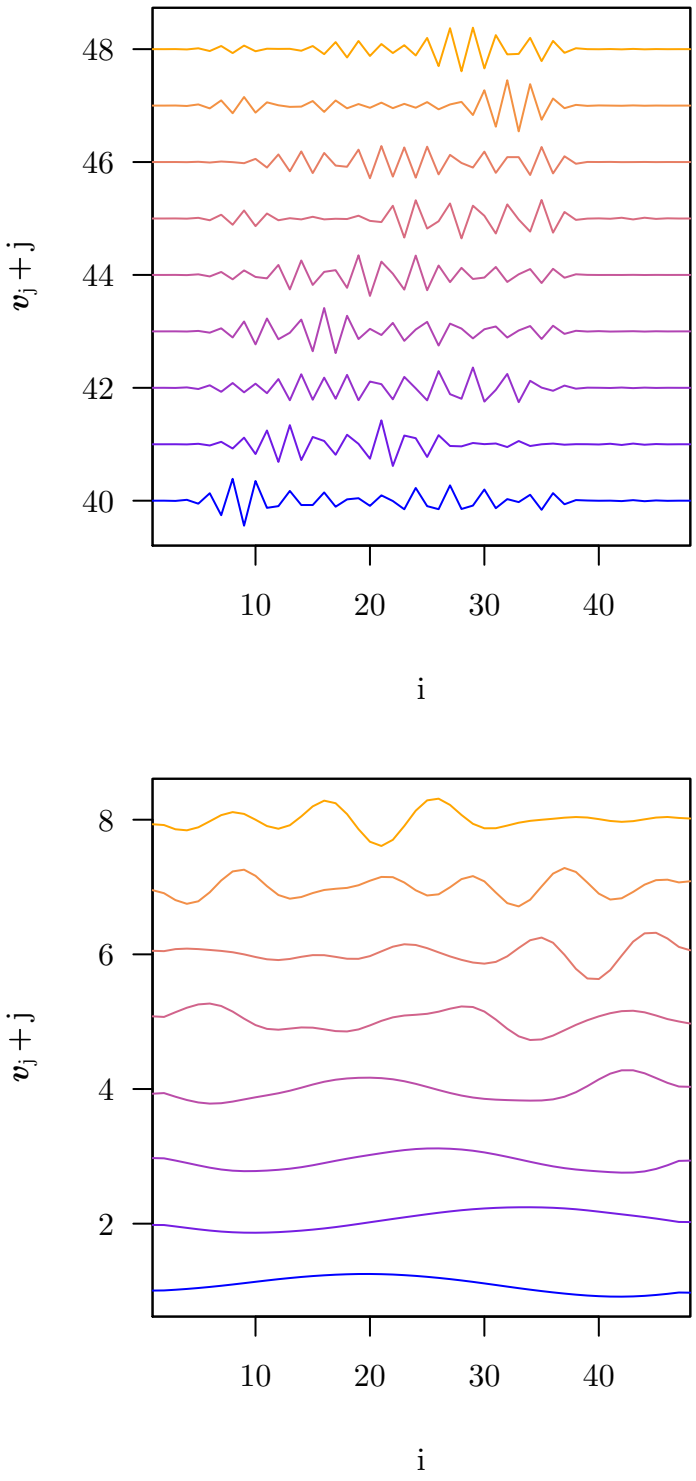

Figure 3.9: Right singular vectors of JL^{-1}, represented as continuous functions. The frequency of oscillations in v_j with respect to z increases slowly with j. As a result the first few singular vectors are smooth (bottom), while the last few are highly oscillatory (top).

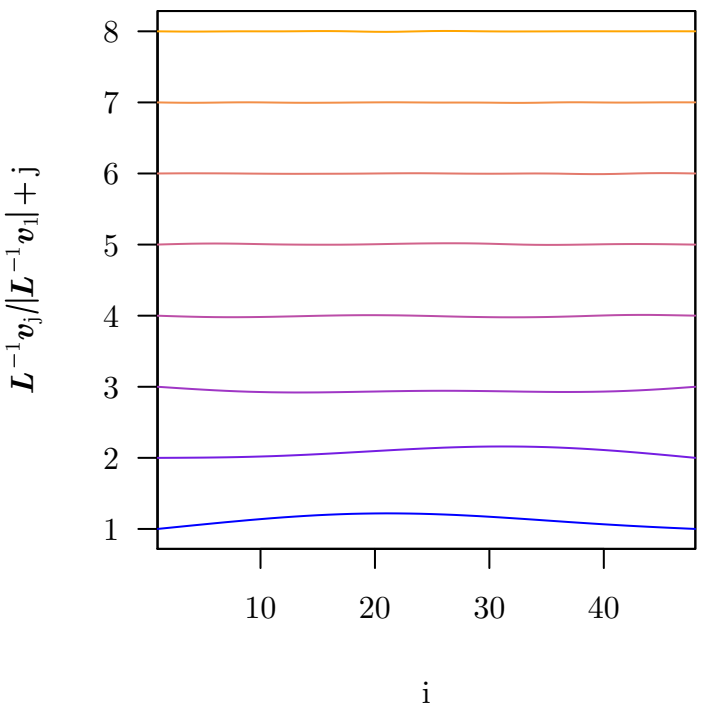

Figure 3.10: The first eight vectors $\boldsymbol{L}^{-1}\boldsymbol{v}_j$, normalised to $\boldsymbol{L}^{-1}\boldsymbol{v}_1$. These vectors are smoother still than the $\boldsymbol{v}_j$, and additionally decrease in amplitude as j grows.

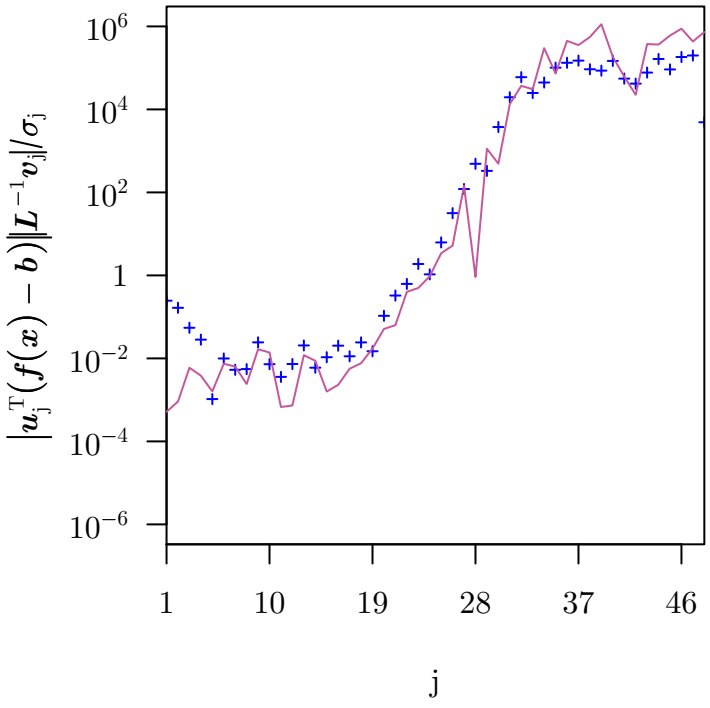

Figure 3.11: The coefficients $|c_j| = |\boldsymbol{u}_j^T(\boldsymbol{f}(\boldsymbol{0})-\boldsymbol{b})||\boldsymbol{L}^{-1}\boldsymbol{v}_j|/\sigma_j$ for two simulated data vectors $\boldsymbol{b}$. Now, in contrast to the unmodified problem, $|c_j|$ decays initially for the synthetic data (crosses). For pseudo-random noise (solid curves), $|c_j|$ grows as before.

nonetheless improves on the unmodified problem. The relevant amplitudes

$$|c_j| = |\boldsymbol{u}_j^T(\boldsymbol{f}(\boldsymbol{0}) - \boldsymbol{b})||\boldsymbol{L}^{-1}\boldsymbol{v}_j|/\sigma_j \tag{3.31}$$

still grow over the whole range of j for both noiseless and noisy data ($\boldsymbol{b}_s$ and $\boldsymbol{b}_r$ respectively). However, in this modified problem, the amplitudes computed when $\boldsymbol{b} = \boldsymbol{b}_s$ do decay initially. Over a region corresponding to the slow decay of singular values, $|c_j|$ decays on average, only starting to grow when the singular values start to decay rapidly. Assuming that these later, highly oscillatory singular vectors should roughly cancel each other out in the real solution, Tikhonov regularization with the matrix $\boldsymbol{L}$ derived from continuum theory should allow useful solutions to be found.

3.3.3 Inclusion of layer depths and permittivities in the model

The previous analyses have assumed that the depth of the liquid crystal layer, its permittivities, and the corresponding quantities for the ITO layers, are known exactly. This is not really the case: there will certainly be some uncertainty in each of these parameters. It will usually be necessary to include them in the inverse problem in addition to the director profile. Furthermore, there will be some aligning treatment, which may well affect the optics of the cell, and would also be included in a real problem.

To examine the effect of these extra variables on the SVD, an augmented model vector

$$\boldsymbol{m} = \begin{bmatrix} \ln d_{\mathrm{ITO}}/d_{\mathrm{ITO}0} \\ \ln \Re\epsilon_{\mathrm{ITO}}/\Re\epsilon_{\mathrm{ITO}0} \\ \ln \Im\epsilon_{\mathrm{ITO}}/\Im\epsilon_{\mathrm{ITO}0} \\ \ln d/d_0 \\ \ln \Re\epsilon_{\perp}/\Re\epsilon_{\perp 0} \\ \ln \Im\epsilon_{\perp}/\Im\epsilon_{\perp 0} \\ \ln \Re\epsilon_{\parallel}/\Re\epsilon_{\parallel 0} \\ \ln \Im\epsilon_{\parallel}/\Im\epsilon_{\parallel 0} \\ \boldsymbol{m}_\theta \end{bmatrix} \tag{3.32}$$

was defined, and the corresponding Jacobian computed. In the above expression, d_{ITO}, for example, refers to the thickness of each ITO layer, and $d_{\mathrm{ITO}0}$ to its expected value. With regard to permittivities, $\Re\epsilon_{\mathrm{ITO}}$ is the real part of the permittivity of ITO, and $\Im\epsilon_{\mathrm{ITO}}$ its imaginary part. Two modified SVDs were then calculated, the first with $L_{11}, L_{22}, \ldots, L_{88} = 1$ and the second with $L_{11}, L_{22}, \ldots, L_{88} = 10$

In the first case, the significant variability of the liquid crystal layer's depth and real

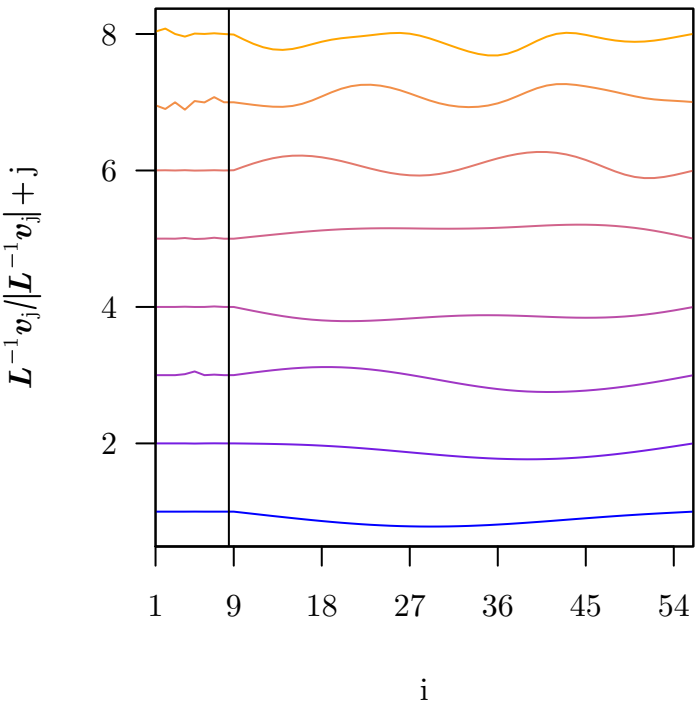

Figure 3.12: The first eight normalised vectors parallel to $\boldsymbol{L}^{-1}\boldsymbol{v}_j$ when there is significant uncertainty in the permittivities and depths of the liquid crystal and ITO layers. The vertical line separates the extra parameters from the contributions to the tilt profile.

parts of its permittivities leads to a serious difficulty. The vector $\boldsymbol{L}^{-1}\boldsymbol{v}_3$ shown in figure 3.12 is not simply a combination of the extra parameters, but includes a sinusoidal contribution to $\theta(z)$. Because it has a low j, it will feature prominently in the regularized solution. It will be impossible to decide whether features in the resulting tilt profile of this sort are genuine, or artifacts caused by variation in the depth of the liquid crystal layer. Variability in the ITO layers has a milder impact, manifesting itself only in the seventh and eighth vectors. The corresponding factors $\sigma_7/|\boldsymbol{L}^{-1}\boldsymbol{v}_7|$ and $\sigma_8/|\boldsymbol{L}^{-1}\boldsymbol{v}_8|$ are not larger than $\sigma_1/|\boldsymbol{L}^{-1}\boldsymbol{v}_1|$ and $\sigma_2/|\boldsymbol{L}^{-1}\boldsymbol{v}_2|$, so these vectors will not be so strongly represented in the solution.

Better knowledge of the additional parameters appears to resolve the difficulties described above. When $L_{11}, L_{22}, \ldots, L_{88} = 10$, the first few vectors $\boldsymbol{L}^{-1}\boldsymbol{v}_j$ no longer include contributions to $m_1, m_2, \ldots, m_8$ (figure 3.13). So, it seems that the real parts of the liquid crystal's real permittivities and the depth of the liquid crystal layer must be known to at worst 10% accuracy if the technique under consideration is to work.

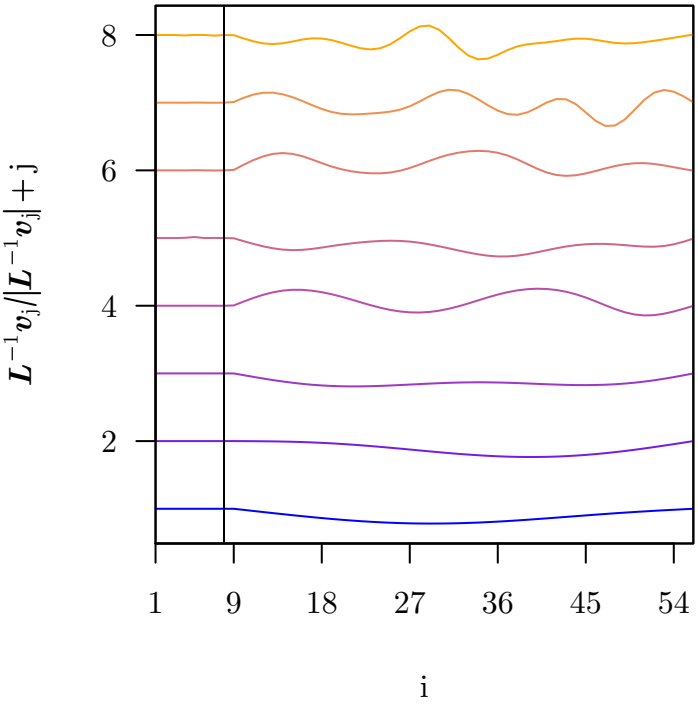

Figure 3.13: The first eight normalised vectors parallel to $\boldsymbol{L}^{-1}\boldsymbol{v}_j$ when there is mild uncertainty in the permittivities and depths of the liquid crystal and ITO layers. The vertical line separates the extra parameters from the contributions to the tilt profile.

3.3.4 The effect of polar and azimuthal angle ranges upon the SVD

SVD analysis has previously been used to show that increasing the range of incident angles would lead to improved sensitivity [120] to depth dependent information. This can be difficult to achieve, however. If the sample is rotated, as in the fully leaky guided mode experiment, the beam spot moves across the sample surface. Since cells are never entirely flat this motion introduces unquantified systematic error into the experiment [54]. To reduce this error, the angle range is usually limited such that motion of the beam is imperceptible.

The experimentalist does, in contrast, have control over the initial internal angle α_0. Choosing a higher value for α_0 improves sensitivity, according to SVD analysis. Jacobian matrices were computed as in section 3.3.1 for five angle ranges $\alpha_0 \leq \alpha \leq \alpha_0 + 12\,^\circ$, with α_0 varying from 12° to 60°. At low angles, the singular values plotted in figure 3.14 decay rapidly from the outset. Only as α_0 is increased does the slow initial decay observed earlier start to appear. It is well known that the guided mode experiments are best performed at higher angles [62]: the SVD result gives quantitative confirmation. That said, the wider the range of angles that can be achieved the better. For the angle range $12^\circ \leq \alpha \leq 72^\circ$ the decay of σ_j is much delayed compared to any of the other curves.

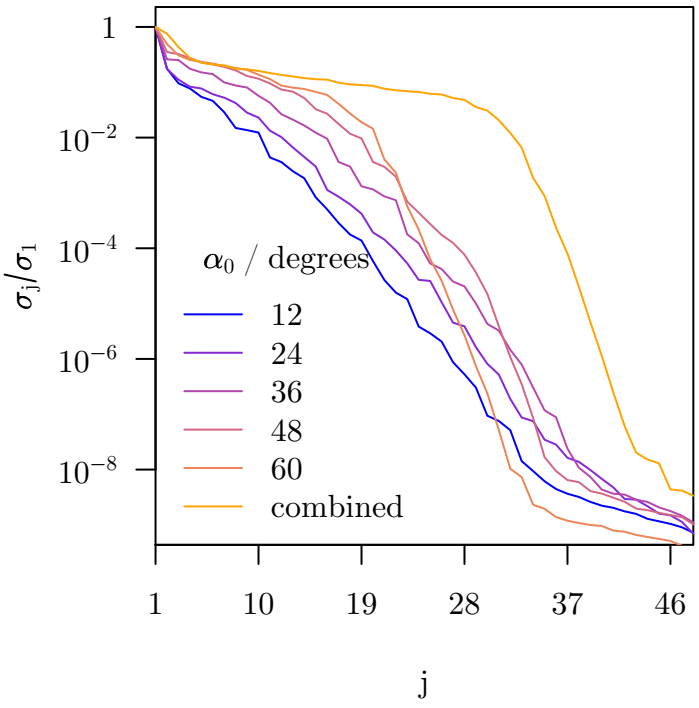

Figure 3.14: σ_j/σ_1 **plotted against** j **for five angle ranges** $\alpha_0 \leq \alpha \leq \alpha_0 + 12°$. As α_0 increases, the singular values' decay is delayed.

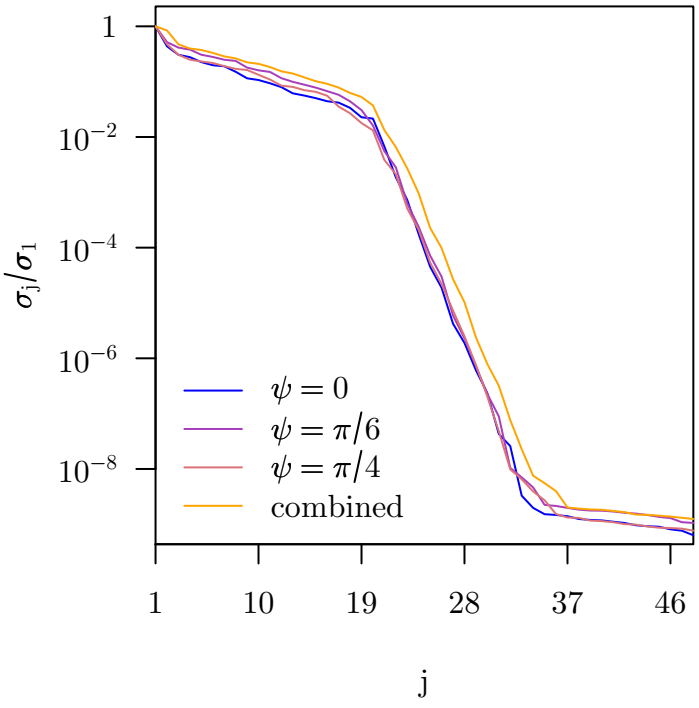

Figure 3.15: σ_j/σ_1 **plotted against** j **for three azimuthal angles** ψ individually and combined. The curves are essentially unchanged.

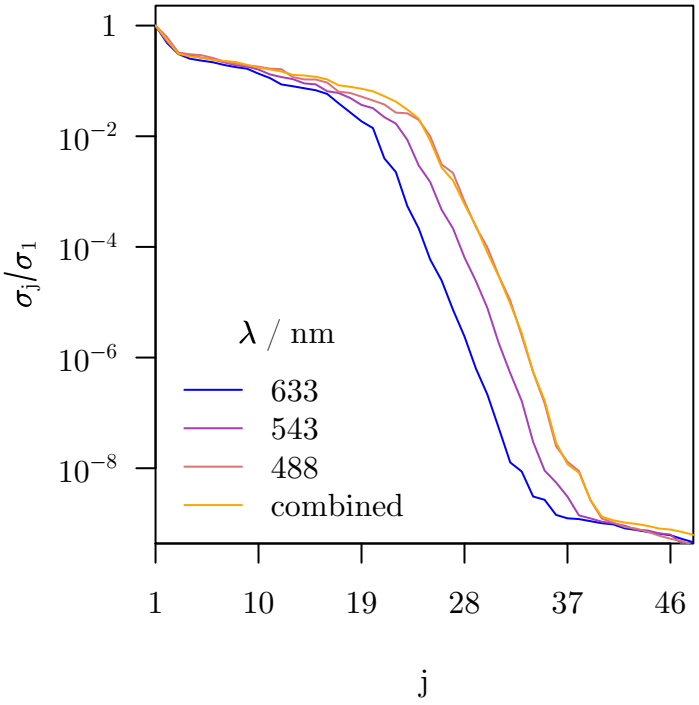

Figure 3.16: σ_j/σ_1 **plotted against** j **for three laser wavelengths** λ individually and combined, assuming the incident angle α varies from 60° to 72°. As λ decreases, the slowly decaying region is extended slightly. When all the data are combined, the singular vectors decay much as for the shortest wavelength alone.

A similar SVD analysis shows that the choice of azimuthal angle, ψ, is unimportant. In this analysis α ranges from 62° to 72°, as in the first simulation. For three different values of ψ, the decay of singular values, plotted in figure 3.15, is essentially identical. In addition, when the combined data from all three simulations is combined, there is barely any difference in the curves. Put another way, all the available information about the director profile is to found when ψ is set to any single value.

3.3.5 The effect of laser wavelength upon the SVD

Another straightforward design parameter for guided-mode experiments is the laser used to illuminate the sample. Obviously, it is easy enough to replace one laser with a different coloured model. It is also possible to probe the same region of the sample with several wavelengths through the use of a mirror arrangement. Such a multi-wavelength experiment would only be useful if the dispersion of the liquid crystal and other materials were well known, or if substantial extra information was retrieved by it.

Assuming the typical angle range for the fully-leaky guided mode experiment, there appears to be little to be gained by using several lasers. Figure 3.16 depicts the decay of singular values calculated for red, green, and blue lasers and also the singular values

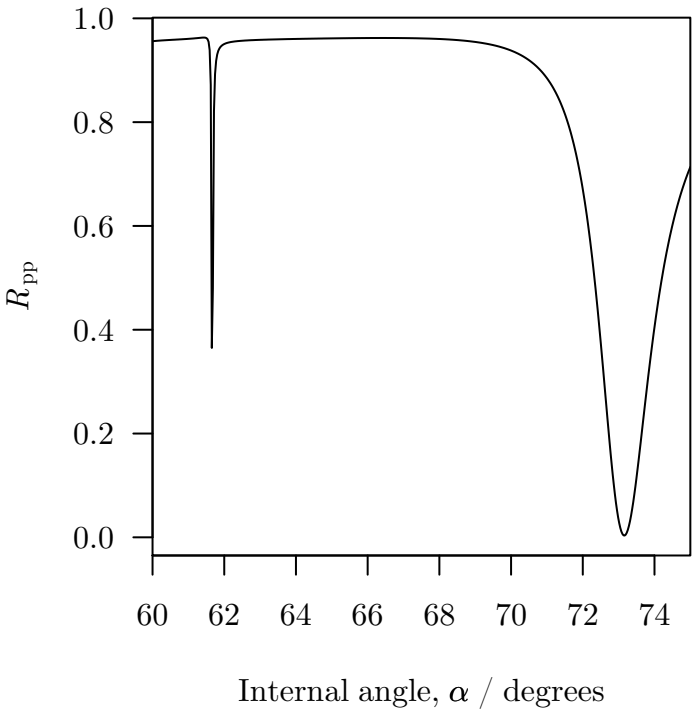

Figure 3.17: Simulated reflection coefficient R_{pp} against angle for the total attenuated reflection experiment. The sharp dip on the left is due to a Fabry-Perot resonance, while the dip on the right is caused by a surface plasmon.

computed assuming all three lasers are used together. As λ decreases, so does the initial rate of decay of σ_j - but only slightly, while the overall condition number does not change. Hence, there is no extra information to be found by choosing any particular laser, but mildly enhanced sensitivity at shorter wavelengths. When all the data are combined, the singular vectors decay much as for the shortest wavelength alone, so there is no benefit in attempting the more complicated experiment.

3.3.6 Comparison of the fully-leaky guide mode and total attenuated reflection experiments

Figure 3.17 shows simulated vales for R_{pp} against internal angle for a total attenuated reflection experiment [97, 97] over a spread of angles typically reported for the fully leaky guided mode experiment. To model this experiment, the ITO layers were replaced with silver layers 50 nm thick and with relative permittivity $-17.6 + 0.7i$. In addition, the permittivity of the semi-infinite layers was set to 3.24, consistent with the silica prisms used in the experiment. The reflectivity data is quite different from that in the full-leaky guided mode experiment, exhibiting one sharp minimum due to Fabry-Perot resonance, and a second due to a surface plasmon polariton. If a wider range of angles were considered,

as was usual in these experiments, several more Fabry-Perot resonances would be observed.

The sharp features in the angle-reflectivity curve suggest that the total attenuated reflection experiment will benefit from a superior signal-to-noise ratio. SVD analysis, however, indicates that this does not necessarily lead to greater sensitivity to depth dependent information. A considerably faster decay of singular values is calculated for the total attenuated reflection experiment (figure 3.18), which suggests that only the first one or two right singular vectors might be recovered. In contrast to the fully-leaky guided mode experiment however, these first few vectors appear to be quite smooth (figure 3.19). They also represent changes to the director profile close to the lower surface, because the surface plasmon's evanescent field is only sensitive to such localised changes.

3.3.7 Comparison of the fully- and half-leaky guided mode experiments

The half-leaky guided mode experiment [94] may be modelled simply by replacing the lower glass layer with a silica ($\epsilon = 3.24$) layer and including only reflected light in $\boldsymbol{f}$. To compare the half- and fully-leaky experiments, numerical Jacobians were computed with the angle range set to $48^\circ \leq \alpha \leq 60^\circ$. At higher angles, the reflection signal for the half-leaky experiment barely changes with angle (due to total internal reflection at the prism-liquid crystal interface), and the experiment is expected to be insensitive to changes in the director profile. Figure 3.20 shows the simulated reflection coefficient R_{pp} over the chosen angles. Since the signal varies from nearly 0 to nearly 1, the signal to noise ratio should be high. Furthermore, the Fabry-Perot modes are quite strong, so that the corresponding modulations in the reflection coefficients are quite sharp.

The resulting SVD and modified SVD are similar to those found for the full leaky experiment, if slightly more encouraging. While the factors $\sigma_j|\boldsymbol{L}^{-1}\boldsymbol{v}_1|/\sigma_j|\boldsymbol{L}^{-1}\boldsymbol{v}_j|$ ultimately decay slightly faster for the half-leaky experiment, they initially decay rather more slowly (and in fact rise slightly). The corresponding vectors $\boldsymbol{L}^{-1}\boldsymbol{v}_j$, shown in figure 3.22 are very much like those calculated for the full-leaky experiment: the first few are smooth, becoming more oscillatory as j increases. So it seems that the half-leaky experiment is sensitive to the same kind of depth dependent information, but slightly more so.

3.4 Summary

In this chapter singular value decomposition analysis was used to examine an inverse problem formulated to determine the tilt profile in a HAN cell from measurements of the reflection and transmission coefficients. An examination of the singular values showed that even though this problem is simpler than the problem originally considered by Lionheart,

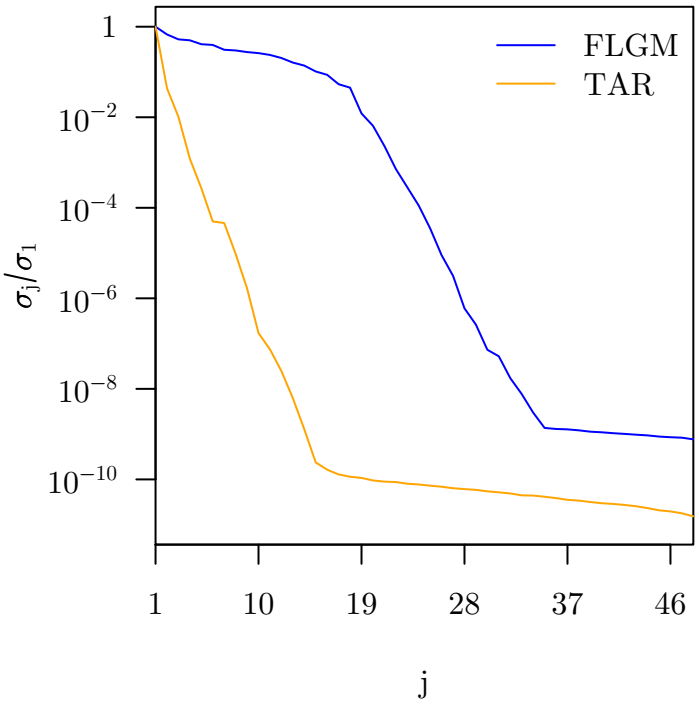

Figure 3.18: σ_j/σ_1 plotted against j for the total attenuated reflection (TAR) and full-leaky guided mode (FLGM) experiments. σ_j decays more rapidly for the TAR experiment.

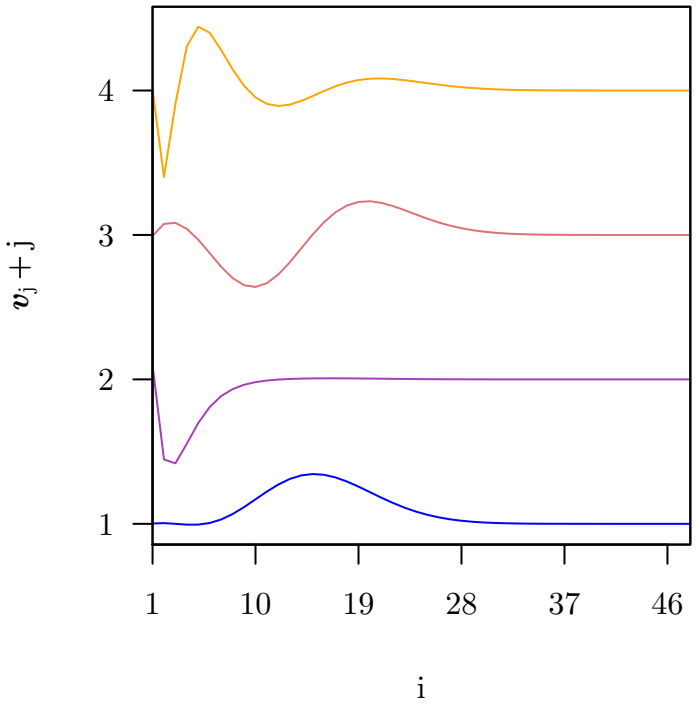

Figure 3.19: The first four right singular vectors computed for the total attenuated reflection (TAR) experiment. The shape of these vectors suggests that the experiment is far more sensitive to changes in the director close to the lower surface.

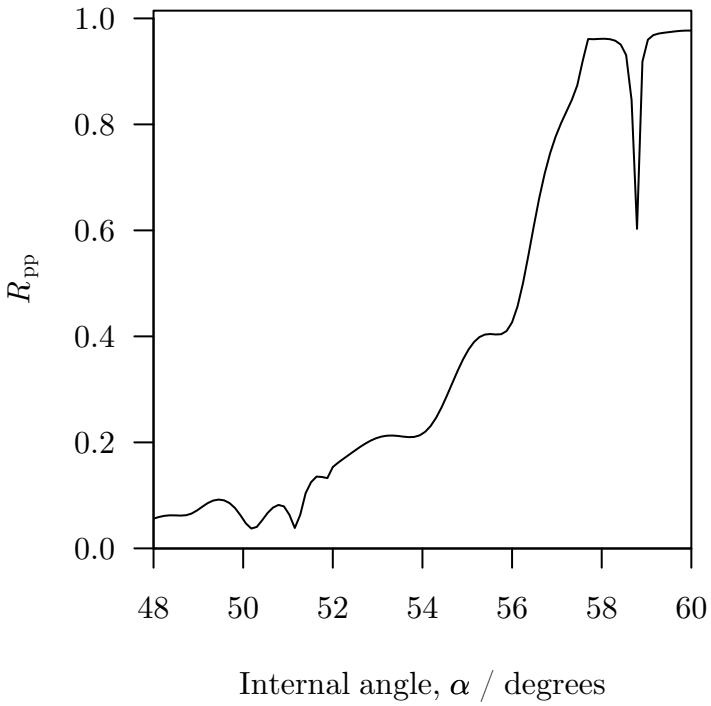

Figure 3.20: Simulated reflection coefficient R_{pp} against angle for the half-leaky guided mode experiment. Beyond the critical angle around 57°, a sharp Fabry-Perot resonance causes a dip in the reflectivity. At lower angles, R_{pp}varies rather more strongly than for the fully-leaky experiment, and features sharper modes.

it is nonetheless ill-posed. Furthermore, consideration of the right singular vectors and the Discrete Picard Condition showed that a standard Tikhonov regularized solution would not be useful. A non-standard Tikhonov regularized solution, based on continuum theory, was proposed, and a modified SVD analysis developed to study it. The right singular vectors computed in this case suggested a regularized solution might be useful, even though the Discrete Picard Condition was still not strictly satisfied.

Once these principal results were obtained, several additional analyses were performed. It was shown that, although the best way to improve the sensitivity of the fully leaky guided mode experiment is to widen the range of angles at which measurements are taken, the next best improvement is to take measurements starting at a high angle. Taking data at multiple azimuths, or multiple wavelengths, seemed to be of little value. SVD analysis was also used to compare the various waveguide experiments, and suggested that the half-leaky guided mode experiment is most sensitive of all to changes in the director profile, while the total attenuated reflection experiment is relatively insensitive, except to the tilt profile near the lower cell wall.

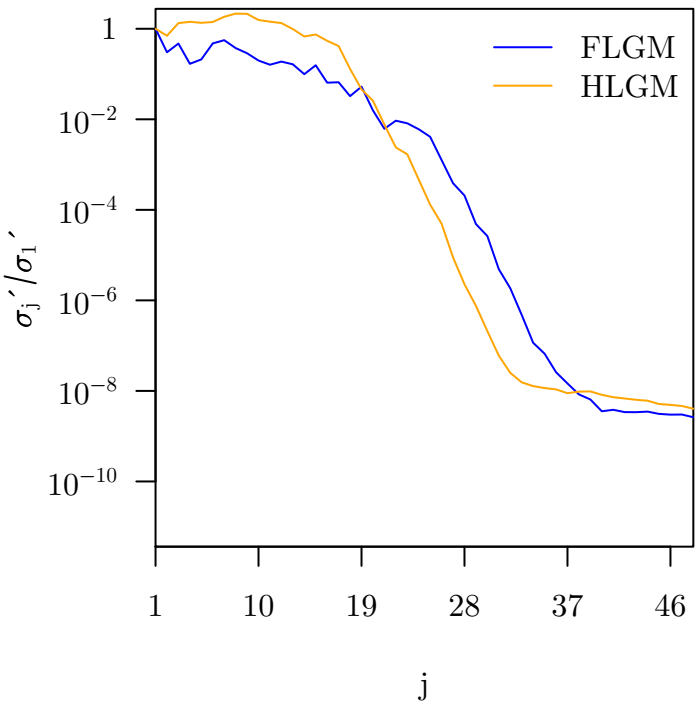

Figure 3.21: Relative values of $\sigma'_j = \sigma_j/|\boldsymbol{L}^{-1}\boldsymbol{v}_j|$ computed for half leaky guided mode (HLGM) and fully-leaky guided mode (FLGM) experiments. The picture is similar for both experiments, but the HLGM curve rises initially.

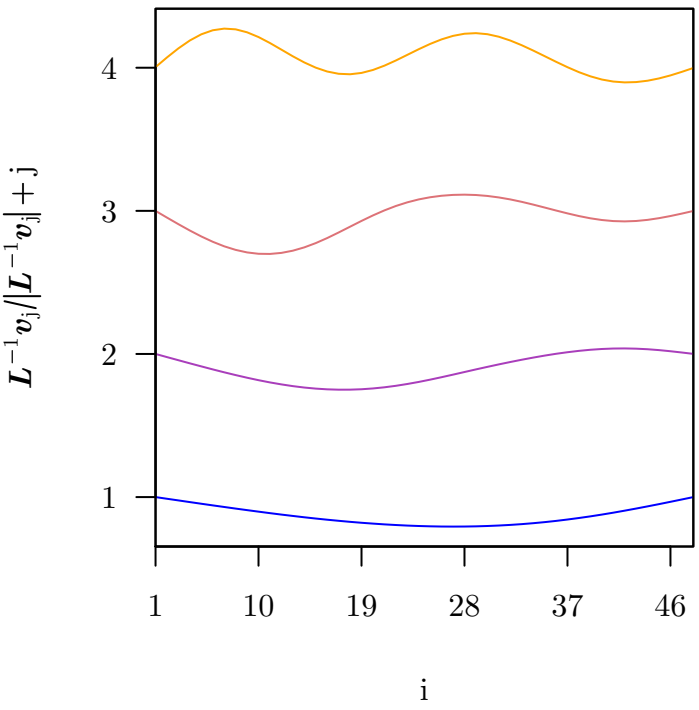

Figure 3.22: Unit vectors parallel to the first four $\boldsymbol{L}^{-1}\boldsymbol{v}_j$, calculated for the half leaky guided mode experiment . As in the fully-leaky results, these vectors represent smooth changes to the tilt profile.

Chapter 4

Development of a numerical model of liquid crystal dynamics.

4.1 Introduction

In this chapter a numerical model is derived from the continuum theory of nematics applicable to simple (one-dimensional) liquid crystal cells. A computer program, which implements the numerical model, is developed and tested, and performance and stability are considered in particular. Here, the dynamical behaviour of liquid crystal are governed by the Ericksen-Leslie equations. In other words, the liquid crystal is described by the director field, rather than the Q-tensor field. The liquid crystal may flow, driven either by director rotation, as in the backflow effect, or by a pressure gradient. Electric fields applied parallel to the $z-$axis will be considered, as will the flexoelectric effect.

The program to be developed in this chapter will find many uses in the remainder of the thesis. It will be used to provide initial tilt profiles for the methods described in the previous chapter. In the next chapter, a second type of inverse problem will be formulated, in which numerical solutions to the Ericksen-Leslie equations will form part of the forward model. The model, and code, will be extended to consider mobile ions in chapter six, and will be used to model pressure-driven flow in chapter seven.

Although computer programs which deal with simple cells have been described elsewhere [62, 131], few fulfil the rather stringent needs of the strongly-constrained inverse problem introduced in chapter five. Whatever means are chosen to attack that problem, the Ericksen-Leslie equations must be solved repeatedly, perhaps hundreds or thousands of times. It is therefore important that the program should execute quickly. For this reason, a number of existing implementations available at Exeter were rejected. The program must also be easily accessible to whatever program is used to solve the inverse problem.

This tends to rule out proprietary programs such as DIMOS. DIMOS is also unsuitable because it does not take account of the flexo-electric effect, ion motion or pressure-driven flow, and could not be extended.

A set of partial differential equations and boundary conditions which govern the director, electric field and flow profiles will be introduced in section 4.2. Then, in section 4.3, numerical solution of this kind of equation will be discussed. In section 4.4, these methods will be applied to the governing equations. To break that discussion down a little, a model of a HAN cell in steady-state is considered first (4.4.1), then supplemented with the flexoelectric effect (4.4.2), twist (4.4.3), and time-dependent behaviour (4.4.4).

4.2 The Governing equations

A nematic liquid crystal inside a simple cell is described by the director field, $\boldsymbol{n}(z,t)$ and a flow field $\boldsymbol{u}(z,t)$. Here, a Cartesian co-ordinate system is chosen such that the cell walls lie parallel to the $xy-$plane at $z = 0$ and $z = d$. The cell is assumed infinitely large in the x and y directions, so only variation parallel to the $z-$axis need be considered. As in the rest of this thesis, the Euler angles $\theta(z,t)$ and $\phi(z,t)$, defined in (1.1), will be used to specify $\boldsymbol{n}$.

4.2.1 Assumptions

Only two variables, u_x and u_y are needed to define $\boldsymbol{u}$. To see this, let

$$\boldsymbol{u} = (u_x, u_y, u_z) \tag{4.1}$$

Any flow which occurs is assumed to be incompressible, so the condition

$$\boldsymbol{\nabla}.\boldsymbol{u} = 0 \tag{4.2}$$

must hold. Since the flow field varies only with respect to z, this reduces to

$$\frac{\partial u_z}{\partial z} = 0. \tag{4.3}$$

There will be no flow through the cell walls, so $u_z(0) = u_z(d) = 0$, and hence $u_z(z) = 0$.

As well as the director and flow fields, the electric field $\boldsymbol{E}$ within the cell must be taken into account. These may be due to a potential applied between the ITO electrodes, the flexoelectric effect, or space charges. Now, the electric displacement vector, $\boldsymbol{D}$, must be constant in a one dimensional system. Provided that no in plane-field is applied, $\boldsymbol{D}$ is

parallel to the $z-$ axis at the cell's boundaries, and so it must be parallel to the $z-$ axis everywhere. Thus, only terms in the $z-$component of $\boldsymbol{E}$, E, enter the energy density (1.8) and hence the governing equations.

4.2.2 The Ericksen-Leslie equations

Provided that the electric field throughout the cell is known, the time- and space dependent behaviour of $\boldsymbol{n}$ and $\boldsymbol{u}$ can be found by solving the Ericksen-Leslie equations. Given the assumptions outlined above, these are four partial differential equations in the variables θ, ϕ, u_x and u_y. Before writing down these equations, some auxiliary functions of θ are defined for convenience:

$$a(\theta) = \left(\alpha_6 + \alpha_3 + 2\alpha_1 \cos^2\theta\right) \sin^2\theta; \tag{4.4}$$

$$b(\theta) = (\alpha_5 - \alpha_2)\cos^2\theta + \alpha_4; \tag{4.5}$$

$$c(\theta) = \alpha_3 \sin^2\theta - \alpha_2 \cos^2\theta; \tag{4.6}$$

$$g(\theta) = \sin^2\theta \left((k_{22} - k_{33})\sin^2\theta + k_{33}\right); \tag{4.7}$$

$$g'(\theta) = \frac{dg}{d\theta}. \tag{4.8}$$

The first equation is derived from (1.40),

$$\begin{aligned}\gamma_1 \frac{\partial\theta}{\partial t} = &\left(k_{11} + (k_{33} - k_{11})\cos^2\theta\right)\frac{\partial^2\theta}{\partial z^2} + \frac{1}{2}(k_{11} - k_{33})\sin 2\theta \left(\frac{\partial\theta}{\partial z}\right)^2 \\ &+ \frac{1}{2}g'(\theta)\left(\frac{\partial\phi}{\partial z}\right)^2 + c(\theta)\left(\cos\phi\frac{\partial u_x}{\partial z} + \sin\phi\frac{\partial u_y}{\partial z}\right) \\ &+ \frac{1}{2}\sin 2\theta\left((e_s - e_b)\frac{\partial E}{\partial z} - \epsilon_0\epsilon_a E^2\right).\end{aligned} \tag{4.9}$$

If both ϕ and $\boldsymbol{u}$ are constant (4.9) is the only equation which need be solved. Therefore, it can reasonably be considered the governing equation for θ. It is second order in z and first-order in t, so boundary conditions which determine $\theta(z=0,t)$, $\theta(z=d,t)$ and $\theta(z,t=0)$ must be provided. For most simulations, the cell evolves from some steady-state at $t=0$, so $\theta(z,t=0)$ can be found by setting $\frac{\partial\theta}{\partial t}$ to zero and solving the resulting equation together with the remaining two boundary conditions.

A governing equation for ϕ is derived, also from (1.40),

$$\gamma_1 \sin^2\theta \frac{d\phi}{dt} = g(\theta)\frac{\partial^2\phi}{\partial z^2} + g'(\theta)\frac{\partial\theta}{\partial z}\frac{\partial\phi}{\partial z} - \frac{1}{2}\alpha_2 \sin 2\theta\left(\cos\phi\frac{\partial u_y}{\partial z} - \sin\phi\frac{\partial u_x}{\partial z}\right). \tag{4.10}$$

Like (4.9), (4.10) is second order in z and first order in t, so similar boundary conditions are needed. Once more, the boundary condition at $t=0$ will usually be found by considering

a cell in steady-state. When $\theta = 0$, this equation becomes meaningless (all its terms vanish), a fact that will lead to some numerical difficulties later on.

The remaining two equations are derived from the linear momentum balance equations, (1.42). They govern the flow field and are rather similar:

$$\frac{\partial}{\partial z}(\tilde{t}_{xz}) = G_x \tag{4.11}$$

and

$$\frac{\partial}{\partial z}(\tilde{t}_{yz}) = G_y \tag{4.12}$$

where

$$\begin{aligned}\tilde{t}_{xz} = &\left[\frac{1}{2}a(\theta)\cos^2\phi + b(\theta)\right]\frac{\partial u_x}{\partial z} + \frac{1}{4}a(\theta)\sin 2\phi\frac{\partial u_y}{\partial z} \\ &- c(\theta)\cos\phi\frac{\partial\theta}{\partial t} - \frac{1}{2}\alpha_2\sin\phi\sin 2\theta\frac{\partial\phi}{\partial t}\end{aligned} \tag{4.13}$$

and

$$\begin{aligned}\tilde{t}_{yz} = &\left[\frac{1}{2}a(\theta)\sin^2\phi + b(\theta)\right]\frac{\partial u_y}{\partial z} + \frac{1}{4}a(\theta)\sin 2\phi\frac{\partial u_x}{\partial z} \\ &- c(\theta)\sin\phi\frac{\partial\theta}{\partial t} - \frac{1}{2}\alpha_2\cos\phi\sin 2\theta\frac{\partial\phi}{\partial t}.\end{aligned} \tag{4.14}$$

The terms on the right-hand sides of (4.11) and (4.12), G_x and G_y, are pressure gradients, directed along the $x-$ and $y-$axes respectivley.

Notice that the only time derivatives in these equations are those of θ and ϕ. As a result, unless the director is changing with time, the solutions to these equations are always time-independent. Furthermore, it is not necessary to know the flow field at $t = 0$. Boundary values of u_x and u_y must be known though, and in most circumstances the no-slip boundary condition [132], where both u_x and u_y are set to zero at the cell walls, is appropriate.

4.2.3 Boundary Conditions for θ and ϕ

Boundary conditions for θ and ϕ are determined by an assumption about the director at the cell walls. In many situations, it is reasonable to assume that the director is fixed at the surfaces: this is referred to as *strong anchoring*. In this case, the boundary condition is simple: values for θ and ϕ at the walls are known. Alternatively, some description of *weak anchoring*, which is not considered in this thesis, may be needed, in which case

relationships between θ and its $z-$derivative, and ϕ and its $z-$derivative would be given.

4.2.4 Gauss' law

In order to solve the Ericksen-Leslie equations, one must know the electric field throughout the cell. That can be calculating an electric potantial, v, which satisfies Gauss' law,

$$\frac{\partial}{\partial z}\left(-\epsilon\frac{\partial v}{\partial z}+(e_s-e_b)\sin 2\theta\frac{\partial\theta}{\partial z}\right)=0, \tag{4.15}$$

and then computing

$$E=-\frac{\partial v}{\partial z}. \tag{4.16}$$

Two contributions to (4.15) depend upon the director profile, the local permittivity

$$\epsilon=\epsilon_0\left(\epsilon_a\cos^2\theta+\epsilon_\perp\right). \tag{4.17}$$

and the flexo-electric term proportional to (e_s-e_b). This means that (4.15) must be solved simultaneously with the Ericksen-Leslie equations.

Only boundary conditions at the cell walls need be specified when solving (4.15). There are no time-dependent terms at all, so the electric field at each instant in time is unaffected by any previous states. A single value for v, say $v(z=0,t)=v_0(t)$, needs to be given, while $v(z=d,t)$ can always be set to zero, since only the electric field, the gradient of v, is meaningful. In other words, the electric potential is measured relative to an arbitrary ground, here chosen to be at $z=d$. $v_0(t)$ will normally be the potential measured across the cell, in volts, during an experiment.

4.3 Solving second order PDEs numerically

Two approaches to solving the governing equations are prevalent in the literature. Deuling [133] determines an integral equation for the maximum value of θ, which can be solved numerically. Once the integral is evaluated, the whole tilt profile can be computed. The approach of Deuling suffers from singularities in the integral, which can be dealt with at low voltages by a change of variable, and by an approximation at high voltages [134, 135].

An more widespread approach [29, 49, 50, 136] will be followed here: the governing equations will be *discretized*, that is, approximated by a set of algebraic equations. The solution to a differential equation is a function (of z and t in our case), but numerical methods deal only with simple values. However, a well-behaved function can be approximated by a set of discrete values, just as $\theta(z)$ was in the previous chapter. For example,

if $\theta(z)$ is defined between $z = 0$ and $z = d$ then it could be represented by n values $\theta_i = \theta(z = d(i-1)/(n-1))$ for $i = 1, 2, \ldots, n$ - in other words by the values $\theta(z)$ at n evenly spaced points. When the differential equations given above are formulated in terms of these discrete values, the result will be a set of algebraic equations, which can be solved to find θ_i and the other state variables.

4.3.1 The control volume method

Patankar [137] developed the *control volume* method to discretize equations much like those described above. That method is designed for use with equations of the form

$$\frac{\partial f}{\partial t} = \frac{\partial}{\partial z}\left(a(z)f - b(z)\frac{\partial f}{\partial z}\right) + s(z). \tag{4.18}$$

This is an example of a *convection-diffusion* equation, and often appears in physical systems where some quantity , such as momentum or energy is conserved. Gauss' law has precisely this form, as do the momentum balance equations (4.11) and (4.12). So will the equations which govern ion motion to be introduced in chapter 6. The equations for θ and ϕ don't, except in the trivial sense that $s(z)$ could represent anything, but they are similar - first order in t and second order in z.

The control volume method is developed by first dividing the liquid crystal layer into many thin sub-layers - the control volumes in question. Figure 4.1 shows such a division into layers, in which the centres of the first and last sub-layers lie upon the cell walls. A single, arbitrary sub-layer is illustrated: at its centre is the plane labelled 'P'. The centres of its neighbours are labelled 'U' and 'L', and the layer faces 'u' and 'l', for 'upper' and 'lower'. Quantities evaluated at these points are labelled with subscripts. For example, z_P is the distance of point P from the cell walls, while $f_P = f(z_P)$.

For simplicity, consider a much reduced version of (4.18), the linear, steady diffusion equation.

$$s(z) - \frac{\partial}{\partial z}\left(b\frac{\partial f}{\partial z}\right) = 0. \tag{4.19}$$

Integrating this equation over the sub-layer labelled P leads to an expression involving the values of $\partial f/\partial z$ at the sub-layer faces, and the mean value of $s(z)$, $\bar{s}$, within the sub-layer,

$$\bar{s} - \frac{b}{h}\left(\left.\frac{\partial f}{\partial z}\right|_u - \left.\frac{\partial f}{\partial z}\right|_l\right) = 0. \tag{4.20}$$

Next, the values of the derivatives are approximated by the central difference scheme,

$$\left.\frac{\partial f}{\partial z}\right|_u \approx \frac{1}{h}(f_U - f_P) \tag{4.21}$$

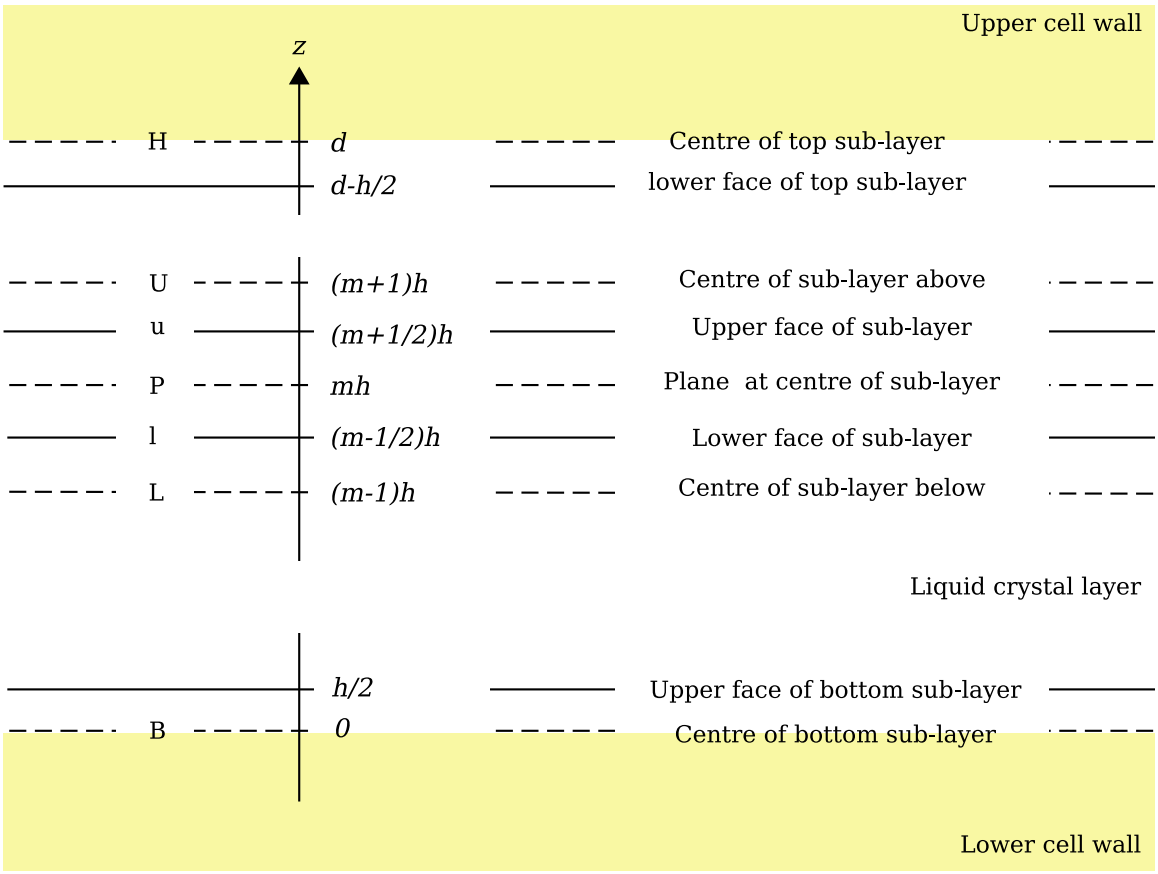

Figure 4.1: A sub-layer, or control volume, within the liquid crystal layer. The liquid crystal layer has been divided into n sub-layers, each of width h. At the centre of the $(m+1)$th sub-layer, counting from the bottom, is the plane labelled 'P'. This sub-layer is bounded by the planes drawn with a solid line and labelled 'u' and 'l', while the planes in the centre of its upper and lower neighbours are denoted 'U' and 'L'. Also shown are the bottom and top sub-layers, whose centres lie upon the boundaries of the liquid crystal layer.

and $\bar{s}$ is taken to be approximately equal to s_P. Substituting these into (4.20), one arrives at a set of n simultaneous linear, algebraic equations,

$$s_P - \frac{b}{h}(f_U - 2f_P + f_L) = 0. \tag{4.22}$$

In other words, the differential equation (4.19) has been discretized.

4.3.2 Boundary conditions

Just as the differential equation (4.19) must be supplemented with boundary conditions before a unique solution can be found, so must the algebraic equations (4.22). At the lower boundary, the quantity f_L is not defined, so (4.22) seems to make no sense. This is resolved by considering the boundary condition. For all the situations considered in this

chapter, all that is necessary is to replace (4.22) at the lower boundary with

$$f_P - f_B = 0 \tag{4.23}$$

where f_B is the known value of f at $z = 0$. Obviously, the upper boundary can be treated similarly.

In chapter six, another type of boundary condition will be considered, where the flux of ions across the cell walls is known. Beyond the scope of this thesis, weak anchoring would be treated as follows: first, approximate the relation between f and its derivative in terms of f_P, f_U, and f_L; second, use this equation to eliminate f_L from (4.22).

4.3.3 Solving the algebraic equations

Now a set of simultaneous equations has been found, the obvious next move is to solve them. Several authors [29, 62, 136] have, effectively, chosen to do this by an iterative procedure, the Gauss-Seidel method. First, each equation is rewritten in the form

$$f_p = F(f_L, f_U, ...). \tag{4.24}$$

An initial guess for all the f_P is made, such as a linear profile. Then, moving from bottom to top of the cell, f_P is updated. This last step is repeated for many iterations, and the values for f_P approach the solution asymptotically. This will be rather slow, requiring a number of operations proportional to n^2 to obtain a given accuracy.

Patankar recommends a different method. The simultaneous equations (4.22) have a rather simple form, which can be written in terms of a *tridiagonal* matrix, as

$$\begin{bmatrix} 2bp & -2b(p-q) & 0 & 0 & \dots & 0 \\ b & -2b & b & 0 & \dots & 0 \\ 0 & b & -2b & b & \dots & 0 \\ \vdots & \vdots & \vdots & \vdots & & \vdots \end{bmatrix} \begin{bmatrix} f_1 \\ f_2 \\ f_3 \\ \vdots \end{bmatrix} = \begin{bmatrix} -hs_1 \\ -hs_2 \\ -hs_3 \\ \vdots \end{bmatrix}, \tag{4.25}$$

or, compactly,

$$\boldsymbol{A}\boldsymbol{f} = h\boldsymbol{s} \tag{4.26}$$

Equations of this form can be solved directly using the Thomas algorithm - see page 52 of reference [137] - , which only requires a number of operations proportional to n. It reveals the solution immediately and without the need for an initial guess, rather than converging upon it.

4.3.4 Nonlinear equations and Newton's method

The scheme outlined above can be extended to nonlinear differential equations through Newton's Method. Now, b and s (and p, q and r) may depend upon f as well as on z. That means that the algebraic equations which result from discretisation will also be nonlinear, taking the form,

$$s(f_P, f_U, f_L) - \frac{1}{h}(b_u(f_U - f_P) + b_l(f_L - f_P)) = 0. \tag{4.27}$$

where $b_u = (b(f_U)+b(f_P))/2$. Starting from some initial guess for the vector $\boldsymbol{f}$, an update, $\Delta\boldsymbol{f}$, is given by solving

$$\boldsymbol{J}\Delta\boldsymbol{f} = -\boldsymbol{R}. \tag{4.28}$$

$\boldsymbol{R}$ is a vector built of elements R_P, the left-hand sides, or residuals, of (4.27), while the elements of the Jacobian matrix are

$$J_{ij} = \frac{\partial R_i}{\partial f_j}. \tag{4.29}$$

Since each R_P only depends upon f_P,f_U and f_L, $\boldsymbol{J}$ is tridiagonal. A sequence of updates are calculated, re-evaluating $\boldsymbol{R}$ and $\boldsymbol{J}$ at each iteration, which will converge upon the solution to (4.27) if the initial guess is good enough.

Newtons method, in principle, may approach the solution to (4.27) asymptotically. In practise, one only needs to know $\boldsymbol{f}$ to within some tolerance ϵ, and so the iterations are terminated when $||\Delta\boldsymbol{f}||$, the 2-norm of $\Delta\boldsymbol{f}$, is smaller than this value. Note that $||\boldsymbol{f}||$ should be defined so that its typical value is around unity, along the lines

$$||\boldsymbol{f}|| = \frac{1}{n\tilde{f}}\sqrt{\boldsymbol{f}^T\boldsymbol{f}} \tag{4.30}$$

where $\tilde{f}$ is a typical, non-zero value for f.

Given a value for ϵ, Newton's method may be written as a recursive function,

$$\text{newton}(\boldsymbol{f}) = \text{if}(||\Delta\boldsymbol{f}|| < \epsilon, \boldsymbol{f} + \Delta\boldsymbol{f}, \text{newton}(\boldsymbol{f} + \Delta\boldsymbol{f})). \tag{4.31}$$

Here, the function $\text{if}(a, x, y)$ maps the Boolean quantity $a \in \{\text{true}, \text{false}\}$ to x when $a =$ true and to y otherwise. This recursive notation, if it appears unnecessary here, will prove to be a useful way of writing down more complicated algorithms.

4.3.5 Time-dependent equations

The Ericksen-Leslie equations (and the ion motion equations to be introduced in chapter 7) include unsteady terms, that is terms proportional to $\partial f/\partial t$. The unsteady diffusion equation, which, once discretized as outlined above becomes

$$\frac{\partial f_P}{\partial t} = s(f_P, f_U, f_L) - \frac{1}{h}(b_u(f_U - f_P) + b_l(f_L - f_P)) \tag{4.32}$$

is the prototype when considering this kind of term. Just as discretisation with respect to space must be performed, so it must with respect to time. Bundling the right-hand side into a single term, σ, and integrating with respect to time, between two limits t and $t + \Delta t$, leads to

$$f_P(t + \Delta t) - f_P(t) = \int_t^{t+\Delta t} \sigma dt \tag{4.33}$$

Choosing an approximation for the right-hand side of (4.33) is the principal distinction between three different methods. In the *explicit* scheme, the approximation

$$\int_t^{t+\Delta t} \sigma dt \approx \Delta t \sigma(t) \tag{4.34}$$

leads to an expression, which, knowing $f_P(t)$, allows $f_P(t + \Delta)$ to be evaluated without further ado. It tends to be numerically unstable, and is not used here. In contrast, the *implicit* method uses the approximation

$$\int_t^{t+\Delta t} \sigma dt \approx \Delta t \sigma(t + \Delta t). \tag{4.35}$$

A system of algebraic equations result, which can be solved by Newton's method as before. Finally, the Crank-Nicholson scheme sets

$$\int_t^{t+\Delta t} \sigma dt \approx \frac{\Delta t}{2} \left(\sigma(t) + \sigma(t + \Delta t)\right). \tag{4.36}$$

and leads to a similar set of equations to the implicit scheme.

While the Crank-Nicholson scheme appears more accurate, the implicit scheme offers a significant advantage. If the time step Δt is very long, the right hand side of (4.33) dominates. When the implicit scheme is chosen, the resulting equations are close to the steady-state equations. In other words, the implicit scheme is consistent with a system which approaches some kind of equilibrium, given sufficient time.

How should the time step, Δt, be chosen? Commonly, the modeller might wish to know the state of the liquid crystal at time t_2, given its state at time t_1, but is setting $\Delta t = t_2 - t_1$ adequate or should several smaller time steps be used? The answer to these

questions can vary. Far from equilibrium, the liquid crystal changes quickly so small time steps are needed. Close to equilibrium, large time steps can be used, and so insisting upon small time steps is wasteful. An adaptive scheme, where the time step is chosen by refining it until some tolerance, ϵ_t, is reached, is employed to find an answer. Expressed as a recursive function, the algorithm is

$$\begin{aligned}\text{adaptive}(\boldsymbol{f}(t), \Delta t) = \text{if}(||\text{newton}(\boldsymbol{f}(t), \Delta t) - \text{newton}(\text{newton}(\boldsymbol{f}, 1/2\Delta t), 1/2\Delta t)|| < \epsilon_t, \\ \text{newton}(\boldsymbol{f}(t), \Delta t), \\ \text{adaptive}(\text{adaptive}(\boldsymbol{f}(t), 1/2\Delta t), 1/2\Delta t))\end{aligned} \tag{4.37}$$

Care is taken in the implementation of (4.37) to store and retrieve, rather than re-evaluate, values of newton$(\boldsymbol{f}, \Delta t)$. A minimum time step is also imposed to prevents infinite recursion when (4.37) fails for some reason.

4.3.6 Multiple equations

So far, the analysis has assumed that only one differential equation needs to be solved. That is not usually the case. Discretizing several equations is no different from discretizing one, but the solution of the resulting algebraic equations is more complicated. One approach would be to use Newton's method directly on the entire set of equations. However, in that case, the Jacobian matrix would no longer be tridiagonal, and some more general (and expensive) method would be needed to invert it.

Following Patankar, an alternative approach is chosen. Say, for example, the governing equation for the tilt profile and Gauss' law are to be solved in steady-state. Starting from an initial guess for $\boldsymbol{v}$ and $\boldsymbol{\theta}$, an update to $\boldsymbol{v}$ is calculated,

$$\Delta \boldsymbol{v} = -\boldsymbol{J}_v^{-1}(\boldsymbol{\theta}, \boldsymbol{v})\boldsymbol{R}_{\boldsymbol{v}}(\boldsymbol{\theta}, \boldsymbol{v}) \tag{4.38}$$

where $\boldsymbol{J}_v$ and $\boldsymbol{R}_v$ are calculated from the right hand side of the discretized Gauss' law. Second , an update to $\boldsymbol{\theta}$ is found,

$$\Delta \boldsymbol{\theta} = -\boldsymbol{J}_\theta^{-1}(\boldsymbol{\theta}, v + \Delta \boldsymbol{v})\boldsymbol{R}_{\boldsymbol{\theta}}(\boldsymbol{\theta}, \boldsymbol{v} + \Delta \boldsymbol{v}). \tag{4.39}$$

These steps are repeated until the updates are smaller than some ϵ. As a recursive function,

one has

$$\begin{aligned}\text{update}(\boldsymbol{\theta}, \boldsymbol{v}) = \text{if}((||\Delta\boldsymbol{\theta}||, ||\Delta\boldsymbol{v}||) < \epsilon,\\ (\boldsymbol{\theta} + \Delta\boldsymbol{\theta}, \boldsymbol{v} + \Delta\boldsymbol{v}),\\ \text{update}(\boldsymbol{\theta} + \Delta\boldsymbol{\theta}, \boldsymbol{v} + \Delta\boldsymbol{v}))\end{aligned} \tag{4.40}$$

4.4 Implementing and testing the model

Obviously, implementing the numerical methods of the previous section means writing some kind of computer program. For the best performance a compiled language, such as FORTRAN or C/C++, is normally chosen. With an eye to solving inverse problems though, a flexible mechanism for specifying various parameters will be needed. A compiled language can be problematic here, as minor changes lead to a potentially lengthy recompilation process. To obtain the best of both worlds, a C++ function was written, which takes the many parameters as arguments, together with arrays which will contain the solution after execution. This function was then invoked from GNU R [138], a free, vector-based, interpreted programming environment similar to MATLAB. GNU R has many features which make it useful in this context: data analysis tools, lexical scoping, high-performance matrix calculations (such as singular value decomposition), and plotting tools.

4.4.1 HAN cells in steady-state

Modelling the HAN cell in steady-state is an obvious place to start the implementation of the methods outlined before. The two equations which describe it in steady-state, (4.9) (with the unsteady term and the flow terms set to zero) and (4.15) also describe planar cells and homeotropic cells. When modelling the dynamics of HAN cells, one needs to find an initial state, which will usually be given by a solution to the steady-state equations. And it will often be necessary to model steady-state solutions in their own right - for example, when studying the equilibrium states that a cell occupies across a range of applied voltages.

First, Gauss law, (4.15), must be discretized. Since (4.15) takes the form

$$\frac{\partial}{\partial z}(F(v, \theta)) = 0 \tag{4.41}$$

it is simple to integrate it over a sub-layer. Its discrete form is

$$F_u(v_E, v_P) - F_l(v_W, v_P) = 0 \tag{4.42}$$

where

$$\begin{aligned} F_u =&(e_s - e_b)(\sin 2\theta_P + \sin 2\theta_U)(\theta_U - \theta_P) \\ &+ \left[\epsilon_a \left(\cos\theta_P + \cos\theta_U\right)^2 + \epsilon_\perp\right](v_P - v_U) \end{aligned} \tag{4.43}$$

and similarly for F_l. Given values for v in each sub-layer, the electric field is approximately

$$E_P = \frac{v_L - v_U}{2h} \tag{4.44}$$

at sub-layer centers and

$$E_u = \frac{v_P - v_U}{h} \tag{4.45}$$

at sub-layer faces. Boundary conditions are simple to implement: at the top of the cell, (4.42) is replaced with

$$v_P = 0 \tag{4.46}$$

and at the bottom with

$$v_P = v_0. \tag{4.47}$$

Equation (4.9) is a little more complicated: it does not have the form of (4.18) (unless $k_{33} = k_{11}$ and there is no electric field). Rather than integrating the equation over each layer, the derivatives are replaced, using the central difference approximation, and other quantities replaced with their values at the centre of the layer. In a HAN cell,

$$\begin{aligned} &\frac{1}{2h}\sin 2\theta_P \left[\epsilon_0\epsilon_a (E_P)^2 - (e_s - e_b)(E_u - E_l)\right] \\ &+ \frac{1}{h^2}\left[k_{11} + (k_{33} - k_{11})\cos^2\theta_P\right](\theta_U + \theta_L - 2\theta_P) \\ &+ \frac{1}{2h^2}(k_{33} - k_{11})\sin 2\theta_P(\theta_U - \theta_L)^2 = 0 \end{aligned} \tag{4.48}$$

Initially, strong anchoring will be assumed, so that at the top of the cell,

$$\theta_P = \frac{\pi}{2} \tag{4.49}$$

and at the bottom

$$\theta_P = 0. \tag{4.50}$$

At this point, the first numerical hurdle is encountered. The iterative scheme,(4.40), does not converge at even moderate voltages if the initial guesses for θ and v vary linearly with z. Now, equation (4.15) is linear in v, so the corrections to $\boldsymbol{v}$ for a given tilt profile will be computed exactly in a single iteration. Therefore, it is the initial estimate of θ that

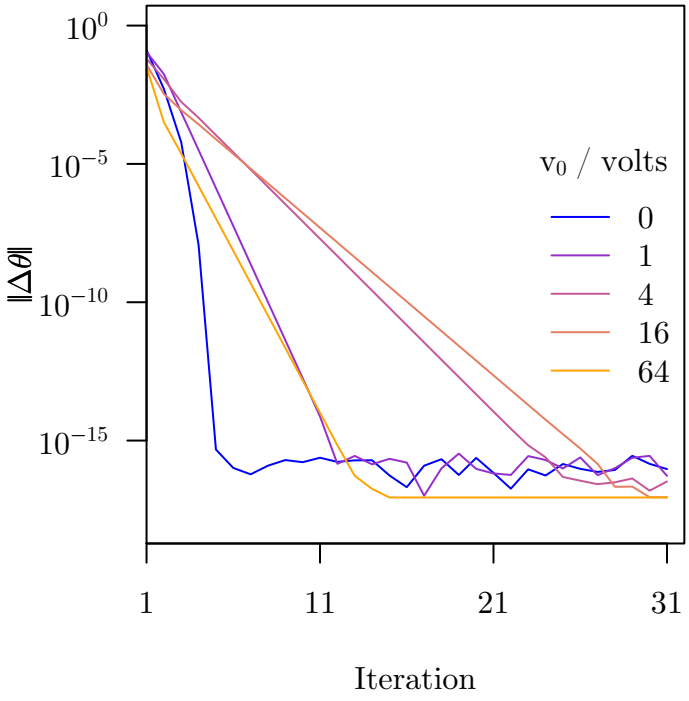

Figure 4.2: Convergence of the iterative scheme when the initial state is the solution for $|v_0| \to \infty$. Corrections to $\boldsymbol{\theta}$ decay exponentially in size with iteration at any voltage.

must be considered. One possibility is to use a solution computed for a lower voltage as the initial estimate, stepping up gradually to higher voltages. However, when v_0 is large this will require the calculation of many additional solutions: performance will be affected. Neither is it clear how to chose the best sequence of voltages.

A superior method is obtained by considering the solution as $|v_0| \to \infty$. At very high voltages, the dielectric contribution to the free energy dominates all others, so that $\theta(z) \to 0$ if $\epsilon_a > 0$, or $\theta(z) \to \pi/2$ if $\epsilon_a < 0$. Using this solution as the initial estimate leads to a scheme which converges at any applied field. As an example, tilt profiles were computed for a 3 μm thick layer of nematic material similar to Merck ZLI-4788-000, divided into 49 sub-layers, with $k_{11} = 13.7$ pN, $k_{33} = 2.06$ pN, $\epsilon_\perp = 10.2$, $\epsilon_\parallel = -4.7$ and $(e_s - e_b) = 0$. Figure 4.2 shows the magnitude of updates to $\boldsymbol{\theta}$ decaying rapidly as the iterations progress, even when $v_0 = 64$ V.

Figure 4.3 shows the computed tilt profiles, ranging from a near-linear profile when $v_0 = 0$ to a strongly distorted profile when $v_0 = 64$ V. These are compared with results from the DIMOS program. Apart from the profile computed for $v_0 = 64$ V, the two calculations of θ differ by no more than 0.0025 radians. When $v_0 = 64$ V, DIMOS calculates a profile which rises more rapidly in the two sub-layers but then differs by no more than 0.0039 radians. This discrepancy is presumably due to a difference in the discretisation method,

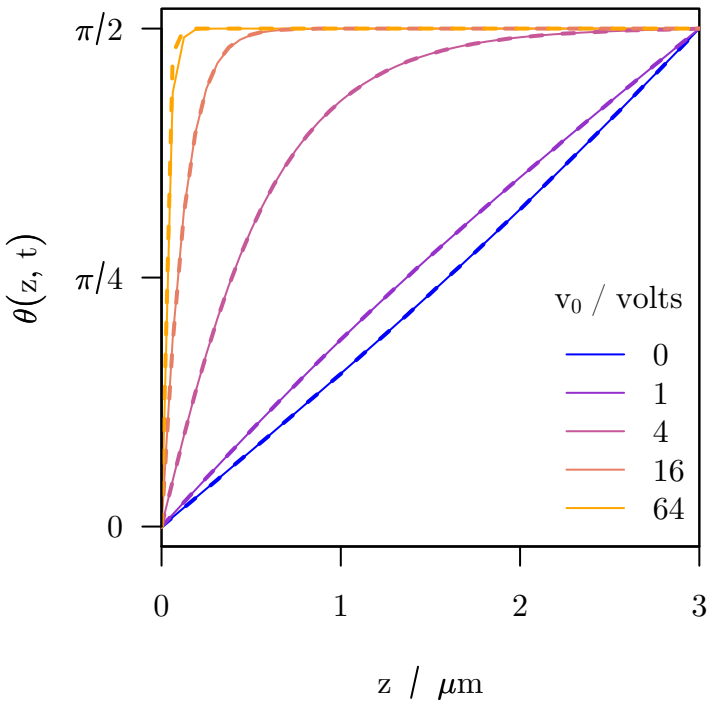

Figure 4.3: Steady-state tilt profiles computed for a HAN cell, compared with DIMOS calculations. $\theta(z)$ ranges from a near-linear profile when $v_0 = 0$ V to a strongly distorted profile when $v_0 = 64$ V. Values for θ calculated by this chapter's numerical model (solid lines) are in good agreement with those computed by DIMOS (dashes)

and, since it only occurs in a rather extreme case, is of little concern.

4.4.2 The flexo-electric effect in HAN cells

Two facets of the flexoelectric effect must be considered in the implementation of the numerical model. The first issue, the correct treatment of the flexoelectric effect when an alternating electric field is applied, is primarily related to performance. The second issue is related to numerical stability.

4.4.2.1 The flexo-electric effect and alternating fields

Equations (4.15) and (4.9) are sufficient to model the flexoelectric effect when either a direct or alternating field is applied, simply by the use of a time-dependent v_0. Such a treatment is inefficient for high frequency alternating currents, since it would be necessary to employ small time steps to describe tiny fluctuations.

An efficient treatment is obtained by explicitly considering high freqeuncy, sinusoidal fluctuations. First, note that viscous dissipation ensures that the response of $\theta(z,t)$ to an oscillating torque $\Gamma \propto \sin \omega t$ decays as $\omega \to \infty$. There is of course no such viscous dissipation in the electric potential and so no relationship between frequency and amplitude

for $v(z,t)$. That means that, while fluctuations in θ may be negligible, fluctuations in v must be considered.

It is convenient to express $v(z,t)$ as a sum of steady (or slowly-varying) and alternating parts:

$$v(z,t) = v_s(z) + v_\omega(z)\sin(\omega t) \tag{4.51}$$

where ω is the angular frequency of the applied field. Substituting (4.51) into equation (4.15) and integrating with respect to time over a whole number of cycles leads to an equation identical to (4.15), replacing v with v_0.

$$\begin{aligned}\frac{\omega}{2n\pi}\int_0^{2n\pi/\omega}\frac{\partial}{\partial z}\left(-\epsilon_0\left(\Delta\epsilon\cos^2\theta+\epsilon_\perp\right)\frac{\partial v}{\partial z}+(e_s-e_b)\sin 2\theta\frac{\partial\theta}{\partial z}\right)dt\\ =\frac{\partial}{\partial z}\left(-\epsilon_0\left(\Delta\epsilon\cos^2\theta+\epsilon_\perp\right)\frac{\partial v_0}{\partial z}+(e_s-e_b)\sin 2\theta\frac{\partial\theta}{\partial z}\right)=0\end{aligned} \tag{4.52}$$

Equation (4.52) is to be solved alongside boundary conditions $v_s(0,t) = v_s(0,t) = 0$ if only an alternating field is applied. If $(e_s - e_b) = 0$ the solution is simply $v_s(z,t) = 0$. When $(e_s - e_b) \neq 0$ a steady (or slowly varying) field will be induced: it is dependent on the magnitude of the applied field because the tilt profile, and hence the flexo-electric polarization, is. Performing the same operations on (4.15) multiplied by $\sin\omega t$ gives

$$\frac{\partial}{\partial z}\left(-\epsilon_0\left(\Delta\epsilon\cos^2\theta+\epsilon_\perp\right)\frac{\partial v_\omega}{\partial z}\right)=0. \tag{4.53}$$

This is simply Gauss' law with no flexoelectric term, and is to be solved alongside the boundary conditions $v_\omega(0,t) = v_0(t)$. Equation (4.9) is also integrated; the resulting equation is identical to (4.9) except for the terms in the electric field:

$$\begin{aligned}\frac{\omega}{2n\pi}\int_0^{2n\pi/\omega}\frac{1}{2}\sin 2\theta\left(\epsilon_0\epsilon_a E^2+(e_s-e_b)\frac{\partial E}{\partial z}\right)dt\\ =\frac{1}{2}\sin 2\theta\left(\epsilon_0\epsilon_a\left[E_s^2+\frac{1}{2}E_\omega^2\right]+(e_s-e_b)\frac{\partial E_s}{\partial z}\right)\end{aligned} \tag{4.54}$$

As one might expect, the sign of E_ω does not affect any of the equations (4.52), (4.53) or (4.54). Any model which was affected would be nonsensical: multiplying the amplitude of an alternating potential by -1 should make no difference over long time-scales. On the other hand, the sign of E_s is important, though only when $e_s - e_b \neq 0$.

To summarise, it has been shown that when modelling the response of a HAN cell to high-frequency alternating fields, it is possible to treat the system as slowly-varying, rather than model detailed time-dependent behaviour. Whenever the coefficient $e_s - e_b \neq 0$, two potential profiles, $\boldsymbol{v}_\omega$ and $\boldsymbol{v}_s$ and hence two contributions to the electric field, must be found by solving two equations, (4.52) and (4.53), derived from Gauss' law. Only the

slowly-varying part, $\boldsymbol{v}_s$, is involved directly with the flexo-electric effect, while both parts contribute to the dielectric energy. Even if no field at all is applied, (4.52) must be solved, as internal fields will result from flexo-electric polarization.

4.4.2.2 The flexoelectric effect and numerical stability

For small values of $(e_s - e_b) \sim 10$ pCm$^-$1, (4.40) rapidly converges to a solution. For larger values, $(e_s - e_b) \sim 100$ pCm$^-$1, the iterations fail, producing spurious solutions. This is resolved by the technique of under-relaxation, in which the update to the slowly-varying voltage field is computed:

$$\Delta \boldsymbol{v}_s = -\alpha \boldsymbol{J}_{vs}^{-1} \boldsymbol{R}_{vs} \tag{4.55}$$

where $\alpha \leq 1$. Table 4.1 shows the effect of varying $(e_s - e_b)$ and α on the performance

		α			
		1	0.5	0.25	Formula (4.56)
$e_s - e_b$ (pCm$^-$1)	20	0.20	0.27	0.48	0.23
	50	0.35	0.32	0.36	0.29
	70	failed	0.27	0.35	0.29
	90	failed	0.27	0.35	0.31
	130	failed	failed	0.35	0.35

Table 4.1: Effect of the flexoelectric coefficient $e_s - e_b$ and the under-relaxation parameter α on performance The table gives CPU times, in seconds, taken to find 81 solutions to the governing equations. Computation was carried out on an AMD Athlon X2 3800+ processor.

of the model. For small values of $e_s - e_b$, decreasing α results in longer calculation times. However, as the value of $e_s - e_b$ increases, α must be reduced in order to obtain a solution. After some experimentation, the formula

$$\alpha = \text{if}\left(\left|\frac{\epsilon_0(e_s - e_b)}{\epsilon_a}\right| < 1, 1, \exp\left(\frac{1 - \left|\frac{\epsilon_0(e_s - e_b)}{\epsilon_a}\right|}{2}\right)\right) \tag{4.56}$$

was found to work well in all cases, as suggested by the last column of table 4.1.

4.4.2.3 Test calculations involving the flexoelectric effect

Figure 4.4 shows the effect of varying $(e_s - e_b)$ on solutions calculated for the HAN cell described earlier when no external field is applied. As the magnitude of $(e_s - e_b)$ is increased, an asymmetric 'S'-shape, of increasing amplitude, is added to the tilt profile. The sign of $(e_s - e_b)$ does not affect the tilt profile at all.

When an alternating electric potential is applied to the cell, the flexo-electric effect causes an apparent stiffening of the liquid crystal. In figure 4.6, the mid-plane tilt is seen to change more slowly with stronger fields as the size of $(e_s - e_b)$ grows. The curve is

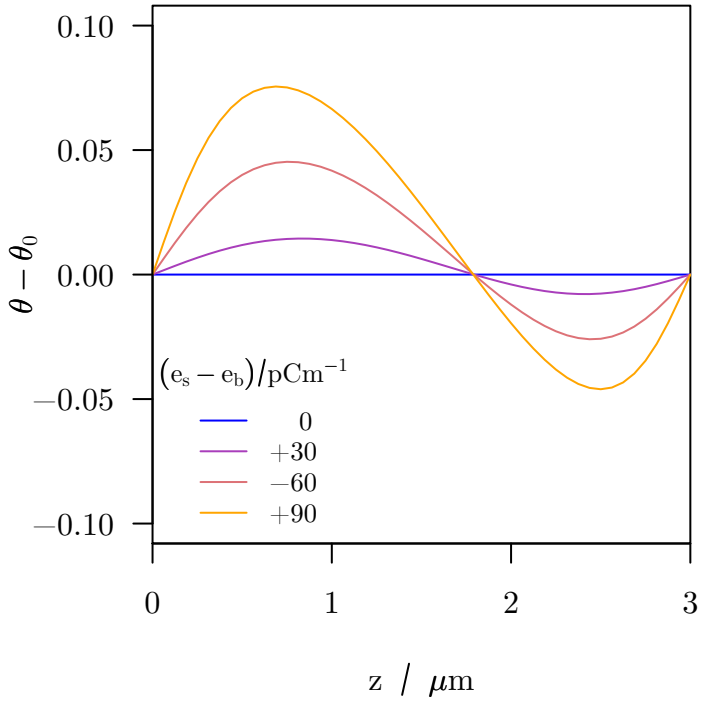

Figure 4.4: Effect of varying $(e_s - e_b)$ on the tilt profile in a HAN cell. Compared to θ_0, a tilt profile computed when $(e_s - e_b) = 0$, the flexoelectric effect adds an asymmetric 'S'-shape to the tilt profile. As the size of $(e_s - e_b)$ grows, so does the perturbation. Changing the sign of $(e_s - e_b)$ has no effect - note the profile for $(e_s - e_b) = -60\text{pCm}^{-1}$ lying midway between those for $(e_s - e_b) = +30\text{pCm}^{-1}$ and $(e_s - e_b) = +90\text{pCm}^{-1}$.

symmetric about $v_\omega = 0$ whatever the value of $(e_s - e_b)$. Overall, increasing the size of $(e_s - e_b)$ appears to be equivalent to increasing the elastic constants. Such stiffening has been reported by Brown *et al* when measuring the Freedericksz transition in planar cells [139].

In contrast, the difference between increasing the elastic constants and $(e_s - e_b)$ is clear when a direct electric potential is applied. A plot of θ at the mid-plane, figure 4.5 is no longer symmetric about $v_s = 0$. The minimum value occurs to the left of $v_s = 0$ when $(e_s - e_b)$ is negative, and to the right when it is positive. This sign-dependent behaviour is well-known, and is vital to several experiments designed to measure $(e_s - e_b)$ using a HAN cell [65–69, 81].

4.4.3 Twisted nematic cells

Whenever the director is not confined to a single plane, the governing equation for ϕ, (4.10) must be solved in addition to (4.9) and (4.15). This equation would be simple enough to discretize, but a serious problem arises due to factors of $\sin\theta$ in every term. Whenever θ approaches zero, all the terms in the equations do so as well. Equation (4.10)

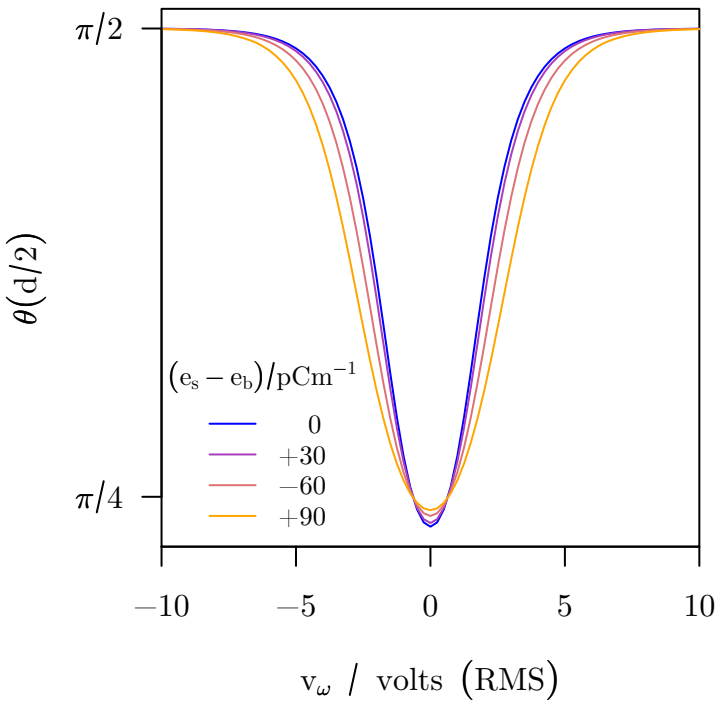

Figure 4.5: Mid-plane tilt in a HAN cell, plotted against alternating voltage for several values of $(e_s - e_b)$**.** Each curve is symmetric about $v_\omega = 0$. The gradient of the curves is reduced as the size of $(e_s - e_b)$ grows.

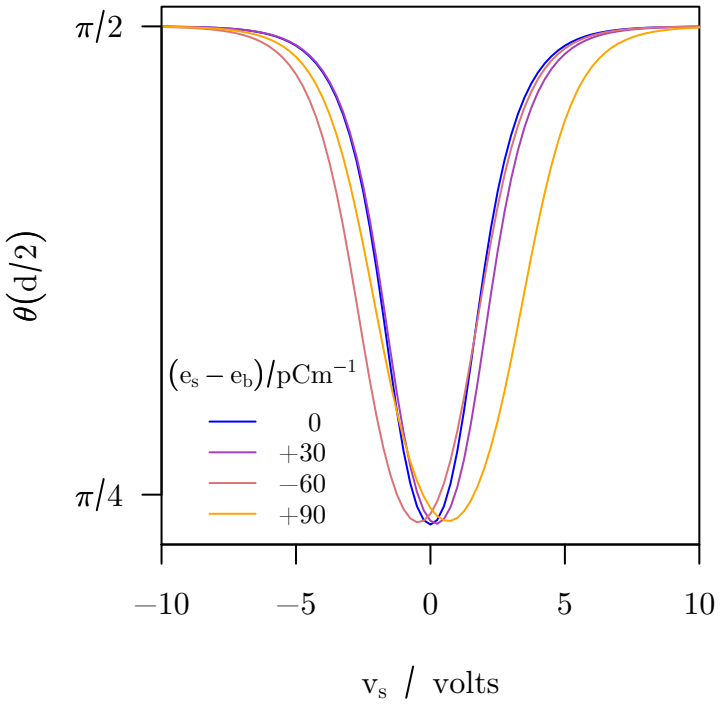

Figure 4.6: Mid-plane tilt in a HAN cell, plotted against direct voltage for several values of $(e_s - e_b)$**.** Now the curves are not symmetric about $v_s = 0$: when $(e_s - e_b)$ is negative the minimum sits to the left, and to the right when $(e_s - e_b)$ is positive.

is barely affected by spatial oscillations in $\phi(z)$ and consequently $\Delta\boldsymbol{\phi}$ at each iteration of (4.40) tends to be spurious. This is in fact another ill-posed problem.

To counter this difficulty, the Ericksen-Leslie equations could be solved in terms of the three components of $\boldsymbol{n}$, rather than the two Euler angles θ and ϕ. Performance would be affected because an additional equation must be solved, so here a different approach is followed. First, re-arrange (4.10) to give

$$\gamma_1'(\theta)\frac{d\phi}{dt} = \frac{\partial^2\phi}{\partial z^2} + \frac{g'(\theta)}{g(\theta)}\frac{\partial\theta}{\partial z}\frac{\partial\phi}{\partial z} - \frac{1}{2}\alpha_2\frac{\sin 2\theta}{g(\theta)}\left(\cos\phi\frac{\partial u_y}{\partial z} - \sin\phi\frac{\partial u_x}{\partial z})\right) \tag{4.57}$$

where

$$\gamma_1'(\theta) = \frac{\gamma}{(k_{22}-k_{33})\sin^2\theta + k_{33}} \tag{4.58}$$

The unsteady term, on the left-hand-side, is now well-behaved as $\theta \to 0$, as is the first term on the right hand side. Each of the remaining terms has a factor which behaves like $1/\theta$ as $\theta \to 0$, so dominating the equation. To replicate this behaviour numerically, the positive-definite function $g(\theta)$ is approximated

$$g(\theta) \approx \min(\epsilon^2, g(\theta)) \tag{4.59}$$

where ϵ^2 is of the order of machine precision. Only when $|\theta| \sim \epsilon$ - when the director is very nearly parallel to the $z-$axis does this result in an equation much different from (4.57). In this case, ϕ really is meaningless, and so the resulting equation,

$$\gamma_1\frac{d\phi}{dt} = k_{33}\frac{\partial^2\phi}{\partial z^2} \tag{4.60}$$

is as good a choice as any.

Twist plays a rather limited role in this thesis: it is briefly considered with regard to steady-state flow in chapter 7 and appendix D. That being the case, the unsteady term can be ignored entirely, while the terms involving flow are similar to those in the equation for θ which will be discussed in section 4.4.4. Only steady-state behaviour in twisted nematic cells will be considered here (in order to test the solutions against DIMOS). The relevant parts of (4.57) are discretized, to give

$$\frac{1}{h^2}\left(\phi_U + \phi_L - 2\phi_P\right) + \frac{g'(\theta_P)}{4h^2 g(\theta_P)}\left(\phi_U - \phi_L\right)\left(\theta_U - \theta_L\right) = 0. \tag{4.61}$$

As well as solving this new equation, a term in ϕ,

$$\frac{1}{8h^2}g'(\theta_P)\left(\phi_U - \phi_L\right)^2 \tag{4.62}$$

must be added to the left-hand side of the equation for θ, (4.48).

Steady-state director profiles computed by solving these equations agree with director profiles computed by DIMOS. A 5 μm twisted nematic cell was simulated, with $\theta = \pi/2$ at both cell walls, $\phi(0) = 0$ and $\phi(d) = \pi/2$. For the elastic and dielectric constants, the values $k_{11} = 6.2$ pN, $k_{22} = 3.9$ pN, $k_{33} = 8.2$ pN, $\epsilon_\perp = 7$, and $\epsilon_\parallel = 18.5$ were used, corresponding to 5CB [13]. Figure 4.7 shows the tilt profile as the applied voltage is increased: the two sets of results are in good agreement, with the maximum difference of 0.061 radians occurring in the sub-layers next to the cell walls at $v_0 = 7$V. At the mid-plane, the maximum discrepancy is 0.0020 radians . Similarly, the twist profiles (figure 4.8) differ by at most 0.055 radians, again at $v_0 = 7$V but in this case at the mid-plane. Figure 4.9 is a plot of mid-plane tilt against applied voltage, showing that both programs compute a Freedericksz transition between $v_0 = 0.7V$ and $v_0 = 0.8V$.

4.4.4 HAN cell dynamics

Two additional terms from (4.9) must be added to the left-hand side of (4.48) if switching is to be modelled. One is the unsteady term,

$$-\gamma_1 \frac{\partial \theta}{\partial t},$$

which is of the kind described in section 4.3.5. To account for backflow and kickback effects, the flow-aligning term

$$c(\theta)\left(\cos\phi \frac{\partial u_x}{\partial z} + \sin\phi \frac{\partial u_y}{\partial z}\right) \tag{4.63}$$

must also be included. It is approximated by

$$\frac{1}{2h} c(\theta_P)\left(\cos\phi_P\left(u_{xE} - u_{xW}\right) + \sin\phi_P\left(u_{yE} - u_{yW}\right)\right). \tag{4.64}$$

Only the first part of this term needs to be evaluated when modelling HAN cells, since both $\phi = 0$.

In order to evaluate the term (4.64), the flow field, u_x must be found. All rotations of the director, and hence all forces which cause flow, are confined to the $xz-$plane. Therefore there is no component of the flow parallel to the $y-$axis and only one momentum balance equation, (4.11) needs to be solved. It has the form of the convection-diffusion equation, (4.18), bar the inclusion of unsteady terms in θ and ϕ within the space derivative. As a

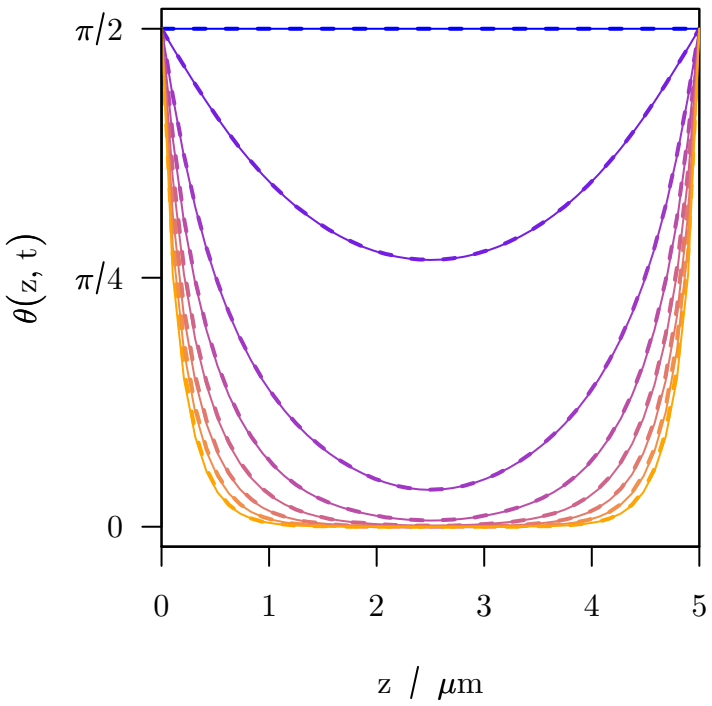

Figure 4.7: Steady-state tilt profiles computed for a twisted nematic cell, compared with DIMOS calculations. DIMOS' results are plotted with dashes: the two programs are in good agreement

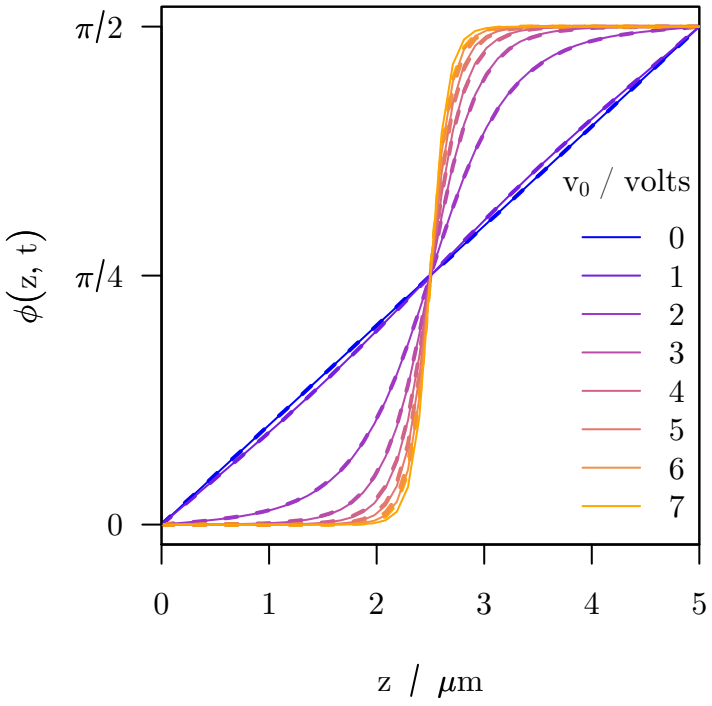

Figure 4.8: Steady-state twist profiles computed for a twisted nematic cell, compared with DIMOS calculations. The two programs are in good agreement, though some discrepancy is visible near the mid-plane.

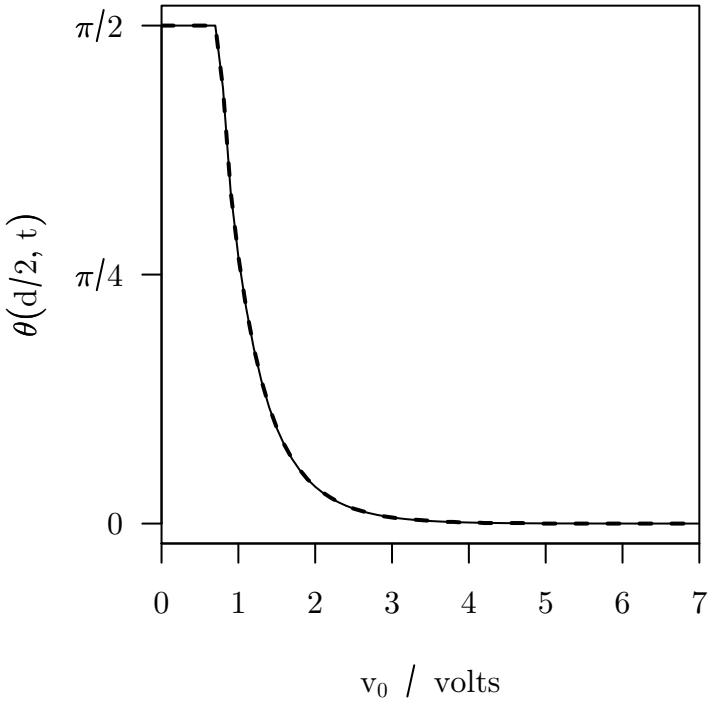

Figure 4.9: Mid-plane tilt plotted against applied voltage computed for a twisted nematic cell, compared with DIMOS calculations. DIMOS' results are plotted with dashes. Both programs compute a Freedericksz transition between $v_0 = 0.7V$ and $v_0 = 0.8V$.

result, it is easily discretized by the control volume method to give

$$U_u - U_l = 0. \tag{4.65}$$

For a HAN cell, the momentum flux between layers E and P, U_u is

$$U_u = \frac{1}{2h}\left[a(\theta_P) + b(\theta_P) + a(\theta_U) + b(\theta_U)\right](u_U - u_P) - \frac{1}{2}\left[c(\theta_U)\frac{d\theta_U}{dt} + c(\theta_P)\frac{d\theta_P}{dt}\right], \tag{4.66}$$

where the backward finite difference formula,

$$\frac{d\theta_P}{dt} \approx \frac{\theta_P(t) - \theta_P(t - \Delta t)}{\Delta t} \tag{4.67}$$

is used to approximate the unsteady terms.

A switching simulation of the HAN cell described earlier serves to compare the accuracy and performance of the adaptive algorithm (4.37) with a simple, fixed time-step algorithm. The relevant Leslie viscosities were set to $\alpha_1 = -10\text{mPas}^{-1}$, $\alpha_2 = 350\text{mPas}^{-1}$, $\alpha_3 = 10\text{mPas}^{-1}$ and $\alpha_4 + \alpha_5 = 360\text{mPas}^{-1}$. Prior to $t = 0$, the cell is assumed to be at rest, with no field applied. At $t = 0$, v_0 is set to 4V, and the evolution of the cell was computed over a period of 25 ms. Figure 4.10 shows the tilt profiles, and figure 4.11 the flow fields

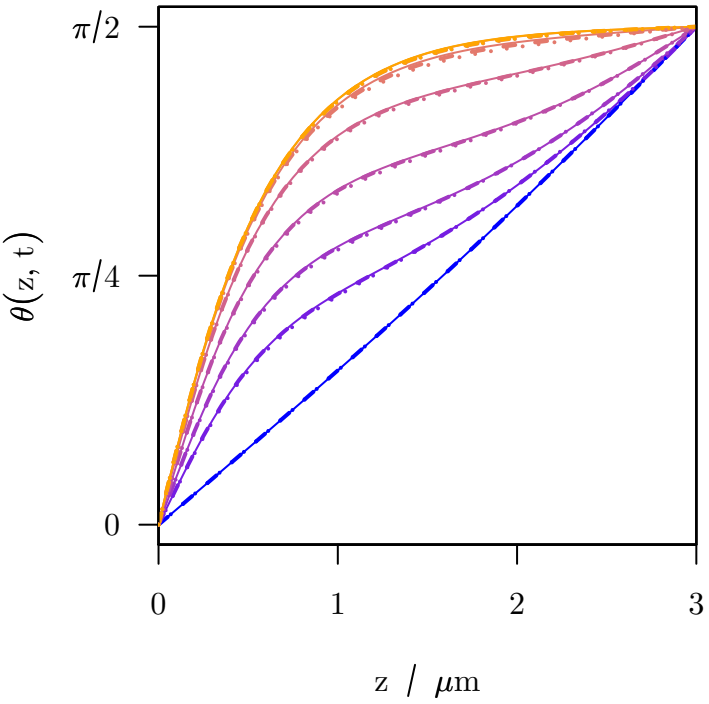

Figure 4.10: Evolution of $\theta(z,t)$ in a HAN cell after a 4V potential is applied. Profiles at $t \in \{0, 1, 2, 4, 8, 16, 25\}$ ms are shown. Results computed by a fixed time-step method (solid curves), the adaptive method with $\epsilon = 8 \times 10^{-6}$ (dashes), and the adaptive method with $\epsilon = 3 \times 10^{-4}$ (dots) are similar

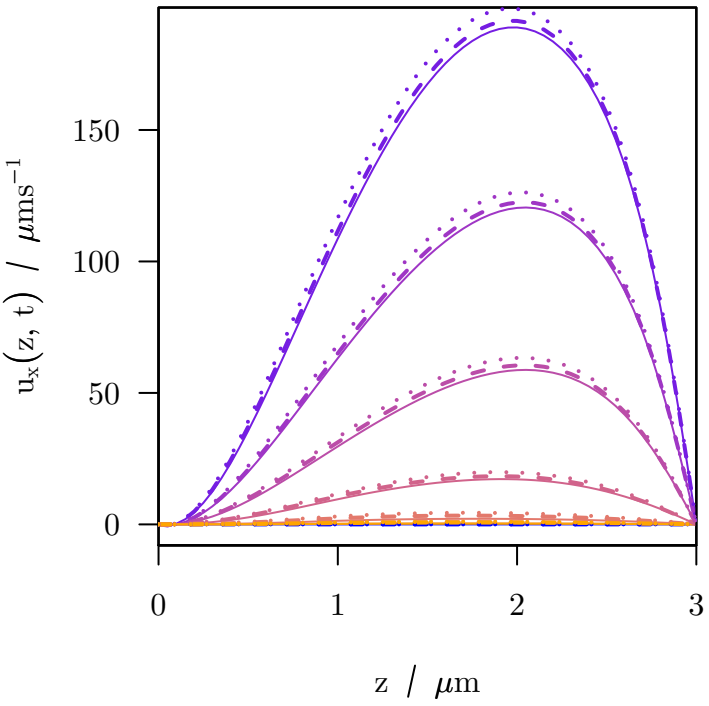

Figure 4.11: Evolution of $u_x(z,t)$ in a HAN cell after a 4V potential is applied.

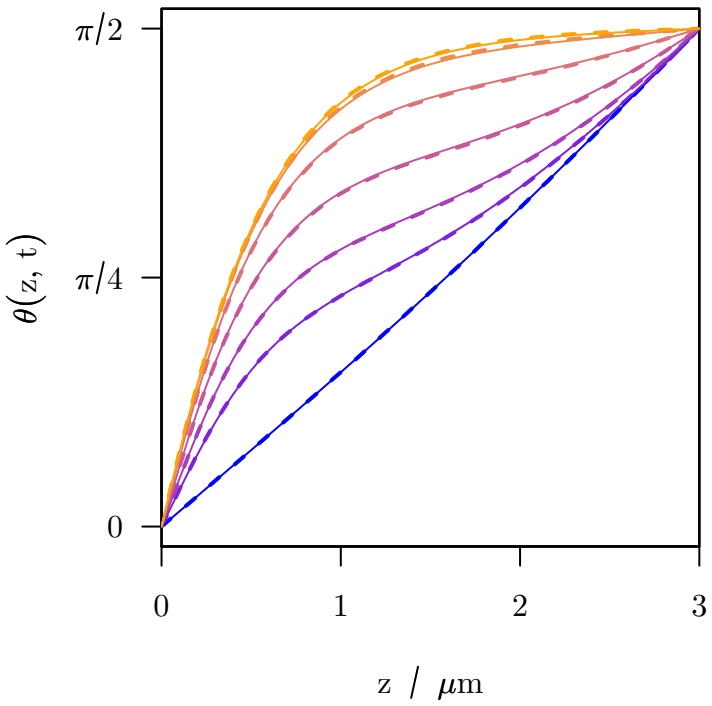

Figure 4.12: Comparsion of tilt profiles computed by DIMOS and the adaptive algorithm. DIMOS' results are plotted with solid curves, while the results of the adaptive algorithm, with $\epsilon = 8 \times 10^{-6}$ are plotted with dashes.

at times $t \in \{0, 1, 2, 4, 8, 16, 25\}$ ms. For the simple algorithm, the time-step was set to $\Delta t = 10$ μs and the calculation took 2.4 s to complete. Two simulations were performed using the adaptive method, with Δt set to 1 ms for the first two steps, then to $2, 4, 8$ and 9 ms. When $\epsilon_t = 3 \times 10^{-4}$ the tilt profile differs from that computed by the fixed time-step method by no more than 0.017 radians: 0.19 s of CPU time was used. Setting $\epsilon_t = 8 \times 10^{-6}$, the second calculation took 0.70 s of CPU time and the tilt profile differs from the simple calculation by at most 0.0069 radians. So, the adaptive algorithm is far more efficient than the simple algorithm. In addition, one can vary ϵ_t to trade speed for accuracy in time-dependent calculations.

Once again, accuracy of the numerical method developed here is comparable to that of DIMOS. In Figure 4.12 the tilt profiles computed by the adaptive method (with $\epsilon_t = 8 \times 10^{-6}$) are plotted alongside DIMOS' results. At no point do the two solutions differ by more than 0.0087 radians.

4.5 Summary

A program has been written which solves the Ericksen-Leslie equations numerically. It includes two phenomena important to this thesis, namely flow, and the flexoelectric effect,

and will be extended to include more in later chapters. Its performance is adequate: since a full switching simulation can be carried out in less than 100 milliseconds, inverse problem calculations which require many thousands of solutions should only take a few minutes. And where it can be compared with the commercial program DIMOS, the solutions are in good agreement.

Chapter 5

Analysis of an AC switching experiment

5.1 Introduction

In this chapter, inverse problem theory is used to analyse a set of experimental data measured by Taphouse [54]. The experiments in question were performed on HAN cells[1] filled with Merck ZLI-4788-000, a nematic liquid crystal with negative dielectric anisotropy. Both steady-state and dynamic experiments were performed. In the steady-state experiments, sequence of AC voltages were applied to each cell, and the reflection and transmission coefficients measured after the cell reached equilibrium. For the dynamical experiments, the change in coefficients with time was recorded as the cell switched from the ground-state to an excited state, and back.

The first type of inverse problem that will be considered is an extension of the problem outlined in chapter 3. As before, the director profile will be described by an initial guess to which simple functions of z are added. There are three key changes: cubic splines will be used to parametrize the corrections to the director profile, the initial guess for θ will no longer be a linear function of z, but a numerical solution to the Ericksen-Leslie equations, and the regularization method will be extended to take electric fields and time-dependence into account. From now on, this sort of inverse problem will be called *weakly-constrained*, because the director will not be forced to be a exactly a solution of the Ericksen-Leslie equations, but close to one.

The second type of inverse problem aims to determine phenomenological parameters such as the elastic constants, the Leslie viscosities, and the dielectric anisotropy. To achieve this, a new forward problem, where reflection and transmission coefficients are defined,

[1] More detail on the construction of these cells is given in appendix A

ultimately, as functions of these parameters will be formulated. That is a two step process: first the Ericksen-Leslie equations are solved for a particular set of parameters, and then the Berreman 4×4 matrix method is used to compute R and T. This type of inverse problem will be called *strongly-constrained*.

Naturally, once a set of phenomenological parameters have been estimated, one would like to known something about the uncertainty of those estimates. In fact, the least-squares formulation of the inverse problem provides values for both the parameters and their exactitude. However, a key assumption, that R and T depend linearly, or nearly linearly, on each parameter, has been made in deciding to solve a least squares problem. A Monte-Carlo method will be employed to explore the validity of this assumption.

5.2 Methodology

Broadly, the methodology pursued in this chapter is as follows

1. Using approximate values for the LC layer thickness, the elastic constants and so on, calculate steady-state director profiles, at several applied voltages, by solving a weakly-constrained problem.

2. Examine these profiles to decide which terms in the steady-state Ericksen-Leslie equations are important.

3. Determine the free parameters in the steady-state equations, and other cell parameters, such as the layer thickness, by solving a strongly-constrained problem.

4. Using those values, solve a second weakly-constrained problem, to find a time-dependent director profile given measurements made as the cell is switched.

5. Examine these profiles, and decide which terms in the time-dependent Ericksen-Leslie equations are important.

6. Determine the free parameters in the time-dependent equations, by solving a second strongly-constrained problem.

5.2.1 Weakly-constrained problem

The basic inverse problem of chapter 3 started with an initial guess for the tilt profile $\bar{\theta}(z)$, and was solved to find a correction $\delta\theta(z)$ so that the true tilt profile would be $\theta(z) = \bar{\theta}(z) + \delta\theta(z)$. A similar approach is taken here, but rather than choosing a linear tilt profile for the initial guess, a numerical solution to the Ericksen-Leslie equations will be used. That will allow a good initial guess to be made when the cell is not in its ground

Parameter	Symbol	Given value	Source
Refractive indices	$n_\perp$	1.49	
(at 632.8 nm)	$n_\parallel$	1.65	
Permittivities	$\epsilon_\perp$	10.2	Data sheet supplied
(at 1Khz)	$\epsilon_\parallel$	-5.8	with ZLI-4788-000
Rotational Viscosity	γ_1	309 mPas	
Elastic constants	k_{11}	13.7 pN	
	k_{33}	18.9 pN	
Director tilt at $z = 0$	θ_0	0	
Director tilt at $z = d$	θ_d	$\pi/2$	cell design
Azimuthal angle	ψ	$\pi/4$	
LC layer thickness	d	3 μm	diameter of spacer beads
ITO layer thickness	d_{ITO}	25nm	manufacturer data
Optical permittivity of ITO	ϵ_{ITO}	3.8 + 0.08i	http://www.luxpop.com, [130]

Table 5.1: Values of LC and cell parameters given prior to the experiment. These values are given by suppliers, or are part of the experimental design.

state: when an electric field has been applied, for example. Of course, the Ericksen-Leslie equations can only be solved if values are known for the elastic constants, the dielectric constants, and so on. In the case of ZLI-4788-000, Merck supplies approximate values for enough of the LC parameters for solutions to be found, provided that shear flow is not considered. Other essential parameters, such as the LC layer thickness, and the boundary tilts, are known roughly from the cell design. These approximate values are given in table 5.1.

No attempt is made to optimize the values of parameters such as the LC layer thickness, or the thickness of the ITO layers when solving weakly-constrained problems. Neither will the azimuthal angle (the angle between the plane of incidence and the rubbing direction) be optimized. The SVD analysis of chapter 3 showed that when these parameters are sufficiently well known, they play no part in the regularized solution. On the other hand, if they are not well known, it will be impossible to distinguish between variations in them and spurious variations in the director profile.

5.2.1.1 Sampling the data

In chapter 3, all measurements of the reflection and transmission coefficients were included in the data vector $\boldsymbol{b}$. Because the measurements vary slowly with angle of incidence, only a sample - around one measurement per degree - of the data is needed, as suggested in 3.3.1. Reducing the length of $\boldsymbol{b}$ means a reduction in the length of $\boldsymbol{f}$ - and hence computational time. For fully leaky guided mode experiments, R and T vary quite evenly with angle, so sampling at a constant frequency is sufficient. Were sharp features present (as in the total attenuated reflection experiment), it would be necessary to concentrate samples around

them.

Although many data points will be ignored while solving the various inverse problems, the final results will be compared with all the data. For clarity, it is best to have a measure of the misfit between data which has comparable size in both cases. The natural measurement is the residual norm $||\boldsymbol{f}(\boldsymbol{m}) - \boldsymbol{b}||_2$. In order that the size of residual norms do not depend on the number of data points considered, the formula

$$||a||_2^2 = \frac{1}{n}\boldsymbol{a}^T\boldsymbol{a} \tag{5.1}$$

will be used, where n is the length of $\boldsymbol{a}$. In other words, the root mean square difference between $\boldsymbol{f}(\boldsymbol{m})$ and $\boldsymbol{b}$ will be discussed, rather than the sum of square differences.

5.2.1.2 The use of cubic splines and a coarse mesh

A coarser subdivision of the LC layer than that used in chapter 3 is used from now on, also for the sake of efficiency. Since a fairly smooth tilt profile is to be expected (and indeed, is all that can justifiably be recovered), this seems to be a reasonable step. The liquid crystal layer is subdivided into a coarse mesh of twelve layers, with the centres of the end layers lying on the cell walls. The elements of the vector $\boldsymbol{m}$ are the values of $\delta\theta$ at the centres of these sub-layers. However, the Berreman calculation must still be performed on a relatively fine mesh, so the values of $\delta\theta$ on that mesh are found by cubic spline interpolation. Likewise, the initial guess is given in terms of the finer layers, so cubic spline interpolation is used to find the values of $\bar{\theta}(z)$ on the coarse mesh.

Using this coarse mesh, and a more sophisticated initial guess, changes the details (though not the general effect) of the regularization method. In steady-state, and when no field is applied, the initial guess, $\bar{\theta}(z)$, satisfies

$$\left(k_{11} + (k_{33} - k_{11})\cos^2\bar{\theta}\right)\frac{\partial^2\bar{\theta}}{\partial z^2} + \frac{1}{2}(k_{11} - k_{33})\sin 2\bar{\theta}\left(\frac{\partial\bar{\theta}}{\partial z}\right)^2 = 0. \tag{5.2}$$

As before, the idea is to find a function, $\delta\theta(z)$, such that $\bar{\theta}(z) + \delta\theta(z)$ roughly satisfies this equation. Substituting $\bar{\theta}(z) + \delta\theta(z)$ into the left hand side of (5.2) assuming $k_{33} \approx k_{11} \approx 1/2(k_{33} + k_{11})$ and retaining only first-order terms in $\delta\theta$ leads to a function

$$r(z) = \begin{cases} 0 < z < d & \frac{1}{2}(k_{33} + k_{11})\frac{\partial^2}{\partial z^2}\delta\theta \\ z = 0, z = d & \frac{1}{2d^2}(k_{33} + k_{11})\delta\theta \end{cases} \tag{5.3}$$

which represents the misfit between $\delta\theta$ and the Ericksen-Leslie equations in the bulk, and between $\delta\theta$ and the assumed tilt angle at the surfaces. $r(z)$ can be evaluated at any point,

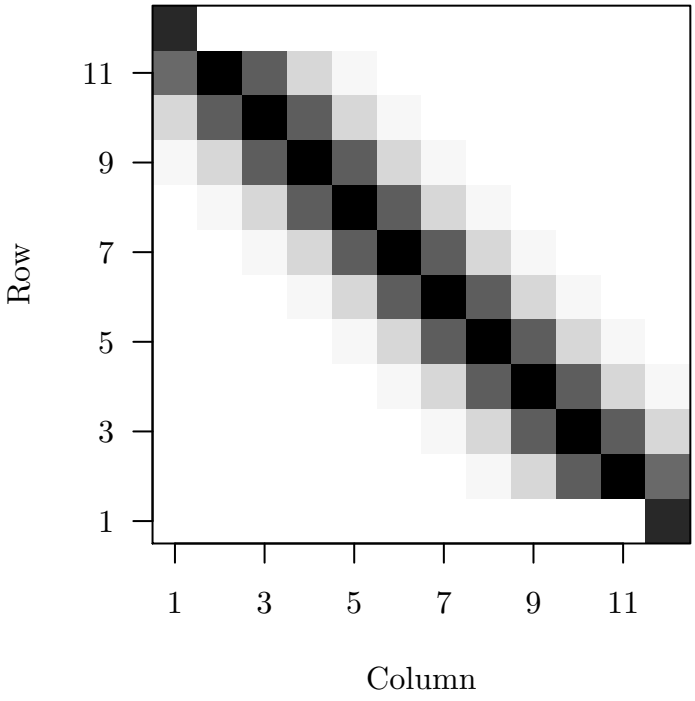

Figure 5.1: Grey-scale plot of the regularization matrix, $\boldsymbol{L}$, for steady-state weakly-constrained problems using cubic spline interpolation. Darker squares correspond to larger elements. The matrix is diagonally dominant, in that elements on the diagonal are two orders of magnitude larger than elements three rows off.

since cubic spline interpolation gives both $\theta(z)$ and its derivatives in terms of the elements of $\boldsymbol{m}$. From there, a penalty term is given by

$$p = \lambda ||\boldsymbol{L}\boldsymbol{m}||_2^2, \tag{5.4}$$

as before, where $m_j = \delta\theta(z_j)$, and

$$L_{ij} = \left.\frac{\partial r}{\partial m_j}\right|_{z=z_i}. \tag{5.5}$$

$\boldsymbol{L}$ plays exactly the same role as in chapter 3. It is no longer sparse, but it is diagonally dominant - the largest elements are closest to the diagonal (see figure 5.1).

5.2.1.3 Regularization and electric fields

If an electric field is applied across the cell, an additional contribution to $\boldsymbol{L}$ arises. Neglecting the flexoeelectric effect, the dielectric term,

$$r_E(\bar{\theta}) = -\frac{1}{2}\epsilon_0\epsilon_a \sin 2\bar{\theta} E^2. \tag{5.6}$$

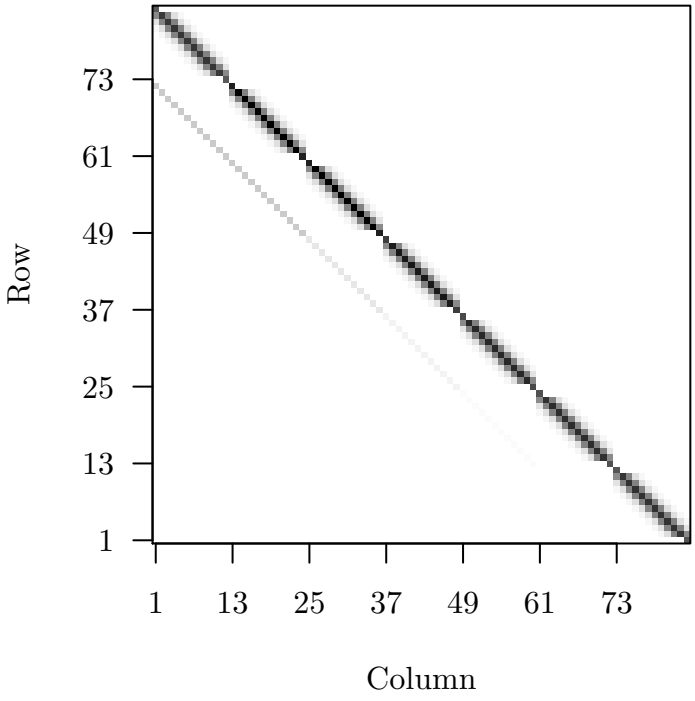

Figure 5.2: Grey-scale plot of the regularization matrix, $\boldsymbol{L}$, for time-dependent weakly-constrained problems using cubic spline interpolation. Darker squares correspond to larger elements. Diagonally dominant 12×12 sub-matrices identical to those of the steady-state problem lie along the diagonal. On the left of each of these sub-matrices from the second onwards lies a diagonal sub-matrix which relates each tilt profile its predecessor through the time-dependent term in (5.10). As the time-step between each profile grows, the size of these elements decreases.

is added to the left hand side of (5.2). Substituting $\bar{\theta} + \delta\theta$ into this term, and retaining only first order terms in $\delta\theta$ gives

$$r_E(\bar{\theta} + \delta\theta) = r_E(\bar{\theta}) - \epsilon_0 \epsilon_a \cos 2\bar{\theta} \delta\theta E^2. \tag{5.7}$$

An approximate value for E can be calculated from the gradient of $\bar{v}$, the voltage profile found at the same time as $\bar{\theta}$. In the bulk, the misfit function is revised to

$$r(z) = \frac{1}{2}(k_{33} + k_{11}) \frac{\partial^2}{\partial z^2} \delta\theta - \epsilon_0 \epsilon_a \cos 2\bar{\theta} \left(\frac{\partial \bar{v}}{\partial z} \right)^2 \delta\theta \tag{5.8}$$

As a result, the diagonal elements of $\boldsymbol{L}$ are altered by an amount proportional to $\epsilon_a E^2$ and to $\cos 2\bar{\theta}$. For ZLI-4788-000, $\delta\theta$ will held closer to zero near the planar surface, where $\cos 2\bar{\theta}$ is negative and allowed to deviate more near the homeotropic surface, where $\cos 2\bar{\theta}$ is positive.

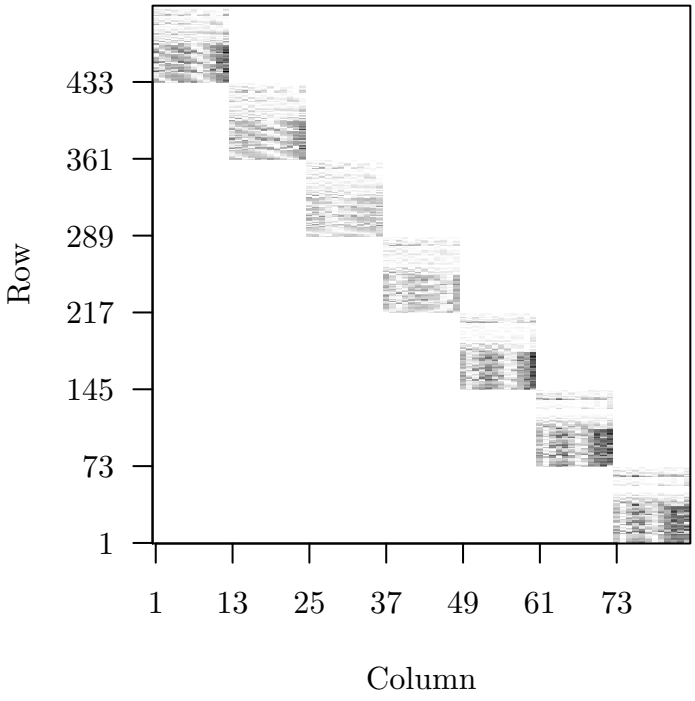

Figure 5.3: Grey-scale plot of the Jacobian matrix, J, for time-dependent weakly-constrained problems using cubic spline interpolation. Darker squares correspond to larger elements. Dense 72×12 sub-matrices lie along the diagonal: changes in the tilt profile at the nth time-step are related to changes in computed transmission and reflection coefficients at the same time by a sub-matrix filling the intersection of rows $72(n-1) - 72n$ and columns $12(n-1) - 12n$.

5.2.1.4 Regularization of time-dependent tilt profiles

Taking time-dependent behaviour into account is conceptually simple enough, but does require additional computational resources. Ignoring shear flow, viscous dissipation contributes a term

$$r_t(\bar{\theta}) = -\gamma \frac{\partial \bar{\theta}}{\partial t} \tag{5.9}$$

to the left hand side of (5.2), and hence the misfit function, in the bulk, becomes

$$r(z,t) = \frac{1}{2}(k_{33} + k_{11}) \frac{\partial^2}{\partial z^2} \delta\theta - \epsilon_0 \epsilon_a \cos 2\bar{\theta} \delta\theta \left(\frac{\partial \bar{v}}{\partial z} \right)^2 - \gamma \frac{\partial}{\partial t} \delta\theta. \tag{5.10}$$

The time derivative $\frac{\partial}{\partial t}\delta\theta$ can approximated using a backward finite difference scheme,

$$\left. \frac{\partial}{\partial t} \delta\theta \right|_{t+\Delta t} \approx \frac{1}{\Delta t} \left[\delta\theta(z, t+\Delta t) - \delta\theta(z,t) \right]. \tag{5.11}$$

It is no longer possible to find each tilt profile separately (as it would be for a sequence

of steady-state profiles at varying voltage). Instead, a longer model vector

$$\boldsymbol{m} = \begin{bmatrix} \boldsymbol{m}_0 \\ \boldsymbol{m}_1 \\ \vdots \\ \boldsymbol{m}_m \end{bmatrix} \tag{5.12}$$

must be built from the sub-vectors $\boldsymbol{m}_i$ representing the tilt profile at time $t = t_i$. Similarly, a data vector $\boldsymbol{b}$ is constructed from sub-vectors standing for the measurements at each time step, and likewise for the vector function $\boldsymbol{f}$. Larger (but sparse, see figures 5.2 and 5.3) matrices $\boldsymbol{J}$ and $\boldsymbol{L}$ must be inverted, which tends to increase the CPU time - doubling the size of the matrices more than doubles the time required to invert them. That said, the matrices dealt with in this chapter are small — $\boldsymbol{L}$ and $\boldsymbol{J}$ have only 120 columns at the most.

Clearly, this new term should only be used if it is valuable. On the surface, it seems to be. Reducing the governing equation for θ to its simplest form, one has

$$k\frac{\partial^2\theta}{\partial z^2} - \gamma_1\frac{\partial^2\theta}{\partial t} = 0, \tag{5.13}$$

the left hand side of which is the penalty function (5.10), neglecting electric fields. If, at $t = 0$, the tilt profile is expressed as a sum of a linear tilt profile and a Fourier series

$$\theta(z,0) = \theta_0 + \frac{(\theta_d - \theta_0)}{d}z + \sum_{n=1}^{n=\infty} b_n \sin(n\pi z) \tag{5.14}$$

then the solution to (5.13) is:

$$\theta(z,t) = \theta_0 + \frac{(\theta_d - \theta_0)}{d}z + \sum_{n=1}^{n=\infty} b_n \exp(-\frac{kn^2t}{\gamma_1}) \sin(n\pi z). \tag{5.15}$$

This solution expresses the most basic time-dependent behaviour of the liquid crystal: any spatial oscillation in the director decays at a rate which increases rapidly with its wavenumber, n. Such a trait is desirable in the regularized solution, but does the value outweigh the cost? Solutions to the weakly-constrained problems will be found both with and without this new term to decide its benefit.

5.2.2 Strongly-constrained problem

Assuming that an image of the director has been recovered, the experimenter will want to understand the resulting tilt profiles in terms of something like the Ericksen-Leslie equa-

tions. In previous studies [54, 51], many solutions to the Ericksen-Leslie would be found, varying the phenomenological parameters which define a particular tilt profile. These tilt profiles would be compared with those found by solving the imaging problem, and the best match identified. If a good match was found, then, presumably, the phenomenological parameters had been found as well.

The intention here is to hunt down the best set of parameters automatically. To this end, a model vector $\boldsymbol{m}$ is defined in terms of various phenomenological coefficients. From there, a least-squares function,

$$\Phi = ||\boldsymbol{f}(\boldsymbol{m}) - \boldsymbol{b}||_2^2 \tag{5.16}$$

can be built by first solving the Ericksen-Leslie equations numerically for a given $\boldsymbol{m}$, then using Berreman's method to compute the elements of $\boldsymbol{f}$ given the numerical director profile. Attempting to minimise Φ naively, however, often results in unrealistic values for the elements of $\boldsymbol{m}$, or fails entirely. Previous attempts [131] have used constrained optimization techniques to avoid this eventuality. In this chapter, a different approach, mathematically equivalent to Tikhonov regularization, will be tried.

First, assume that prior information about each parameter m_j exists, namely an expected value of 0, and a variance σ_m. An application of Bayes theorem (see Appendix B) leads to an objective function identical to that used in Tikhonov regularization,(2.32),

$$\Phi = ||\boldsymbol{f}(\boldsymbol{m}) - \boldsymbol{b}||_2^2 + \frac{\sigma_b^2}{\sigma_m^2}||\boldsymbol{m}||_2^2 \tag{5.17}$$

Replace σ_b^2/σ_m^2 with λ^2, and one has exactly (2.32). Just as in chapter 3, the Gauss-Newton method can be used to minimise this objective function, leading to a new expected value for $\boldsymbol{m}$, denoted $\bar{\boldsymbol{m}}$. Doing so means evaluating the Jacobian matrix numerically, which requires the Ericksen-Leslie equations to be solved twice for each relevant parameter, at every iteration. That is one of the main reasons that execution speed was seen as so important in the previous chapter.

Permitted value	Example	Formula	Assumed probability density
any	θ_0, $(e_s - e_b)$	$a = a_0 + m(\sigma_a/\sigma_m)^2$	normal
positive	d, k_{33}	$a = a_0 \exp(m(\sigma_a/\sigma_m)^2)$	log-normal

Table 5.2: Calculation of the parameter a from an element of $\boldsymbol{m}$. Each element of $\boldsymbol{m}$ is defined such that $p(m)$ is a Gaussian function with variance σ_m^2 and expected value 0. The *a priori* expected value of a is a_0, and either a, or $\ln a$ is distributed normally with variance σ_a.

Now, it will be necessary to build each m_j from parameters whose expected value is not zero, and whose variance is not σ_m. Two kinds of parameters will be encountered: those which may take any value, and those which take only positive values. Table 5.2 shows how an arbitrary parameter, a, is related to one element of $\boldsymbol{m}$ in each of these cases. When a may take any value, prior knowledge of it will be represented by a normal distribution. In contrast, if a is positive definite, the *a priori* probability density is taken to be log-normal: that is, $\ln a$ is distributed normally.

5.2.2.1 Steady-state problem

Several liquid crystal parameters (such as the elastic constants) together with other parameters (such as the cell thickness) were found by minimising a function like (5.17). It was simple enough to define the forward model : for a given set of parameters, solve the steady-state Ericksen-Leslie equations at the appropriate voltages to find a sequence of tilt profiles, then compute the reflection and transmission coefficients.

Defining the model vector $\boldsymbol{m}$ was a little more complicated, because the desired prior knowledge, both an expected value and a variance for each parameter, was not available. Merck provide expected values for some of the liquid crystal parameters, but not variances. Likewise, the ITO layer is known to be around 25 nm thick, but little more. The approach taken here is to set λ to as small a value as possible in (5.17), that is, assuming that the variance is as large as possible. This was done by finding several solutions, varying λ, and examining the behaviour of the $\boldsymbol{m}$ as λ grows.

5.2.2.2 Time-dependent problem

Once the parameters which affect the steady-state problem were found, the Leslie viscosities could be estimated, given time-dependent data. Only four linear combinations affect the HAN cell: α_1, α_2, α_3, and $\alpha_4 + \alpha_5$. Because Merck only provide a value for the rotational viscosity, $\gamma_1 = \alpha_3 - \alpha_2$, it is a natural choice for one element of $\boldsymbol{m}$. Its complement, $\gamma_2 = \alpha_2 + \alpha_3$ is chosen for another. An additional piece of information is available from literature [13]: for many nematic materials, $\alpha_4 \sim \alpha_5 \sim \gamma_1$ while $\alpha_1 \sim \alpha_3 \ll \gamma_1$, so the initial values, given in table 5.3, were chosen to reflect this.

Viscosity	Initial value / mPa s
α_1	0
α_2	-309
α_3	0
$\alpha_4 + \alpha_5$	618

Table 5.3: Initial values of the nematic viscosities.

The Leslie viscosities are subject to a set of inequality constraints (1.29) - (1.33), which ensure that energy dissipation is positive definite. In a HAN cell, given the Parodi relation, and subsuming the requirement $\alpha_4 \geq 0$ into the other constraints, these reduce to

$$\gamma_1 \geq 0, \tag{5.18}$$

$$2(\alpha_4 + \alpha_5) + \gamma_2 \geq 0, \tag{5.19}$$

$$\alpha_1 + 2(\alpha_4 + \alpha_5) + \gamma_2 \geq \frac{\alpha_4}{2} \geq 0, \tag{5.20}$$

$$\gamma_1(2(\alpha_4 + \alpha_5) + \gamma_2) - \gamma_2^2 \geq 0. \tag{5.21}$$

If these constraints are violated, the Ericksen-Leslie equations cannot be solved. There is, of course, no probability that the Leslie viscosities lie outside this region, so, rather than Φ,

$$\Phi' = \begin{cases} \text{all constraints satisfied} & \Phi \\ \text{otherwise} & \infty \end{cases} \tag{5.22}$$

is minimized. The Gauss-Newton method is not suitable in this case: the simplex method of of Nelder and Mead (which does not need derivatives with respect to $\boldsymbol{m}$ to be computed) was used instead. Note that the third constraint provides an upper bound for α_4 when the four viscosities given above are known.

5.2.3 Error analysis for the strongly-constrained problems

Both the elements of $\bar{\boldsymbol{m}}$ and their uncertainties should be specified. Provided that $\boldsymbol{f}$ is nearly linear close to $\bar{\boldsymbol{m}}$, Φ can be rewritten

$$\Phi \approx (\boldsymbol{m} - \bar{\boldsymbol{m}})^T (\frac{1}{2\sigma_b} \boldsymbol{J}^T \boldsymbol{J} + \frac{1}{2\sigma_b} \boldsymbol{I})(\boldsymbol{m} - \bar{\boldsymbol{m}}) + K \tag{5.23}$$

where the Jacobian matrix is evaluated at $\boldsymbol{m} = \bar{\boldsymbol{m}}$, and K is simply a constant [116]. In other words, the conditional probability density $p(\boldsymbol{m}|\boldsymbol{b})$ is a Gaussian function, with *covariance matrix*

$$\boldsymbol{C} = (\frac{1}{2\sigma_b^2} \boldsymbol{J}^T \boldsymbol{J} + \frac{1}{2\sigma_m^2} \boldsymbol{I})^{-1}. \tag{5.24}$$

The covariance matrix describes the uncertainty in $\boldsymbol{m}$ completely, but is not so easy to interpret. Its diagonal values C_{jj} are the variances in the elements m_j, so it is usual to state:

$$m_j = \bar{m}_j \pm \sqrt{C_{jj}} \tag{5.25}$$

but this is not the complete story. Every surface of constant Φ is an ellipsoid, whose axes are parallel to the eigenvectors of $\boldsymbol{C}$. When the off-diagonal elements of $\boldsymbol{C}$ are zero this ellipsoid is a sphere, otherwise the uncertainties in the m_j are said to be covariant. In other words, error in one parameter implies error in another. Covariance is rather difficult to visualize: one way is to plot the 68% confidence ellipse for each pair of parameters m_j, m_k [140]. The probability that m_j and m_k lie inside that ellipse is 0.68.

While the error analysis described so far is convenient, the assumptions behind it may not be reasonable. In particular, the Berreman calculation is not linear in $\theta(z)$, and the solutions to the Ericksen-Leslie equations are not obviously linear in the phenomenological parameters. So, there seems no good reason to assume that $\boldsymbol{f}$ is a linear, or even a weakly non-linear, function of $\boldsymbol{m}$. If $\boldsymbol{f}$ is strongly nonlinear, then there may be multiple solutions to the inverse problem, or even an infinity of them. Even if that is not the case, the uncertainties estimated may be inaccurate. But plotting the whole probability density, especially in a high-dimensional space, would be prohibitively expensive.

The Metropolis algorithm [2] [141, 142] can be used to test whether the objective function is Gaussian, or close to it, less expensively. The idea is to take a random walk around the space of $\boldsymbol{m}$, concentrating on those regions where $p(\boldsymbol{m}|\boldsymbol{b})$ is largest. At each iteration, a pseudo-random step $\delta\boldsymbol{m}$ is generated. This step is accepted (that is, $\boldsymbol{m}$ is set to $\boldsymbol{m} + \delta\boldsymbol{m}$) with a probability

$$P = \begin{cases} 1 & \Phi(\boldsymbol{m} + \delta\boldsymbol{m}) \leq \Phi(\boldsymbol{m}) \\ \frac{\Phi(\boldsymbol{m})}{\Phi(\boldsymbol{m}+\delta\boldsymbol{m})} & \Phi(\boldsymbol{m} + \delta\boldsymbol{m}) > \Phi(\boldsymbol{m}) \end{cases} . \tag{5.26}$$

Eventually, many samples of $\boldsymbol{m}$ will have been generated, most densely in regions of high probability. Once sufficient samples are taken, the sample density will cease to change appreciably, and can be taken to represent the probability density. The GNU R package 'mcmc' provides an implementation of the Metropolis algorithm [143], which is used here.

So, if the Metropolis algorithm is started at the maximum likelihood point found earlier, and $p(\boldsymbol{m}|\boldsymbol{b})$ is close to Gaussian, around 68% of the realizations of $\boldsymbol{m}$ should fill the 68% confidence region. And, if $p(\boldsymbol{m}|\boldsymbol{b})$ is not Gaussian, it should be clear. Figure 5.4

[2] 'The Metropolis algorithm is known as a Markov Chain Monte Carlo method. 'Markov chain' means that each step in the random walk is independent of any previous steps, while the Metropolis algorithm was named 'Monte Carlo' by its original author due to the association of that city with random events.

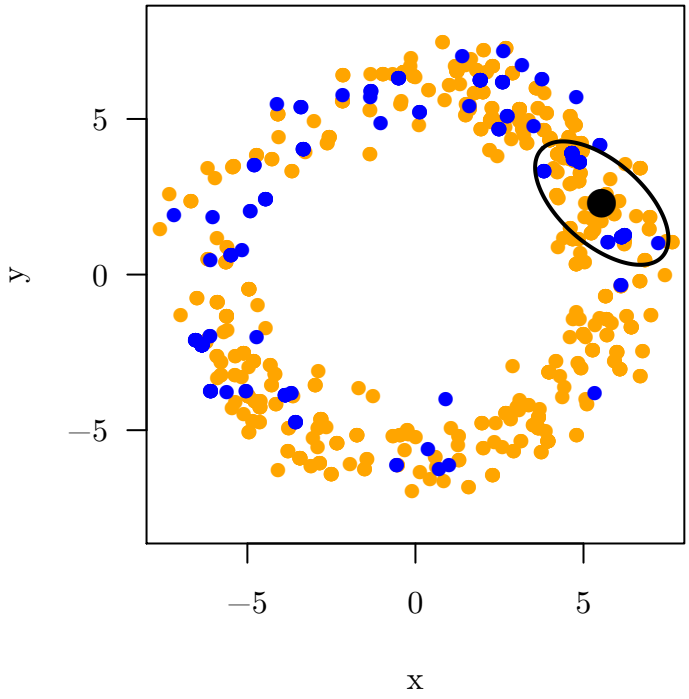

Figure 5.4: Example use of the Metropolis algorithm. In this example, a simple probability density $p = \exp(-(5 - \sqrt{(x^2 + y^2)}))$ was used. Starting from the black point, the Metropolis algorithm explores a region that extends far beyond the 68% confidence ellipse computed from the Hessian of $ln(p)$ at that point after 200 iterations (blue points). After a further 800 iterations, it has mapped out an annular region of high probability (orange points).

shows an example where the probability density in two parameters,

$$p(x, y) = \exp(-(r - \sqrt{(x^2 + y^2)^2}) \tag{5.27}$$

is maximal anywhere on a circle with radius $r = 5$. The Metropolis algorithm was started at $(x = r\cos(\pi/3), y = r\sin(\pi/3))$. After 200 iterations, it has explored an area much larger than the 68% confidence ellipse, while after 800 iterations an annular region of high probability has been mapped out. If neighbouring maxima in $p(\boldsymbol{m}|\boldsymbol{b})$ existed, they would be found in a similar manner.

5.3 Results

5.3.1 Steady-state

While the initial parameters, given in table 5.1, lead to a set of reflection and transmission coefficients which are in broad agreement with the observations, there are discrepancies. Figure 5.5 shows both the modelled and measured transmission coefficients T_{ps}, varying with incident angle and applied voltage. At each voltage, the modelled curve is modulated

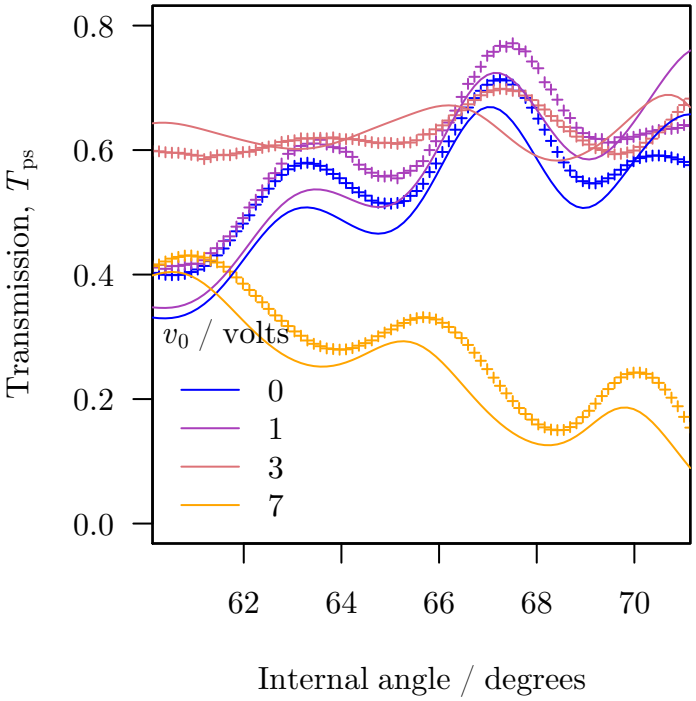

Figure 5.5: Comparison between modelled and measured transmission T_{ps}, before any kind of optimization. Although the broad trends are the same in both the model (solid curves) and data (crosses), there is considerable discrepancy between them. Clearly, there is some room to improve the model.

at a similar frequency to the observations, and follows a similar broad trend. However, modulations in each modelled curve are somewhat out of phase with those apparent in the measurements. There is also a systematic difference of about 0.05 between each pair of corresponding curves. In other words, while the initial parameters are a reasonable first guess, there is room for optimization.

5.3.1.1 Weakly-constrained tilt profiles

When seeking the ground state director profile, the nature of the Gauss-Newton iterations changes dramatically as the regularization parameter, λ, is varied. Figure 5.6 plots the size of each step, $||\delta \boldsymbol{m}||_2$ as the iterations progress, while figure 5.7 plots the discrepancy between the data and the model, represented by the residual norm $||\boldsymbol{f}(\boldsymbol{m}) - \boldsymbol{b}||_2$. When λ is large $||\delta \boldsymbol{m}||_2$, is rather small, and decays slowly, while the residual norm also decays slowly. As λ is decreased, large steps are taken to begin with, and their size decays more rapidly. Likewise, the residual norm decays quickly. However, as $\lambda \to 0$ the Gauss-Newton iterations misbehave: the step size remains approximately constant, while the residual norm oscillates.

Provided the Gauss-Newton iterations are well-behaved, decreasing λ normally leads to

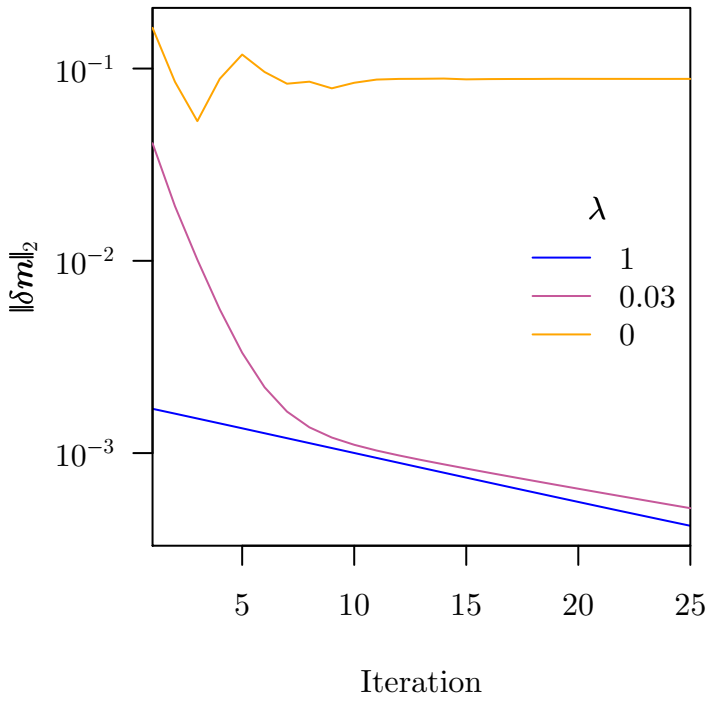

Figure 5.6: Plot of the length of the Gauss-Newton step, $||\delta \boldsymbol{m}||_2$, against iteration number, when seeking the ground state director profile. When the regularization parameter λ is large enough, the size of the Gauss-Newton step decays with each iteration. Otherwise, it remains roughly constant.

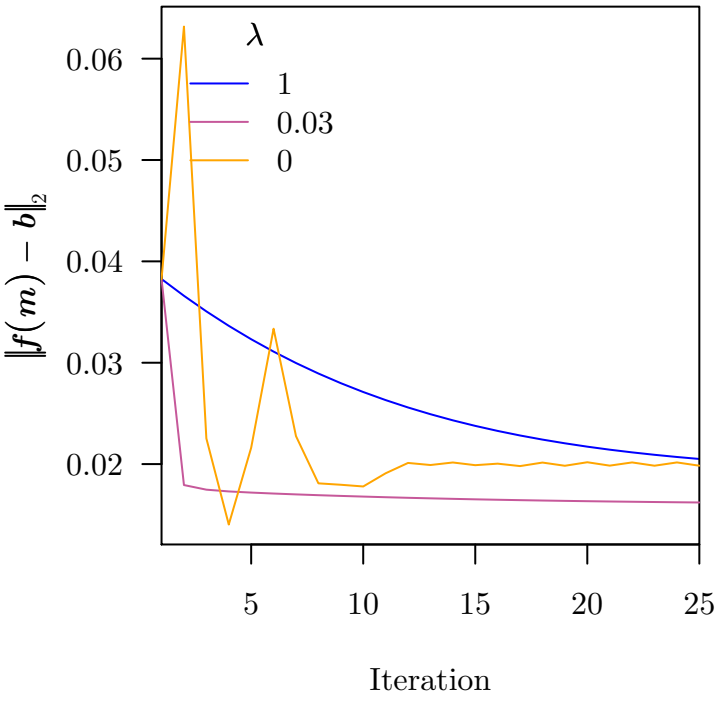

Figure 5.7: Plot of the residual norm, $||\boldsymbol{f}(\boldsymbol{m}) - \boldsymbol{b}||_2$, against iteration number. Without regularization ($\lambda = 0$), the discrepancy between the model and data oscillates around some fixed value. With regularization, the discrepancy decays, but more rapidly when λ is smaller.

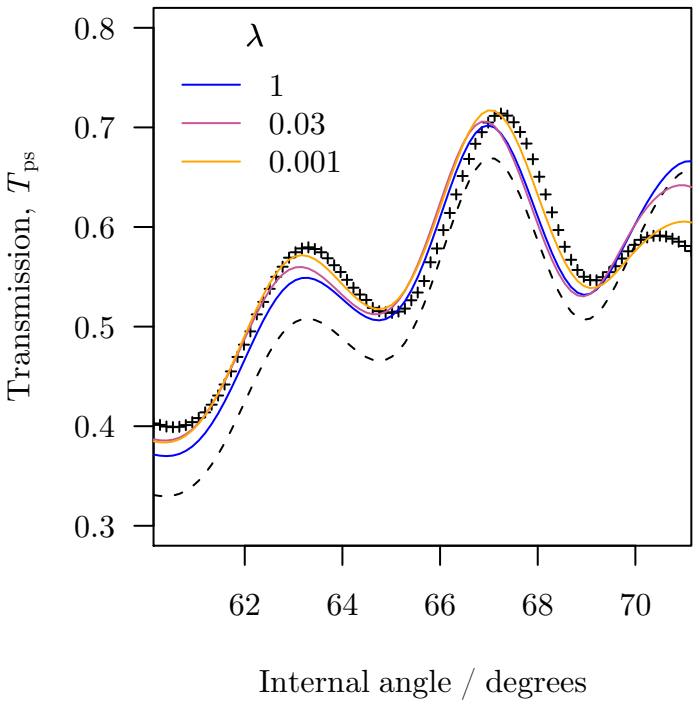

Figure 5.8: Comparison of model against data, for different values of λ. As λ is decreased, the agreement between data (crosses) and model (solid curves curves) is incrementally improved over the initial guess (dashes).

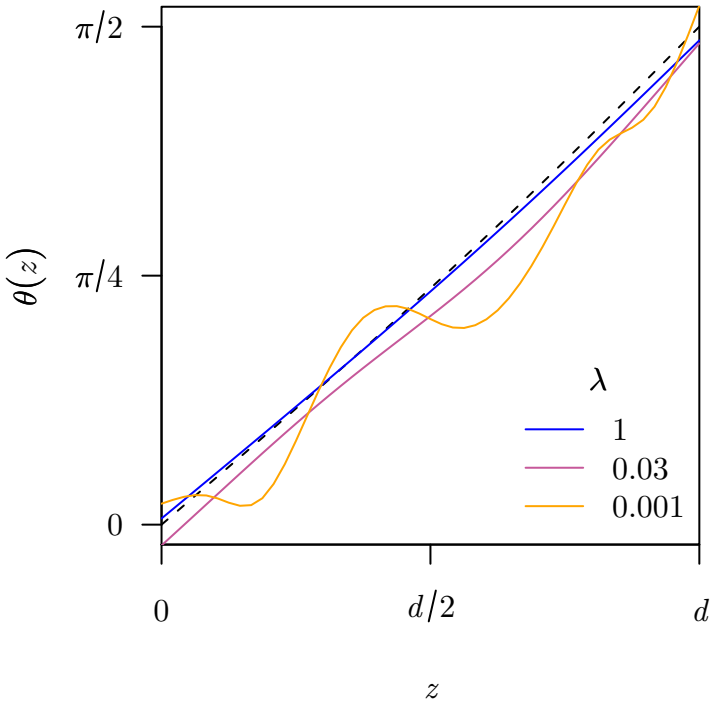

Figure 5.9: Weakly-constrained ground state tilt profiles, computed as λ is varied. When λ is not too small ($\lambda = 1$, $\lambda = 0.03$), realistic tilt profiles , different from the initial guess, are computed. If the solution is not regularized sufficiently ($\lambda = 0.001$), spurious oscillations start to dominate the solution

an improved match between model and data. Figure 5.8 illustrates this for the transmission coefficient T_{ps}. As λ is decreased, the model curves become progressively closer to the data. However, the smallest value of λ leads to a tilt profile which is unrealistic, as seen in figure 5.9. So a value of λ around 0.03 seems to give the best compromise between minimising the misfit between model and data and recovering a realistic tilt profile.

Looking at the tilt profiles computed at $\lambda = 0.03$, and at $\lambda = 1$ (figure 5.9), there are a few obvious departures from the initial guess. At the planar-treated surface, the pre-tilt angle is the same for both solutions: the director is close to, but not quite, planar. At the homeotropic surface, the situation is unclear, with the two solutions falling either side of $\theta = 0$. Remember though that the $\lambda = 0.03$ profile is in better agreement with the data. While the $\lambda = 1$ looks much like the initial guess, the $\lambda = 0.03$ profile curves rather more, which suggests that the assumed ratio k_{33}/k_{11} may be too small. A hint of an S-shaped modulation can be seen, which might be caused by the flexoelectric effect.

Having chosen $\lambda = 0.03$ (the smallest value that gives realistic tilt profiles), some additional observations can be made when an electric field is applied. Figure 5.10 shows a sequence of director profiles, calculated as the applied voltage is increased, compared with those in the unoptimized model. At the planar boundary, four out of the six profiles, at $v_0 \in 0, 1, 5, 7$ have a pre-tilt angle around $-4°$. At the homeotropic boundary, most of the profiles are close to $\theta = 0$. Finally, the distance between successive tilt profiles is very similar to those between the initial guesses. That indicates that the ratio ϵ_a/k_{11} is close to the value supplied by Merck.

Figure 5.11 shows the transmission coefficient T_{ps} computed for these weakly-constrained tilt profiles compared with the experimental data. Although there is still some discrepancy between model and data, it is much improved over the unoptimized results plottted in figure 5.5 and reproduced in the outset of figure 5.11. That there is some diecrepancy remaining suggests that some parameters should be optimized in addition to the tilt profiles. This will be considered as part of the strongly-constrained problem.

5.3.1.2 Strongly-constrained tilt profiles

Having examined the weakly-constrained tilt profiles, a set of parameters were chosen for optimization, with the remainder fixed. Table 5.4 gives a list of these parameters. Clearly, the pre-tilt angles, the dielectric anisotropy ϵ_a and one elastic constant, k_{33}, needed to be considered. As well as those, there is some uncertainty in the depth of the LC and ITO layers, the azimuthal angle at which the cell is mounted, and the angle between the cell and laboratory $z-$axis. Finally, the flexoelectric effect is included in the model, with an initial estimate for $(e_s - e_b)$ of 10 pCm^{-1} - a similar value to that measured for E7 [65].

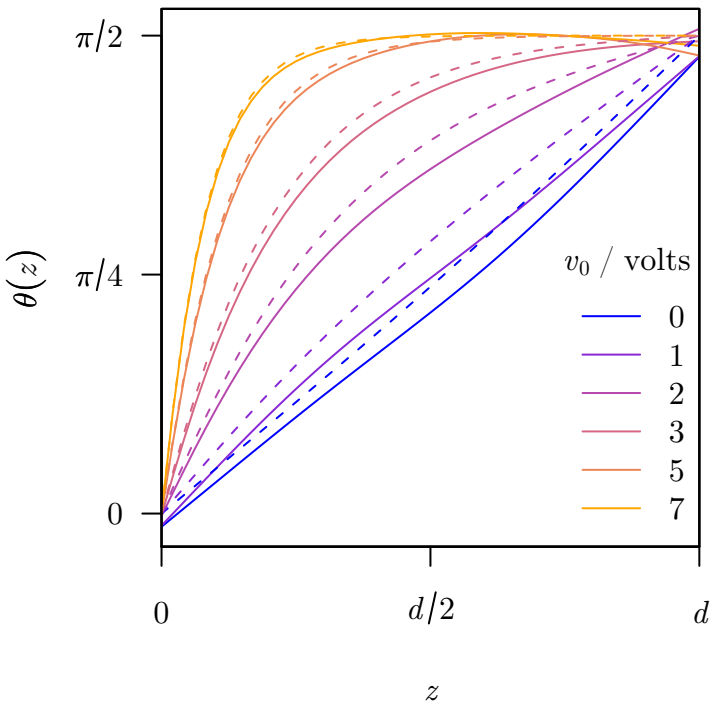

Figure 5.10: Weakly-constrained steady-state tilt profiles, computed for several applied voltages. The difference between the initial guess (dashes), and the weakly constrained tilt profiles(solid curves) is quite pronounced, particularly at low voltages.

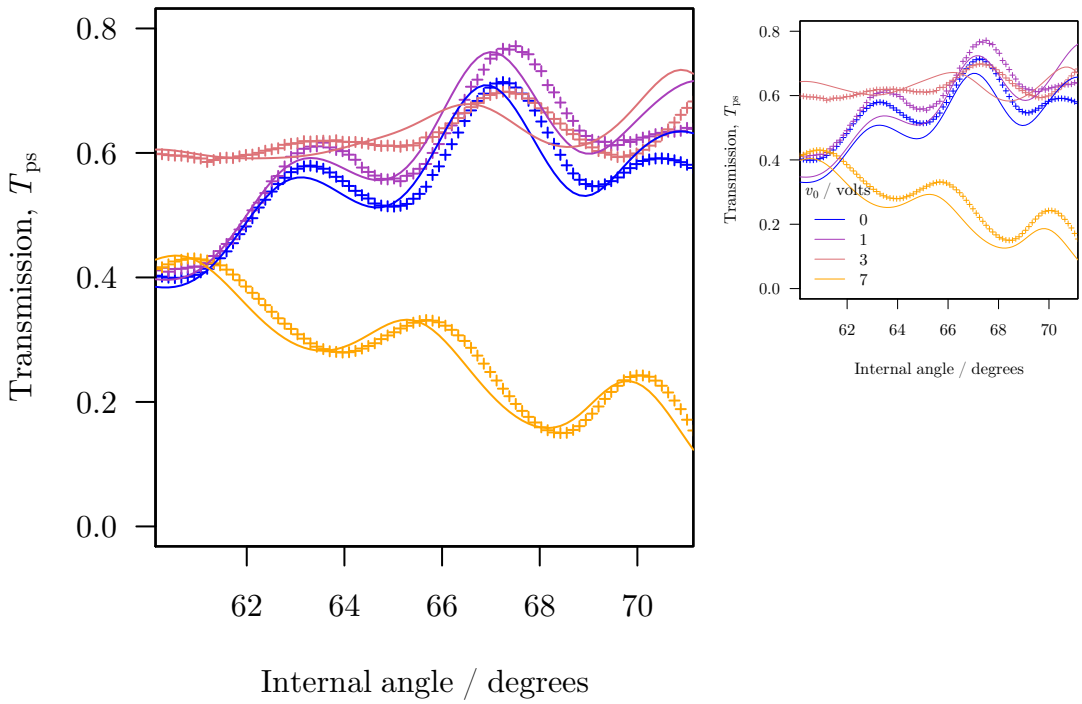

Figure 5.11: Comparison between modelled and measured transmission T_{ps} for the weakly-constrained tilt profiles. Agreement between the initial guess (dashes), and the weakly constrained tilt profiles (solid curves) is improved at all voltages compared with the initial model (figure 5.5 and reproduced in the outset).

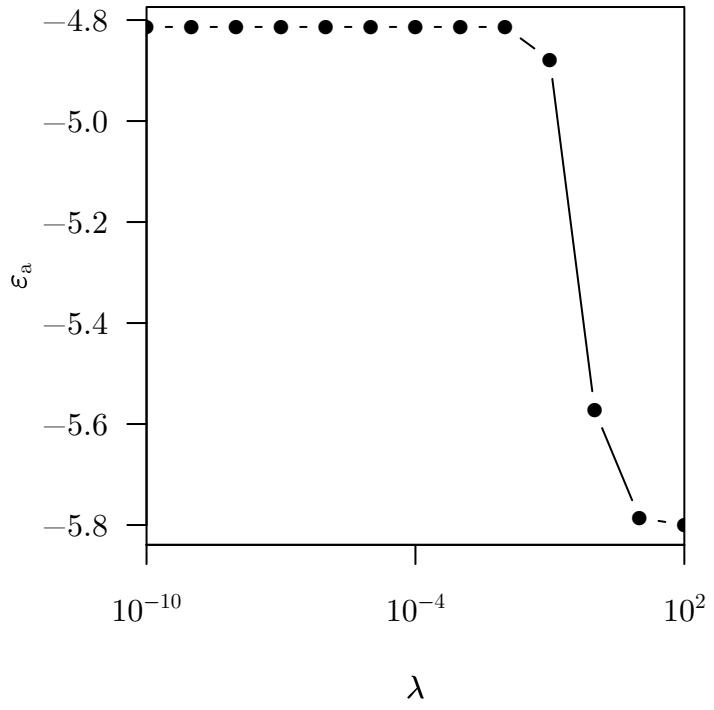

Figure 5.12: Variation of the estimated dielectric anisotropy ϵ_a with the regularization parameter λ. As λ decreases, ϵ_a converges on the value -4.81.

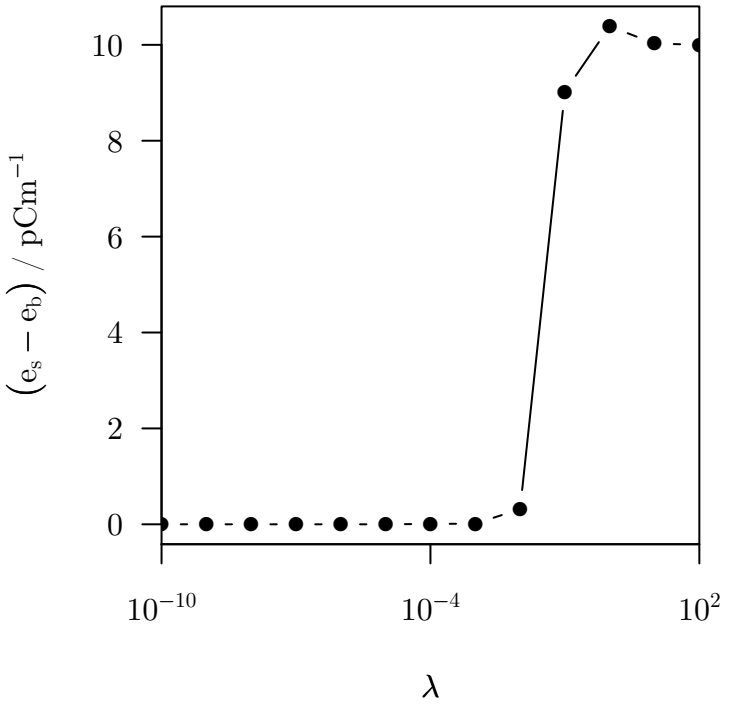

Figure 5.13: Variation of the estimated flexoelectric coefficient $(e_s - e_b)$ with the regularization parameter λ. As λ decreases,$(e_s - e_b)$ converges on 0.

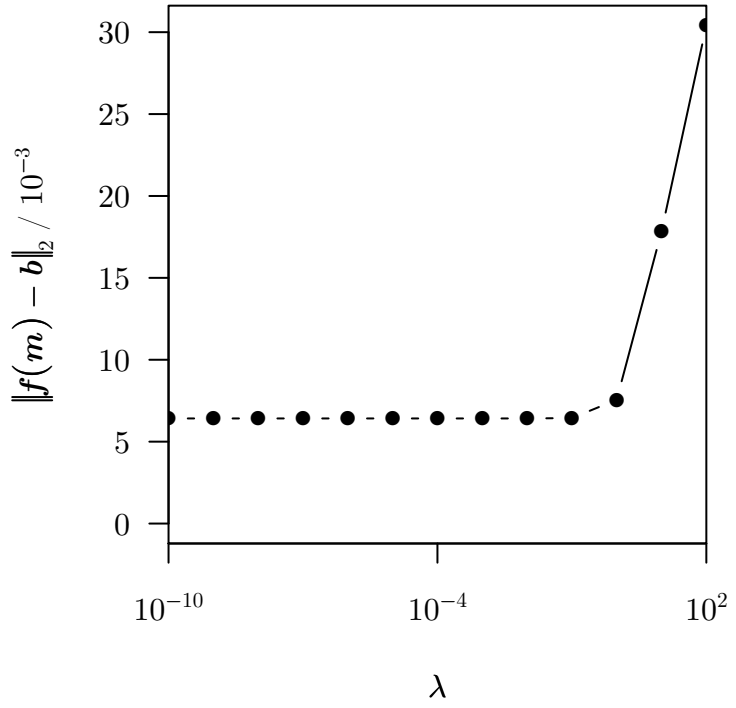

Figure 5.14: Variation of the residual norm $||\boldsymbol{f}(\boldsymbol{x}) - \boldsymbol{b}||$ with the regularization parameter λ. As λ decreases, so does $||\boldsymbol{f}(\boldsymbol{x}) - \boldsymbol{b}||$, decaying by a factor of 5 to converge on 6×10^{-3}.

A sequence of strongly-constrained inverse problems, varying the regularization parameter λ, were solved. Figure 5.12 shows the rapid convergence of estimated dielectric anisotropy ϵ_a on the value -4.81 as λ decreases, down to $\lambda = 10^{-10}$: at values lower than that, the Gauss-Newton iterations diverged. Similar decay is seen for the flexoelectric coefficient $(e_s - e_b)$ in figure 5.13, and for the residual norm, $||\boldsymbol{f}(\boldsymbol{x}) - \boldsymbol{b}||$, in figure 5.14. That rapid convergence demonstrates that the use of a small, finite λ does not affect the estimates significantly, and simply stabilises the Gauss-Newton iterations.

Those phenomenological parameters found by solving the strongly-constrained problem are given in table 5.4. In particular, there is a pre-tilt of $-2.4°$ at the planar surface, slightly smaller than the value anticipated by the weakly-constrained tilt profiles. The error in the tilt angle, $\Delta\theta$, might be seen as a rather arbitrary parameter: in fact it addresses a discrepancy between the high voltage tilt profiles (which must be close to $\pi/2$ in much of the bulk), and the observations. Both k_{33} and ϵ_a are different from the initial values, so that that the LC responds less readily to an applied field. Notice that the flexoeelectric difference $(e_s - e_b)$ vanishes, a matter which will be discussed in more detail in chapter 6.

Figure 5.15 shows the strongly-constrained tilt profiles, computed for several applied voltages. As in the weakly-constrained case, these tilt profiles generally lie below those computed with the given set of LC parameters. Primarily, this is due to the pre-tilt at

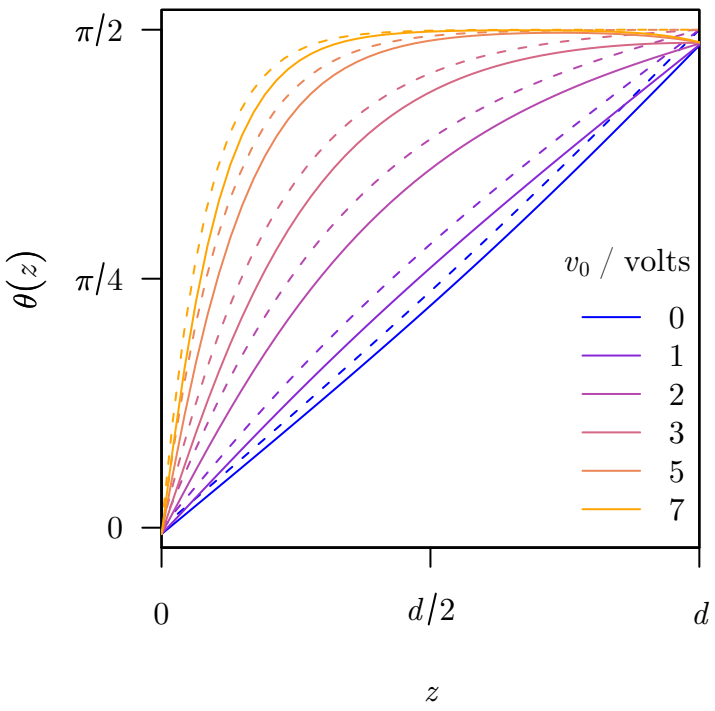

Figure 5.15: Strongly-constrained steady-state profiles, computed for several applied voltages. As in the weakly-constrained case, the difference between the initial guess (dashes) strongly-constrained tilt profiles (solid curves) is clear.

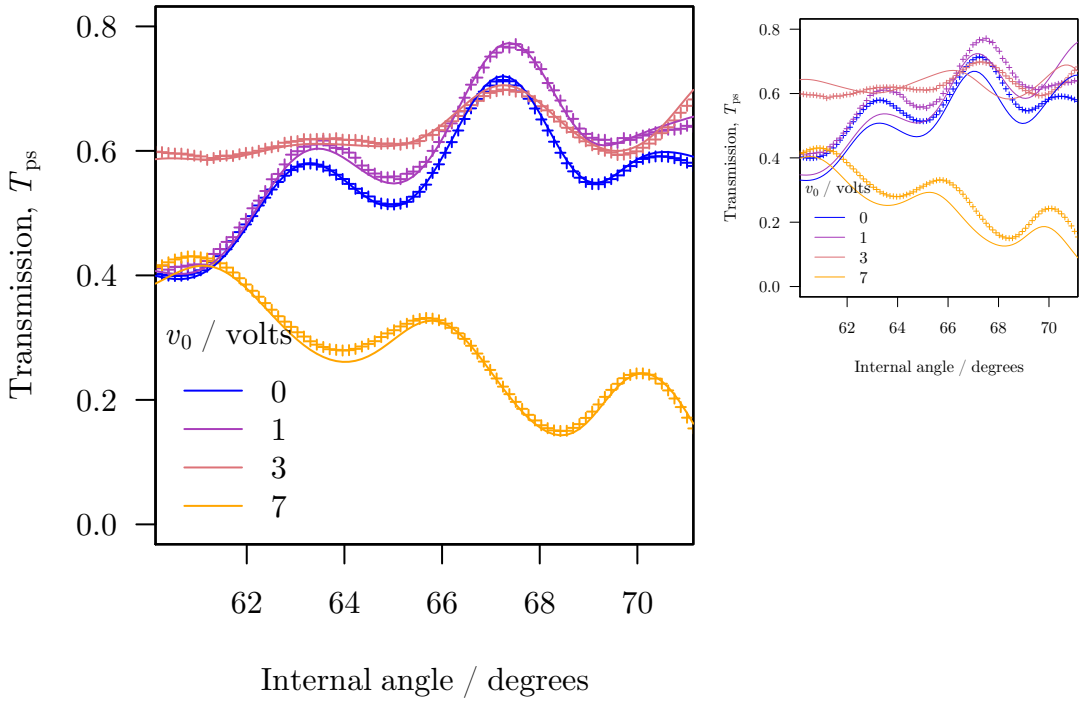

Figure 5.16: Comparison between modelled and measured steady-state transmission T_{ps}, for strongly-constrained tilt profiles. Now the model and data are in close agreement, much more so than in the initial model (figure 5.5 and reproduced in the outset).

Parameter	Symbol	Estimated value	Error
Refractive indices	$n_\perp$	1.4896	± 0.0002
(at 632.8 nm)	$n_\parallel$	1.6565	± 0.0009
Dielectric anisotropy	ϵ_a	-4.8	± 0.4
Elastic constants	k_{11}	13.7 pN	—
	k_{33}	20.9 pN	± 0.7 pN
Flexoelectric difference	$(e_s - e_b)$	10 pCm^{-1}	$\pm < 0.1$ pCm^{-1}
Pre-tilt at $z = 0$	θ_0	$-1.2°$	$\pm 0.4°$
Pre-tilt at $z = d$	θ_d	$-2.4°$	$\pm 0.2°$
Error in azimuthal angle	$\Delta\psi$	$0.4°$	$\pm 0.2°$
Error in tilt angle	$\Delta\theta$	$-0.6°$	$\pm 0.2°$
LC layer thickness	d	3.014 μm	± 5 nm
ITO layer thickness	d_{ITO}	25.2 nm	± 0.2 nm

Table 5.4: Values of LC and cell parameters estimated by solving a steady-state, strongly-constrained inverse problem. Note that k_{11} is fixed at its initial value, but is included for comparison with k_{33}.

the planar surface - as indicated by the weakly-constrained profiles. In contrast with the weakly-constrained case, the tilt profiles lie some distance below the initial guesses even at the highest voltages (because the ratio ϵ_a/k_{33} is smaller).

The modelled and measured transmission and reflection coefficients are in even closer agreement than they were in the weakly-constrained results. That must be due to the small changes in parameters such as LC layer thickness, which were fixed in the earlier results. In figure 5.16, the only clear differences between the model and data are to be found at the extreme ends of the angle range, and in the $v_0 = 7$V curve near around 64°. Overall, the fit between experiment and the model, as represented by the residual norm, has improved by a factor of 5 over the initial guess.

5.3.1.3 Error analysis

The error estimates listed in table 5.4 were given by the diagonal of a covariance matrix calculated from the Jacobian of $\boldsymbol{f}$. Error ellipses, derived from the off-diagonal components are plotted in figures 5.17 - 5.20. On each graph, the scale is chosen so that the major axis of the ellipse is inclined at $\pm\pi/4$ with respect to the horizontal. Strong correlation in the uncertainty of two parameters is indicated by an eccentric ellipse, independence by a circle. While errors in k_{33} and ϵ_a are strongly correlated with each other (figure 5.17), they are independent of optical parameters, for example the layer thickness (figure 5.18). In their turn, optical parameters, such as the refractive indices and the layer thickness are correlated with each other (figure 5.19 and figure 5.20).

The results of the Metropolis algorithm indicate that in most cases, the picture of uncertainty given by the covariance matrix is adequate. In each of figures 5.17, 5.18 and 5.19, the bulk of the samples fill the inside of the ellipses. Figure 5.20 clearly represents

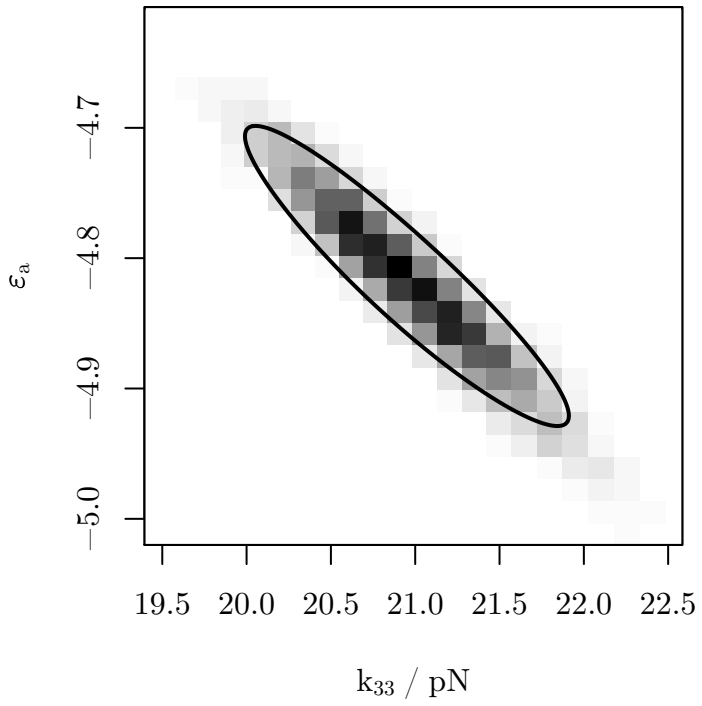

Figure 5.17: Correlation of the uncertainty in k_{33} and ϵ_a. k_{33} and ϵ_a are strongly correlated, so the major axis of the error ellipse (solid curve) is far longer than the minor axis. The sample density found by the Metropolis algorithm (grey-scale squares) are concentrated within the error ellipse, and fill it.

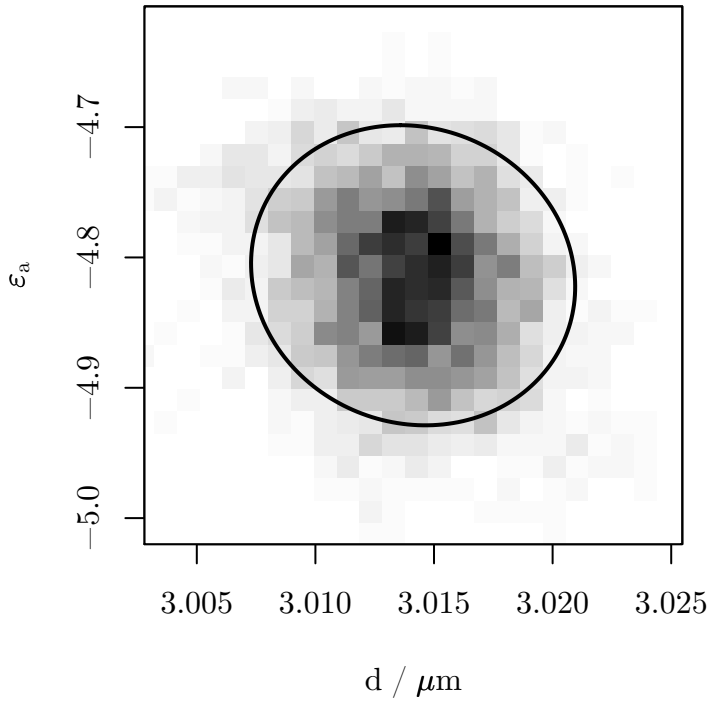

Figure 5.18: Correlation of the uncertainty in d and ϵ_a. These parameters are only weakly correlated, so the axes error ellipse is nearly circular.

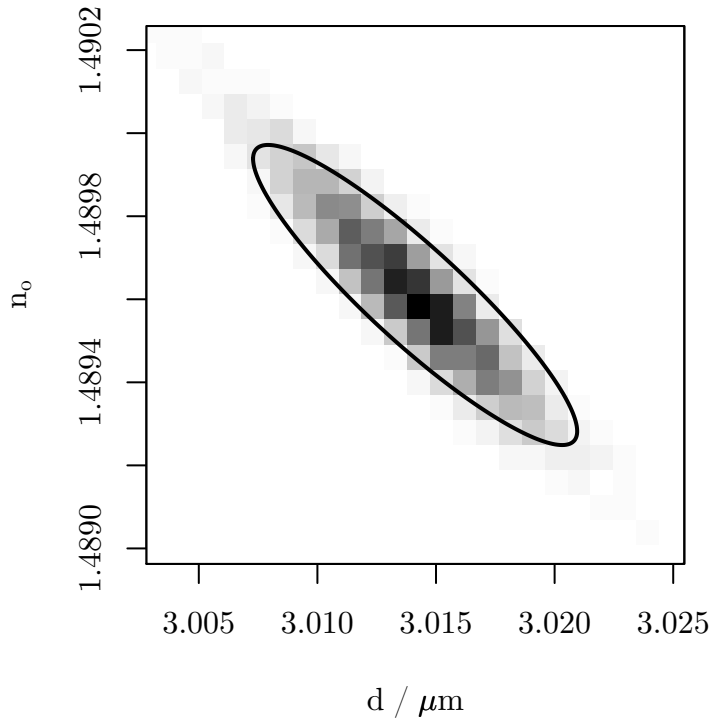

Figure 5.19: Correlation of the uncertainty in d and n_0. Once more, strong correlation is indicated by an eccentric ellipse.

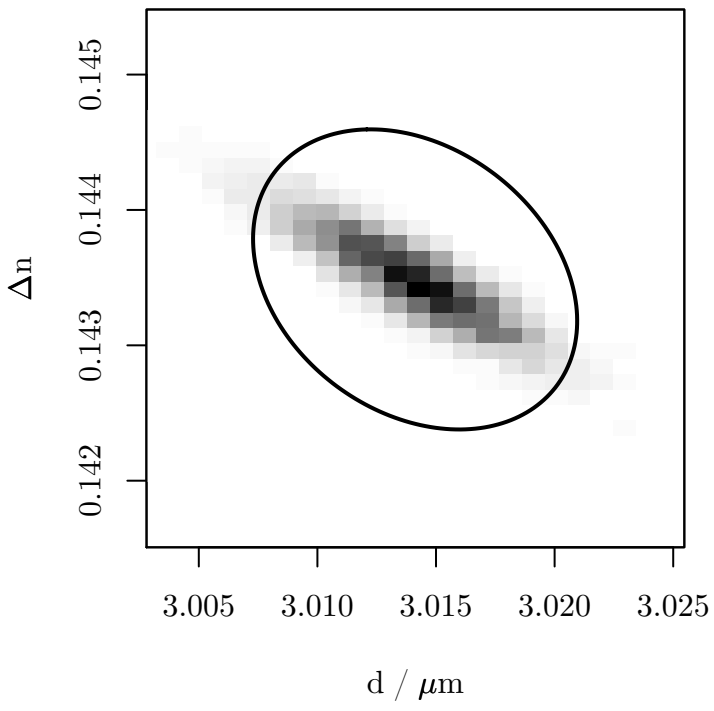

Figure 5.20: Correlation of the uncertainty in d and Δn. The Metropolis sample are concentrated within the error ellipse but do not fill it. The simpler description underestimates the correlation between these parameters.

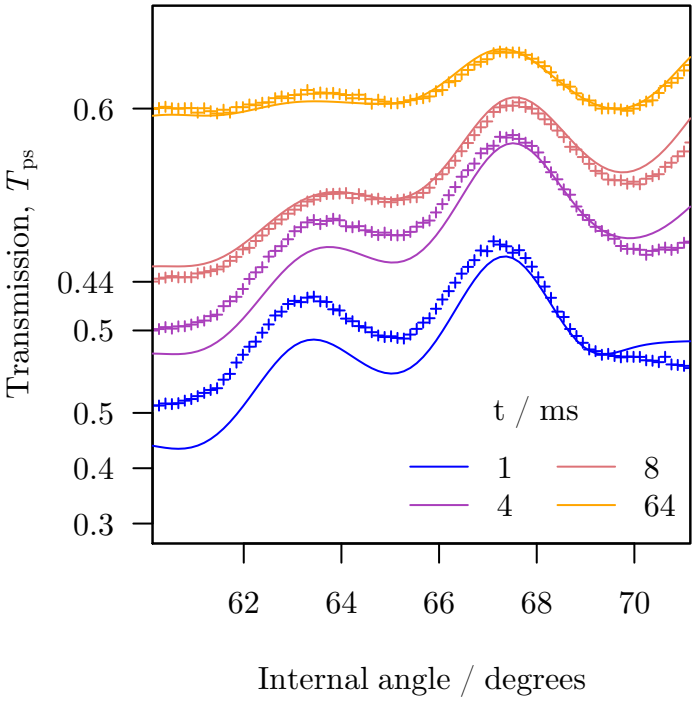

Figure 5.21: Comparison between modelled and measured dynamic transmission T_{ps}, prior to any kind of optimization. Each set of data corresponds to a snapshot of the cell during it evolution from the ground state to the $v_0 = 3$V steady state. Shear flow is neglected in the computation of the tilt profiles. Early on, there are significant differences between the model of data.

an exception. While axes of the sample density are parallel to the axes of the ellipse, the decay along the minor axes is much quicker than would be expected from the covariance matrix. That means that while the model depends near-linearly on one combination of d and Δn, it depends on some higher power of the other. This failure is quite mild though - the simple description tends to underestimate the correlation, but overestimate the uncertainty.

5.3.2 Dynamics

Once the parameters which affect the cell in steady-state are known, it is possible to study its AC dynamics. Specifically, the detailed evolution of the cell after an external field is applied or removed can be measured. Figure 5.21 shows a sequence of T_{ps} measurements. Each set of data corresponds to a snapshot of the cell during its evolution from the ground state to the $v_0 = 3$V steady state. Plotted alongside the data are computations of T_{ps} made using the set of parameters determined previously and the value of γ_1 supplied by Merck, and neglecting shear flow.

There is a clear, systematic difference between the model and the data at this stage,

which is largest just after the field is applied. Overall, the cell seems to be evolving more rapidly than expected, which might simply mean that the rotational viscosity is smaller than the supplied value. In this section, a set of weakly-constrained tilt profiles will be found, and will show that something more complex - the backflow effect - must be taken into account. That will lead on to a strongly-constrained inverse problem, which allow four of the five independent Leslie viscosities to be estimated.

5.3.2.1 Weakly-constrained problem

Figure 5.22 shows a set of tilt profiles, found by solving a weakly-constrained problem. To this end, the full regularization matrix, described in 5.2.1.4, was used. Because parameters such as the LC layer thickness are now known, the regularization parameter may be set to a lower value than in the steady-state case: here it was set to $\lambda = 5 \times 10^{-3}$. The misfit between the model and the data is reduced by a factor of 4.5, from 3.1×10^{-2} to 6.8×10^{-3} overall, and by a larger factor at earlier times, for example 7.2 at $t = 1$ ms. A clear improvement in the match between experimental and theoretical T_{ps} is seen by comparing the main figure of figure 5.23 with its outset reproduced from figure 5.21.

There are some notable differences between the weakly-constrained tilt profiles and the initial profiles. Director rotation near the homeotropic end of the cell is faster than at the mid-plane,and slower at the homogeneous end. Consequently, non-equilibrium tilt profiles curve toward $\theta = \pi/2$ between $z = 0$ and the mid-plane, and toward $\theta = 0$ between the mid-plane and $z = d$. The distinctive shape of the director is reminiscent of the backflow effect, where a flow field induced by the rotation of the director acts to speed up re-alignment in some parts of the cell, and slow it down in others. This is an important test, showing that the solution to the weakly-constrained inverse problem can differ from the solution to the simplified equations used to regularize it.

Although inclusion of the viscous term in (5.10) is a little more expensive computationally, it helps to suppress unphysical tilt profiles. The weakly-constrained tilt profiles computed when it is neglected (figure 5.24) are indicative of the backflow effect, much as before. But, around $z = 3d/4$, the $t = 4$ ms and $t = 8$ ms profiles overlap. Such as feature isn't known from Ericksen-Leslie theory, but perhaps it is a genuine anomaly revealed by the experiment? Comparing the residual norm in both cases suggests not. Neglecting the viscous term (essentially relaxing the constraints a little) does lead to a smaller residual norm - 6.4×10^{-3} compared with the earlier figure of 6.8×10^{-3} - but not by a significant amount. It is difficult to decide which match is the better by eye - see figure 5.23. Even considering the $t = 4$ ms profiles (which differ most) alone, the improvement to residual norm is tiny - 7.8×10^{-3} compared with 8.3×10^{-3}. Therefore, it seems that the new

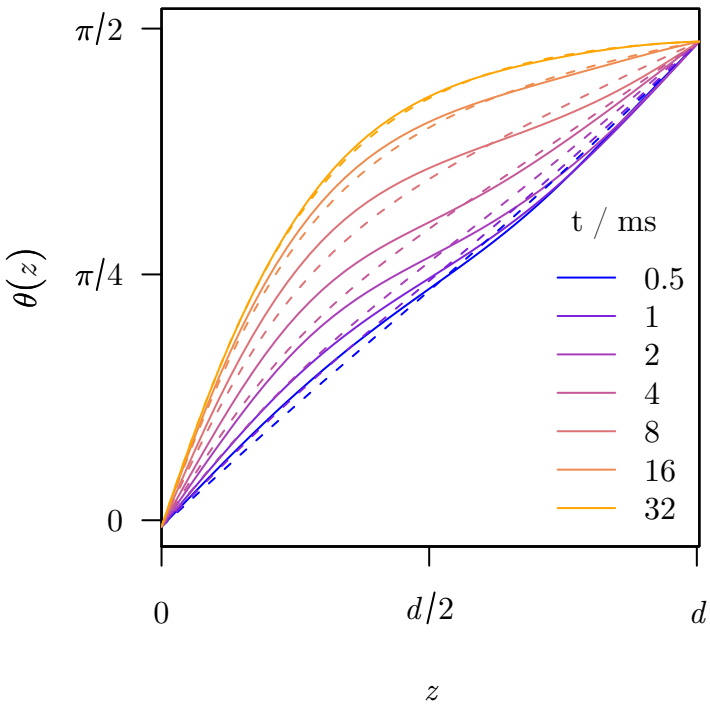

Figure 5.22: Weakly-constrained, unsteady tilt profiles, computed when the viscous term is included in the regularization matrix. Compared to the initial guess (dashes), the weakly-constrained tilt profiles have a quite different shape. Between $z = 0$ and the mid-plane, the profiles curve toward $\pi/2$, while they curve toward $\theta = 0$ between the mid-plane and $z = d$.

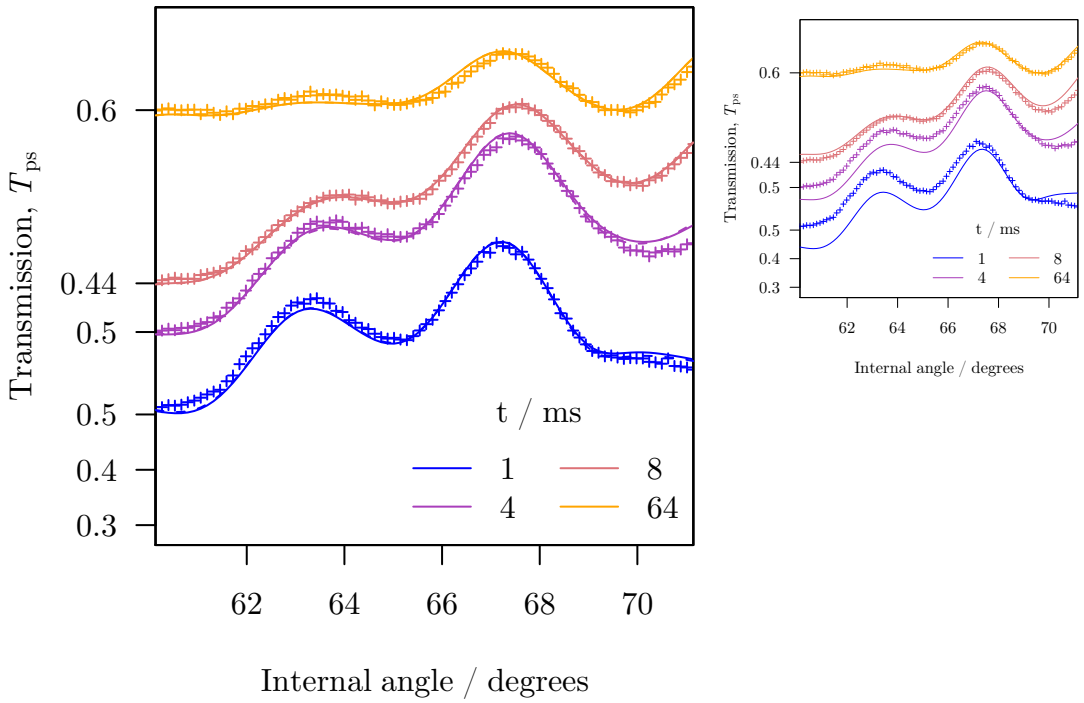

Figure 5.23: Comparison between modelled and measured dynamic transmission T_{ps}, for weakly-constrained tilt profiles. The solid lines are computed from tilt profiles found when the full regularization matrix was used, while the dashed lines were found when the viscous term was neglected. Both are much closer to the data (crosses) than the initial model, shown in figure 5.21 and reproduced in the outset.

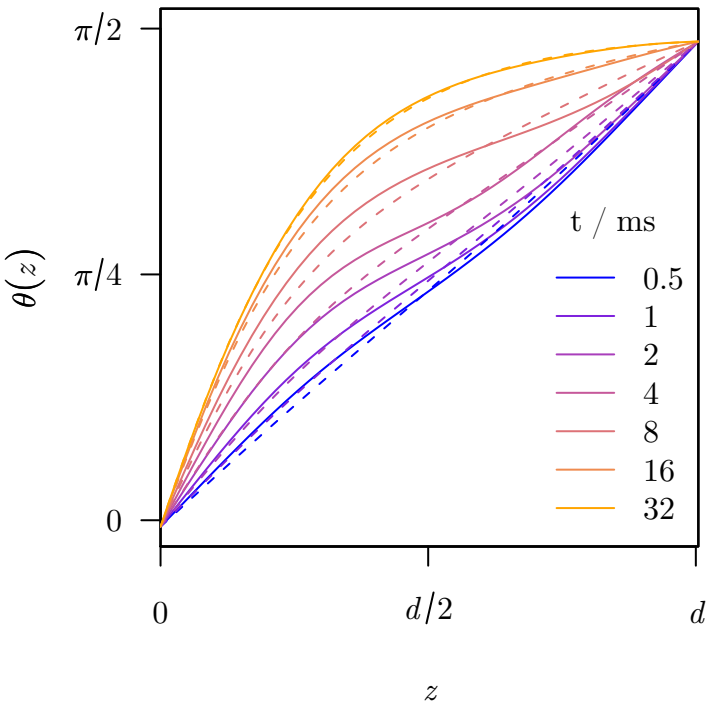

Figure 5.24: Weakly-constrained, unsteady tilt profiles, computed when the viscous term is neglected in the regularization matrix. Once more, the weakly-constrained tilt profiles (solid curves) are suggestive of the backflow effect when contrasted with the initial profiles (dashes). However, a spurious feature is present - the $t = 4$ ms and $t = 8$ ms profiles overlap.

feature is spurious, and the viscous term should be included.

5.3.2.2 Strongly-constrained problem

Since the weakly-constrained tilt profiles are suggestive of the backflow effect, this was explored by solving two strongly-constrained problems. In the first problem, shear flow was neglected to decide whether a set of tilt profiles uninfluenced by the backflow effect could account for the observations. The only important parameter was the rotational viscosity, γ_1. In the second problem, shear flow was included, and optimal values for four Leslie viscosities found. For both problems, observations made as the cell was switched on and off were included.

The experimental data cannot be explained if shear flow is neglected in the Ericksen-Leslie equations. A strongly-constrained inverse problem was solved, seeking a value for γ_1 which gives the best fit to the experimental data. At the optimum value $\gamma_1 = 215$ mPa s, the overall residual norm has only improved a little, from 2.2×10^{-2} to 1.9×10^{-2}. Most of this improvement occurs later on in the evolution, where the weakly-constrained profiles do not curve so much. This is illustrated in figure 5.25, where agreement between model and data is better than in the initial model at $t \geq 8$ ms, at earlier times it has hardly

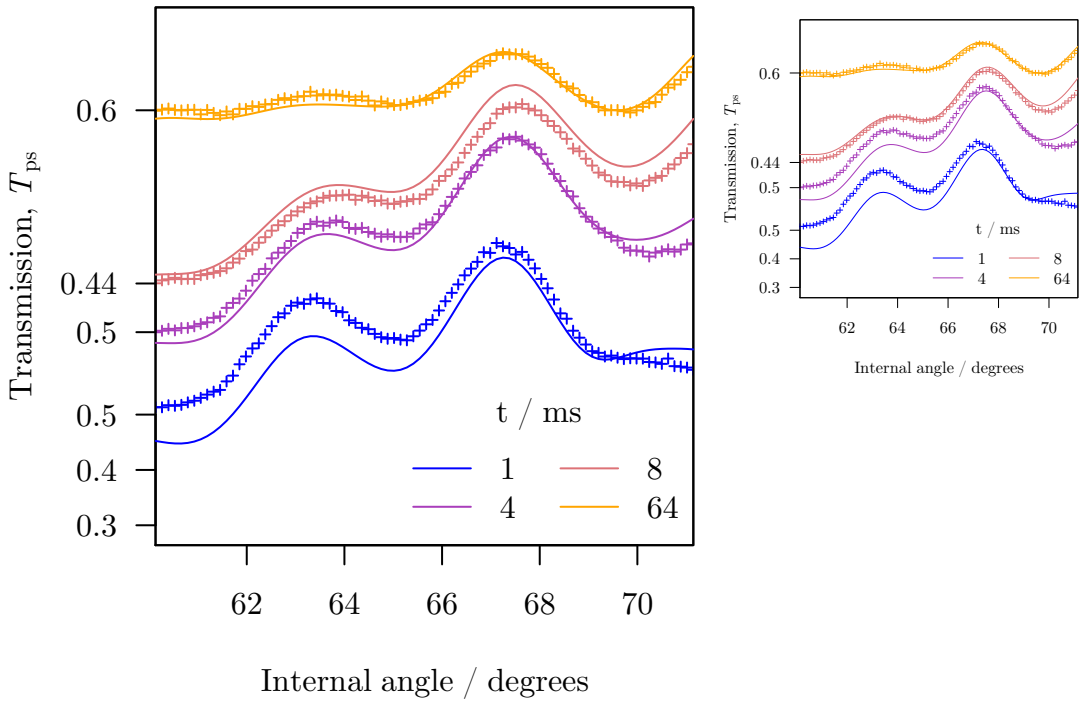

Figure 5.25: Comparison between modelled and measured dynamic transmission T_{ps}, for strongly-constrained tilt profiles neglecting shear flow. Although the fit at $t \geq 8$ ms is improved, at earlier times it is little better than in the initial model (figure 5.21 and outset).

improved at all . So, although the overall rate of evolution has been optimised, the detailed tilt profiles must be quite different.

Including shear flow in the model improves the situation, even prior to any optimization. When the initial values, given in the second column of table 5.5 are used, a weak backflow effect is predicted, resulting in tilt profiles that have a similar shape to the weakly-constrained profiles. Data and model are in better agreement than in the previous case, with an overall residual norm of 1.5×10^{-2}.

Once the Leslie viscosities have been optimised, the strongly-constrained tilt profiles resemble the weakly-constrained profiles closely. The two are plotted together in figure 5.26. At no point do they differ by more than $\theta = 0.04$, that is by more than 3°, while the average difference is around a quarter of that. Agreement between the model and the experiment is a factor of 2 better it was than for the initial viscosities, with an overall residual norm of 7×10^{-3}. In particular, there is now a good match at early times, which was not the case when shear flow was ignored. This can be seen clearly in figure 5.27.

A list of the optimal viscosity coefficients is given in the third column of table 5.5. The rotational viscosity, γ_1 is similar to the value supplied by Merck: the difference might simply be due to performing the experiment at a lower ambient temperature -

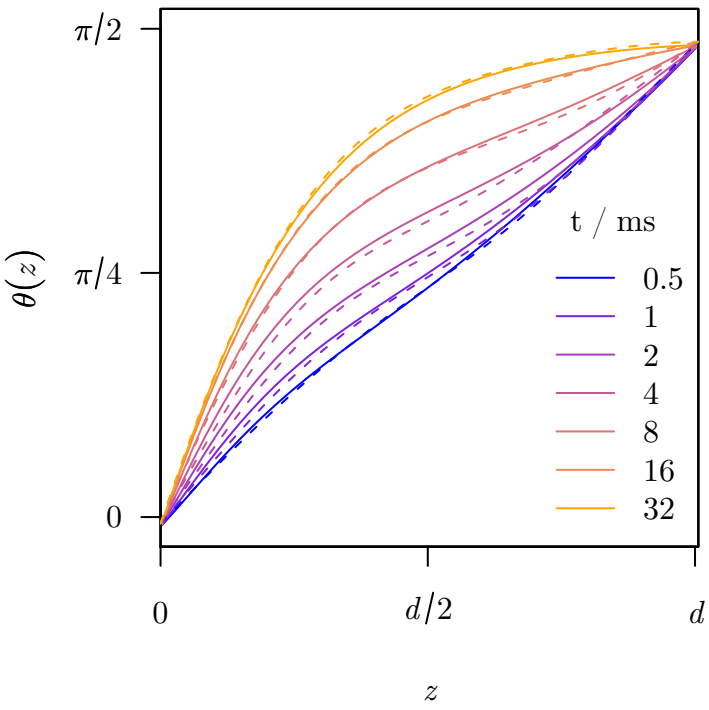

Figure 5.26: Strongly and weakly -constrained time-dependent tilt profiles. The backflow effect influences the strongly-constrained profiles (solid curves), so that they resemble the weakly-constrained profiles (dashes).

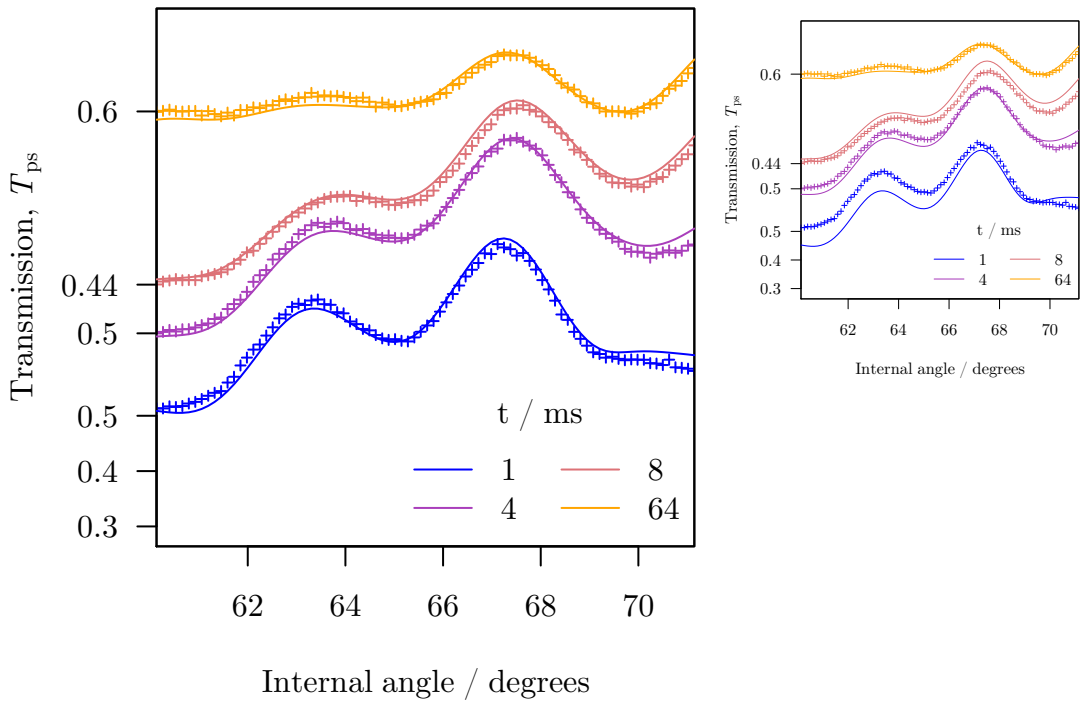

Figure 5.27: Comparison between modelled and measured dynamic transmission T_{ps}, for strongly-constrained tilt profiles including shear flow. Now the data (crosses) and model (solid curves) fit closely, and at all times. The match is much improved over the earlier model, where shear flow was neglected (figure 5.25 and outset).

Viscosity	Initial value / mPa s	Optimal value / mPa s	Error / mPa s
α_1	0	-24	± 30
α_2	-309	-360	± 8
α_3	0	9	± 8
$\alpha_4 + \alpha_5$	618	359	± 8
γ_1	309	369	± 6
γ_2	-309	-351	± 9
η_{12}	0	-24	± 30
η_1	464	360	± 8
η_2	155	9	± 10

Table 5.5: Initial and optimal values of the nematic viscosities. Optimal values were found by solving a strongly-constrained inverse problem. The Leslie viscosities are given in the upper part of the table, while the alternative Miesowicz viscosities are given in the lower part.

17° C as opposed to20° C . When measurements were taken at a higher temperature (23° C), the value of γ_1, obtained by the method described here, dropped to 302 mPa s [54]. Interestingly, $\alpha_4 + \alpha_5$ (and so η_2) is far lower than the initial value chosen by noting that $\alpha_4 \sim \alpha_5 \sim \gamma_1$ for several materials[3].

5.3.2.3 Error analysis

Simple estimates of the uncertainty in each of the viscosity coefficients are given in table 5.5. With the exception of α_1 the standard errors in each viscosity are similar, suggesting that the experiment is similarly sensitive to each. In the case of α_1, reduced sensitivity is not surprising: it enters the Ericksen-Leslie equations through a term multiplied by both $\sin^2\theta\cos^2\theta$ and the gradient of u_x. The first of these terms is largest near the centre of the cell, where the second vanishes.

Metropolis sampling suggests that the simple error estimates are of the correct size, or slightly too large. In each of figures 5.28 — 5.30, the sample density is largest at the centre of each error ellipse, and are concentrated within a similar area. In most cases, of which figure 5.28 is typical, there is close agreement between the simple estimate and the Metropolis calculation. There are exceptions. In figure 5.29, the sample density decays more rapidly as α_1 and γ_1 decrease together than it does as they grow together. And in figure 5.30, the Metropolis density decays more rapidly than expected, and is slightly-off axis. Once more, both of these disagreements are mild.

[3]Solving a strongly-constrained problem, with $\alpha_4 + \alpha_5$ restricted to large values simply did not fit with the data.

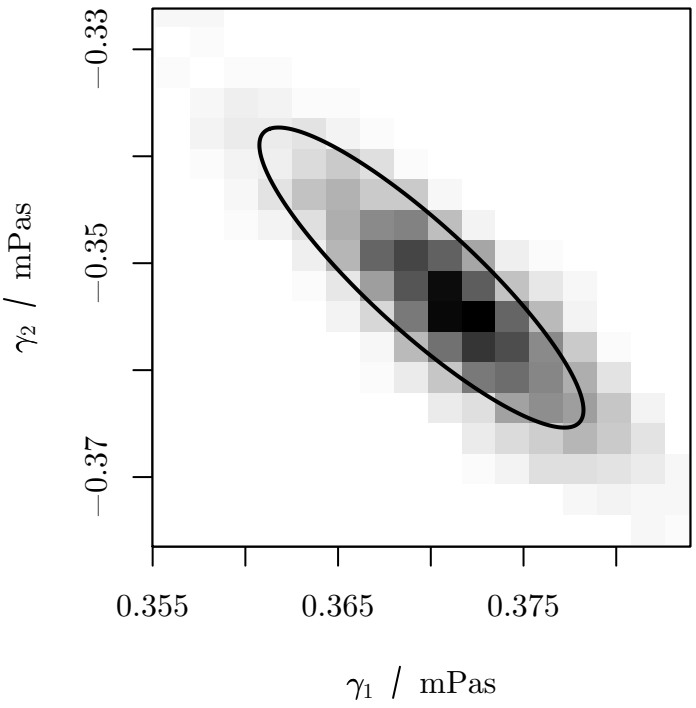

Figure 5.28: Correlation of the uncertainty in γ_1 and γ_2. The uncertainty in γ_1 and γ_2 is strongly correlated, as indicated by the eccentric error ellipse (solid curve). The size and shape of the error ellipse agrees well with a sample density found by the Metropolis algorithm (grey-scale squares).

5.4 Summary

The weakly- and strongly- constrained inverse problems described in this problem are complementary techniques which can quickly analyse the results of the full-leaky guided mode experiment. The solution to a weakly-constrained problem is a set of tilt profiles, found by making only mild assumptions about them. It is much easier to decide what is happening inside the cell by looking at these profiles, than by looking directly at the reflection and transmission coefficients. From there, the next step is to decide what kind of strongly-constrained problem to solve. Looking at the steady-state profiles, it was clear that finite pre-tilts had to be considered. When time-dependent data was examined, the shape of the tilt profiles indicated a small backflow effect, prompting estimation of the Leslie viscosities.

Solving the strongly-constrained problems leads to estimates for phenomenological constants, such as the dielectric anisotropy, and the nematic viscosities. As well as expected values, an estimate of the uncertainty in each parameter is found. A key assumption is made in those calculations: that the reflection and transmission coefficients depend on the phenomenological constants in a near linear fashion. This assumption was tested, and

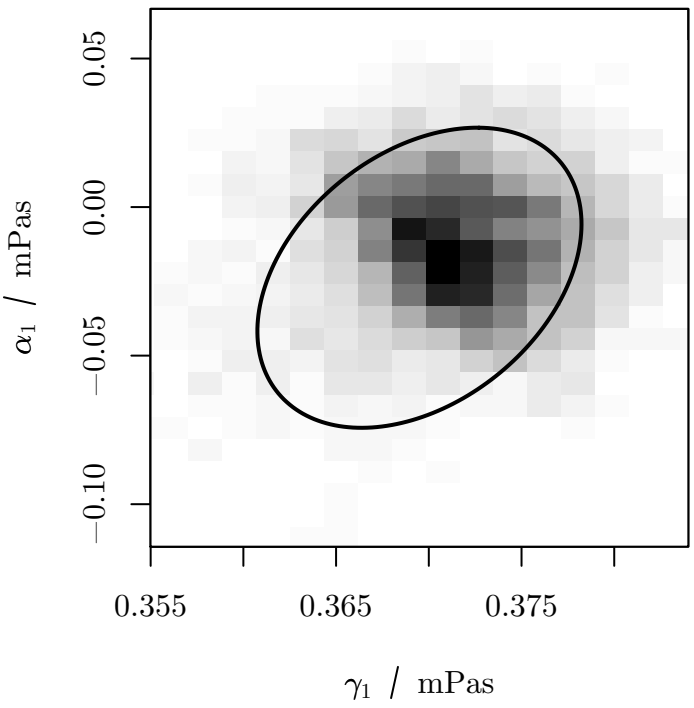

Figure 5.29: Correlation of the uncertainty in γ_1 and α_1. The uncertainty in α_1 is not as strongly correlated with that of the other viscosities as the uncertainty between other pairs. The Metropolis sample density decays more rapidly than expected when γ_1 and α_1 decrease together.

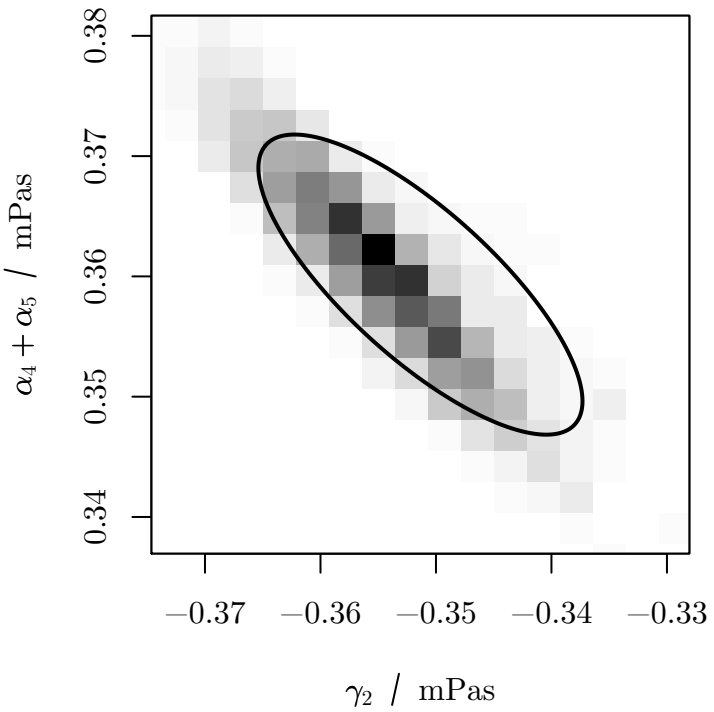

Figure 5.30: Correlation of the uncertainty in γ_2 and $\alpha_4 + \alpha_5$. While both the error ellipse and the Metropolis sample density show a similar, negative correlation in the errors in γ_2 and $\alpha_4 + \alpha_5$, the Metropolis density decays more rapidly than expected, and is slightly-off axis.

found to be broadly acceptable, by the use of the Metropolis algorithm. In particular, no surfaces of constant likelihood, or additional maxima were found.

Chapter 6

DC switching and ion drift in a HAN cell

6.1 Introduction

After completing the AC experiments described in the previous chapter, Taphouse [54] performed DC switching experiments on the same cell. The intention was simple - to measure the flexoelectric difference $(e_s - e_b)$ of ZLI-4788-000. Mazulla [81], and later Jewell [65], had already studied the equilibrium states of HAN cells filled with other materials with the fully-leaky guided mode experiment to this end. A cursory examination of Taphouse's data indicated that the cell was further from its ground state when the applied voltage (with respect to the planar surface) was negative than when it was positive, suggesting that $(e_s - e_b)$ was positive. Taphouse made time-dependent as well as steady-state measurements, which revealed transient behaviour over timescales far longer than expected. From these it was clear that, despite efforts during cell construction, charged impurities were present.

Mazulla's method, and indeed many other methods for the measurement of $(e_s - e_b)$ rely on the asymmetric director profile in a HAN cell [67, 66, 68, 64]. In contrast to a planar or homeotropic cell, the gradient of the tilt angle has the same sign through the entire depth of a HAN cell. Consequently, the flexoelectric polarization always points in the same direction, and there is a net polarization across the cell. When a DC voltage is applied across the cell, that polarization may oppose or enhance it, depending upon its sign. Thus, DC voltages of the same sign but different magnitudes produce different director profiles, and by measuring this sign dependence, $(e_s - e_b)$ may be found.

However, both Mazulla and Jewell found that the flexoelectric effect alone could not account for the sign dependence they observed. Had $(e_s - e_b)$ been as large as the sign

dependence suggested, the ground-state tilt profile would have been noticeably S-shaped. It was not, and so it was assumed that a surface polarization caused by preferential alignment of dipolar molecules at the homeotropic surface was responsible for a portion of the sign dependence.

Another possible source of sign dependence is ionic contamination. Some concentration of charged impurities are to be expected in any cell, through the breakdown of impurity molecules into ions [42, 38, 40]. These ions are mobile, and so can respond to electric fields. Modelling in this chapter shows that ions can drift to oppose the flexoelectric polarization in the ground state, suppressing the S-shaped tilt profile. They can also be adsorbed onto the cell surfaces. In a HAN cell, with its two different surface treatments, it is possible that this adsorption is asymmetric, so that an electric field is sustained across the cell, much like the surface polarization observed in the earlier experiments.

This chapter is a study of the complications caused by ionic contamination of the liquid crystal. Two drift-diffusion equations, one for positive ions, and one for negative ions, are added to the numerical model described in chapter 4. The interaction of mobile ions with the flexo-electric effect, and with ions adsorbed onto the cell walls is modelled both in steady-state and as the cell is switched. Comparing the model results with the experiment suggests that sign dependent switching in ZLI-4788-000 is dominated not by the flexoelectric effect, but by a surface effect. A secondary experiment confirms this by showing that sign dependent switching changes dramatically if the surfactant used to promote homeotropic alignment is changed.

6.2 Methodology

6.2.1 Experimental details

The main experiment described in this chapter was a fully-leaky guided mode experiment, performed by Taphouse. The same cell was used as in the previous chapter, so a great deal is already known about it. Measurements were made as a bipolar potential difference

$$v_0 = \begin{cases} 0, & t \leq 0 \\ +V, & 0 < t < \tau \\ -V, & \tau \leq t < 2\tau \\ 0, & t \geq 2\tau \end{cases} \tag{6.1}$$

was applied between the ITO electrodes, and repeated for several values of V. Note that v_0 is the potential of the homeotropic surface, at $z = 0$ relative to the planar surface at $z = d$. The time constant, $\tau = 250$ ms, is easily sufficient to allow the liquid crystal to

reach equilibrium at each stage when driven by alternating fields; that is, when viscous dissipation determines the relaxation rate.

A secondary experiment was also performed, by Cornford, to investigate further the results of the original experiment. Two HAN cells were built, differing only in the treatment used to provide the homeotropic surface. One employed the proprietary aligner also chosen in the earlier experiment. For the second, a polyimide, Nissan 1211, was spin coated onto the ITO coated glass substrate. Each cell was placed in turn between parallel polarizers, with the rubbing direction inclined at $\pi/4$ to the plane of polarization. The whole assembly was illuminated with a He-Ne laser, and a photo-diode used to measure transmission through it. A sequence of bipolar pulses of the form above was applied and measurements taken as a function of time.

6.2.2 Numerical model of ions in liquid crystal cells

A simple model of mobile charge carriers was added to the numerical model described in chapter 4. It was assumed that two ion species were present, one positively and one negatively charged[1]. The total space charge in the cell is zero, so that no electric field exists beyond the cell walls. Each species could be adsorbed onto the cells walls in arbitrary quantities, leaving an excess of surface charge density, σ, at the homeotropic surface. Meanwhile, a charge density $Q(z,t)$ is left in the bulk. Note that, although the cell is neutral,

$$\sigma + \int_0^d Q(z,t)dz \neq 0 \tag{6.2}$$

in general.[2]

6.2.2.1 Ions bound to the cell walls

Ions bound to the cell walls are accounted for by splitting the electric field into two contributions,

$$E = \frac{\sigma}{2\epsilon\epsilon_0} - \frac{\partial v}{\partial z}. \tag{6.3}$$

The first term is due to the difference, σ, in surface charge density between the cell walls, while the second term is due to the applied field, ions in the bulk, and the flexoelectric polarization. Since the first term contributes only a constant, $\sigma/2$, to the electric

[1] Actually, the capacity to model an arbitrary number of species was added to the code, but only two species are considered in this chapter

[2] For example, assume N positive and N negative ions are present at first. All the negative ions are adsorbed, with twice the quantity adsorbed onto the homeotropic wall as onto the planar wall. Then the left hand side of (6.2) is $2/3N$.

displacement, Gauss law' reduces to an equation in v,

$$\frac{\partial}{\partial z}\left(-\epsilon\frac{\partial v}{\partial z}+(e_s-e_b)\sin 2\theta\frac{\partial\theta}{\partial z}\right)=Q \tag{6.4}$$

which is identical to (4.15), apart from the right hand side.

6.2.2.2 Ions free to move in the bulk

To find $Q(z,t)$, it will be necessary to calculate particle densities, $\rho_i(z,t)$ for each ion species. Once those densities are known, the charge density can be computed from the formula

$$Q(z,t)=\sum_i q_i\rho_i(z,t) \tag{6.5}$$

where q_i is the charge upon a single ion of species i. The positive ions may have quite distinct chemical properties from the negative ions, so in most cases the speed at which they travel through the liquid crystal will differ. Were that not the case, a single equation would govern $Q(z,t)$. As it is, a separate equation must be solved for each species.

Each density ρ_i is governed by an hydrodynamic continuity equation,

$$\frac{\partial\rho_i}{\partial t}+\frac{\partial j_i}{\partial z}=0, \tag{6.6}$$

both of which must be solved simultaneously with the Ericksen-Leslie equations. The ion currents j_i are each made up of a diffusive contribution proportional to the density gradient, and a drift term proportional to the electric field:

$$j_i=-D\frac{\partial\rho_i}{\partial z}+\mu_i\frac{q_i}{|q_i|}\rho_i E. \tag{6.7}$$

This ion current contains two phenomenological parameters for each ion species - the mobility μ_i and the diffusivity D_i. The number of free parameters is halved by assuming that the Einstein relation,

$$D_i=k_BT\mu_i/|q_i| \tag{6.8}$$

holds, as has been assumed elsewhere [37].

Since (6.6) has exactly the same form as (4.18), it is easy to discretize it by the control volume method. Some care must be taken in treating the drift term, however. Patankar [137] would identify this as *convective* term, but with the force qE in place of a fluid velocity: the treatment here is adapted from his. Naively, one might compute the ion current through face u, midway between points P and U, by linearly interpolating ρ,

so that

$$j_u = -\frac{D}{h}(\rho_U - \rho_P) + \frac{\mu \frac{q}{|q|} E_u}{2}(\rho_U + \rho_P) \tag{6.9}$$

where the index i was dropped for convenience. However, unphysical results with $\rho < 0$ in some parts of the cell might be calculated as the mesh Peclet number,

$$T_u = -\frac{h\mu \frac{q}{|q|} E_u}{D} \tag{6.10}$$

increases. This can be seen by considering a simple example. Imagine that the cell is subdivided into three layers, and that E and hence T is constant. Only one algebraic equation results, linking the density at the mid-plane, ρ_P, to the densities at the lower and upper walls, ρ_L and ρ_U respectively,

$$4\rho_P = \rho_U(2 - T) + \rho_L(2 + T). \tag{6.11}$$

Looking at this, ρ_P will be negative whenever $T > 2$ and $\rho_U(T - 2) > \rho_L(T + 2)$ — clearly an unphsyical solution. Although simple, this example is illustrative - it represents a situation where ions are driven to one wall by a strong electric field.

One way to deal with this would be to decrease the mesh spacing h as the electric field grows, thus keeping the Peclet number down, but that would be inefficient. A better treatment is reached by noting that, if E is constant between points P and U (an assumption consistent with a piecewise linear voltage profile), then the steady state solution to (6.6) between those points is not linear, but

$$\rho = \frac{1}{\exp T_u - 1}\left[(\rho_U - \rho_P)\exp T_u \frac{z - z_P}{h} + \rho_P \exp T_u - \rho_U\right] \tag{6.12}$$

From there, the ion current at u can be expressed as

$$j_u = \frac{T_u D}{h}\frac{\rho_P \exp T_u - \rho_U}{\exp T_u - 1}. \tag{6.13}$$

Of course, (6.13) tends to (6.9) as T_u tends to zero. Using this expression, unphysical results are avoided, no matter how coarse the mesh. Returning to the earlier example, the single equation is

$$\rho_P \exp(T + 1) = \rho_U + \rho_L \exp T \tag{6.14}$$

and ρ_P is always positive.

Since adsorption and desorption of charges at the cell walls are assumed to occur slowly

over the time scale of the experiment, isolating boundary conditions are imposed:

$$j_i(0,t) = j_i(1,t) = 0. \tag{6.15}$$

These boundary conditions do not specify a unique steady-state solution - in other words, an ill-posed problem of the second kind has arisen. It manifests itself through the Jacobian of the discrete equations, which is singular, so that at each iteration the Newton step $\Delta\boldsymbol{\rho}_i$ is undetermined. Looking at the SVD of $\boldsymbol{J}$, only one singular value is zero, corresponding to a change in $\rho_i(z)$ which is uniform in z. Clearly, that change should be zero, since ions are conserved, so the minimum norm solution (3.15) can be chosen. Therefore, the initial guess for each $\rho_i(z)$ should satisfy

$$\int_0^d \rho_i(z)dz = d\rho_{i0}. \tag{6.16}$$

- in other words, the mean ion concentration ρ_{i0} must be specified for each species. For best performance, the initial $\rho_i(z)$ are given by exact solutions to (6.6), (6.15) and (6.16) when $E(z)$ is constant and $\theta(z) = \pi/2$. Like σ and μ_i, the ρ_{i0} are unknown, and will need to be determined from the experiment.

6.2.3 Inverse problems

Weakly-constrained problems much like the time-dependent problem described in the previous chapter were solved for each set of time dependent data. The principal difference was the initial guess for the tilt profile: the full set of Ericksen-Leslie equations, including flow, were solved. Once again, the intention was to determine how the director profile deviated from that expected.

It was somewhat harder to define a sensible strongly-constrained problem for this experiment. Parameters that might affect DC switching above and beyond AC switching include σ, ρ_{i0}, μ_i, and $(e_s - e_b)$, so they would be natural candidates for the model vector. There is very little information available which would suggest initial values for any of these, though. Worse, there is no reason to assume that only two ion species are present, bar Occam's razor.

At least the strongly-constrained problem could be broken down into two parts. Initial modelling had suggested that low concentrations of mobile ions did not affect the steady-state tilt profiles, apart from the ground state, very much. So, strongly-constrained problems were formulated to determine σ and $(e_s - e_b)$. Three models were optimized: one in which only $(e_s - e_b)$ was non-zero (model 1), one in which only σ was non-zero (model

Parameter		Model			
		1	2	3	4
$(e_s - e_b)$ / pCm^{-1}	minimum	14	0	10	-2.0
	initial	24	0	20	-5.0
	maximum	34	0	30	-8.0
σ / μCm^{-2}	minimum	0	11	2.7	13
	initial	0	12	3.0	15
	maximum	0	14	3.3	25
ρ_{+0}, ρ_{-0} / 10^{20}m^{-3}	minimum	1.1			
	initial	1.9			
	maximum	3.1			
μ_+, μ_- / 10^{10}m^{2}V^{-1}s^{-1}	minimum	37			
	initial	100			
	maximum	272			

Table 6.1: Initial values and constraints for three strongly-constrained inverse problems. The models vary only in terms of $(e_s - e_b)$ and σ: all the other parameters are identical.

2), and a third in which both were optimized (model 3). In all three, σ was constrained to be negative-definite, and $(e_s - e_b)$ constrained to be positive-definite, ensuring that in models 1 and 2 the director was further from the ground state when a negative voltage was applied. As the results will show, it was difficult to decide which model, if any, to believe.

For the dynamic data, four strongly-constrained problems were solved, three corresponding to the three steady-state models and a fourth in which a negative value of $(e_s - e_b)$ was considered. Their initial values are given in table 6.1. The plan was to produce a best fit solution for each of the models, and then compare their relative merits. To prevent all the solutions from converging on the overall best fit, a constrained optimization method, as in the time-dependent problem in the previous chapter, had to be used. Simple box constraints were imposed, with each parameter varying within the interval given in table 6.1.

6.3 Results

6.3.1 Steady-state behaviour

Sign dependent behaviour is immediately obvious from experimental measurements taken at $t = 250$ ms, that is, after the cell appears to have reached equilibrium. Figure 6.1 shows this clearly - predictions of T_{ps} computed assuming no sign dependent effects are the same whether $v_0 = -V$ or $v_0 = +V$, but the data is obviously different. Notice that $V = \pm 1$ data is not included in this part of the analysis, as the cell had clearly not reached equilibrium. Figure 6.2 shows weakly-constrained tilt profiles which fit the remaining data.

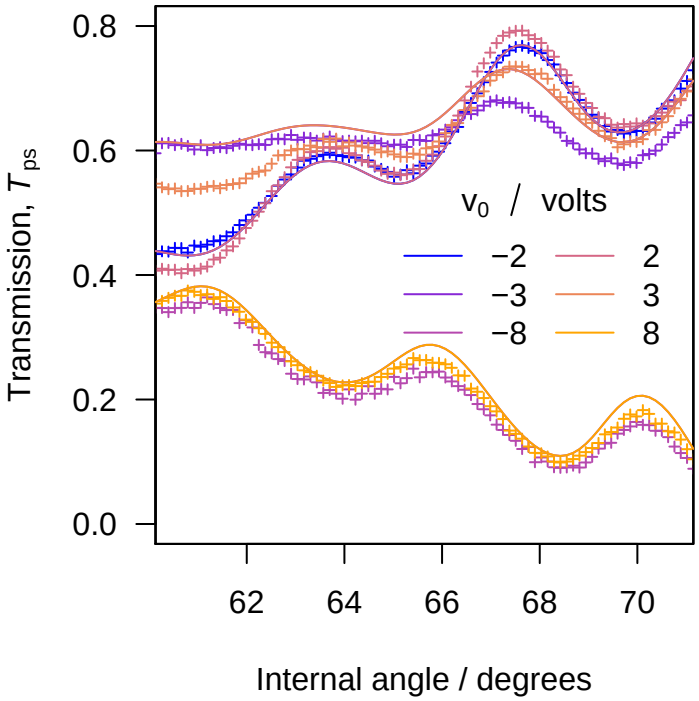

Figure 6.1: Steady-state transmission T_{ps} under DC fields. Without the flexoelectric effect or bound surface charges, no difference is expected between $v_0 = -V$ and $v_0 = +V$ stable states (solid curves), so pairs of these plots are identical. Experimental measurements (crosses) are significantly different if the sign of v_0 is changed.

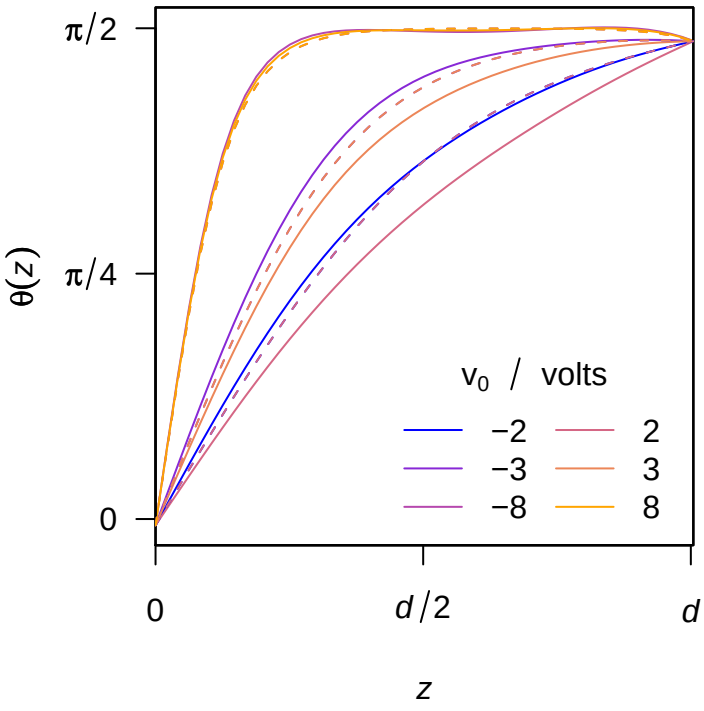

Figure 6.2: Weakly-constrained tilt profiles under DC fields. While the initial guess (dashes) is insensitive to the sign of v_0, the weakly-constrained tilt profiles computed from the experimental data (solid curves) are not.

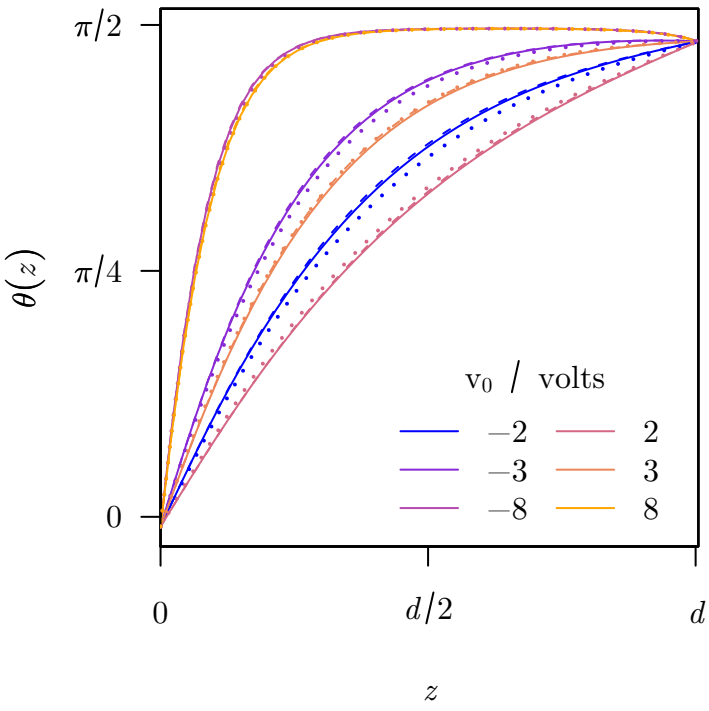

Figure 6.3: Strongly-constrained tilt profiles under DC fields. The tilt profiles computed for models 2 (dashes) and 3 (solid curves) are very similar, despite the different parameters which define them. Model 1 (dots) is somewhat different - its sign dependence is weaker - but never by more than 3°.

For any positive V, the tilt profile at $v_0 = -V$ lies above that for $v_0 = -V$. At moderate V, the tilt profiles are separated by as much as 8°. At higher voltages, the difference is smaller.

Any number of strongly-constrained models could explain the observed sign dependence. Values found for σ and $(e_s - e_b)$ are shown for each model in table 6.2. While the best fit, with a residual norm of 0.096, is model 3, model 2 is only a little worse with a residual norms of 0.099. Compared to a reference model without any sign dependent effect, which has a residual norm of 0.015, these both represent a similar improvement. Model 1 is appreciably worse than the other two (with a residual norm of 0.011), but is still a significant improvement over the reference model. Tilt profiles for each of the models are shown in figure 6.3: models 2 and 3 are much the same, while model 1 is somewhat different, but overall exhibits similar sign dependence. At its largest, the difference in tilt angle between the models is less than 3° while there is no qualitative feature that would prefer any one of the models. That being the case, neither $(e_s - e_b)$ nor σ can be reliably determined from this steady-state data.

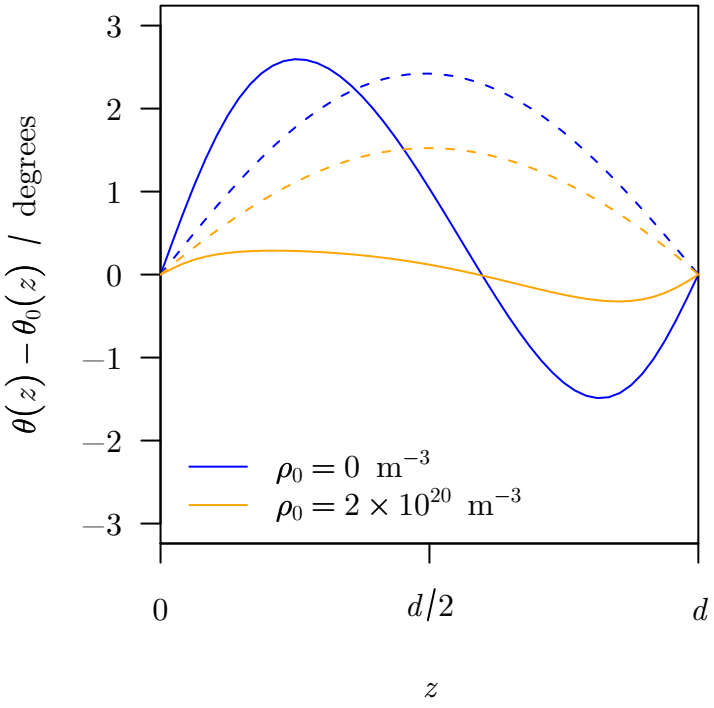

Figure 6.4: Ground state tilt profile due to the flexoelectric effect, bound surface charge, and mobile ions. The flexoelectric effect (with $(e_s - e_b) = 60$ pCm^{-1}) causes the ground state tilt profile, $\theta(z)$ to have an S-shape (solid curve) compared $\theta_0(z)$, where $(e_s - e_b) = 0$. Bound surface charge (with $\sigma = 27$ μCm^{-2}) results in a C-shape (dashes). Both features are suppressed by only a tiny concentration (2×10^{20} m^{-3}) of mobile ions.

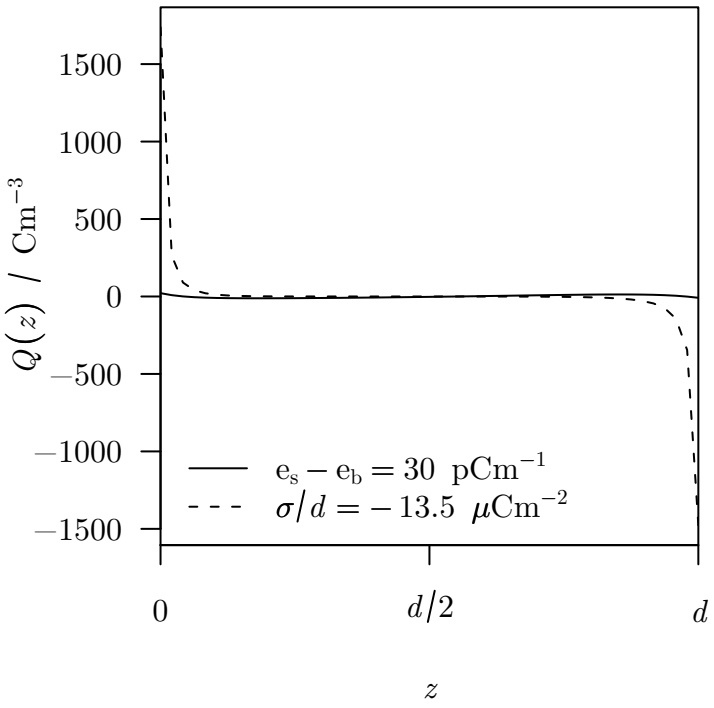

Figure 6.5: Charge concentration due to the flexoelectric effect and bound surface charge. In the ground state, bound surface charge causes mobile ions to plate the cells walls (dashes), but the flexoelectric effect does not (solid curve).

Parameter	Model			
	1	2	3	Reference
$(e_s - e_b)$ / pCm^{-1}	20.1	0.0	14.3	0.0
σ / μCm^{-2}	0.0	- 11.9	- 6.5	0.0
$\|\|\boldsymbol{f}(\boldsymbol{m}) - \boldsymbol{b}\|\|_2$	0.011	0.099	0.096	0.015

Table 6.2: Parameters found by solving the three strongly-constrained steady-state inverse problems.

6.3.1.1 Ionic impurities and ground-state tilt profiles

Were it not for mobile ions, it might be possible to distinguish between the models by considering the ground state tilt profile. If the flexoelectric effect is dominant, then the ground state tilt profile should adopt a distinctive S-shape, relative to a tilt profile computed with $(e_s - e_b) = 0$ and $\sigma = 0$ (figure 6.4). In contrast, if bound surface charges prevail, then the tilt profile should be C-shaped. As soon as mobile ions are introduced into the model, even at the tiny concentration of 2×10^{20} m^{-3} - approximately one ion for every ten million liquid crystal molecules - this distinction is diminished. In both situations ions move to oppose the internal DC fields, and cause the tilt profile to move toward the ground state that would be expected in the absence of either effect.

Although the ground state tilt profiles are similar whatever the values of $(e_s - e_b)$ and σ, the ground state charge distributions, shown in figure 6.5 are not. When the flexoelectric effect is most significant, the charge distribution within the cell is close to uniform. Alternatively, when bound surface charges dominate, ions tend to migrate to - or *plate* - the cell walls.

This difference between ground state charge distributions might help to distinguish between flexoelectricity and surface charge. First, assume σ is negative. In this case, the ground state charge distribution resembles the charge distribution that occurs when a negative voltage is applied, and is quite different from that resulting from a positive voltage. When the cell is switched from ground to negative, the ion distribution does not change much, but changes significantly when the cell is switched from ground to positive, or from negative to positive. On the other hand, if σ is insignificant, ions always migrate, whatever voltage is applied. So, if ion dynamics are observable experimentally, bipolar switching could be used to determine σ, and hence $(e_s - e_b)$.

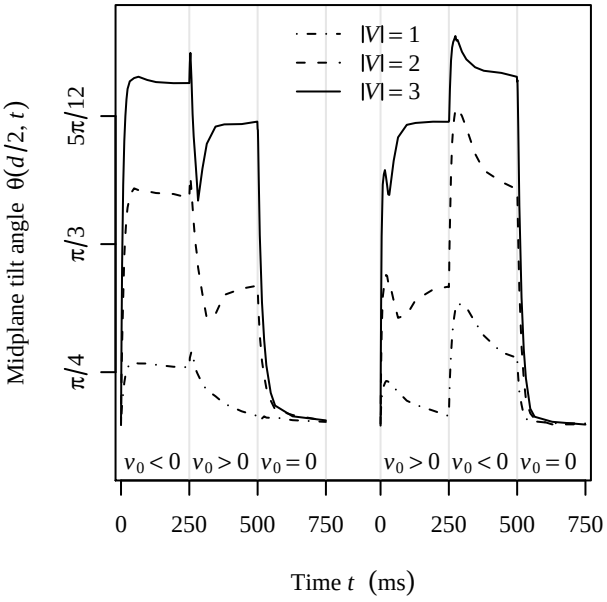

Figure 6.6: Weakly-constrained mid-plane tilt evolving with time. One weakly constrained tilt profile was computed for each of the crosses: the connecting lines simply serve to guide the eye. As well as the difference between equilibrium states at $v_0 > 0$ and $v_0 < 0$, transient behaviour not explained by the Ericksen-Leslie equations alone is apparent. In particular, there is a dip in the mid-plane tilt shortly after the cell is switched to a positive voltage, whatever its previous state.

6.3.2 Time-dependent behaviour

While the steady-state results are well described by the Ericksen-Leslie equations without the ion diffusion equations, the time-dependent behaviour of the cell is not. The mid-plane tilt angle inferred from the observations (by solving a weakly-constrained problem) is plotted as a function of time in figure 6.6 for several values of V. All the curves tend to equilibrium values that depend upon both the magnitude and the sign of the applied voltage. They also exhibit several transient features which occur over timescales that shrink as the magnitude of the applied voltage grows. In comparison, mid-plane tilts found by solving the Ericksen-Leslie equations alone (including the flexoelectric effect but not ions) are plotted in figure 6.7. The equilibrium values are similar to those observed experimentally, but there are no significant transients. In fact, the timescales of the transients - around 100 ms, is far longer than the $\sim$ 10 ms timescales seen in the AC switching of the same cell[144], where ion motion is negligible, and so we should not expect to find them when modelling the DC switching this way.

All of the transients observed occur immediately after the applied voltage is changed, and over a timescale of around 100 ms. When the polarity of the applied field is switched from $v_0 > 0$ to $v_0 < 0$, the director initially rotate beyond the $v_0 < 0$ steady state, as though the field was supplemented for a short period. Another pair of transients suggest

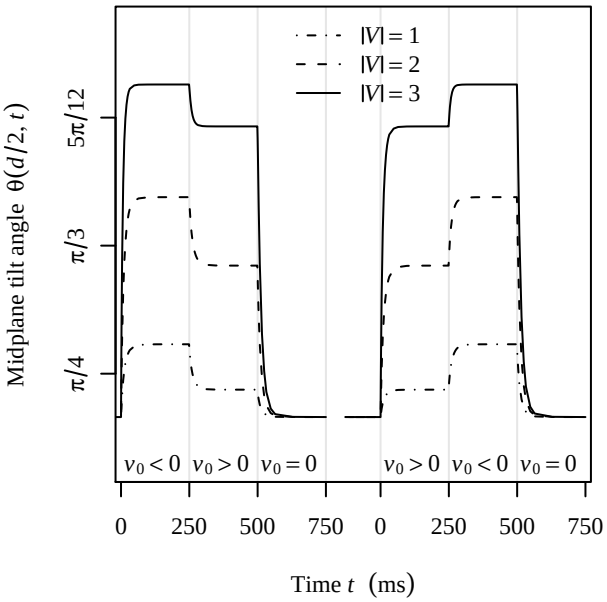

Figure 6.7: Modelled evolution of the mid-plane tilt with no ions present. Sign dependence is due to the flexoelectric effect, with $(e_s - e_b) = 30$ pCm^{-1}. Although the equilibrium states are in agreement with the observations in figure 6.6, the large amplitude transients are missing entirely.

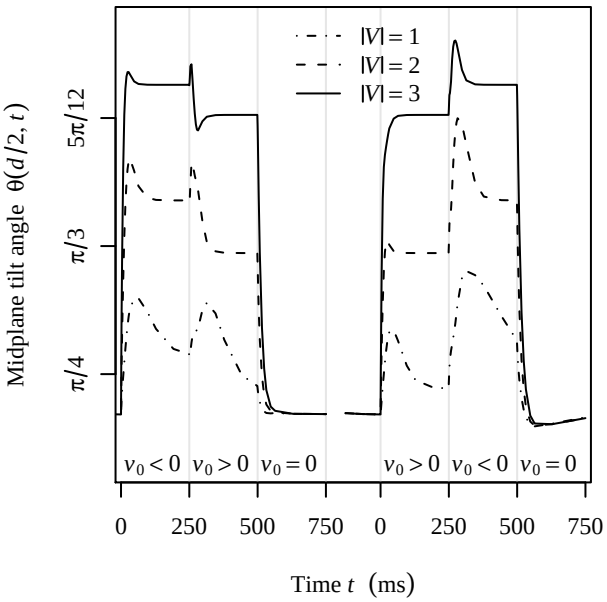

Figure 6.8: Modelled evolution of the mid-plane tilt when the linear effect is dominated by the flexoelectric effect Here, $(e_s - e_b) = 22$ pCm^{-1}. In contrast to figure 6.6, the time-dependent behaviour immediately after the cell is switch from $v_0 = 0$ to $v_0 > 0$ does not resemble that when the cell is switched from $v_0 < 0$ to $v_0 > 0$ - there is no dip in the mid-plane tilt.

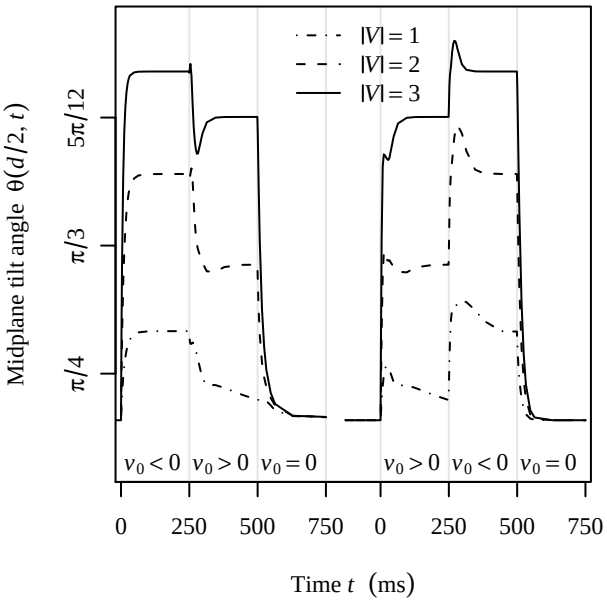

Figure 6.9: Modelled evolution of the mid-plane tilt when the linear effect is dominated by surface charges. For this simulation, $\sigma = 13.5\ \mu\mathrm{Cm}^{-2}$. The director evolves in a similar manner when the cell is switched from $v_0 = 0$ to $v_0 > 0$ and when it is switched from $v_0 < 0$ to $v_0 > 0$, as in figure 6.6.

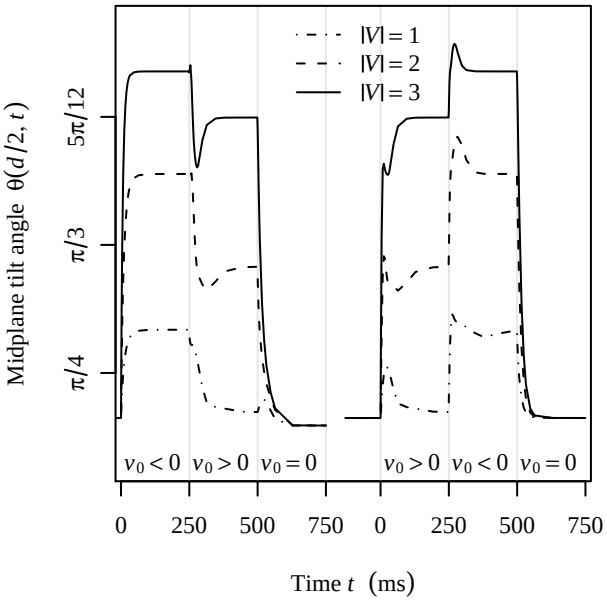

Figure 6.10: Modelled solution of the mid-plane tilt in the best fit case. The best match to the data occurs when $(e_s - e_b) = -7\ \mathrm{pCm}^{-1}$ and $\sigma = 16\ \mu\mathrm{Cm}^{-2}$. As in the previous case figure 6.9, the transient features are consistent with those in figure 6.6.

Parameter	Model			
	1	2	3	4
$(e_s - e_b)$ / pCm^{-1}	22.0	0.0	17	-7.1
σ / $\mu\mathrm{Cm}^{-2}$	0.0	14	4.1	17
ρ_{+0} / $10^{20}\mathrm{m}^{-3}$	2.8	3.0	3.1	3.1
ρ_{-0} / $10^{20}\mathrm{m}^{-3}$	1.1	1.1	1.4	1.1
μ_+ / $10^{-10}\mathrm{m}^2\mathrm{V}^{-1}\mathrm{s}^{-10}$	1.27	1.45	1.35	1.48
μ_- / $10^{-10}\mathrm{m}^2\mathrm{V}^{-1}\mathrm{s}^{-10}$	2.72	2.61	2.72	2.72
$\|\|\boldsymbol{f}(\boldsymbol{m}) - \boldsymbol{b}\|\|_2$	0.09	0.13	0.11	0.06

Table 6.3: Parameters found by solving the four strongly-constrained time-dependent inverse problems.

that the ground state of the cell and the $v_0 < 0$ steady-state are similar to each other and distinct from the $v_0 > 0$ steady-state: a few milliseconds after the field is switched from negative to positive *and* from off to positive, the director rotates away from the $v_0 > 0$ steady state toward the ground state, then back toward the $v_0 > 0$ steady state, resulting in a distinctive dip in plots of the mid-plane tilt against time.

These initial results suggest that σ is large and negative, and consequently that $(e_s - e_b)$ is not large and positive. As noted above, a dip in the mid-plane tilt occurs under two circumstances. One is observed when switching from the ground state to $v_0 > 0$, and another when switching from $v_0 < 0$ to $v_0 > 0$. No dip is observed when switching from $v_0 > 0$ to $v_0 < 0$ or from the ground state to $v_0 < 0$. That suggest that the ground state and the $v_0 < 0$ steady state are similar in a way that the $v_0 > 0$ steady-state is not. In the models of the ground state described earlier, only significant negative charge bound to the homeotropic surface (or equivalently, positive charge bound to the planar surface) could cause this.

These medium-scale transients appear to be caused by mobile ions, with mean densities $\rho_{0+} \approx 3 \times 10^{20}\ \mathrm{m}^{-3}$ and $\rho_{0-} \approx 1.5 \times 10^{20}\ \mathrm{m}^{-3}$, mobilities $\mu_- \approx 1.5 \times 10^{-10}\ \mathrm{m}^2\mathrm{V}^{-1}\mathrm{s}^{-1}$ and $\mu_+ \approx 3.0 \times 10^{-10}\ \mathrm{m}^2\mathrm{V}^{-1}\,\mathrm{s}^{-1}$, and unit charge. Similar mobilities have been reported elsewhere [37, 35]. The exact values vary slightly between each of the models initially specified in table 6.1, with best fit values for all the parameters given in table 6.3. The inclusion of mobile ions causes transients to be calculated with the correct amplitudes and timescales in all of the models, but the details depend noticeably on the sign dependent

mechanism.

Sign dependent behaviour in the first numerical model, shown in figure 6.8, is due to the flexoelectric effect, with $(e_s - e_b) = 22$ pCm^{-1}. Model 4, which, with a large flexoelectric effect and a little adsorption is most similar to the best fit model from the static study, gave similar results. These models have the largest residual norms, but rather than these numbers, qualitative features in the mid-plane tilt rule them out. While the director behaves in the correct manner when the cell is switched from $v_0 > 0$ to $v_0 < 0$, at several other points it does not. Shortly after the switch from $v_0 = 0$ to $v_0 < 0$, the director briefly rotates beyond the steady-state position by an angle which increases as $|v_0|$ decreases. While an over-rotation is observed experimentally, it is weak and decreases in amplitude as $|v_0|$ decreases. A dip in the mid-plane tilt is calculated after the switch from $v_0 < 0$ to $v_0 > 0$ only when $|v_0| = 3$, and not at all after the switch from $v_0 = 0$ to $v_0 > 0$. Finally, when the field is switched from $v_0 > 0$ to $v_0 = 0$, the director rotates beyond the ground-state and then back.

If surface charges, with $\sigma = 14$ μCm^{-2}, are assumed to dominate over the flexoelectric effect, the numerical results, shown in figure 6.9, resemble the observations rather more closely. As in the previous case, the director rotates beyond the equilibrium state when the cell is switched from $v_0 > 0$ to $v_0 < 0$. But, unlike the previous case, and in common with the experimental results, a dip in the mid-plane tilt is present both at switch-on to $v_0 > 0$ and at the switch from $v_0 < 0$ to $v_0 > 0$. There is one qualitative difference between these calculations and the experiment - no over-rotation is seen as the cell evolves from the ground state toward the $v_0 < 0$ steady state. This might be explained if additional, slower moving ion species were considered.

The underlying difference between these two cases, at least in terms of the ion dynamics, is in their ground state charge distributions, and this is reflected in the transient behaviour of the director. Figure 6.5 shows that when surface charge is the primary sign dependent mechanism, positive charge is strongly concentrated near the homeotropic wall at $z = 0$ when no voltage is applied. A similar concentration will occur if a negative voltage is applied. As a result, whenever a positive voltage is applied, whether the cell is initially in the ground state or the $v_0 > 0$ steady state, a similar migration of positive ions to the opposite wall is expected. For a short period there is an even distribution of charge across the cell, and it is during these periods that the distinctive dips in the tilt profile occur. In other words, the dip is seen only if the initial charge distribution is higher at one wall, and that occurs in two places for this model: when the cell is switched on to a positive voltage, and when it is switched from a negative to a positive voltage.

On the other hand, when the flexoelectric effect is the cause of sign dependence, positive

charge is not concentrated near the homeotropic wall. In this case the charge distribution is nearly uniform. Only when the cell is switched from a negative to a positive voltage is a dip in the tilt profile computed.

Model 3 is the best-fit model, where the parameters $(e_s - e_b) = -7.1$ pCm^{-1} and $\sigma = 17$ μCm^{-2} minimise the difference between the observed optical data and the model. As shown in figure 6.10, evolution of the mid-plane tilt is similar to the second model. Notably, the flexoelectric polarization is small, and directed in the opposite sense to the flexoelectric polarization in the first model. In other words, this model appears to fit the data best primarily because its sign dependence is dominated by surface charges.

6.3.3 Changing the surface treatment

Only a minimal analysis of the secondary experiment is needed to support the natural conclusion of the primary experiment. If the observed sign dependent switching were principally due to the flexoelectric effect, then the results should not depend much upon the choice of surface treatments. $(e_s - e_b)$ is a property of the bulk material, so any HAN cell filled with ZLI-4788-00 should behave similarly. Put simply, the total birefringence of the cell should hardly change if the surface treatments are changed.

Swapping the homeotropic aligner changed the sign dependent behaviour profoundly. Figure 6.11 shows transmission, measured as a function of time, through a similar cell to the one used in the primary experiment, when $|v_0| = 1.5$ volts. As before, the measurements are further from the ground state when a *negative* voltage is applied with respect to the planar surfaces. Figure 6.12 shows the comparable results for a third cell, in which the Nissan polyimide is used to promote homeotropic alignment. Now, the results are further from the ground state when a *positive* voltage is applied. If the flexoelectric effect dominated the sign dependence in both cells, the sign of $(e_s - e_b)$ must vary for the same bulk material! It is far easier to believe that σ changed sign after a change in surface chemistry.

6.4 Summary

A treatment of mobile ions was added to the numerical model described in chapter 4, to help explain slow transients observed during a DC switching experiment. This meant that for a given cell, equations governing not just the director tilt, fluid flow and electric field had to be solved, but also one additional equation for each species of ions present in the bulk. Furthermore, Gauss' law had to be modified to include both bulk and surface charges.

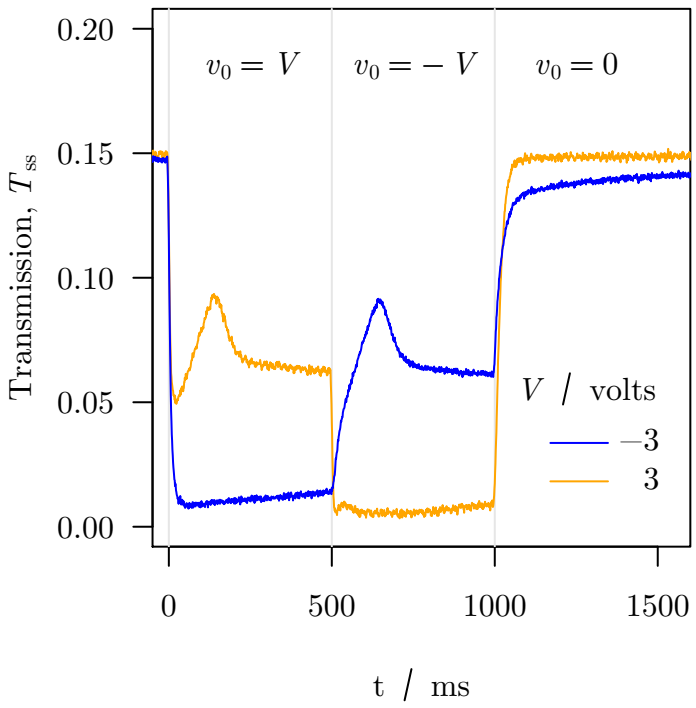

Figure 6.11: Transmission between parallel polarizers at normal incidence measured for a cell with the Merck homeotropic aligner. The cell is further from its ground state when a *negative* voltage is applied, relative to the planar surfaces.

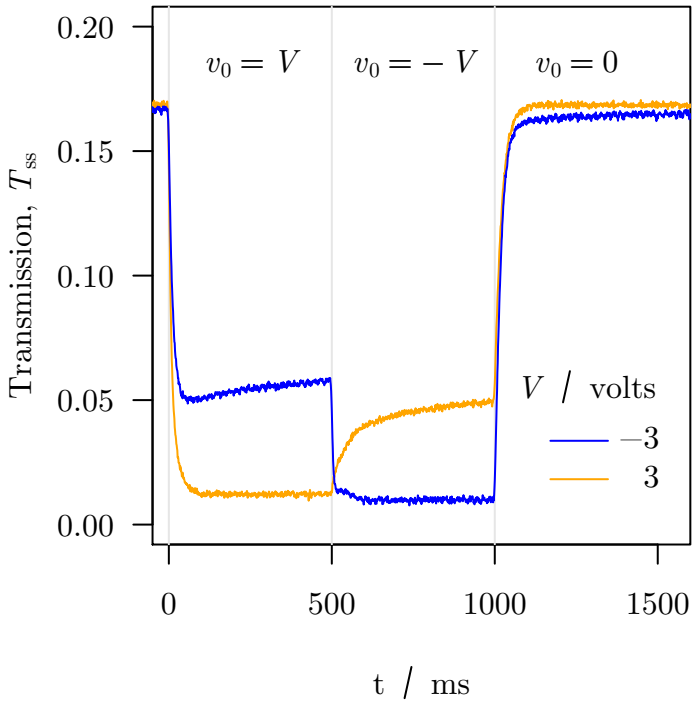

Figure 6.12: Transmission between parallel polarizers at normal incidence measured for a cell with the Nissan homeotropic aligner. The cell is further from its ground state when a *positive* voltage is applied, relative to the planar surface.

Bound surface charges, or some other surface effect, dominate sign dependence in the DC switching of HAN cells filled with ZLI-4788-000. Models involving mobile ions only predicted certain qualitative features in the time-dependent mid-plane tilt when that was the case. When the flexoelectric effect was assumed to be responsible for the sign dependence, some observed features were not predicted, while some additional features were predicted but not observed. This is a surprising conclusion. After all, PABN cells filled with ZLI-4788-000 can be switched between their two stable states [74], and the flexoelectric effect is often assumed to be responsible [76]. Changing the treatment used to promote homeotropic alignment reversed the sign dependent effect, reinforcing the earlier conclusion.

Chapter 7

Conoscopic observations of pressure driven flow

If your experiment needs statistics, you ought to have done a better experiment.

7.1 Introduction

Rutherford is usually credited with the remark above, and he might well have substituted the solution of ill-posed problems for statistics. Considering the complexity of the analysis in chapters 3, 5 and 6, an obvious question is: given that the full-leaky guided mode experiment can only reveal broad spatial trends in the director profile, could a simpler experiment achieve the same? The answer, in general, is probably no. In this chapter, however, a special case, steady-state flow along a channel, is described, where information about the director profile comparable to that which can be obtained from a guided mode experiment is recovered, simply, from conoscopy figures.

Much can be learnt about flow in nematic liquid crystals by studying the time-dependent behaviour of conventional cells, as shown in chapter 5 and elsewhere [51, 63]. On the other hand, steady-state experiments are inherently simpler - there is less data to collect - so it is desirable to conduct them.

In the literature, steady-state flow experiments are usually conducted by setting the upper substrate of a cell into motion relative to the lower [100, 145, 60]. A uniform velocity gradient in the $z-$direction results, which in turn causes the liquid crystal to rotate. There is a difficulty here: the upper substrate is moving, so it is unlikely that a constant layer thickness will be maintained. An alternative cell design is considered in this chapter, where liquid crystal is driven along a wide channel by a pump. Similar configurations have been described before, and used to study the interaction between elastic and viscous forces [61, 59]. Here, a further seam will be mined by studying the competition between

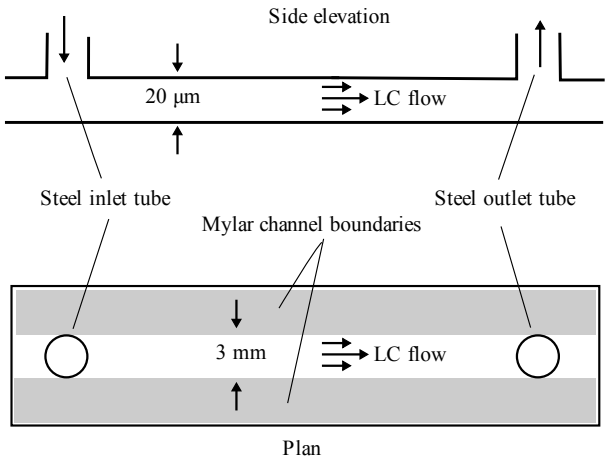

Figure 7.1: Plan and side elevations of a flow cell. Strips of mylar form a channel along the length of the cell. Liquid crystal is driven along this channel by a pump attached to the steel inlet tube, and exits the cell through the outlet tube.

these and the effect of applied electric fields.

Four basic cell geometries could be considered, each defined by the alignment of the liquid crystal at the cell walls. They are: a homeotropic cell, a planar cell with the rubbing direction parallel to the flow, a planar cell with the rubbing direction perpendicular to the flow, and a planar cell with the rubbing direction inclined at $\pi/4$ to the flow. Simple models show that in each case the director adopts a distorted tilt profile which is antisymmetric about $z = d/2$, and a twist profile which is symmetric about $z = d/2$. Measuring the amplitudes of these distortions as the flow rate varies would, in principle, allow independent estimates to be made of four of the five nematic viscosities. This chapter consists of computational and experimental studies of the homeotropic cell: numerical studies of the other configurations will be described in Appendix C.

Initial analysis suggests that, at least for the homeotropic cell, conoscopy can be highly informative. Waton [59] has noted that, for thick ($\sim$ 50 μm), homeotropic cells, the interference figure is quite distinctive. Here, that analysis is extended to thinner ($\sim$ 20 μm) cells, and it is shown that a simple observation and measurement reveals much about the tilt profile. By repeating that measurement for several pumping rates, and as an applied voltage is varied, the Leslie viscosity α_2 is measured. In addition, a nucleated transition to a newly-observed state is predicted, and observed, when the flow rate reaches a critical point.

7.2 Cell Design

Figure 7.1 presents the plan and the side elevation of a flow cell built by Fuzi Yang and Pete Cann for the purpose of this chapter. Holes 3 mm in diameter were drilled through the first of two ITO-coated glass plates, and steel tubes fixed into them with epoxy resin. Each of the glass plates was then dip-coated with lecithin to promote homeotropic alignment. Next, two strips of 20 μm thick Mylar, both several millimetres wide, were laid onto the second plate so that a channel $d_y \approx 3$ mm wide and running the length of the cell was formed between them. Then the first plate was laid down on top, and the cell sealed all around with epoxy resin.

Once the cell was built, liquid crystal could be pumped through at a known rate. One end of a rubber pipe was slipped over one of the metal tubes, and the other end fitted over the needle of a Hamilton 250 μl syringe filled with 5CB. The flow rate is controlled at the pump, which could be set to multiples of 1 μlh^{-1}. The rubber pipes must fit snugly, or liquid crystal will leak out from the system, causing the intended and actual flux of liquid crystal through the cell to differ.

7.3 Theory

Although the cell described above is a three-dimensional system, a one-dimensional model will suffice to determine at least some of its behaviour. Little variation is expected over a length of the channel far from the inlet and outlet, reducing the problem from three dimensions to two. In other words, within most of the cell, the flow is parallel to x, and varies with respect to y and z only. Furthermore, the fluid velocity profile will vary across the channel, such that it is fastest in the middle. Since the channel is much wider than it is high, the flow varies slowly with respect to y. So, the cell is expected to behave much as though it were infinitely wide, that is varying only in z.

7.3.0.1 Nonlinear Ericksen-Leslie equations

Adapting the Ericksen-Leslie equations, and hence the numerical model described in chapter 5, is fairly straightforward. Rather than introducing a flow speed directly, a constant pressure gradient, G, is added to the right-hand side of (4.11) [13]. A negative value of G will cause the liquid crystal to flow parallel to the $x-$axis. Because the flow velocity is zero at the cell walls, imposing a pressure gradient will result in a flow field $u_x(G; z)$ which in fastest at the mip-plane, that is, where $z = d/2$. A value for G is sought such

that

$$\frac{1}{d}\int_0^d u_x(G;z)dz = \bar{u}. \tag{7.1}$$

In other words, an average flow rate $\bar{u}$ across the cell with respect to z is specified, which in turn determines G.

Equation (7.1) is solved numerically using the GNU R function 'uniroot', which requires the Ericksen-Leslie equations to be solved several times for given values of G. It restricts its search to an interval of G, specified here by

$$0 < G \leq 2G_0, \tag{7.2}$$

where

$$G_0 = -\frac{12\eta_1\bar{u}}{d^2} \tag{7.3}$$

is found by linearizing the Ericksen-Leslie equations as described in 7.3.0.3.

There is a complication here, due to the finite width of the channel. If the flow profile did not depend upon y then the relationship between $\bar{u}$ and the the volume of liquid crystal pumped through a cross-section of the channel per unit time, U would be simple:

$$U = \bar{u}d_y d. \tag{7.4}$$

Since U corresponds directly to the flow rate set at the pump, $\bar{u}$ would be known. However, the reality is more complicated, with $\bar{u}$ varying, roughly quadratically, from 0 at the channel's mylar walls to a maximum in the middle of the channel: in this case

$$U \approx \frac{2}{3}\bar{u}d_y d. \tag{7.5}$$

at $y = d_y/2$. For simplicity, the first of these formulae will be used, assuming that elastic forces tend to smear out any variations of tilt profile in y.

7.3.0.2 V and H states

Two distinct solutions to the governing equations, depending upon the choice of boundary conditions. In the obvious case, the V state, θ is zero at both cell walls. The resulting tilt profile, shown in figure 7.2, is an odd function of $z - d/2$ whose amplitude increases with $\bar{u}$. It is easier to understand this profile by examining the schematic, figure 7.3. No matter how high the flow rate, the director remains homeotropically aligned in the cell centre because the gradient of u_x, and hence the net torque, is zero there. But in the lower half of the cell, it has a positive gradient, resulting in the director tilting forward. And in

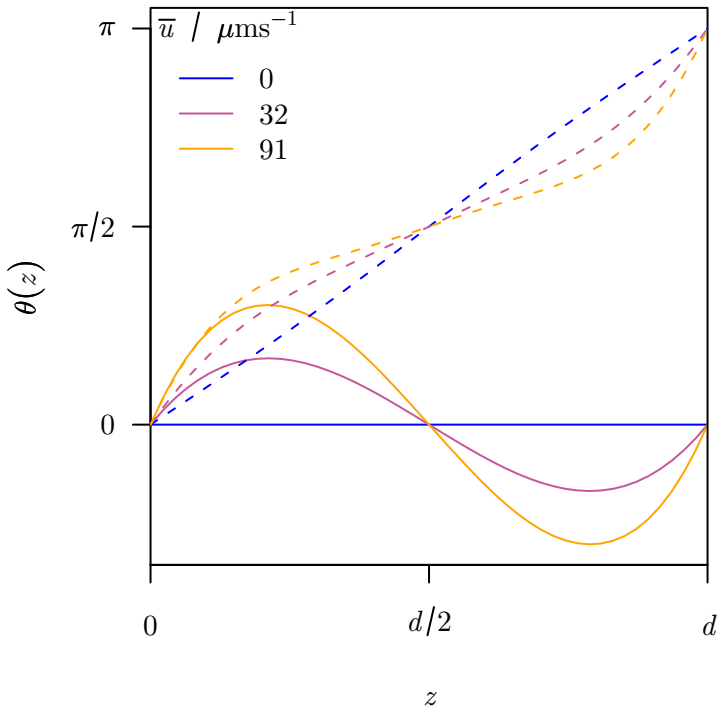

Figure 7.2: Modelled V and H state tilt profiles under pressure driven flow. For the V states (solid curves) the director is aligned homeotropically at the walls and mid-plane. The H states (dashes) maintain planar alignment at the mid-plane.

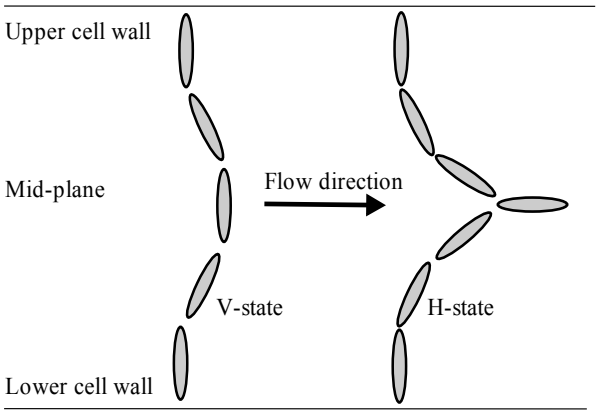

Figure 7.3: Schematics of the V and H states. In both states, the director profile is mirror-symmetric about the cell's mid-plane.

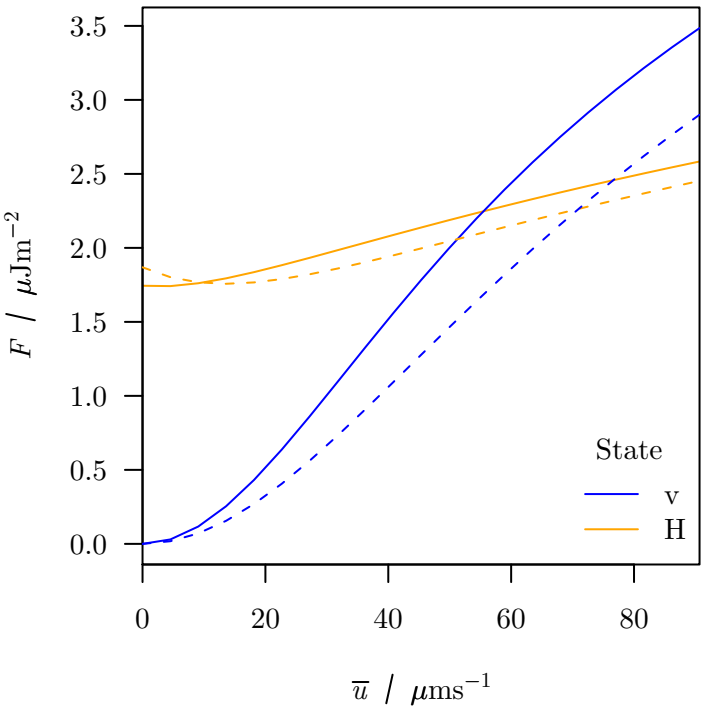

Figure 7.4: Free energy of V and H states plotted against flow rate. When there us no flow, the H state has much higher total free energy, F, than the V state. But the energy of the V state increases more quickly with the flow rate, eventually exceeding the other at around $\bar{u} = 50\ \mu\text{ms}^{-1}$ (solid curves). If a voltage is applied (dashes), the transition occurs at a higher flow rate

the upper half, the gradient of u is negative, so that the director tilts backward. Overall, the cell is mirror-symmetric about the mid-plane.

A second state, the H state, where $\theta = \pi$ at one cell wall must also be considered, because $\boldsymbol{n}$ is equivalent to $-\boldsymbol{n}$. In this state, also illustrated in figure 7.2 and figure 7.3, θ varies smoothly from 0 at $z = 0$ through $\pi/2$ at the mid-plane, to π at $z = d$. Although θ is no longer an odd function of $z - d/2$, $\theta - \pi/2$ is, and so the cell is still mirror-symmetric about the mid-plane.

While the cell will not be found in the H state at zero flow, it is the stable state beyond a critical flow rate. The liquid crystal layer has an elastic free energy per unit area

$$F = \int_0^d (k_{11} \sin^2\theta + k_{33} \cos^2\theta) \left(\frac{\partial\theta}{\partial z}\right)^2 dz. \tag{7.6}$$

When the cell is at rest, the H state has a higher free energy than the V state, in which the tilt profile is uniform (so $F = 0$). However, as the rate of flow increases, the free energy of the V state grows more rapidly (figure 7.4), eventually exceeding that of the H state at around $\bar{u} = 50\ \mu\text{ms}^{-1}$. Why does this occur? Primarily because $|\alpha_2| \gg |\alpha_3|$. A torque proportional to α_2 acts to rotate the director in the near-homeotropic regions of

the cell, while a torque proportional to α_3 acts in the near-planar regions. Since the V state is nearly homeotropic, it is distorted rather more for a given flow rate, than the H state, which has a near-planar region

The cell can only move from the V state to the H state (or back) by a *nucleated transition*. These states are similar to the V and H states found in the $\pi-$cell [146], and like them are topologically distinct. In other words, the cell cannot change continuously from one state to the other. Nucleated transitions begin in a small area (the nucleus) of a cell, and propagate to the rest slowly, over a timescale proportional to the square of the width and/or length of the cell.

If a transition from the V state to the H state is to be expected as the flow rate is increased, the reverse will take place if a strong electric field is applied (and $\epsilon_a > 0$). The dashed curves in figure 7.4 plot the total free energy of both V and H states against the mean flow speed $\bar{u}$. Compared to the solid curves (where no field is applied) the energy of the H-state is initially larger, but behaves much as it did while the flow increases. On the other hand, the energy of the V state increases much more slowly than before, so that it is the lower energy (and thus stable) state up to a higher flow rate. Put simply, applying a large enough electric field results in the V state becoming energetically favourable at a given flow rate, when it had not been in the absence of the field.

7.3.0.3 Linearised Ericksen-Leslie equations

It is possible to linearise the Ericksen-Leslie equations and solve them analytically, at least when the flow rate is small and the cell is in the V state. For the homeotropic cell, assuming that θ is small everywhere, the momentum balance equation becomes

$$\eta_1 \frac{d^2 u_x}{dz^z} = G. \tag{7.7}$$

This equation can be solved directly, with no-slip boundary conditions, to give a quadratic velocity profile,

$$u_x = \frac{z(z-d)G}{2\eta_1},$$

which can be re-expressed as

$$u_x = -\frac{6z(z-d)\bar{u}}{d^2},$$

where, as before, $\bar{u}$ is the mean fluid speed. Once u_x is known, the linearised angular momentum equation

$$k_{33}\frac{d^2\theta}{dz^z} + \alpha_2 \frac{du_x}{dz} - \epsilon_0\epsilon_a \left(\frac{v_0}{d}\right)^2 \theta = 0 \tag{7.8}$$

can be solved. If the liquid crystal is strongly anchored,

$$\theta = \frac{-6\bar{u}\alpha_2}{dk_{33}c^2}\left(\frac{\exp(c(d-z)) - \exp(cz)}{\exp(cd) - 1} + \frac{(2z-d)}{d}\right) \tag{7.9}$$

where

$$c = \frac{v_0}{d}\sqrt{\frac{\epsilon_0\epsilon_a}{k_{33}}} \tag{7.10}$$

If no electric field is applied, (7.9) becomes simply

$$\theta = -\frac{\bar{u}\alpha_2}{k_{33}d^2}\left(2z^3 - 3z^2d + d^2z\right). \tag{7.11}$$

There are only three free parameters in (7.9). One is the cell thickness, d, which is known (at least to some extent) from the cell design. The remaining two are the ratios α_2/k_{33} and ϵ_a/k_{33}. If v_0 and U are known, then there is a one-to-one correspondence between these ratios and the amplitude (or the root mean square value) of $\theta(z)$. So, if that amplitude could be measured as a function of v_0, α_2/k_{33} and ϵ_a/k_{33} could be estimated. Alternatively, α_2/k_{33} alone could be obtained from measurements varying U and setting $v_0 = 0$.

7.3.0.4 Modelling and Analysing the interference figure

Next, it will be shown that, at least for the homeotropic flow cells discussed here, conoscopy figures, or interference figures, reveal a great deal about the director profile. Simply inspecting the figure is enough to tell whether the kind of director profile described earlier is present. And, for the V-state, a straightforward measurement is sufficient to reveal the RMS tilt angle.

The Berreman (or Jones) matrix methods used throughout this thesis can be adapted to compute interference figures: such adaptations have been reported elsewhere [147, 104]. First, a Cartesian co-ordinate system is chosen for the plane of the figure and aligned with the sample's $x-$ and $y-$axes . Each point (x, y) in that plane can be described by a pair of angles, α and Ψ, such that

$$\sin\alpha = x^2 + y^2 \tag{7.12}$$

$$\tan\Psi = \frac{y}{x} \tag{7.13}$$

Figure 7.5 shows a ray of light passing through both the point (x, y) and the focus. It strikes the sample at an angle of incidence α, within a plane of incidence inclined at an angle Ψ with respect to the figure's $x-$axis, and at an angle Ψ' with respect to the

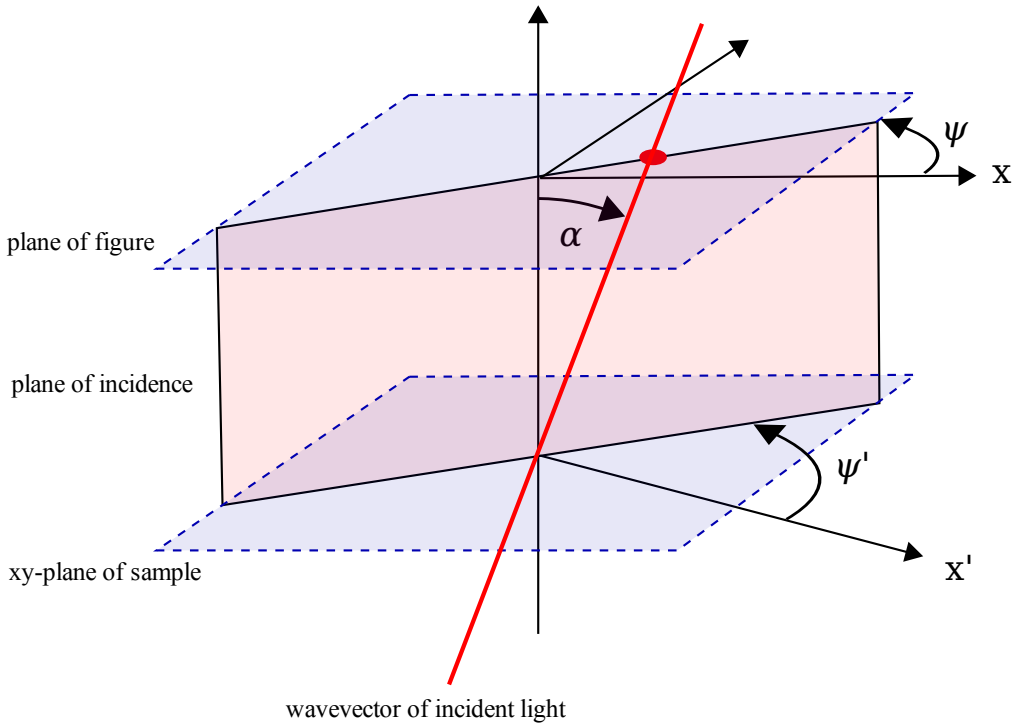

Figure 7.5: Geometry of the conoscope A ray, representing a small solid angle of the light cone formed by the objective lens, makes an angle α with both the sample's xy-plane and the plane of the figure. Its plane of incidence makes an angle Ψ with the sample's (and figure's) $x-$axis, and an angle Ψ' with the polarizers transmission axis.

transmission axis of the polarizer. Now, provided that light intersects with the sample some distance from the focus, so that diffraction can be neglected, a small solid angle of the light cone centred on (α, Ψ) can be treated as a plane wave of infinite extent in x and y. For each ray the coefficients E_{pp}, E_{ps}, E_{sp}, and E_{ss} are calculated, where E_{pp} is the complex, p-polarized component of the electric field transmitted through the sample if the incoming ray were wholly p-polarized, and so on. Knowing these, the intensity at any point (x, y) is given by the formula

$$I(\alpha, \Psi) = \left|(E_{\mathrm{pp}} - E_{\mathrm{ps}})\sin(\Psi')\cos(\Psi') - E_{\mathrm{ps}}\cos^2\Psi' + E_{\mathrm{sp}}\sin^2\Psi'\right|^2. \tag{7.14}$$

To calculate the whole figure, one simply needs to choose a set of pixels (x, y) which evenly cover the disc bounded by $\sin\alpha \leq \sin(NA)$, where NA is the numerical aperture of the light cone. A final note: as in the guided mode simulations, the air-glass interfaces are dealt with by Snell's law, rather than by the Berreman calculation.

Interference figures simulated for the flow cell are quite distinctive. When the cell is in the ground state, one expects to see the Maltese cross figure characteristic of the homeotropic state, such as the image shown in figure 7.6. Now, if the tilt profile were

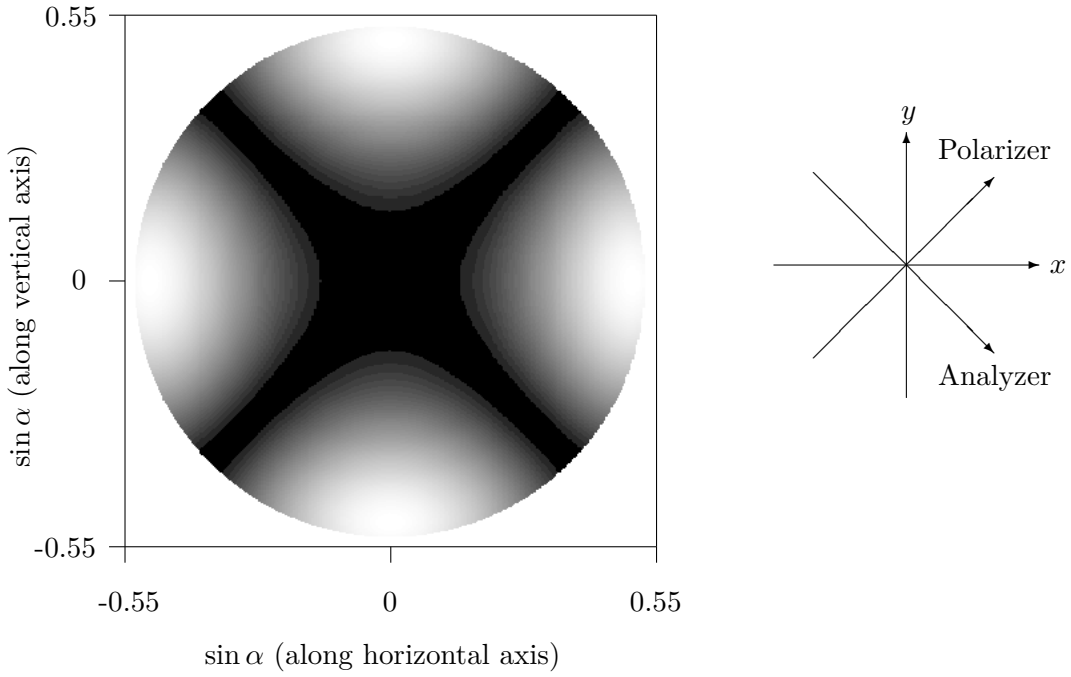

Figure 7.6: Interference figure calculated for a 20 μmhomeotropic cell. The gray-scale is gamma corrected, so that the contrast is greater near black then white. Because the cell is thin, only the isogyres - the dark Maltese cross - and the first of many bright isochromes are visible. If the cell were thicker, more isochromes - alternate bright and dark circles would be seen. The circular modulations are caused by multiple beam interference.

non-zero but uniform, or indeed any even function of $z-d/2$, the centre of the cross would move horizontally, but would otherwise look similar (figure 7.7) to the first figure. On the other hand, if $\theta(z)$ or $\theta(z)-\pi/2$ is an odd function of $z-d/2$, as predicted for the flow cell, the resulting image is quite different. For the V state, the dark isogyres split into two lobes (figure 7.8), which are vertically separated by a distance increasing with flow rate. The H state's figure does not have such signal features: it may have a dark stripe - an isochrome- along the horizontal axis, caused when the extraordinary wave emerges 2π out of phase with the ordinary ray, as in figure 7.9.

Simply looking at an interference figure reveals some depth dependent information. Recall the discussion of 2.1.1.1. If the conoscopy figure is mirror-symmetric about its horizontal axes, then the director must be confined to the $xz-$plane. All the figures shown above are of that type. Provided that is true, then the figure will be mirror-symmetric about its vertical axes if and only if the cell is mirror symmetric about its mid-plane. So, both the V and H states, and the homeotropic state, will give rise to figures which are mirror symmetric about both axes while the uniform state gives rise to a figure which is only mirror symmetric about its horizontal axis. Note that the V and uniform states

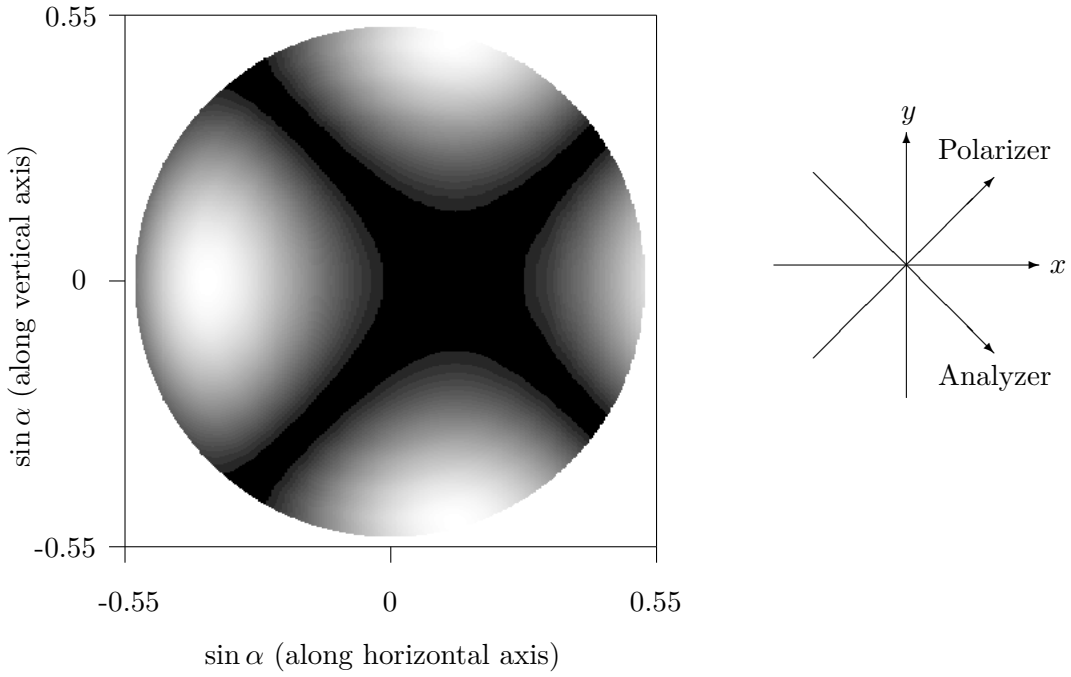

Figure 7.7: Interference figure calculated for a 20 μmcell, with $\theta = 5°$ throughout the cell. Compared to the homeotropic cell, the centre of the dark cross has moved horizontally by around 5°.

would appear identical under polarizing microscopy, so these conoscopy figures do indeed reveal depth-dependent information that would be hidden to the simpler experiment.

Although the majority of the information in these figures is due to birefringence, a little is due to thin film interference. This isn't very obvious in figures 7.6-7.8, because the ordinary refractive index of 5CB - about 1.5 - is near to that of glass. However, there are clear circular fringes in 7.9, because light passing through experiences a much higher index contrast, between the extraordinary index of 5CB - about 1.7, and glass. The distance between these fringes can help to determine the cell thickness, and in this case, their appearance indicates when the cell is far from homeotropic.

For V states the amplitude of the distortion can be found approximately by measuring the separation along the $y-$axis (or rather, perpendicular to the direction of flow) between the dark lobes apparent in interference figures like those of figure 7.8. To see this, consider a simplified tilt profile where $\theta = \theta_{\mathrm{RMS}}$ in the bottom half of the cell and $\theta = -\theta_{\mathrm{RMS}}$ in the top: preliminary computations showed that this was a good approximation. Light incident in the $yz-$plane can be split into s- and p-components having equal magnitudes

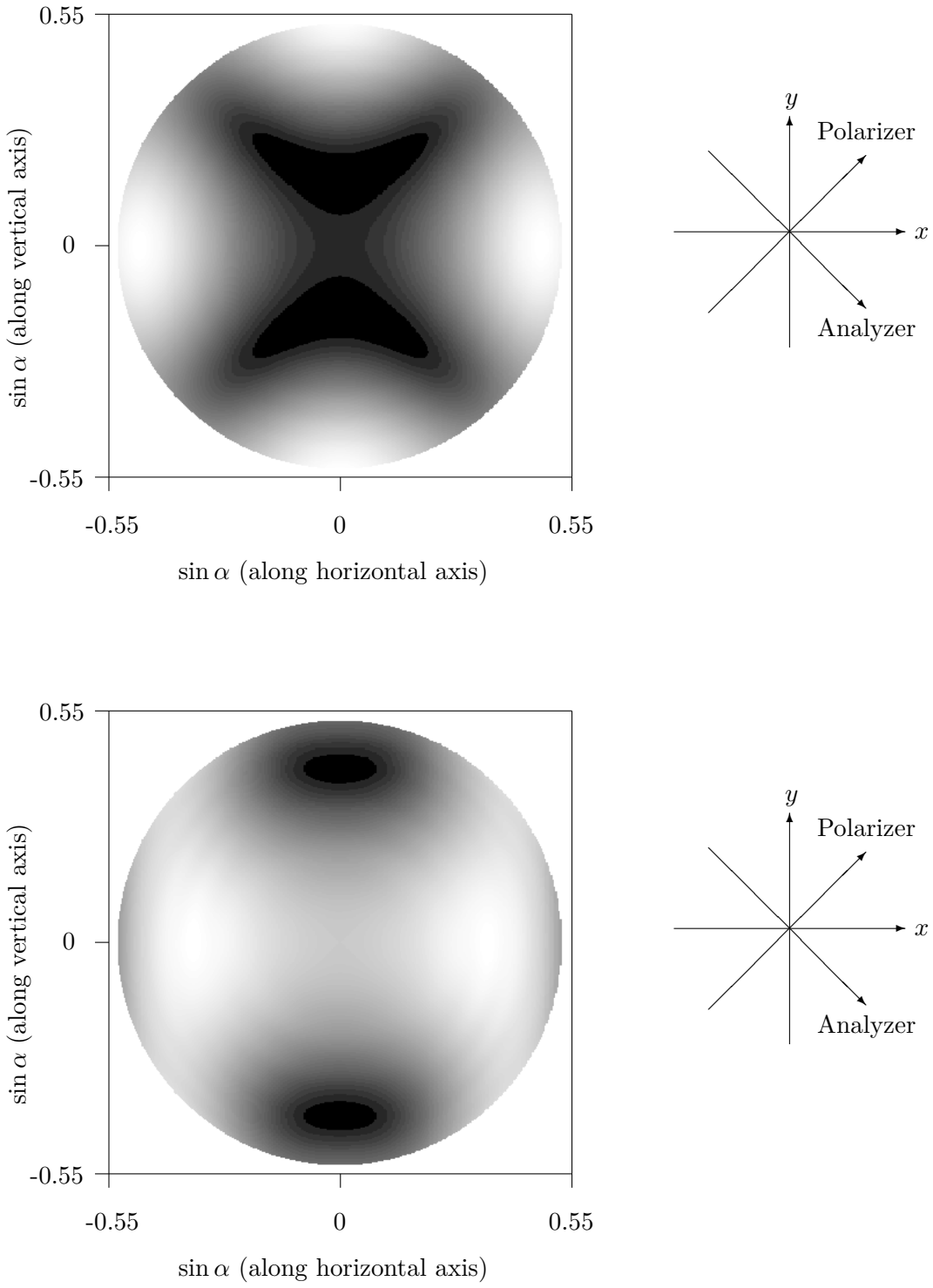

Figure 7.8: Interference figures calculated for a 20 μmcell in the V state In each case the figure is both up-down and left-right mirror symmetric. The isogyres have split into two dark lobes, whose vertical separation increases with the flow rate, 2 μlh^{-1} along the $x-$axis in the upper figure, and 5 μlh^{-1} in the lower. In fact, the centres of these lobes are displaced by approximately $\pm\theta_{\mathrm{RMS}}$ from the origin

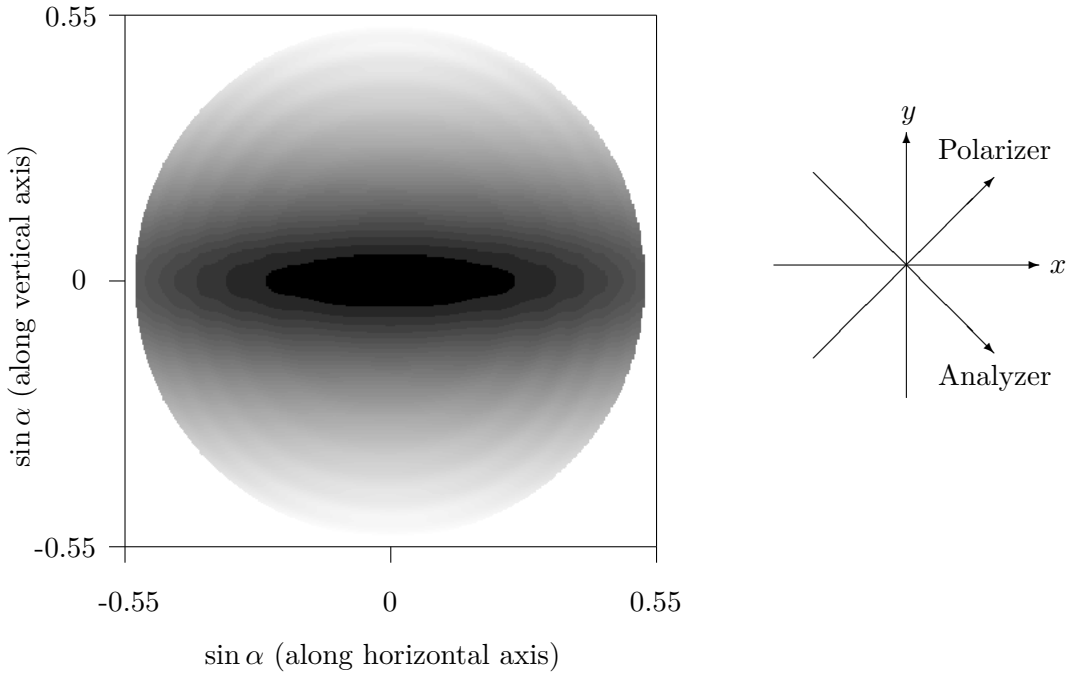

Figure 7.9: Interference figures calculated for a 20 μmcell in the H state Just as in the V state, interference figures computed for the H state are both up-down and left-right mirror symmetric. This figure has a dark isochrome along its horizontal axis, which indicates that the extraordinary wave is retarded by around 2π relative to the ordinary wave.

because the polarizer's transmission axis makes an angle $\pi/4$ with the $y-$axis. These are

$$\boldsymbol{E}_s = E(1, 0, 0) \tag{7.15}$$

$$\boldsymbol{E}_p = E(0, \cos\alpha', -\sin\alpha'), \tag{7.16}$$

where α' is the angle of refraction, which is approximately $n_\perp \alpha$ when the liquid crystal is close to the homeotropic state. Let the $\boldsymbol{c}$ be the projection of the director onto a plane perpendicular to the wavevector, that is to the plane made by E_s and E_p. For an extraordinary wave, the electric field is parallel to c, so that

$$\boldsymbol{E}.\boldsymbol{c} = |c|E \tag{7.17}$$

which implies that

$$\boldsymbol{E}_s.\boldsymbol{n} = \boldsymbol{E}_p.\boldsymbol{n}. \tag{7.18}$$

Similarly, for an ordinary wave,

$$\boldsymbol{E}.\boldsymbol{c} = 0 \tag{7.19}$$

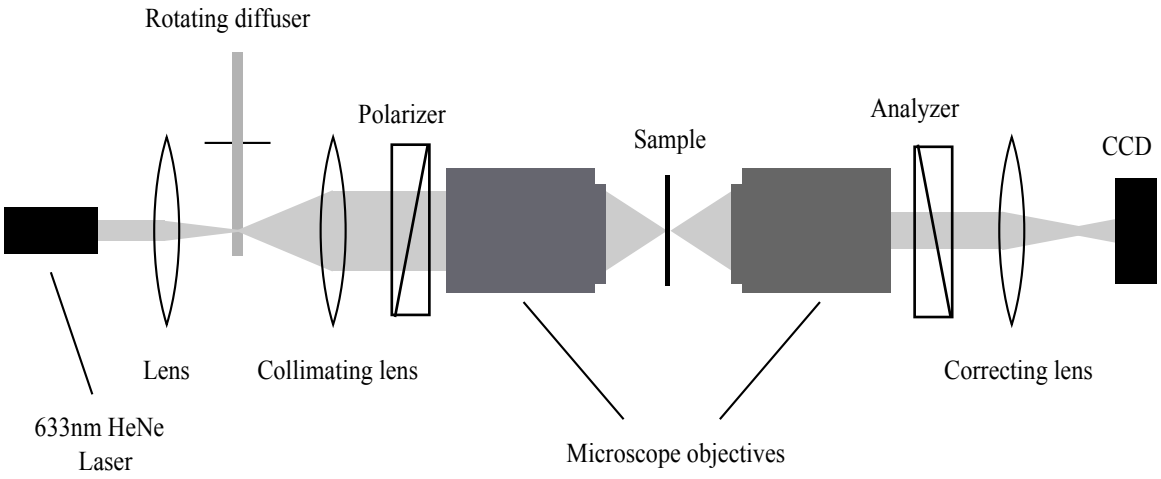

Figure 7.10: Laser conoscope apparatus.

which is true only when

$$\boldsymbol{E}_s.\boldsymbol{n} = -\boldsymbol{E}_p.\boldsymbol{n}. \tag{7.20}$$

If the incident wavevector is travelling in the positive y direction, condition (7.18) will be satisfied in the lower layer and condition (7.20) in the top layer when $n_\perp\alpha = \theta_{\mathrm{RMS}}$. The exact converse will be true when the incident light propagates in the direction of negative y and $n_\perp\alpha = -\theta_{\mathrm{RMS}}$. So, whenever, $|n_\perp\alpha| = |\theta_{\mathrm{RMS}}|$, the wave is entirely extraordinary for half of its journey, and entirely ordinary for the other half. Such a wave will emerge from the sample in the same polarization state as it entered and then be stopped by the analyzer, resulting in intensity minima on the figure's $y-$axis at $n_\perp\alpha = \pm|\theta_{\mathrm{RMS}}|$.

7.4 Experimental Method

7.4.1 Building and using a laser conoscope

A laser conoscope, shown in figure 7.10, was built, based upon devices reported in the literature [103, 104]. It is also similar to the convergent beam experiment previously built at Exeter [92], in that it is capable of observing signal variation due to both birefringence (as with any conoscope) and multiple-beam interference (because of its monochromatic light source).

7.4.1.1 Apparatus and design

The first section of the apparatus, at the top of figure 7.10, is essentially a light source. Laser light is focussed onto a small region of the diffuser, which then acts as an array

of point sources, randomly distributed over the illuminated region. Rotating the diffuser alters this distribution, so that averaged over the period of rotation, a uniform cone of light is emitted. This cone is collimated, resulting in beam of light which is uniform in cross section over more than a square centimeter. The beam then passes through a polarizer, set so that the principal axis is inclined at $\pi/4$ to the laboratory $y-$axis.

Next, light passes through the main assembly, consisting of the sample and two Mitotouyo Plan-Apo 50$\times$ long working distance microscope objectives. These are rather complex, but on a basic level the first of these allows a parallel beam of light about 3 mm in diameter to enter at one end, expands it, and then focusses it onto the sample. The resulting convergent beam has a numerical aperture of .55, and a working distance of 13 mm . Having passed through the sample, the second objective then collimates the light before it passes through the analyzer.

A correcting lens was introduced between the main assembly and the CCD because light exiting the second objective is not quite a parallel beam. The convergent beam passes through the two thick ($\sim$ 1 mm) glass substrates of the sample, resulting in changes to its focus. To first order, it is simply shifted along the $z-$axis by around 600 μm. However, the lights cone's angle spread is rather large, so rays from the outer part of the beam reach focus approximately 100 μm further along the $z-$axis than paraxial rays do. That means that when the outer part of the beam exiting the second objective, is parallel, the inner part is convergent. This is clearly visible: the center of the beam is much brighter than its edges. Only after this complex beam has passed through the final lens, is it uniform anywhere at all, and then only in a single plane parallel to the $xy-$plane - which is where the CCD must be located.

7.4.1.2 Alignment technique

Setting up the various components of the conoscope on a lathe bed is an involved procedure, in which each component must be added one at a time.

1. The laser is fixed so that its beam is parallel to the bed, forming the laboratory z-axis, and the spot at which it strikes the wall, more than 2 m from the source, marked. At the same time, two apertures are set up so that the beam passes through them wherever they are positioned along the bed.

2. One at a time, every lens but those in the main assembly is set on the bed and adjusted so that it focusses the beam onto the centre of one aperture, and its reflection strikes the center of the other.

Figure 7.11: Image projected onto the CCD when the analyzer is removed. This is the flat-field image: it is close to uniform, and has been lined up with the reticule.

3. The main assembly is placed on the bench, minus the sample. It is in line when the beam hits the spot marked on the wall, and when two sets of fringes of equal inclination, one reflected from each objective, are centered on an aperture placed between the laser and the first objective.

4. The sample is introduced and the first objective moved in the $-z$ direction so that a tight spot is formed on the wall. Then it is set so that the beam strikes its mark, and a new set of circular fringes, due to weak Fabry-Perot modes in the liquid crystal, are centred on the aperture. Next, it is moved along the laboratory $z-$axis until the beam spots visible on the outer surfaces of each substrates are both small.

5. The collimating lens is then placed on the bench, which results in a set of interference rings being projected onto the wall. These are centered on the mark before the diffuser is placed at the lens' focus.

6. The first aperture is moved in the $-z$ direction until the outer part of the beam exiting the second objective is parallel. This ensures that all of the diverging light is captured.

7. The polarizer is added.

8. Both the correcting lens and the CCD are set on the bed, and moved along the $z-$axis until a close-to-uniform disc fills the reticule superimposed on the captured image, visible on a PC screen (figure 7.11). The image won't be quite uniform, for four reasons. Fabry-Perot modes excited in the liquid crystal layer give rise to weak,

circular fringes. At the same time, the reflectivity of the glass slide increases with incident angle. These first two don't present a problem on their own, because the Berreman model predicts them. More seriously, the image is brighter along a line parallel to the polarizer's axis than perpendicular to it, because the entrance to the first objective presents a curved glass face to the beam. And dust in the light path causes the small, dark spots. Because of these effects, the close-to-uniform image is captured at this point to be used for flat-field correction.

9. The analyzer is positioned, and rotated so that the interference figure occupies the same disc as the close-to-uniform background.

7.4.1.3 CCD operation

The CCD, a Lumenera Infinity 1, is an RGB device and is used in two modes, 'normal' and 'saturated' in conjunction with a variable attenuator, of the two-wheel kind. In the normal mode, the attenuator and the exposure time are set so that the red sub-pixels in brightest parts of a typical image give a reading about midway through their range. For the results in this chapter, the exposure time was set to 30 ms, the coarse wheel of the attenuator to 2.0, and the fine wheel to 0.2. Once the normal mode has been set, a saturated mode, where the red sub-pixels frequently reached their maximum value, but the green pixels never did, could be obtained by setting the coarse wheel on the attenuator to 1.0. This mode proved useful when finding minima in the figure.

7.4.2 Inverse problems

It is possible, of course, to formulate the same kind of inverse problems for the conoscopy experiment as for the guided mode experiments, and indeed, that was the original intention. However, it turned out that the requisite information could be determined by considering simpler problems. Mirror symmetry in the interference figures has already been discussed, and inferring (limited) depth dependent information from it is well-posed.

There is a minor ill-posed problem to be considered: finding the position of the minima, y_{min}, (and hence θ_{RMS}) along the vertical axis in images captured at low flow rates. The CCD data is quite noisy ($\sigma \approx 0.05$), so simply looking for the lowest value is error-prone. Instead, cubic splines $I(y)$, smoothed using Tikhonov regularization, are fitted to the data, and the minima found from them. An estimate of the error in y_{min} is given by

$$\Delta y_{min} = \frac{\sigma}{|I''|} \tag{7.21}$$

where I'' is the second derivative of I with respect to y. This is standard procedure, and

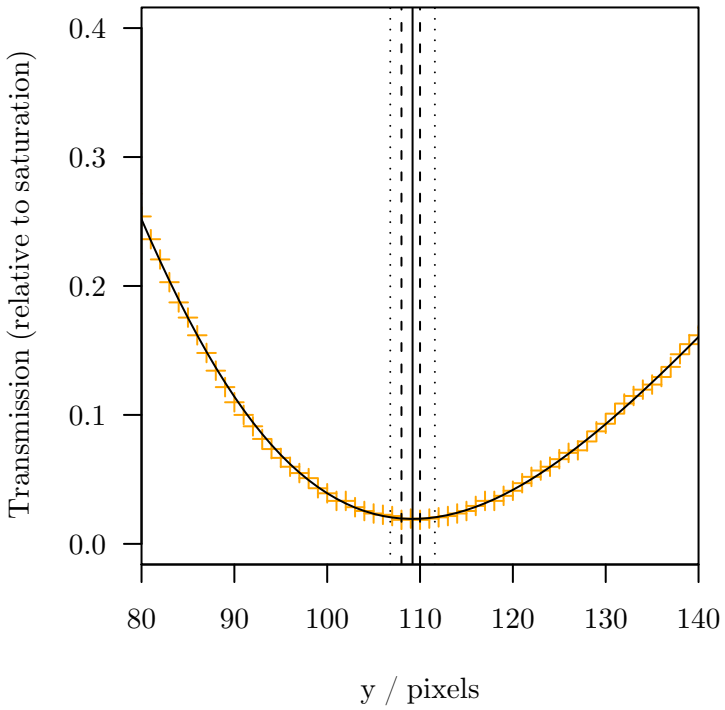

Figure 7.12: Smoothed spline fitted to a slice of conoscopy data parallel to the y-axis. Finding the minimum in the data is mildly ill-posed, leading in this case to two values (dashed lines). The smoothed spline has only one minimum (solid line), and also provides an error estimate (dotted lines).

is built into GNU R as part of the 'splines' package. Figure 7.12 shows a smoothed spline fitted to a sample of the data, together with its minumum, the minima in the data, and error estimates. To improve accuracy, images captured in saturated modes are used: the slopes either side of the minimum are much steeper (and hence I'' much larger), and the saturated areas are irrelevant.

7.5 Results and Discussion

Notably, the cells take much longer to reach equilibrium after the pump is switched on (or the flow rate is changed) than would be expected from the Ericksen-Leslie equations alone. It takes around 10 minutes, rather than the expected 100 ms, before the interference figure stops changing. This means that some component of the experiment must be compressible. Assuming the liquid crystal is not compressible (much like water) it seems that the rubber pipes which connect the syringe to the cell must be responsible. So, dynamical experiments driven by changes of pump speed are not possible with this set-up. Steady-state experiments should not be much affected, and neither should dynamical experiments driven by changing the applied field.

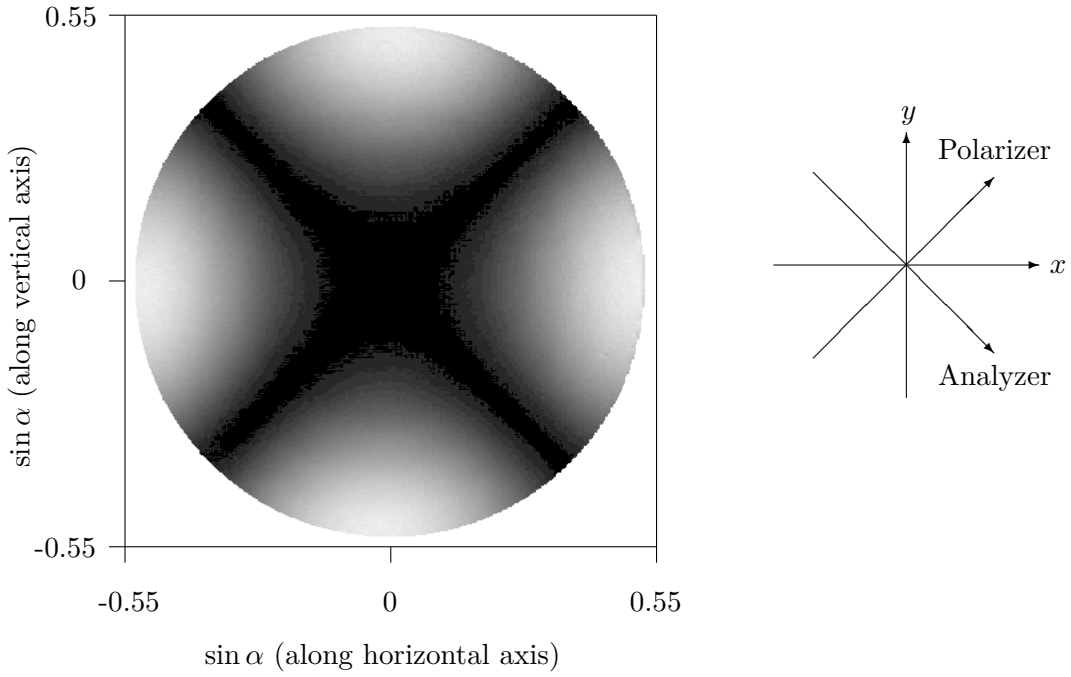

Figure 7.13: CCD image captured when the cell is in the ground state. This image was taken in the unsaturated mode, so the intensity grey-scale is taken from the red pixel. The gray-scale is gamma corrected, so that the contrast is greater near black then white. Clearly, the cell is homeotropically aligned.

7.5.1 V state

It is immediately obvious, looking at the conoscopy figures, that the cell is behaving as expected at low flow rates. Figure 7.13 and figure 7.14 show experimental CCD images, in the ground state and at flow rates of 2, and 5 μlh^{-1}. These compare well to the simulated figures of figure 7.6 and figure 7.8. Both theoretical and experimental images are mirror-symmetric about their horizontal axis - showing that the director has reflection symmetry about the cell mid-plane - and their vertical axis - implying that the director is confined to the $xz-$plane. As the flow rate is increased, the isogyres contract into dark lobes which move apart along the horizontal axis, just as they did in the simulations. It is safe to conclude that the cell is occupying a series of V states, with progressively increasing curvature.

Applying an electric field pulls the cell back toward the homeotropic state, more strongly as v_0 is increased. This is seen in figure 7.15, showing images captured at a flow rate of 5 μlh^{-1}, and at AC voltages of 1.77 V_{RMS} (upper) and 3.5 V_{RMS} (lower). Compared to the image with no voltage applied, the upper figure resembles an image captured at a lower flow rate. At the higher voltage, the cell must be nearly homeotropic - the image is much like that of figure 7.13, although the Maltese cross does not quite reach

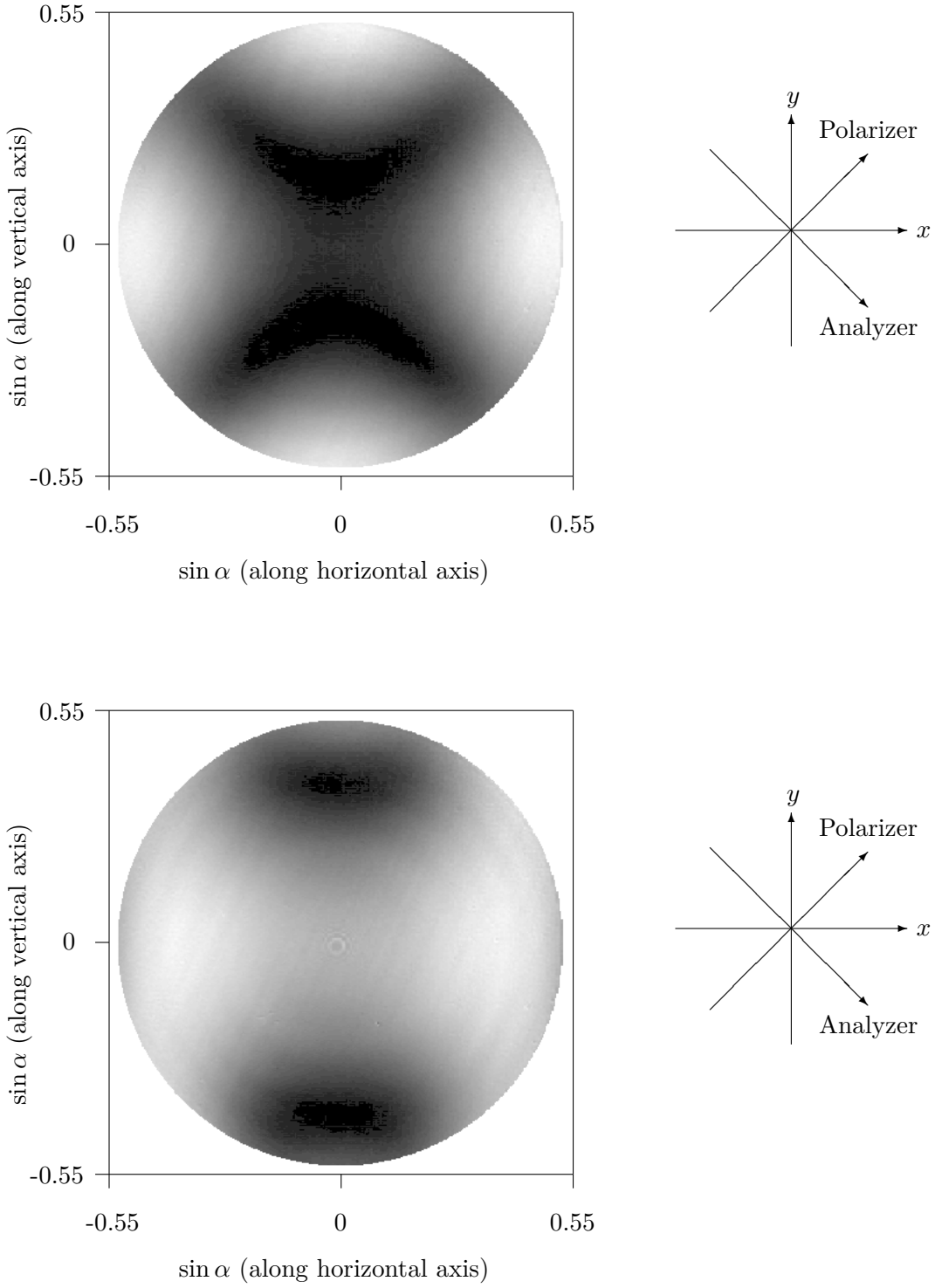

Figure 7.14: CCD image captured when the cell is in the V state. In the upper figure, liquid crystal is pumped through the cell at 2 μlh^{-1}, in the lower at 5 μlh^{-1}.

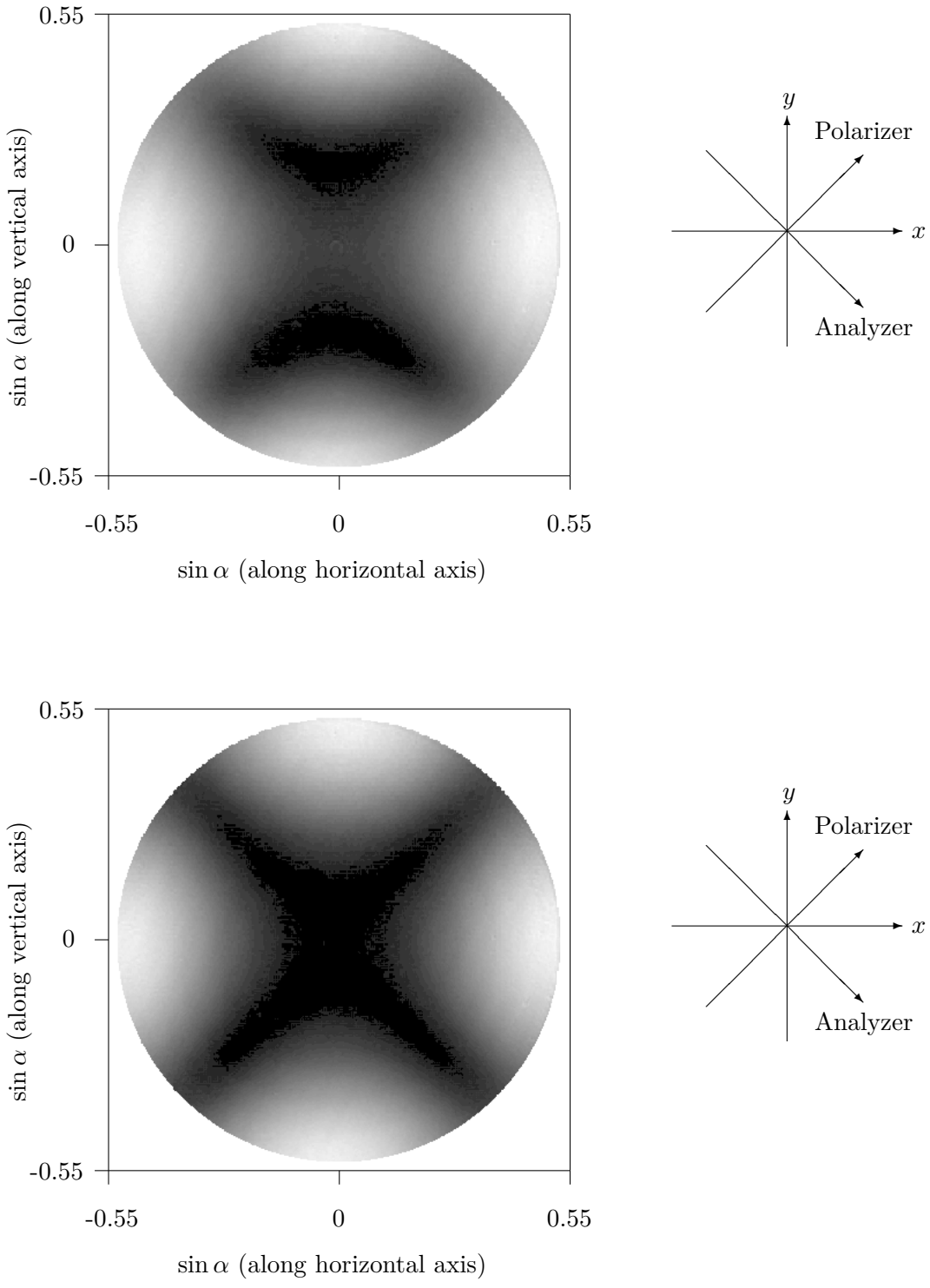

Figure 7.15: CCD images captured when the cell is in the V state, with voltages applied. In both figures the flow rate is 5 μlh^{-1}. The upper figure was captured after an AC voltage of 1.77V$_{\mathrm{RMS}}$ was applied, the lower after 3.5 V$_{\mathrm{RMS}}$ was applied. As the voltage is increased, the cell tends toward the homeotropic state.

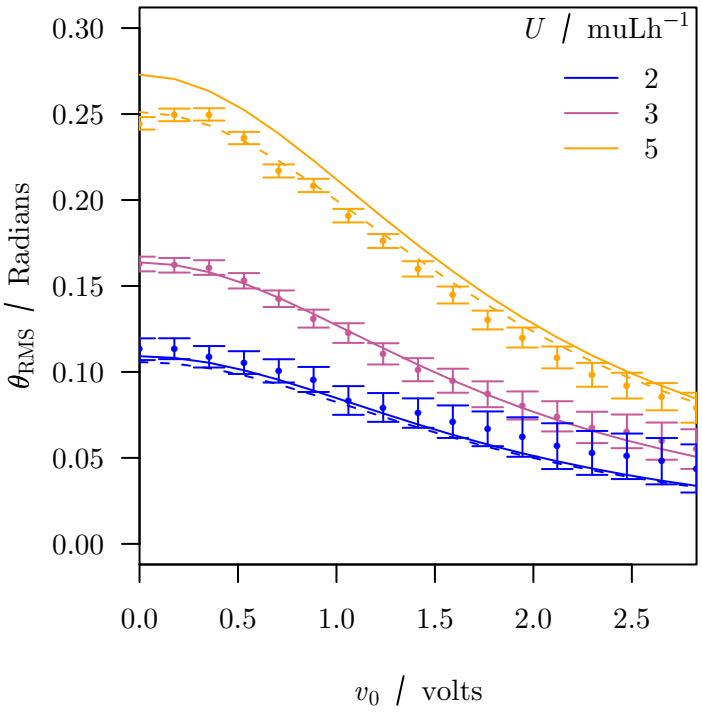

Figure 7.16: Plots of θ_{RMS} against applied voltage Experimental data (with error bars) is given by circles, linear theory by solid curves, and nonlinear theory by dashes.

to the disc's edge.

Following the procedure described earlier θ_{RMS}, was determined for each figure, and then α_2 and ϵ_a estimated. By comparing the 5 μlh^{-1} data with the linearised theory, the values $\alpha_2 = -0.77$ and $\epsilon_a = 10.7$ were obtained, which are similar to the literature values of $\alpha_2 = -0.81$ and $\epsilon_a = 11.5$ (summarized in reference [13] Appendix D). Figure 7.16 shows theoretical values of θ_{RMS} at three flow rates, all computed using these parameters together with the corresponding measurements. Notice that the error bars on θ_{RMS} grow as the voltage increases - as the figure approaches homeotropic, the minimum becomes obscured by a set of interference rings at the centre of the figure.

Agreement between the measurements and the linearized theory, that is (7.9), is worse at the highest flow rate (5 μlh^{-1}) than at the lowest (2 μlh^{-1}). Such a discrepancy is to be expected: the linear theory tends to overestimate θ_{RMS} compared to solutions of the nonlinear equations, more so as the flow rate increases. Values of the θ_{RMS} computed by solving the nonlinear equations numerically are also plotted in figure 7.16. These solutions were found using literature values for all the parameters bar α_2 and ϵ_a, for which the value given above are used.

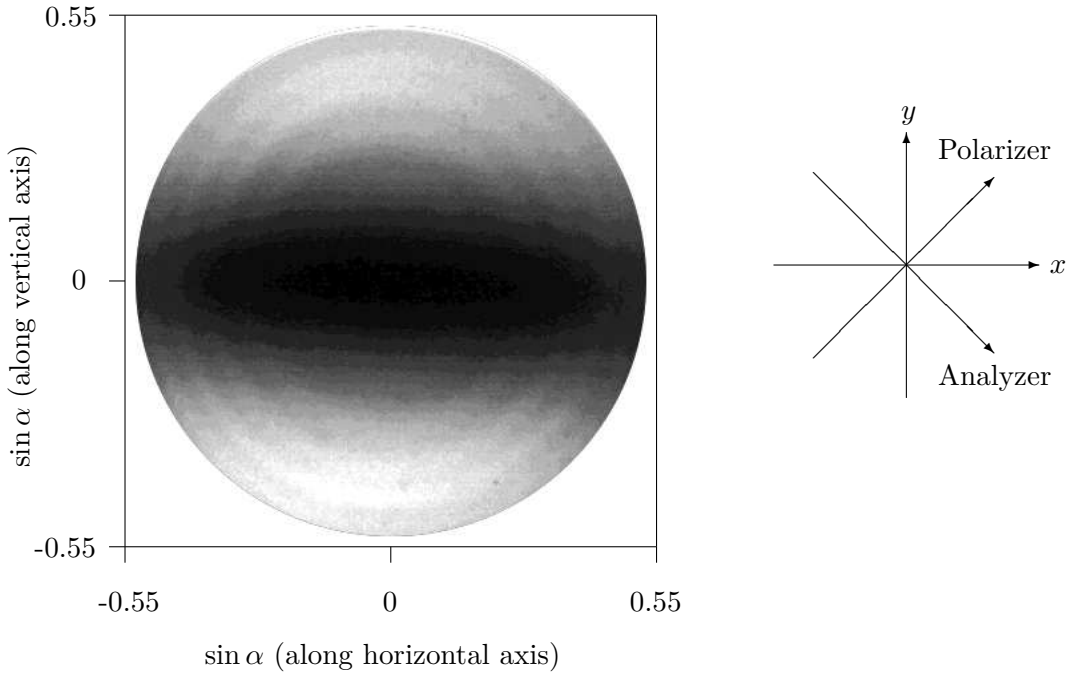

Figure 7.17: CCD image captured when the cell is in the H state The figure is close to mirror-symmetric about both of its axes, and features a dark isochrome parallel to its horizontal axes..

7.5.2 Transition to and from the H state

At flow rates of 7 μlh^{-1} and above, a transition into the H state is observed. Figure 7.17 is a CCD image taken after the system had been left flowing for several minutes. It is very much like the computed figure shown in figure 7.9: there is a dark stripe parallel to the horizontal axes, and like all the images seen in this chapter it is mirror-symmetric about its horizontal axes, indicating that the director is mirror-symmetric about the mid-plane. Just as in the calculations, circular fringes of equal inclination are much clearer for this state than for the V states.

The cell switches into the H state at a lower rate (about 7 μlh^{-1}, corresponding to $\bar{u} \approx 30$ μms^{-1}) than was expected from modelling (around 12 μlh^{-1}). There are several factors which might cause this. If weak anchoring is taken into account, in other words if surface energy is included in (7.6), the H state's energy increases even more slowly than before, so that the curves cross at a lower flow rate. Alternatively, the assumption that the liquid crystal responds primarily to the average flow across the width of the channel may not be adequate when considering the transition. If the faster flow speed at the centre of the channel, that is at $y = d/2$, is used instead, the transition is expected at a pumping rate of around 8 μlh^{-1}.

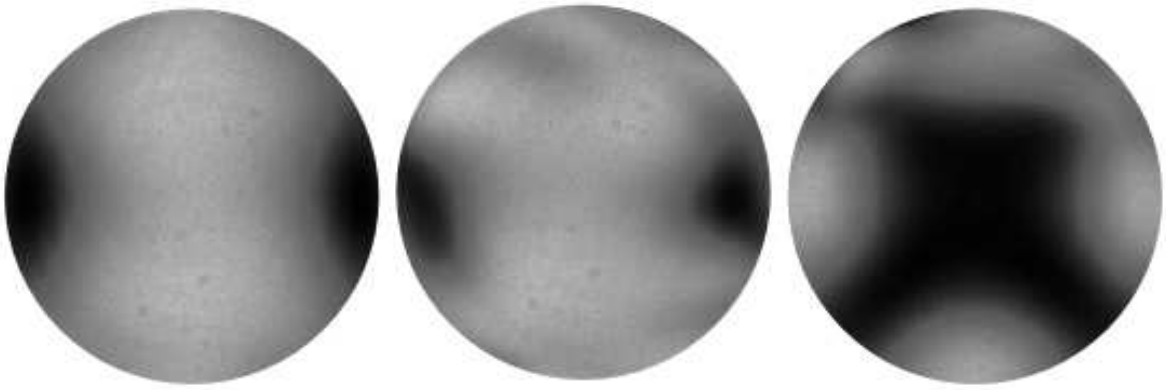

Figure 7.18: CCD images captured when the cell is switched from an H state to a V state The first image developed rapidly after a potential of 3.5 volts was applied. The second and third were taken 8 and 12 seconds later, and show the cell tending toward a homeotropic state, starting at the bottom of the image.

When a potential difference of 3.5 V was applied across the cell, it returned to the V state via a nucleated transition. When the field was first turned on, the first CCD image shown in figure 7.18 was recorded. Then, after several seconds, a new state swept through the image, starting at the bottom, as illustrated in the second and third images in figure 7.18. In other words, the transition was both slow, and spread across the cell rather taking place simultaneously throughout it. Fifteen seconds after the voltage was applied, the cell has settled into a homeotropic state. After the voltage was removed, the cell quickly relaxed to a V state and after several minutes, via another, slower, nucleated transition to an H state.

All of the transitions to an H state started near the inlet pipe. Figure 7.19 shows a sequence of polarizing microscopy images of a 7 mm length of the cell, taken by removing the microscope objectives from the conoscope apparatus. For each of these, the flow rate was 9 μlh^{-1}. Initially, the entire region was in a V state, and appeared bright. After a few seconds, a dark, spear shaped region entered the image on the left, moving in the same direction as the flow. If the polarizer and analyzer were rotated, so that one was parallel to the flow and the other perpendicular, the bright regions turned dark, while the dark regions remained as they were. Therefore, inside the spear the extraordinary wave must have experienced a phase delay of 2π relative to the ordinary wave, and so that part of the cell was in the H state. Ultimately, the spear travelled the length of the cell, leaving the regions behind it in the H state.

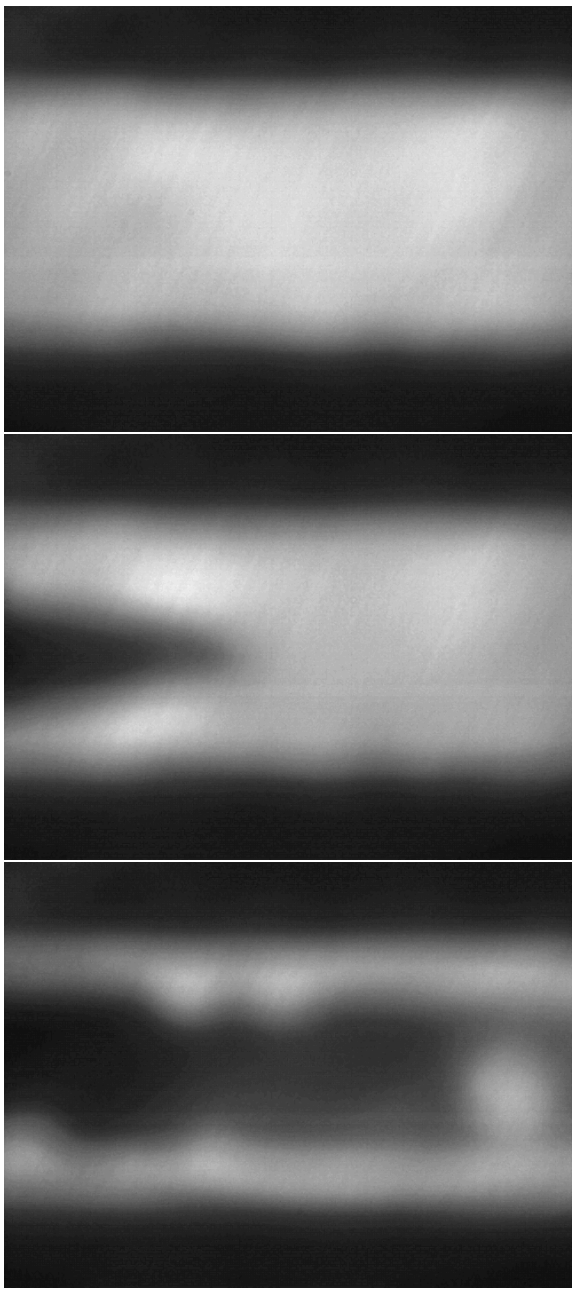

Figure 7.19: Sequence of polarizing microscopy images taken as the cell switches from a V state to an H state. In the top image, the cell is in the V state, and the whole channel is uniformly bright. Seconds later, a dark spear enters the field of view (second image), following the flow and leaving the cell behind it in the H state (third image).

7.6 Summary

Conoscopic observations of nematic liquid crystal pumped along a wide channel agreed well with theoretical predictions. At low flow rates, the liquid crystal adopted a V state, where the director was homeotropic at the walls and mid-plane but tilted forward, by a small amount, in the bottom half of the cell and backward, by the same amount, in the top. Distinctive interference figures were predicted, and observed for this state. Measuring the position of a dark region in this figure determined the root-mean-square tilt angle over the

cell. From there, it was possible to characterize the competition between viscous forces and an applied field, and estimate one Leslie viscosity, α_2, finding a value close to that known from the literature. At higher flow rates, an H state, where the director is horizontally aligned at the mid-plane, was predicted, and observed. The cell switched from a V state to this new state via a nucleated transition beginning at the channels inlet, and carried along the cell by the flow. By applying an electric field, a cell in an H state was switched to a V state, by another nucleated transition.

Chapter 8

Conclusions

8.1 Summary of the thesis

The central theme in this work was the recovery and subsequent analysis of the director profile within a nematic liquid crystal cell from optical measurements. Each of the cells studied was essentially one-dimensional, and the director was confined to a single plane: in other words, only untwisted configurations were considered. Several experiments, such as the fully leaky guided mode experiment, which characterise a cell by measuring its reflectivity and transmissivity as a function of incident angle and polarization state, were reviewed in chapter 2. It is simple enough to calculate this optical character for a cell whose nature is known, using Berreman's 4×4 matrix method. Performing the inverse operation, determining the structure within the cell from measurements, is rather more troublesome. Chapter 2 formulated a so-called *inverse problem*, intended to exploit Berreman's method for this purpose.

Chapter 2 also introduced the notion of an *ill-posed* problem. A *well-posed* problem has a solution, only one solution, and is not severely affected by experimental error. Inverse problems are usually ill-posed in at least the first of these senses, because an experimenter generally takes more measurements than the number of parameters he or she wants to find. Resolving that is simple enough: make an assumption about the errors in the data and then solve the resulting optimization problem. But they are often ill-posed in the second, or the third sense as well. These are more severe, and are treated in a similar manner - some kind of additional information must be introduced into the problem.

Singular value decomposition (SVD) analysis led to several observations on the inverse problem, presented in chapter 3. It had previously been observed that determining the entire, depth-varying dielectric tensor was an ill-posed problem of the third type. Here, it was shown that a simple problem, finding the deviation from an initial guess of the tilt profile in a HAN cell, when everything else is known, is still ill-posed in this same sense.

It was also shown that while the standard approach to this kind of problem, Tikhonov regularization, would not work, a variant upon it derived from continuum theory might. And finally, SVD analysis was used to compare the sensitivity of different experimental configurations to the tilt profile.

The inverse problem developed in chapter 3 needed a good initial guess of tilt profile. And looking forward to chapter 5, a program capable of finding solutions to the Ericksen-Leslie quickly would be needed. Both of these requirements were met by a computer program developed in chapter 4. The program proved to be both robust, and performed well: its source code is freely available to anyone who cares to use or modify it [1].

In chapter 5, the regularization technique introduced in chapter 3 was extended to include contributions due to electric fields, and due to rotational viscosity. It was then used to recover both steady-state and time-dependent tilt profiles from fully leaky guided mode experiments performed, by Tim Taphouse, on a HAN cell subjected to AC electric fields. Because these tilt profiles were not solutions of the Ericksen-Leslie equations, but close to them, they were called *weakly-constrained*. Looking at the steady-state weakly-constrained tilt profiles, it was clear that finite pre-tilt existed at the planar surface, while the backflow effect was recognizable in the unsteady profiles.

Strongly-constrained inverse problems were also examined in chapter 5, where the tilt profiles were solutions to the Ericksen-Leslie equations. They allowed estimates of many phenomenological parameters such as the elastic constants, and four Leslie viscosities, to be made. Furthermore, the uncertainties in these estimates were quantified. To this end, it was assumed that the reflection and transmission coefficients had nearly linear depenenence on each of the phenomenological parameters, at least over the region indicated by the uncertainties. Making this assumption allows for easy calculations: it is tantamount to a claim that the uncertainty in the parameters is described by a normal (or log-normal) probability density, which has a single maximum and a well-known rate of decay away from that. Since that seems to be a substantial assumption, the Metropolis algorithm was used to explore the probability density, and verify it. No additional maxima were found, and where the rate of decay was different from the normal distribution, it was faster, showing that the estimated uncertainties were, if anything, too large.

In chapter 6, the same cell was studied, but subjected to essentially DC fields. The weakly-constrained tilt profiles which were found were very different from those observed in AC experiments. First, the tilt profile depended not just on the magnitude, but on the sign of the electric field. Second, there were a number of transient features in the tilt profile

[1] The source code, or compiled packages for GNU/Linux, Mac OSX, and Windws, can be obtained from R-Forge
`http://r-forge.r-project.org/projects/photonics/`.

inconsistent with the Ericksen-Leslie equations. It was assumed that these transients were due to tiny concentrations of ions dissolved in the liquid crystal. To model them in detail, a drift-diffusion description of ionic contaminants was added to the computer program of chapter 4. It was only possible to model certain qualitative features of the experiment if its sign dependence was due to an excess of negative charge stuck to the homeotropic wall, and not substantially due to the flexoelectric effect. That conclusion was reinforced by a secondary experiment: when the surface chemistry at the homeotropic wall was altered, so was the sense of the sign dependence.

A new experiment, where determination of the basic shape of the director profile from the measurements is only a mildly ill-posed problem, was designed and run in chapter 7. Modelling showed that two interesting phenomena should be observed when liquid crystal is pumped through a homeotropically aligned cell. At low flow rates, the liquid crystal adopts a *V state*, in which the director is vertically aligned at the mid-plane, tilted forward in the lower half of the cell, and tilted backward in the upper half. The amplitude of this tilt increases as the flow rate does, and for a material whose dielectric anisotropy is positive, can be decreased by applying an electric field. At higher flow rates, the cell ought to switch into an *H state*, where the liquid crystal is aligned horizontally at the mid-plane. It should possible to switch the cell back from the H state to the V state by applying an electric field. It is impossible for the liquid crystal to move from one of these states to the other uniformly: instead a nucleated transition must occur.

A laser conoscope was built, and used to observe these states. It proved capable of extracting sufficient depth-dependent information through fairly simple analyses. In each of states described above the director is confined to the $xz-$plane, and is mirror symmetric about the cell's mid-plane. When and only when the first of these is true will the resulting conoscopy image be symmetric about its horizontal axis. Likewise, the second condition is linked to an image which is symmetric about its vertical axis. For the V state, the resulting figure is quite dramatic: as the flow rate increases, the Maltese cross figure found for the homeotropic state is continuously morphed into a pair of dark lobes, separate by a distance proportional to the RMS tilt angle in the cell. By measuring this separation as a function of flow rate and applied voltage, it was possible to estimate the Leslie viscosity α_2. For the H-state, the figure is usually less informative. Nonetheless, at one flow rate it was distinctive, and a nucleated transition from the H to the V state was observed as an electric field was applied.

8.2 Further work

One avenue worth further study is the inclusion of director twist in the weakly-constrained inverse problems discussed in chapters 3 and 5. Just as recovery of the tilt profile is an ill-posed problem, so is the recovery of twist profile. Extending the SVD analysis would be simple enough - one just needs to add a set of additional parameters, quantifying the twist in each layer to the forward problem. Likewise, the regularization technique should be easy to extend, by adding a term

$$r_\phi(z) = \begin{cases} 0 < z < d & \frac{1}{2}(k_{22}) \sin^2 \bar{\theta} \frac{\partial^2}{\partial z^2} \delta\phi \\ z = 0, z = d & \frac{1}{2d^2}(k_{22}) \sin^2 \bar{\theta} \delta\phi \end{cases} \tag{8.1}$$

to (5.3). Of course, the coefficient $\sin^2 \bar{\theta}$ may lead to some undesirable behaviour in near-homeotropic cells.

The growing importance of devices with nonuniform surfaces, such as the PABN cell and ZBD naturally leads to a interest in higher dimensional analogues of the weakly-constrained inverse problem. Polydorides [125] began some work in this area, limited to steady-state, using a similar regularization technique as that used here, with regard to guided-mode type experiments. Another, perhaps more promising line of enquiry is the analysis of Fluorescence Polarizing Confocal Microscopy (FCPM) data. This device provides a three dimensional view of the liquid crystal, but is limited to resolution of the order of several microns, due to stimulation of the dye for a substantial spread around the focal point. Improving this resolution would appear to be a deconvolution problem, a classic ill-posed problem.

Regarding sign dependent effects, a systematic study of surface chemistries and bulk liquid crystals is indicated. Substantial progress along this route has been made by Kisckha [77]. Trabi [56] has introduced a new experimental method for measuring $(e_s - e_b)$, while Smith [148] has investigated theoretically the effect of ionic contamination. Most recently, an entirely new approach to measuring $(e_s - e_b)$ and $(e_s + e_b)$ has been reported, which depends on the observation of domains which form when an electric field is applied to a planar homogeneous cell [149].

The laser conoscope is potentially an interesting device beyond its application here. Because it primarily measures birefringence effects, its results are somewhat easier to interpret than those of the guided-mode experiment. It could be extended to make dynamic measurements, using a faster diffuser. The sample could be index matched between glass hemispheres, removing the need for the correcting lens, and allowing a wider light cone.

Perhaps the most promising paths for future research start with the pressure driven

flow discussed in chapter 7. Sharon Jewell has begin to work on this system, characterising similar homeotropic cells under FCPM. A simple extension of this might be to use a channel whose width grows downstream. That way, one has continuous variation in the flow speed. What, for example, would happen as the fluid slows down through the point where the H to V transition would occur in uniform cells? Perhaps the entire cell would remain in one or other state, or perhaps a defect plane would form, with the cell divided into two, topologically distinct regions.

Then, of course, there are many alignments other than homeotropic to consider. If the cell has planar alignment, parallel to the flow, a state analogous to the V state should form at low flow rates. In contrast though, there would be no analogue to the H state - because $|\alpha_2| >> |\alpha_3|$, this state's free energy grows more quickly with flow rate, as well as starting out greater. If the cell is planar aligned, and inclined at, say $\pi/4$ to the flow, the director should twist into the flow toward the cell center. Finally, a bistable surface could be investigated. Imagine a ZBD type cell, in its VAN state. Driving liquid crystal through the cell would drive it toward the HAN state, perhaps causing it to switch. And it could be driven back toward the VAN state by a similar flow. Would it be possible to study the bistable anchoring with such a setup?

8.3 Publications and Presentations

8.3.1 Publications

1. "*Determination of the director profile in a nematic cell from guided wave data: an inverse problem*",
   S L Cornford, T S Taphouse, C J P Newton, and J R Sambles,
   New Journal of Physics **9**, 166 **2007**

2. "*Dynamic control of visible radiation by a liquid crystal filled Fabry-Perot etalon*"
   S A Jewell , S L Cornford, and J R Sambles,
   Journal of Applied Physics **102**, 093108 **2007**

3. "*Time-resolved sign dependent switching in a hybrid aligned nematic liquid crystal*",
   T S Taphouse, S L Cornford, J E Birkett, and J R Sambles
   New Journal of Physics **10** 083045 **2008**

4. "*Analysis of the sign dependent switching observed in a hybrid aligned nematic cell*",
   S L Cornford, T S Taphouse, and J R Sambles,
   accepted for publication in New Journal of Physics

5. "*Flow-driven transition observed in a vertically aligned nematic liquid crystal*",
   S L Cornford, S A Jewell, Fuzi Yang, P Cann, and J R Sambles,
   to be submitted to Physical Review Letters

8.3.2 Presentations

1. "*An inverse problem: determination of director profiles from waveguide experiments*".
   Poster, BLCS 2006, University of York, March 2006

2. "*An inverse problem: Characterisation of liquid crystal cells by waveguide experiments*".
   Poster , ILCC 2006, Keystone, Colorado, July 2006

3. "*Modelling flexoelectricity and ion transport in hybrid-aligned nematic cells*".
   Poster, Department of Engineering Science, University of Oxford, October 2006

4. "*Linear electro-optic effects and slow transients in hybrid-aligned cells*".
   Poster, BLCS 2007, University of Sheffield, March 2007

5. "*Pressure driven flow of nematic liquid crystals in thin cells*".
   Oral presentation, BLCS 2008, University of East Anglia, March 2008

Appendix A

Construction of HAN cells

The HAN cells discussed in chapters five and six of this thesis were constructed at HP Labs, Bristol either by Tim Taphouse, or by Stephen Cornford following instruction by Tim. Their design is shown in figure A.1. Overall, one needs to:

1. treat a pair of clean ITO coated glass slides so that one slide promotes planar homogeneous alignment and the other homeotropic alignment;
2. assemble a cell with a gap 3 μm thick;
3. fill the cell with liquid crystal.

The whole process must be carried out in a clean room, otherwise the cell will be full of dust particles, and so unlikely to have the correct thickness. Even so, the proportion of

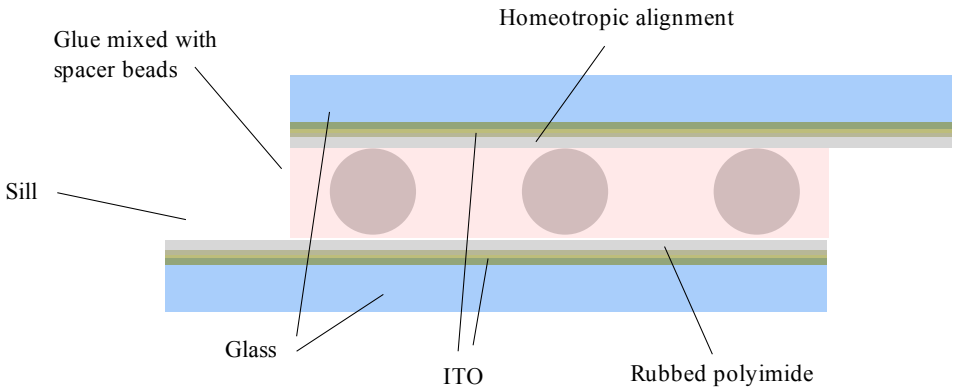

Figure A.1: Side view of a HAN cell

cells which must be discarded along the way is large: perhaps one in four will be uniformly thick, with a single domain of well aligned liquid crystal.

A.1 Planar homogeneous alignment

Rubbed Nissan SE-150 polyimide was use to promote planar homogeneous alignment in each HAN cell. A cold ITO coated glass substrate was fixed to the vacuum chuck of a spinner, which was set into motion at 6000 rpm. A 50 μl volume of the polyimide, a viscous liquid, was dropped onto the substrate, which was allowed to spin for 30 seconds. After spinning, each substrate would be inspected to ensure that it was coated evenly - the polyimde left a faint brown patina. Typically substrates were discarded if a splash shape, rather than an even coating, could be seen. Following spinning, the substrate was set on a hot plate, maintained at 95 °C, for 60 seconds, evaporating excess liquid. Several such substrates would be prepared this way, then allowed to cool before the whole batch was put in an oven at 185 °C for one hour. Next, the substrate was rubbed along its long axis, by passing it at grazing incidence underneath a velvet-surfaced drum spinning at 1000 rpm. Finally, the rubbed substrate was washed in isopropyl alcohol then deionised water.

A.2 Homeotropic alignment

Two homeotropic treatments were employed in this thesis. All Taphouse's cell, and some of Cornford's used a proprietary treatment supplied by Merck, and also used in HP Labs PABN cells. A further group of cells, made for the secondary experiment in chapter six, made use of Nissan SE-1211, a polyimide. A cold ITO coated glass substrate was fixed to the vacuum chuck of a spinner. 100 μl of the polyimide, also a viscous liquid, was dropped onto the substrate *before* turning on the spinner. The spinner was then run at 4000rpm for 30 seconds. After spinning, each substrate placed on a hot plate at 95 °C, for 60 seconds allowed to cool, then put in an oven at 185 °C for one hour. Visually, a properly coated substrate had an even, faint brown patina, fading to green at the very edges.

A.3 Assembly and Filling

Successful assembly of the cell relied, in part, on luck. One substrate was placed face-up on a flat surface, then lines of UV curing glue mixed with latex beads, each 3 μm in diameter, drawn along its edges with a metal wire. The other substrate was then be dropped onto the first. Sliding it around sometimes led, after curing, to a cell with a fairly uniform gap,

with only one or two visible fringes of equal depth visible. If not, the cell was discarded.

Finally, the cells were filled with the liquid crystal Merck ZLI-4788-000. The empty cell is set upon a hot-plate at 95 °C and a drop of liquid crystal placed on the sill. The liquid crystal melts into the isotropic phase, and is drawn into the gap by capillary forces. Once the liquid crystal has cooled back into the nematic phase, a last cull is performed: cells which do appear uniformly coloured when viewed between crossed polarizers are thrown away.

Appendix B

Optics formulae

B.1 Berreman's matrix

Berreman's matrix, Δ, which appears in the linear ordinary differential equation (2.11) is given below for a uniaxial system. This matrix is reduced from the general expression of Berreman [111] by assuming that the magnetic permeability tensor is unity, and that optical activity and Faraday rotation can be neglected. It has been given given by Lionheart (in S.I. units) for any dielectric tensor [120], and for the uniaxial case (in Gaussian units) by Wöhler [114]. It is assumed that the plane of incidence is the $xz-$plane, so that the components n_x and n_y of the director (or equivalently, the twist angle ϕ) must be transformed accordingly, while n_z and hence the tilt angle θ are unaffected.

$$\mathbf{\Delta} = \begin{bmatrix} \Delta_{11} & \Delta_{12} & \Delta_{13} & 0 \\ \Delta_{21} & \Delta_{11} & \Delta_{23} & 0 \\ 0 & 0 & 0 & \mu_0 c \\ \Delta_{23} & \Delta_{13} & \Delta_{43} & 0 \end{bmatrix}, \tag{B.1}$$

where

$$\Delta_{11} = -\frac{\epsilon_{xz}}{\epsilon_{zz}}\frac{k_x}{k_0}, \tag{B.2}$$

$$\Delta_{12} = \frac{\mu_0 c}{\epsilon_{zz}}\left(\epsilon_{zz} - \left(\frac{k_x}{k_0}\right)^2\right), \tag{B.3}$$

$$\Delta_{13} = -\frac{\epsilon_{yz}}{\epsilon_{zz}}\frac{k_x}{k_0} \tag{B.4}$$

$$\Delta_{21} = \epsilon_0 c\left(\frac{\epsilon_\perp}{\epsilon_{zz}}\left[\epsilon_\parallel - \epsilon_a n_y^2\right]\right), \tag{B.5}$$

$$\Delta_{23} = \epsilon_0 c\frac{\epsilon_\perp \epsilon_a}{\epsilon_{zz}} n_x n_y, \tag{B.6}$$

$$\Delta_{43} = \epsilon_0 c\left(\frac{\epsilon_\perp}{\epsilon_{zz}}\left[\epsilon_\parallel - \epsilon_a n_x^2\right] - \left(\frac{k_x}{k_0}\right)^2\right) \tag{B.7}$$

In the above, k_x is the $x-$component of the wavevector, which is conserved throughout the system,

$$\frac{k_x}{k_0} = n_I \sin\alpha \tag{B.8}$$

where n_I is the refractive index of the lowest layer (that is, the substrate), and α is the angle of incidence.

B.2 The scattering matrix

Recall that the the general solution to (2.11) is

$$\boldsymbol{\psi}(z_d) = \boldsymbol{P}\boldsymbol{\psi}(z_0), \tag{B.9}$$

when the initial values $\boldsymbol{\psi}(z_0)$ are known. Since $\boldsymbol{\psi}(z_0)$ describes both incoming and reflected waves, some manipulation is required. The procedure outlined below is well known,and is reported in the appendix of reference [120], for example.

At the lower interface, vectors $\boldsymbol{a}_0$ and $\boldsymbol{b}_0$ are defined in terms of the electric field components on the incident (propagating in the direction of positive z) and reflected (propagating in the direction of negative z) beams respectively, as

$$\boldsymbol{a}_0 = \begin{bmatrix} E_{x+}(z=0) \\ E_{y+}(z=0) \end{bmatrix} \tag{B.10}$$

and

$$\boldsymbol{b}_0 = \begin{bmatrix} E_{x-}(z=0) \\ E_{y-}(z=0) \end{bmatrix}. \tag{B.11}$$

A similar pair of vectors $\boldsymbol{a}_d$ and $\boldsymbol{b}_d$ are defined in terms of the electric field at the upper boundary. These are related to the $\boldsymbol{\psi}$ vectors through

$$\boldsymbol{\psi}_i = \boldsymbol{Q}_i \begin{bmatrix} \boldsymbol{a}_i \\ \boldsymbol{b}_i \end{bmatrix}. \tag{B.12}$$

where i stands for either 0 or d and

$$\boldsymbol{Q}_i = \begin{bmatrix} \cos\alpha & 0 & -\cos\alpha & 0 \\ \epsilon_0 c n_i & 0 & \epsilon_0 c n_i & 0 \\ 0 & 0 & 1 & 0 \\ 0 & \epsilon_0 c n_i \cos\alpha & 0 & \epsilon_0 c n_i \cos\alpha \end{bmatrix} \tag{B.13}$$

Then a *scattering matrix*, $\boldsymbol{S}$, is defined by the relation

$$\begin{bmatrix} \boldsymbol{a}_d \\ \boldsymbol{b}_0 \end{bmatrix} = \boldsymbol{S} \begin{bmatrix} \boldsymbol{a}_0 \\ \boldsymbol{b}_d \end{bmatrix}. \tag{B.14}$$

Since there is no incoming wave at the $z = d$ boundary, $\boldsymbol{b}_d = 0$, and hence (B.14) allows the transmitted wave $\boldsymbol{a_d}$ and the reflected wave $\boldsymbol{b}_0$ to be calculated for any incident wave $\boldsymbol{a}_0$. Denoting a 4×4 matrix in terms of 2×2 sub-matrices,

$$\boldsymbol{A} = \begin{bmatrix} \boldsymbol{A}_{11} & \boldsymbol{A}_{12} \\ \boldsymbol{A}_{21} & \boldsymbol{A}_{22} \end{bmatrix}, \tag{B.15}$$

some algebraic manipulation leads to a relationship between $\boldsymbol{P'} = \boldsymbol{Q_d}^{-1}\boldsymbol{P}\boldsymbol{Q_0}$, $\boldsymbol{I} = \boldsymbol{P'}^{-1}$ and $\boldsymbol{S}$:

$$\boldsymbol{S} = \begin{bmatrix} \boldsymbol{P'}_{11} & -\boldsymbol{P'}_{11}\boldsymbol{I}_{12} \\ \boldsymbol{I}_{21}\boldsymbol{P'}_{11} & \boldsymbol{I}_{22} - \boldsymbol{I}_{21}\boldsymbol{P'}_{11}\boldsymbol{I}_{12} \end{bmatrix}. \tag{B.16}$$

So, once $\boldsymbol{P}$ is known, all that is needed to calculate the reflection and transmission coefficients is a suitable choice of $\boldsymbol{a}_0$.

B.3 Fresnel's equations

The reflection and transmission coefficients measured at the prism-sample interface, $R'_{\mathrm{pp}}, \ldots, T'_{\mathrm{ss}}$ are related to those at the prism-air interface, $R_{\mathrm{pp}}, \ldots, T_{\mathrm{ss}}$ through Fresnel's equations. These take the form:

$$R_{\mathrm{pp}} = A_p B_p R'_{\mathrm{pp}}, \tag{B.17}$$

$$R_{\mathrm{ps}} = A_p B_s R'_{\mathrm{ps}}, \tag{B.18}$$

$$R_{\mathrm{sp}} = A_s B_p R'_{\mathrm{sp}}, \tag{B.19}$$

$$R_{\mathrm{ss}} = A_s B_s R'_{\mathrm{ss}}, \tag{B.20}$$

$$T_{\mathrm{pp}} = A_p B_p T'_{\mathrm{pp}}, \tag{B.21}$$

$$T_{\mathrm{ps}} = A_p B_s T'_{\mathrm{ps}}, \tag{B.22}$$

$$T_{\mathrm{sp}} = A_s B_p T'_{\mathrm{sp}}, \tag{B.23}$$

$$T_{\mathrm{ss}} = A_s B_s T'_{\mathrm{ss}}. \tag{B.24}$$

where

$$A_p = \left(\frac{n_I \cos\beta' + \cos\beta}{2\cos\beta'\cos\beta} \right)^2, \tag{B.25}$$

$$A_s = \left(\frac{\cos\beta' + n_G \cos\beta}{2\cos\beta'\cos\beta} \right)^2, \tag{B.26}$$

$$B_p = \left(\frac{\cos\beta' + n_G \cos\beta}{2n_G\cos\beta'\cos\beta} \right)^2, \tag{B.27}$$

$$B_s = \left(\frac{n_I \cos\beta' + \cos\beta}{2n_G\cos\beta'\cos\beta} \right)^2. \tag{B.28}$$

In the expressions above, β is the angle of incidence at the air-prism interface and β' is the angle of refraction.

Appendix C

Bayes Theorem and Tikhonov regularization

Bayes theorem links conditional probabilities by the formula

$$p(\boldsymbol{m}|\boldsymbol{b}) = \frac{p(\boldsymbol{b}|\boldsymbol{m})p(\boldsymbol{m})}{p(\boldsymbol{b})}. \tag{C.1}$$

The notation $p(\boldsymbol{m}|\boldsymbol{b})$ indicates a conditional probability density for $\boldsymbol{m}$, given $\boldsymbol{b}$, while $p(\boldsymbol{m})$ is the unconditional probability density for $\boldsymbol{m}$.

Assume that prior knowledge of $p(\boldsymbol{m})$ exists, usually from previous measurements such as a manufacturer's data sheet, and takes the form of a normal probability density

$$p(\boldsymbol{m}) = \exp(-\frac{||\boldsymbol{m}||_2^2}{2\sigma_m^2}), \tag{C.2}$$

- the *a priori* probability density for $\boldsymbol{m}$. Note that each element of $\boldsymbol{m}$ has been cast into units such that the variance of each is σ_m. Now, the conditional probability that the data is $\boldsymbol{b}$ given that the model vector is $\boldsymbol{m}$ is also assumed to be Gaussian:

$$p(\boldsymbol{b}|\boldsymbol{m}) \propto \exp(-\frac{||\boldsymbol{f}(\boldsymbol{m}) - \boldsymbol{b}||_2^2}{2\sigma_b^2}). \tag{C.3}$$

Provided the data, $\boldsymbol{b}$, may take any value (between 0 and 1) with equal probability $p(\boldsymbol{b})$ can be treated as just a constant factor - it does not affect the shape of $p(\boldsymbol{m}|\boldsymbol{b})$. Substituting (C.2) and (C.3) into (C.1),

$$p(\boldsymbol{m}|\boldsymbol{b}) \propto \exp\left(-\frac{||\boldsymbol{f}(\boldsymbol{m}) - \boldsymbol{b}||_2^2}{2\sigma_b^2} - \frac{||\boldsymbol{m}||_2^2}{2\sigma_m^2}\right). \tag{C.4}$$

This *Likelihood function* is greatest when $\ln p(\boldsymbol{m}|\boldsymbol{b})$ is also greatest, that is, when

$$\Phi = ||\boldsymbol{f}(\boldsymbol{m}) - \boldsymbol{b}||_2^2 + \frac{\sigma_b^2}{\sigma_m^2}||\boldsymbol{m}||_2^2 \tag{C.5}$$

is smallest. Replace σ_b^2/σ_m^2 with λ^2, and one has exactly (2.32) - the formula used in Tikhonov regularization.

Appendix D

Pressure driven flow in planar homogeneous cells

Some simulation results for a cell similar to that of chapter 7, but whose surfaces are treated to promote planar homogeneous alignment, are presented here. Two cases are considered: in section D.1, the alignment direction at both surfaces is parallel to the flow direction, that is, the $x-$axis, while in section D.2 it has been rotated, in the $xy-$plane, by $\pi/4$. In both cases, as in chapter 7, a 20 μm thick cell filled with 5CB is modelled.

D.1 Alignment and flow directions parallel

While pressure driven flow in a planar homogeneous cell resembles that of the homeotropic cell of chapter 7, there are marked differences. Figure D.1 shows modelled tilt profiles for the H states[1] of such a cell. Inasmuch as the director is mirror symmetric (because $\theta - \pi/2$ is antisymmetric) about the cell mid-plane, it is similar to that of the homeotropic case. However, the torque acting to pull the director out of planar orientation is proportional to α_3, in contrast to the torque proportional to α_2 pulling it away from homeotropic orientation. Since $|\alpha_3| \ll |\alpha_2|$, a much larger rate of flow will be needed to produce noticeable curvature in the director profile.

A second, qualitative difference can been seen in the plot of maximum tilt angle against flow rate, figure D.2. Its rate of change decreases, saturating a little below the point where the angle between the director and the fluid velocity, $\boldsymbol{u}$, is the Leslie angle,

$$\theta_L = \tan^{-1}\sqrt{\frac{\alpha_3}{\alpha_2}} \tag{D.1}$$

[1] I have named these H states because the director is horizontal at the cell mid-plane, so in that sense they are analagous to the H states of the homeotropic cell. But in another sense, they are analagous the V states, being close to uniform, and stable in the absence of flow

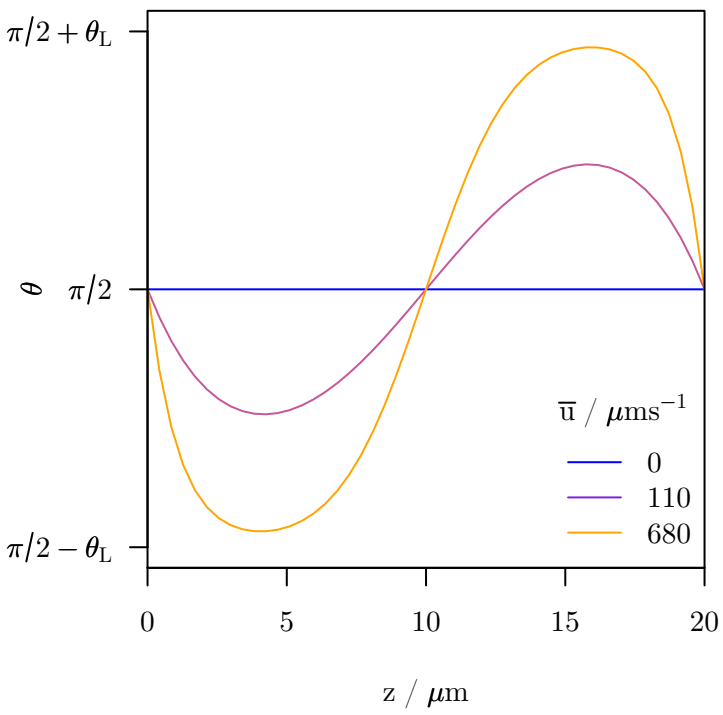

Figure D.1: Modelled H state tilt profiles for an in a planar homogeneous cell under pressure driven flow The director is aligned parallel to the flow at both cell walls

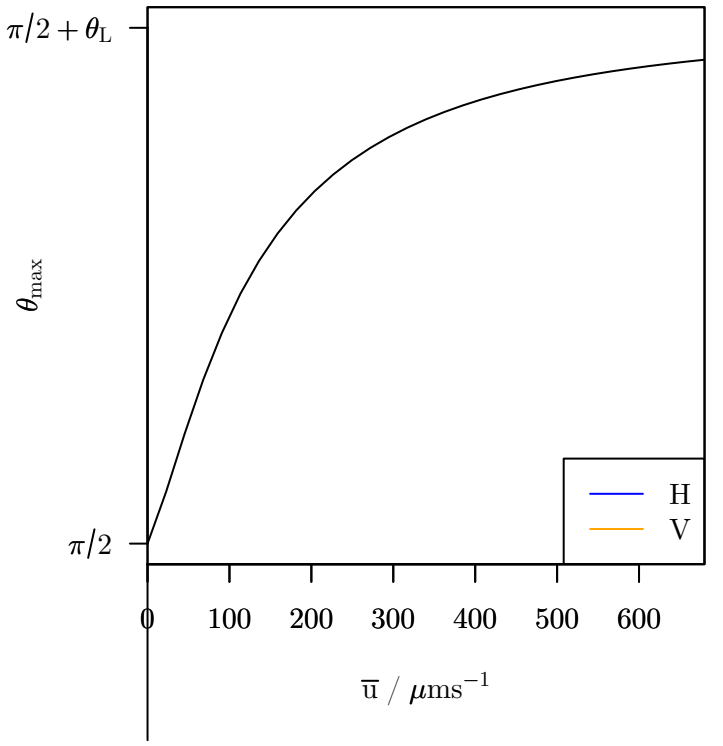

Figure D.2: Maximum tilt angle plotted against flow rate for a planar homogeneous cell The maximum tilt angle saturates close to the Leslie angle $\theta = \pi/2 - \theta_L$.

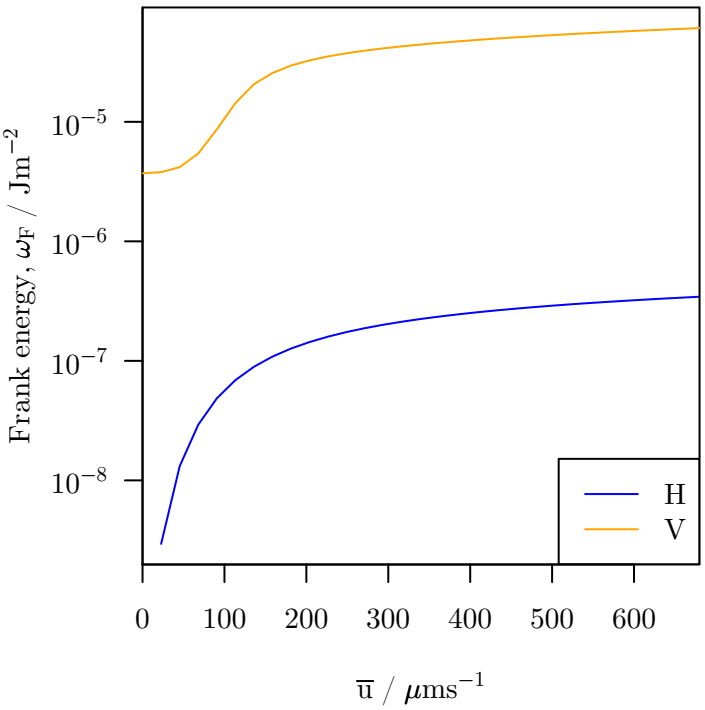

Figure D.3: Frank energy density plotted against flow rate for the H and V states of a planar homogeneous cell The vertical axis is logarithmic, so that the trends in both curves can be seen on the same plot.

This is perhaps not surprising, since, if $\boldsymbol{\nabla u}$ were uniform, the torque upon the director, which is proportional to

$$g = \alpha_3 \sin^2\theta - \alpha_2 \cos^2\theta \tag{D.2}$$

vanishes when $\theta = \pi/2 - \theta_L$. Note that saturation is only expected if α_2 and α_3 have the same sign, because the Lelsie angle is only defined in that case.

No transition analagous to the V to H transition seen in chapter 7 is expected for the planar homogeneous cell. The V state, in which the director must rotate by π across the cell, has a higher energy than the H state in the absence of flow, much as the H state has a higher energy than the V state in chapter 7. However, the elastic energy of the V state grows more quickly as well, as shown in figure D.3, so that it is never energetically favourable.

D.2 Alignment and flow directions oblique

When the alignment direction makes some oblique angle with the direction of flow, the situation becomes more complicated. Intuitively, one expects that the director will tend to twist into the flow, lining up with it at the mid-plane when the flow is fast. So the twist

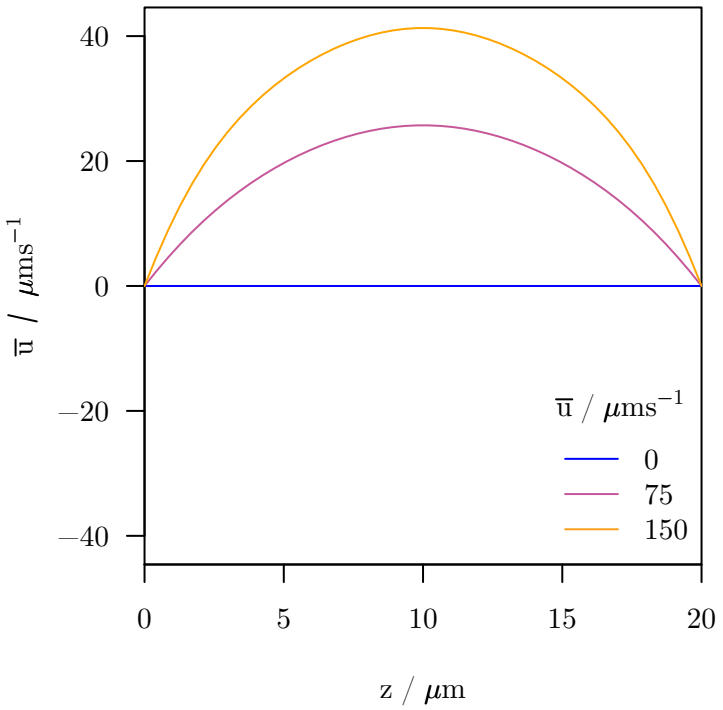

Figure D.4: Plots of the $y-$component of flow speed against z when $G_y = 0$ The net flow is not zero unless there is no flow along the $x-$axis.

angle, ϕ, varies across the cell. That being the case, the governing equation for ϕ, (4.10) must be solved. In addition, *both* momentum balance equations, (4.11) and (4.12), must be solved, with, at least, a pressure gradient G_x added to the right hand side of (4.11) , because they contain terms which couple the two components of the fluid velocity $\boldsymbol{u}$ when ϕ is non-zero.

What should the pressure gradient on the right hand side of the $y-$component of the momentum equation be? If it is zero, a net flow of liquid crystal parallel to the $y-$axis will be induced. Figure D.4 shows the $y-$component of the flow profile for three net flow rates along the $x-$axis. Such a flow could not exists in the channels built in chapter 7, although it might if the liquid crystal was free to flow out of the cell in any direction. In an alternative model, a pressure gradient, G_y parallel to the $y-$axis is sought for a given G_x such that the net flow parallel to the $y-$axis is zero: flow fields in this case are shown in figure D.5. Ultimately, the two models predict slightly different director profiles. Figure D.6 shows the twist angle at the cell mid-plane as a function of net flow rate along the x-axis in each case. When no net flow is permitted along the $y-$axis, the director twists a little more.

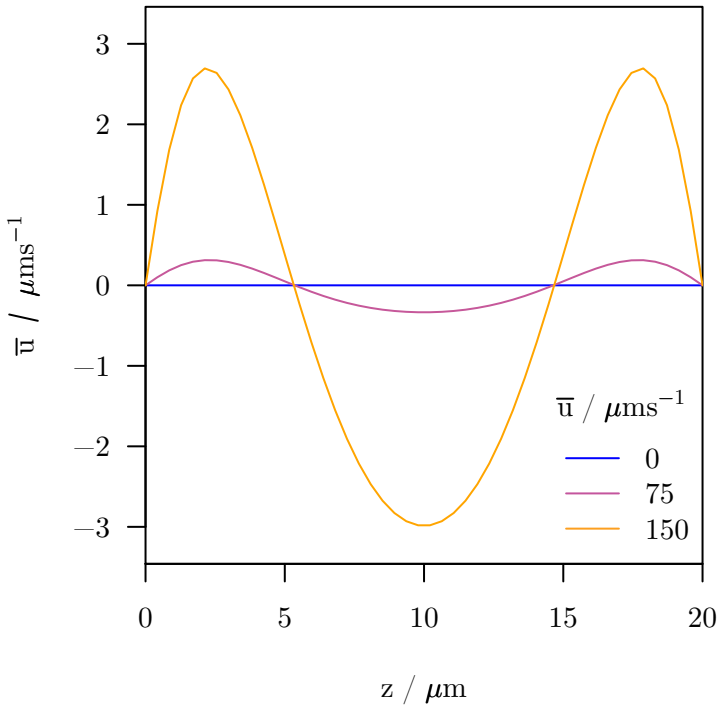

Figure D.5: Plots of the $y-$component of flow speed against z when $G_y \neq 0$ G_y is chosen so that the net flow along the $y-$ axis is zero

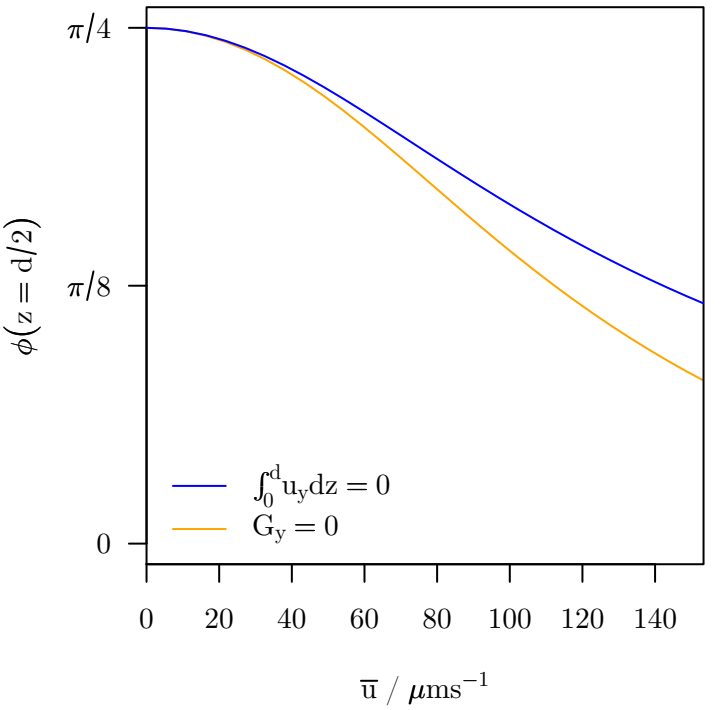

Figure D.6: Plots mid-plane twist angle against net flow rate along the $x-$axis. If no flow is permitted along the $y-$axis, the director twists a little more.

Bibliography

[1] D Adams. *The Hitch Hiker's Guide to the Galaxy*. Ballantine Books, 1979.

[2] J H Burroughes, D D C Bradley, A R Brown, R N Marks, K Mackay, R H Friend, P L Burns, and A B Holmes. Light emitting diodes based on conjugated polymers. *Nature*, 347: 539, 1990.

[3] F Reinitzer. Contributions to the understanding of Cholesterol. *Monatshefte für Chemie (Wien)*, 9:421, 1888. English translation available as paper A1 in [4].

[4] T J Sluckin, D A Dunmur, and H Stegemeyer. *Crystals that flow: classic papers from the history of liquid crystals*. Taylor and Francis, 2004.

[5] O Lehmann. On flowing crystals. *Zeitschrift für Physikalische Chemie*, 4:462, 1889. English translation available as paper A2 in [4].

[6] F C Bawden, N W Pirie, J D Bernal, and I Fankuchen. Liquid crystalline substances from virus-infected plants. *Nature*, 138:1051, 1936.

[7] A N H Creager. *The Life of a Virus: Tobacco Mosaic Virus as an Experimental Model 1930-1965*. The University of Chicago Press, 2002.

[8] G W Gray, K J Harrison, and J A Nash. New family of nematic liquid crystals for displays. *Electronics Letters*, 9:130, 1979. Available as paper D7 in [4].

[9] G W Gray and S M Kelly. Liquid crystals for twisted nematic display devices. *Journal of Materials Chemistry*, 9:2037, 1999.

[10] G Friedel. The mesomorphic states of matter. *Annales de Physique*, 18:273, 1922. Extracts translated to English available as paper B1 in [4].

[11] M J Stephen and J P Straley. Physics of liquid crystals. *Reviews Of Modern Physics*, 46: 607, 1974.

[12] S Chandrasekhar. *Liquid crystals*. Cambridge University Press, second edition, 1992.

[13] I W Stewart. *The static and dynamic continuum theory of liquid crystals*. Taylor and Francis, 2004.

[14] W Zwetkoff. On molecular order in the anisotropic liquid phase. *Acta Physicochmica U.R.S.S.*, 15:131, 1942. English translation available as paper C2 in [4].

[15] W Maier and A Saupe. A simple molecular theory of the nematic liquid-crystalline state. *Zeitschrift Naturforschung*, 13a:564, 1958. English translation available as paper C3 in [4].

[16] L A Madsen, T J Dingemans, M Nakata, and E T Sumulski. Thermotropic biaxial nematic liquid crystals. *Physical Review Letters*, 92:145505, 2004.

[17] M J Freiser. Ordered states of a nematic liquid crystal. *Physical Review Letters*, 24:1041, 1970.

[18] F C Frank. On the theory of liquid crystals. *Discussions of the Faraday Society*, 25:19, 1958. Available as paper C4 in [4].

[19] P G de Gennes. Short range order effects in the isotropic phase of nematics and cholesterics. *Molecular Crystals and Liquid Crystals*, 12:193, 1971. Available as paper C7 in [4].

[20] A A Sonin. *The surface physics of liquid crystals*. Gordon and Breach, 1995.

[21] J A Castellano. Surface anchoring of liquid crystal molecules on various substrates. *Molecular Crystals and Liquid Crystals*, 94:33, 1983.

[22] Ch Mauguin. On the liquid crystals of Lehmann. *Bulletin de la Société francaise de Minéralogie*, 34:71, 1911. English translation available as paper A8 in [4].

[23] F Grandjean. The orientation of anisotropic liquids on crystals. *Bulletin de la Société francaise de Minéralogi*, 39:163, 1916. English translation available as paper A10 in [4].

[24] P Chatelain. On the orientation of liquid crystals by rubbed surfaces: experimental study. *Comptes rendus de l'Académie des Sciences*, 213:875, 1941. English translation available as paper B11 in [4].

[25] D W Berreman. Solid surface shape and the alignment of an adjacent nematic liquid crystal. *Physical Review Letters*, 28:1683, 1972.

[26] A Rapini and M Papoular. Distortion d'une lamelle nematique sous champ magnetique conditions d'ancrage aux parois. *Journal de Physique Colloques*, 30:C4, 1969.

[27] C W Oseen. The theory of liquid crystals. *Transactions of the Faraday Society*, 29:883, 1933. Available as paper B5 in [4].

[28] V Freedericksz and V Zolina. On the use of a magnetic field in the measurement of the forces tending to orient an anisotropic liquid in a thin homogeneous layer. *Transactions of the American Electrochemical Society*, 55:85, 1929. Available as paper B3 in [4].

[29] P D Brimicombe, L A Parry-Jones, S J Elston, and E P Raynes. Modeling of dual frequency liquid crystal materials and devices. *Journal of Applied Physics*, 98:104104, 2005.

[30] S A Jewell, T S Taphouse, and J R Sambles. Rapid switching in a dual-frequency hybrid aligned nematic liquid crystal cell. *Applied Physics Letters*, 87:021106, 2005.

[31] M Born and E Wolf. *Principles of optics*. 7th expanded edition, 1999.

[32] R B Meyer. Piezoelectric effects in liquid crystals. *Physical Review Letters*, 22:918, 1969.

[33] J Prost and J P Marcerou. On the microscopic interpretation of flexoelectricity. *Journal de Physique*, 38:315, 1976.

[34] P Rudquist and S T Lagerwall. On the flexoelectric effect in nematics. *Liquid Crystals*, 23: 503, 1997.

[35] A Sugimura, N Matsui, Y Takahashi, H Sonomura, H Naito, and M Okuda. Transient currents in nematic liquid crystals. *Physical Review B*, 43:8272, 1991.

[36] G Barbero and L R Evangelista. Comment on "Optical determination of flexoelectric coefficients and surface polarization in a hybrid aligned nematic cell". *Physical Review E*, 68: 023701, 2003.

[37] K Neyts, S Vermael, C Desimpel, G Stojmenovik, A R M Vershueren, D K G de Boer, R Snijkers, P Machiels, and A van Brandenburg. Lateral ion transport in nematic liquid-crystal devices. *Journal of Applied Physics*, 94:3891, 2003.

[38] G Barbero, A K Zvezdin, and L R Evangelista. Ionic adsorption and equilibrium distribution of charges in a nematic cell. *Physical Review E*, 59:1846, 1999.

[39] L R Evangelista and G Barbero. Intrinsic characteristic times in the drift-diffusion problem. *Liquid Crystals*, 31:1399, 2004.

[40] L R Evangelista and G Barbero. Adsorption-desorption phenomenon and the kinetic equation at interfaces in liquid crystalline systems. *Liquid Crystals*, 33:1, 2006.

[41] L R Evangelista and G Barbero. Adsorption phenomenon and external field effect on an isotropic liquid containing impurities. *Physical Review E*, 64:021101, 2001.

[42] G Barbero, L R Evangelista, and D Olivero. Asymmetric ionic adsorption and cell polarization in liquid crystals. *Journal of Applied Physics*, 87:2646, 2000.

[43] F M Leslie. Some constitutive equations for liquid crystals. *Archives for Rational Mechanics and Analysis*, 28:265, 1968. Available as paper C6 in [4].

[44] F M Leslie. Some topics in continuum theory of nematics. *Philospohical Transactions of the Royal Society of London, A*, 309:155, 1983.

[45] F M Leslie. Continuum theory for nematic liquid crystals. *Continuum Meachnics and Thermodynamics*, 4:167, 1992.

[46] T Carlsson and F M Leslie. The development of theory for flow and dynamic effects for nematic liquid crystals. *Liquid Crystals*, 26:1267, 1999.

[47] J L Ericksen. On equations of motion for liquid crystals. *Quarterly Journal of Mechanics and Applied Mathematics*, 29:203, 1976.

[48] F. Brochard, P. Pieranski, and E. Guyon. Dynamics of the orientation of a nematic-liquid-crystal film in a variable magnetic field. *Physical Review Letters*, 28:1681, 1972.

[49] C V van Doorn. Dynamic behavior of twisted nematic liquid-crystal layers in switched fields. *Journal of Applied Physics*, 46:3738, 1975.

[50] D W Berreman. Liquid-crystal twist cell dynamics with backflow. *Journal of Applied Physics*, 46:3746, 1975.

[51] S A Jewell and J R Sambles. Observation of backflow in the switch-on dynamics of a hybrid aligned nematic. *Applied Physics Letters*, 84:46, 2004.

[52] O Parodi. Stress tensor for a nematic liquid crystal. *Journal de Physique*, 31:581, 1970.

[53] M Meisowicz. The three viscosity coefficients of liquid crystals. *Nature*, 158:27, 1946.

[54] T S Taphouse. *Time resolved optical characterisation of hybrid aligned nematic cells.* PhD thesis, University of Exeter, 2007.

[55] Fuzi Yang, J R Sambles, and G W Bradberry. Half-leaky guided wave determination of azimuthal anchoring energy and twist elastic constant of a homogeneously aligned nematic liquid crystal. *Journal of Applied Physics*, 85:728, 1999.

[56] C L Trabi, C V Brown, A A T Smith, and N J Mottram. Interferometric method for determining the sum of the flexoelectric coefficients $e_1 + e_3$ in an ionic nematic material. *Applied Physics Letters*, 92:223509, 2008.

[57] M Schadt and W Helfrich. Voltage-dependent optical activity of a twisted nematic liquid crystal. *Applied Physics Letters*, 18:127, 1971.

[58] E P Raynes and C M Waters. Supertwisted nematic liquid crystal layers. *Displays*, 8:59, 1987.

[59] G Waton, A Ferre, A Candau, J N Perbet, and Hareng M. Characterization of distortions induced by a flow or an electric field in nematic films using conoscopic experiments. *Molecular Crystals and Liquid Crystals*, 78:237, 1981.

[60] J A Müller, R S Stein, and H H Winter. Director dynamics of uniformly aligned nematic liquid crystals in transient shear flow. *Rheologica Acta*, 33:473, 1994.

[61] S V Pasechnik, V G Chigrinov, D V Shmeliova, V A Tsvetkov, and A N Vornonv. Anisotropic shear viscosity in nematic liquid crystals: new optical measurement method. *Liquid Crystals*, 31:585, 2004.

[62] S A Jewell. *Optical waveguide characterisation of hybrid aligned nematic liquid crystal cells.* PhD thesis, University of Exeter, 2002.

[63] S A Jewell and J R Sambles. Dynamic response of a dual-frequency chiral hybrid aligned nematic liquid-crystal cell. *Physical Review E*, 73:011706, 2006.

[64] S R Warrier and N V Madhusudana. An AC electrooptic technique for measuring the flexoelectric coefficient ($e_1 + e_3$) and anchoring energies of nematics. *Journal de Physique*, 7:1789, 1997.

[65] S A Jewell and J R Sambles. Fully leaky guided mode study of the flexoelectric effect and surface polarization in hybrid aligned nematic cells. *Journal of Applied Physics*, 92:19, 2002.

[66] T Takahashi, S Hashidate, H Nishijou, M Usui, M Kimura, and T Akahane. Novel measurement method for flexoelectric coefficients of nematic liquid crystals. *Japanese Journal of Applied Physics*, 37:1865, 1998.

[67] N V Madhusudana and G Durand. Linear flexo-electro-optic effect in a hybrid aligned nematic liquid crystal cel. *Journal de Physique Lettres*, 46:L195, 1985.

[68] N T Kirkman, T Stirner, and W E Hagston. Continuum modelling of hybrid-aligned nematic liquid crystal cells: optical response and flexoelectricity-induced voltage shift. *Liquid Crystals*, 30:1115, 2003.

[69] S Ponti, P Ziherl, C Ferrero, and S Zumer. Flexoelectro-optic effect in a hybrid nematic liquid crystal cell. *Liquid Crystals*, 26:1171, 1999.

[70] R A Ewings, C Kischka, L A Parry-Jones, and S J Elston. Measurement of the difference in flexoelectric coefficients of nematic liquid crystals using a twisted nematic geometry. *Physical Review E*, 73:011713, 2006.

[71] N A Clark and S T Lagerwall. Submicrosecond bistable electro-optic switching in liquid crystals. *Applied Physics Letters*, 36:899, 1980.

[72] S J Elston. Recovery of symmetry in flc devices for useful grey-scale performance. *Displays*, 16:141, 1995.

[73] G P Bryan-Brown, C V Brown, J C Jones, E L Wood, I C Sage, P Brett, and J Rudin. Grating aligned bistable nematic device. In *Proceedings of the Electronic Information Displays Conference*, page 37, 1997.

[74] S Kitson and A Geisow. Controllable alignment of nematic liquid crystals around microscopic posts: Stabilization of multiple states. *Applied Physics Letters*, 80:3635, 2002.

[75] S C Kitson, E G Edwards, and A D Geisow. Designing liquid crystal alignment surfaces. *Applied Physics Letters*, 92:073503, 2008.

[76] A J Davidson and N J Mottram. Flexoelectric switching in a bistable nematic device. *Physical Review E*, 65:051710, 2002.

[77] C Kischka, L A Parry-Jones, S J Elston, and E P Raynes. Measurement of the flexoelectric coefficients e_1 and e_3 in nematic liquid crystals. *Molecular Crystals and Liquid Crystals*, 480: 103, 2008.

[78] L A Parry-Jones and S J Elston. Flexoelectric switching in a zenithally bistable nematic device. *Journal of Applied Physics*, 97:093515, 2005.

[79] I Dozov, M Nobili, and G Durand. Fast bistable nematic display using monostable surface switching. *Applied Physics Letters*, 70:1179, 1997.

[80] J G McIntosh and F M Leslie. Flow induced surface switching in a bistable nematic device. *Journal of Engineering Mathematics*, 73:129, 2000.

[81] A Mazzulla, F Cuichi, and J R Sambles. Optical determination of flexoelectric coefficients and surface polarization in a hybrid aligned nematic cell. *Physical Review E*, 64:021708, 2001.

[82] S R Arridge. Optical tomography in medical imaging. *Inverse problems*, 15:R41, 1998.

[83] R Al-Khoury, A Scarpas, C Kasbergen, and J Blaauwendraad. Spectral element technique for efficient parameter identification of layered media part I: Foward calculation. *International Journal of Solids and Structures*, 38:1605, 2001.

[84] R Al-Khoury, C Kasbergen, A Scarpas, and J Blaauwendraad. Spectral element technique for efficient parameter identification of layered media part II: Inverse calculation. *International Journal of Solids and Structures*, 38:8753, 2001.

[85] K Mosegaard and A Tarantola. Monte Carlo sampling of solutions to inverse problems. *Journal of Geophysical Research*, 100:12431, 1995.

[86] A Tarantola and B Valette. Generalized nonlinear inverse problems solved using the least squares criterion. *Reviews of Geophysics and Space Physics*, 20:219, 1982.

[87] H Wöhler, G Haas, M Fritsch, and D A Mlynski. Characteristic matrix method for stratified anisotropic media: optical properties of special configurations. *Journal of the Optical Society of America A*, 8:536, 1990.

[88] I I Smalyukh, S V Shiyanovskii, and O D Lavrentovich. Three-dimensional imaging of orientational order by fluorescence confocal polarizing microscopy. *Chemical Physics Letters*, 336:88, 2001.

[89] Fuzi Yang and J R Sambles. Optical fully leaky mode characterization of a standard liquid-crystal cell. *Journal of the Optical Society of America B*, 16:488, 1999.

[90] Fuzi Yang, J R Sambles, Youmei Dong, and Hongjin Gao. Fully leaky guided wave determination of the polar anchoring energy of a homogeneously aligned nematic liquid crystal. *Journal of Applied Physics*, 87:2726, 2000.

[91] Fuzi Yang, Lizhen Ruan, and J R Sambles. Homeotropic polar anchoring energy of a nematic liquid crystal using the fully leaky waveguide technique. *Journal of Applied Physics*, 88:6175, 2000.

[92] N J Smith and J R Sambles. Convergent beam guided mode technique for use in liquid crystal studies. *Journal of Applied Physics*, 85:3984, 1999.

[93] L Z Ruan and J R Sambles. Dynamics of a twisted nematic cell using a convergent beam system. *Journal of Applied Physics*, 92:4857, 2002.

[94] Fuzi Yang and Sambles J R. Optical characterization of liquid crystals by means of half-leaky guided modes. *Journal of the Optical Society of America B*, 10:858, 1993.

[95] Fuzi Yang, Jewell S A, Lizhen Ruan, and Sambles J R. Complex permittivities of a nematic liquid crystal in a hybrid-aligned cell. *Journal of the Optical Society of America B*, 24:527, 2007.

[96] Lavers C and Sambles J R. An examination of the optical dielectric tensor of a liquid crystal waveguide. *Ferroelectrics*, 113:339, 1991.

[97] K R Welford, J R Sambles, and M G Clark. Guided modes and surface plasmon-polaritons observed with a nematic liquid crystal using attenuated total reflection. *Liquid Crystals*, 2: 91, 1987.

[98] S J Elston and J R Sambles. The configuration in a ferroelectric liquid crystal cell in terms of a rigid chevron structure. *Molecular Crystals and Liquid Crystals*, 200:167, 1991.

[99] B L Van Horn and H H Winter. Analysis of the conoscopic measurement for uniaxial liquid-crystal tilt angles. *Applied Optics*, 40:2089, 2001.

[100] D M Boudreau, H H Winter, C P Lillya, and R S Stein. Conoscopic observations of shear-induced rotations in nematic liquid crystals. *Rheologica Acta*, 38:503, 1999.

[101] N A Vaz, J W Doane, and M E Neubert. Polymorphism in a lamellar liquid-crystal bilayer system. *Physical Review Letters*, 42:1406, 1979.

[102] Ewa Gorecka, A D L Chandani, Yukio Ouchi, Hideo Takezoe, and Atsuo Fukuda. Molecular orientational structures in ferroelectric, ferrielectric and antiferroelectric smectic liquid crystal phases as studied by conoscope observation. *Japanese Journal of Applied Physics*, 29:131, 1990.

[103] T Fujikawa, K Hiraoka, T Isozaka, K Kajikawa, H Takezoe, and A Fukuda. Construction of dynamic conoscope observation system using CCD camera and image processor. *Japanese Journal of Applied Physics*, 32:985, 1993.

[104] L A Parry-Jones, E Kriezis, and S J Elston. Conoscopic observations of a homeotropically aligned antiferroelectric liquid crystal device: a comparison of theory and experiment. *Japanese Journal of Applied Physics*, 41:L1485, 2002.

[105] E K Tidey, L A Parry-Jones, and S J Elston. Determination of the difference of flexoelectric coefficients in a nematic liquid crystal using a conoscopic technique. *Liquid Crystals*, 34:251, 2007.

[106] R C Jones. A new calculus for the treatment of optical systems. *Journal of the Optical Society of America*, 31:488, 1941.

[107] Pochi Yeh. Extended Jones matrix method. *Journal of the Optical Society of America*, 72: 507, 1982.

[108] A Lien. Extended Jones matrix representation for the twisted nematic liquid-crystal display at oblique incidence. *Applied Physics Letters*, 57:2767, 1990.

[109] A Lien. A detailed derivation of extended Jones matrix representation for twisted nematic liquid crystal displays. *Liquid Crystals*, 22:171, 1997.

[110] C Gu and Pochi Yeh. Extended Jones matrix method. II. *Journal of the Optical Society of America A*, 10:966, 1993.

[111] D W Berreman. Optics in stratified and anisotropic media: 4 x 4-matrix formulation. *Journal of the optical society of America*, 62:502, 1972.

[112] S Teitler and B W Henvis. Refraction in stratified, anisotropic media. *Journal of the Optical Society of America*, 60:830, 1970.

[113] R E Camley, N Raj, and D R Tilley. Numerical modeling of guided optical waves in liquid-crystal structures. *Journal of the Optical Society of America B*, 7:367, 1990.

[114] H Wöhler, G Haas, M Fritsch, and D A Mlynski. Faster 4 X 4 matrix method for uniaxial inhomogeneous media. *Journal of the Optical Society of America A*, 5:1554, 1988.

[115] D Y K Ko and J R Sambles. Scattering matrix method for propagation of radiation in stratified media: attenuated total reflection studies of liquid crystals. *Journal of the Optical Society of America A*, 5:1863, 1988.

[116] A Tarantola. *Inverse problem theory*. SIAM, 2005.

[117] J Hadamard. *Lectures on Cauchy's problem in linear partial differential equations*. Courier Dover Publications, 2003. Reprint of a volume originally printed in 1902.

[118] P C Hansen. Regularization tools: A MATLAB package for analysis and solution of discrete ill-posed problems. *Numerical Algorithms*, 6:1, 1994.

[119] A N Tikhonov, A S Leonov, and A G Yagola. *Nonlinear ill-posed problems*, volume Volume 1. Chapman and Hall, English language edition, 1998.

[120] W R B Lionheart and C J P Newton. Analysis of the inverse problem for determining nematic liquid crystal director profiles from optical measurements using singular value decomposition. *New Journal of Physics*, 9:63, 2007.

[121] M T Heath. *Scientific computing: an introductory survey*. McGraw-Hill, second edition, 2002.

[122] J C Lagarias, J A Reeds, M H Wright, and P E Wright. Convergence properties of the Nelder–Mead simplex method in low dimensions. *SIAM Journal on Optimization*, 9:112, 1998.

[123] N Polydorides. Interior point methods for ill-posed problems: A primal-dual solver for the box-constrained inverse conductivity problem. Pre-print available at `http://www.ma.umist.ac.uk/np/pdipm.pdf`.

[124] S Twomey. On the numerical solution of fredholm integral equations of the first kind by the inversion of the linear system produced by quadrature. *Journal of the Association for Computing Machinery*, 10:97, 1963.

[125] N Polydorides. Electromagnetic inverse problems for nematic liquid crystals and capacitance imaging. MIMS EPrint 2007.15, University of Manchester, 2007.

[126] P C Hansen. Analysis of discrete ill-posed problems by means of the L-curve. *SIAM Review*, 34:561, 1992.

[127] P C Hansen. The truncated SVD as a method for regularization. *BIT Numerical Mathematics*, 27:534, 1987.

[128] P C Hansen. The discrete picard condition for discrete ill-posed problems. *BIT Numerical Mathematics*, 30:658, 1990.

[129] P C Hansen. Regularization, GSVD and truncated GSVD. *BIT Numerical Mathematics*, 29: 491, 1989.

[130] S Laux, N Kasier, A Zöller, R Götzelmann, H Lauth, and Bernitzki. Room-temperature deposition of indium tin oxide thin films with plasma ion-assisted evaporation. *Thin Solid Films*, 335:1, 1998.

[131] J Birkett. *Chiral HAN cells : a novel liquid crystal arrangement*. PhD thesis, University of Exeter, 2007.

[132] R P Feynman, R B Leighton, and M Sands. *The Feynmann Lectures on Physics, volume II, chapter 41*. Addison-Wesley, 1964.

[133] H J Deuling. Deformation pattern of twisted nematic liquid crystal layers in an electric field. *Molecular Crystals and Liquid Crystals*, 27:81, 1972.

[134] K R Welford and J R Sambles. Analysis of electric field induced deformations in a nematic liquid crystal for any applied field. *Molecular Crystals and Liquid Crystals*, 147:25, 1987.

[135] T W Preist, K R Welford, and J R Sambles. Response of a twisted nematic liquid crystal to any applied potential. *Liquid Crystals*, 4:103, 1989.

[136] Qian Wang, Sailing He, Feihong Yu, and Nairong Huang. Iterative finite-difference method for calculating the distribution of a liquid-crystal director. *Optical Engineering*, 40:2552, 2001.

[137] S V Patankar. *Numerical heat transfer and fluid flow*. Taylor and Francis, 1980.

[138] R Development Core Team. *R: A Language and Environment for Statistical Computing*. R Foundation for Statistical Computing, Vienna, Austria, 2008.

[139] C V Brown and N J Mottram. Influence of flexoelectricity above the nematic Fréedericksz transition. *Physical Review E*, 68:031702, 2003.

[140] I A Gura and R H Gersten. Interpretation of n-dimensional covariance matrices. *AIAA Journal*, 9:207, 1970.

[141] N Metropolis and S Ulam. The Monte Carlo method. *Journal of the American Statistical Association*, 44:335, 1949.

[142] N Metropolis, A W Rosenbluth, M N Rosenbluth, H Teller, and E Teller. Equation of state calculations by fast computing machines. *Journal of Chemical Physics*, 21:1087, 1953.

[143] C Geyer. GNU R package 'mcmc'. available on CRAN at http://cran.r-project.org/web/packages/mcmc/, 2005.

[144] S L Cornford, T S Taphouse, C J P Newton, and J R Sambles. Determination of the director profile in a nematic cell from guided wave data: an inverse problem. *New J Physics*, 9:166, 2007.

[145] S Meiboom and R C Hewitt. Measurements of the rotational viscosity coefficient and the shear-alignement angle in nematic liquid crystals. *Physical Review Letters*, 30:261, 1972.

[146] P D Brimicombe and E P Raynes. Symmetric H state lifetime in splayed nematic liquid crystal devices. *Applied Physics Letters*, 89:031121, 2006.

[147] Toyokazu Ogasawara, Tomoo Akizuki, Yoichi Takanishi, Ken Ishikawa, and Hideo Takezoe. Simulation of conoscopic figures using 4 x 4 matrix method. *Molecular Crystals and Liquid Crystals*, 362:255, 2001.

[148] A A T Smith, C V Brown, and N J Mottram. Theoretical analysis of the magnetic Freedericksz transition in the presence of flexoelectricity and ionic contamination. *Physical Review E*, 75:041704, 2007.

[149] S J Elston. Flexoelectricity in nematic domain walls. *Physical Review E*, 78:011701, 2008.